INVESTIGATION OF THE STRUCTURE-PROPERTY-PROCESSING RELATIONSHIPS IN PAPER AND CARBON NANOTUBE COMPOSITE MATERIALS

A Dissertation
Presented to
The Academic Faculty

by

Rachel Lynn Muhlbauer

In Partial Fulfillment
of the Requirements for the Degree
Doctor of Philosophy in the
School of Materials Science and Engineering

Georgia Institute of Technology
August 2014

INVESTIGATION OF THE STRUCTURE-PROPERTY-PROCESSING RELATIONSHIPS IN PAPER AND CARBON NANOTUBE COMPOSITE MATERIALS

Approved by:

Dr. Rosario Gerhardt, Advisor
School of Materials Science and Engineering
Georgia Institute of Technology

Dr. David Bucknall
School of Materials Science and Engineering
Georgia Institute of Technology

Dr. Dong Qin
School of Materials Science and Engineering
Georgia Institute of Technology

Dr. Jud Ready
Georgia Tech Research Institute
Georgia Institute of Technology

Dr. Jason Nadler
Georgia Tech Research Institute
Georgia Institute of Technology

Date Approved: June 24, 2014

To Dr. Billy Jones, the catalyst for my love of chemistry

ACKNOWLEDGEMENTS

I would like to start out by acknowledging my advisor, Dr. Gerhardt, for her ability to keep me motivated and to always push me. I want to also express my gratitude to my committee members for their kindness, assistance, and flexibility: Dr. Ready, Dr. Qin, Dr. Bucknall, and Dr. Nadler. I would also like to express my gratitude to everyone in MSE's front office and especially Susan Bowman: you are the heart of this department, and we'd all be lost without you.

I would also like to acknowledge the funding and financial support I've received to help complete this thesis: Boeing Fellowship, Georgia Tech Integrative Graduate Education and Research Training: Nanomaterials for Energy Storage and Conversion, and the National Science Foundation DMR- 120732. In addition, I would like to extend a huge thank you to the people at the Georgia Tech IEN, Dr. Meisha Shofner, Dr. Salil Joshi (HR-TEM images), Dr. Vladimir Tsukruk, Seth Young, and Dr. Zac Combs for their assistance in my research along the way.

To my labmates Tim Pruyn, Salil Joshi, Justin Brandt, Ryan Gussenhoven, Waylon Puckett Anna Janoff, Gregory Cooke, and Brian Betram for your invaluable amount of help in completing my thesis. Thank you to Dr. Sanders and Dr. Thadhani for your open office doors over the years. To all of the friends I've made throughout my many years here at Tech: I am so fortunate that there are so many of you that I don't have the space to list you all. You all hold a special place in my heart. In particular, I don't know how I would have survived this process without my best friends, Tim Pruyn,

Rachel Guim, and Michael Feldman. You've been there every step of the way, and I don't know if it is possible to repay you for everything you've done for me.

Finally, I am endlessly thankful to my loved ones who never wavered in their belief in me. To my parents, Carla and Walter Muhlbauer, thank you for letting me follow my path and supporting me as I walk it. To Rochelle Kallish, your advice has been invaluable in keeping me moving. To Logan Weaver, your support makes each day a little bit easier to get through, and I will always appreciate being able to lean on you.

TABLE OF CONTENTS

LIST OF TABLES

LIST OF FIGURES

LIST OF SYMBOLS AND ABBREVIATIONS

CNT	Carbon Nanotube
SWNT	Single Walled Carbon Nanotube
MWNT	Multiwalled Carbon Nanotube
DC	Direct Current
AC	Alternating Current
AFM	Atomic Force Microscopy
I-AFM	Current-Atomic Force Microscopy
SDBS	Sodium dodecylbenzenesulfonate
SEM	Scanning Electron Microscopy
OM	Optical Microscopy
TEM	Transmission Electron Microscopy
HR-TEM	High Resolution-Transmission Electron Microscopy
FTIR	Fourier Transform Infrared Spectroscopy
DSC	Differential Scanning Calorimeter
TGA	Thermogravimetric Analysis
L-MWNT	Long-Multiwalled Carbon Nanotube
wt%	Weight Percent
Z^*	Complex Impedance (Ω)
Z’	Real Impedance (Ω)
Z”	Imaginary Impedance (Ω)
$\|Z\|$	Impedance Magnitude (Ω)
f	Frequency (Hz)
I	Current (A)
V	Voltage (V)
θ	Phase Angle (°)
ω	Angular Frequency ($\omega = 2\pi f$)
j	The imaginary unit
R	Resistance (Ω, Ohm)
C	Capacitance (F, Farad)
L	Inductance (H, Henry)
mg/mL	milligram/milliliter
L_b	Bundle Length
d_p	Pore Diameter
nm	Nanometer
μm	Micron
$R_{percolation}$	Resistance at Percolation Threshold (Ω)
L_c	Critical Number of Layers Required for Percolation
L	Layer Number
β	Percolation Scaling Law Critical Exponent
$R_{in\text{-}plane}$	In-Plane Resistance (Ω)
$R_{thru\text{-}plane}$	Thru-Plane Resistance (Ω)

CPE	Constant Phase Element
R	Resistor
C	Capacitor
L	Inductor
R_b	Bundle Resistance (Ω)
R_j	Junction Resistance (Ω)
R_{cb}	Coiled/Curved Bundle Resistance (Ω)
R_p	Resistance of Uncoated Paper Surface (Ω)
R_t	Transitional Resistance (Ω)
R_B	Bulk Resistance (Ω)
$R_{internal}$	Resistance of Uncoated or Coated Paper Pores (Ω)
$R_{surface}$	Resistance of Surface Network Measured Through its Thickness (Ω)

SUMMARY

In this research, multiwalled carbon nanotube (MWNT) and paper composite materials were fabricated by dropcasting aqueous dispersions containing MWNTs onto filter paper using vacuum filtration, a highly unidirectional drying technique. By varying the pore size of the paper backbone as well as the number of deposited MWNT layers, composites with distinct architectures and properties were created. This thesis provides numerous examples that show how the processing methodology used influences the location of the MWNTs, the amount of MWNTs deposited, and the interaction between the MWNTs and the paper backbone. These three factors work in tandem to form the structures and properties presented.

Understanding how the structures and properties come about allows for the tailorability of these composites for different applications and devices. The pore size of the backbone material combined with the directionality of the drying methodology controlled the location of MWNT deposition. MWNT deposition occurred in three ways: on the paper surface only, within the paper material only, or combined surface and internal deposition. By varying the number of deposition steps, the properties of the composite could be altered in the location of deposition. Surface charge, dispersion concentration, paper pore size, drying methodology, MWNT length, the number of deposited MWNT layers, and post-processing techniques were all factors studied in this thesis which could successfully vary the interaction between the MWNTs and between the MWNT and paper materials and, ultimately, alter the properties of the composite.

Regardless of the processing methodology employed and the starting materials used, structure and property evolutions in the composite materials were characterized using impedance spectroscopy, optical microscopy, scanning electron microscopy, and Current-AFM. Combining equivalent circuit fitting of the impedance data with the information obtained from the imaging techniques allowed for the elucidation of structural mechanisms which contribute to the electronic response measured for each composite. An overall equivalent circuit was built for each composite plane which could then be used to extract the electrical properties of the individual conduction mechanisms within the composite. In the in-plane, the electrical properties of the paper backbone, MWNT-MWNT junctions, MWNT bundles, and MWNT curved bundles could be determined. In the thru-plane, the electrical properties within the paper thickness, either paper-dominated or MWNT-dominated, could be measured. The resistance through the thickness of a bulk MWNT surface network could be also measured when the density of the MWNT network is sufficiently high.

CHAPTER 1

INTRODUCTION AND LITERATURE REVIEW

1.1 Introduction

Paper is commonplace in day-to-day life, spanning the mundane, such as taking notes, to the extraordinary, including usage in transformer boards, because of its mechanical flexibility, low weight, wide variance in architecture, and low cost. The cost/area (in $\$/m^2$) for paper is orders of magnitude lower than that of other commonly used substrate materials [1]. Since cost and weight reduction often motivates research and eventually commercialization, the drive to use paper in new ways and in new applications has never been greater.

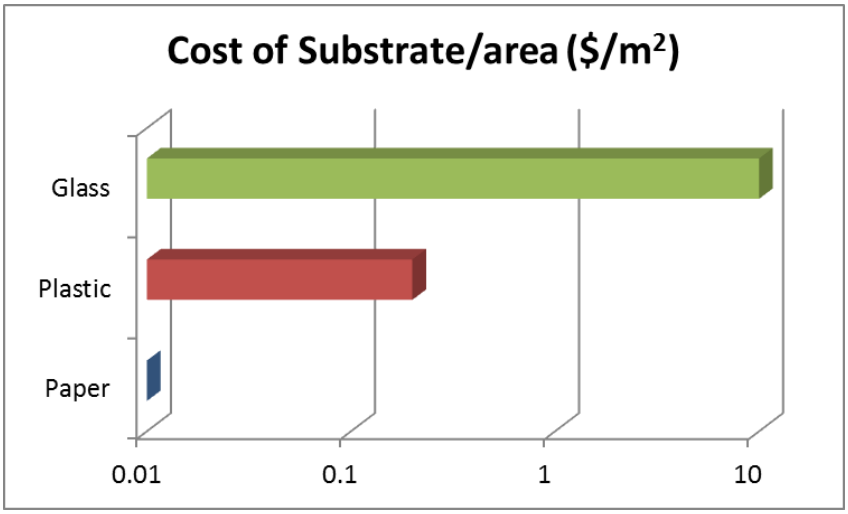

Figure 1.1: Comparison of the cost of different substrate materials (in $\$/m^2$) showing a 10x decrease in cost when paper is employed rather than a PET plastic and a 1000x decrease in cost when paper is employed rather than borosilicate glass [1].

Filter paper is an interesting but underutilized substrate, particularly in the field of electronics and energy storage (limited to a single study on supercapacitor materials [2]), although it has been used liberally in the biomedical and environmental fields [3, 4]. Unlike many of the other types of paper, filter paper contains a filler-free internal structure, a coating-free surface, and a pore network whose diameter can be controlled. These structural properties result in a unique opportunity during fabrication: material can be deposited within the paper, on the surface of the paper, or in both locations simultaneously by controlling the properties of the deposited material as well as the deposition parameters. A multitude of morphologies and properties can be formed as a function of deposition location which results in the ability to tailor structure and properties for specific applications or devices.

The objective of this research is to enhance the understanding of how the addition of multiwalled carbon nanotubes (MWNTs) to paper affects the structure which develops during fabrication and how this structure leads to the properties of the final material. Composite materials will be formed by dropcasting MWNTs onto filter paper substrates from aqueous dispersions as water is a low cost and safe dispersant and then by drying using vacuum filtration. Employing vacuum filtration as a drying methodology allows for deposition which relies heavily on the pore size of the paper backbone as well as the length of the MWNT [5]. Determining how these processing parameters work together to form the composite material is paramount to understanding how the properties of these composite materials arise and, eventually, how the properties can be varied.

The relevant literature for this research is presented in the rest of Chapter 1. Chapter 2 gives a detailed description of the composite fabrication methodology as well

as several characterization techniques employed in this thesis. In Chapter 3, the structure-property relationships for the vacuum filtered multilayered composite materials are described for chemical, thermal, and electronic properties. An empirical percolation-based model which can be used to predict the DC electrical resistance of these materials is presented.

In Chapter 4, impedance spectroscopy is used to further develop an understanding of the structure-property relationships. From the results determined using impedance spectroscopy as well as the structural results given in Chapter 3, equivalent circuit models and structural models are developed which can be used to describe the conduction mechanisms present in the composite materials as well as their individual properties. This chapter shows a direct correlation between the spatial arrangement of the MWNTs and the paper fibers and the electrical properties which are exhibited, all of which can be determined using impedance spectroscopy.

In Chapters 5 and 6, alterations are made to the processing methodology which results in new composite morphologies and properties. These alterations include variations to both the dropcasting and the drying methods as well as the addition of further processing steps. In Chapter 7, a methodology for predicting the electronic behavior of the composite materials presented in Chapters 3-6 from structural parameters is described and validated. Finally, Chapter 8 will summarize the highlights of this thesis and provide context for future work. Some of the figures, tables, and data presented in this thesis have already been published by the authors. References are provided in all of those cases.

1.2 Literature Review

1.2.1 Properties of Paper

Since paper will be used as the backbone material in this project, it is important to understand the different types of paper available as well as their properties. Paper consists of a random network of cellulose fibers (chemical structure = $(C_6H_{10}O_5)_n$) which are held together by moisture-aided hydrogen bonding between two contacting fibers. In hydrogen bonding of the cellulose fibers, an electromagnetic attractive bond is created between polar components of the chemical structure (-OH). As the paper is dried and the water in the structure is removed, the bond strength increases [6]. During the processing of the paper material, the properties of the paper material can be changed depending on its final application. Paper surfaces can be made rough or smooth and coated or uncoated. The pores which exist between paper fibers can be left unfilled, such as is the case for filter papers, or other constituents can be added to fill in the pores to change the properties of the paper [7].

Historically, paper has been constrained to being used as a dielectric or separator material due to its insulating nature [8]. When an electric field is applied to an insulator/dielectric medium, point charges in the dielectric polarize in order to reduce the electric field. The ability of a material to charge separate and dissipate the electric field is quantified as the dielectric constant. Materials with high dielectric constants dissipate more of the electric field: the higher the dielectric constant, the more charge that can be stored in the material. In addition, the dielectric constant is frequency-dependent.

Because polarization mechanisms respond to electric fields by shifting mass around, the ability of the material to constantly adjust to a sinusoidal force is impacted by the frequency of oscillation. As frequency increases, it becomes more difficult for charge to separate and the field to be mitigated, decreasing the dielectric constant of the material. For dry paper, the dielectric constant generally falls between 2 and 4; however, this number is highly variable depending on the frequency of the measurement, measurement direction, relative humidity, paper type, and filler content [9]. These trends are shown graphically in Figure 1.2 which plots dielectric constant vs. frequency for different types of paper (1.2a) and dielectric constant vs. relative humidity for different papers and measurement directions (1.2b) [9].

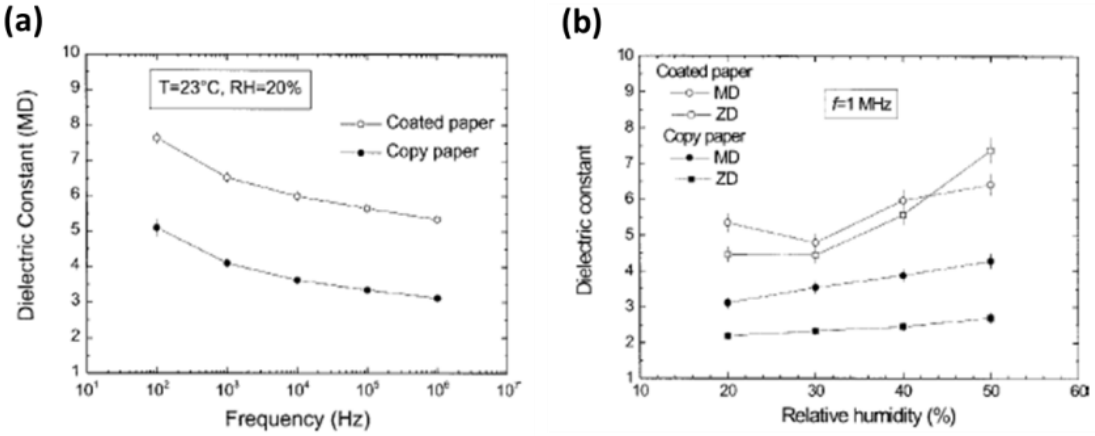

Figure 1.2: Variation of dielectric constant for coated paper and copy paper at (a) varying frequency and constant temperature and pressure; (b) varying relative humidity and measurement direction at constant frequency [9].

The electrical properties of paper substrates are also controlled by relative humidity. In a study where relative humidity was increased from 1% to 99%, the resistance of cellulose was found to decrease 8 orders of magnitude, from 10^{12} Ω to 10^{4} Ω [10]. At 20-40% relative humidity, resistivity values of 10^{10}-10^{14} Ω*cm and sheet resistances of 10^{11}-10^{15} Ω/sq have been measured for paper networks [11]. Since the resistivity and sheet resistance of paper is so high, in order to use paper in electronics in

non-traditional ways, it is necessary to add a filler material to the paper which will enable current to flow. Filler material can be added during or after the papermaking process.

1.2.1.1 Paper in Electronics and Energy Storage

While the cost of the substrate is very low, the cost of the techniques used to create electrically conductive paper-based materials are often not cost effective. It is possible to add conducting materials during a part of the papermaking process such that the paper which is made contains the conductive filler. However, this process also requires specialized equipment as well as a considerable amount of time to coat the fibers in the conductive material [12].

Inkjet printing is one of the more popular methods for creating conductive films on the surface of the paper after the papermaking process [13]. A very fine resolution and interesting patterns can be printed using this methodology. A successful ink for printing requires either harsh solvents to disperse the printing material or functionalization of the printing material for dispersion in water. Harsh solvents add a degree of cost due to safety concerns. Functionalization decreases the electrical properties of the ink, leading to a large number of printing steps required to achieve only mediocre electrical properties. For example, after 90 printing steps of functionalized carbon nanotubes (CNTs), sheet resistances of ~0.1 MΩ/sq were measured [13]. While interesting shapes can be printed, materials costs, equipment costs, and safety costs increase the price of fabrication, potentially negating the cost savings by using paper as the substrate material.

Field emission has been demonstrated previously for multiwalled carbon nanotube (MWNT) and paper devices created using a dipcoating procedure using papers with varying surface roughness [14]. Lyth et al. used MWNTs which were dispersed in water only after being oxidized through a harsh acid treatment step. It was determined that as the surface roughness of the paper increased, the threshold field decreased and the geometric enhancement factor increased by an order of magnitude [14]. In addition, increasing the roughness of the MWNT film yielded the same decrease in threshold field [15]. Additionally, single walled carbon nanotubes (SWNTs) have been deposited from aqueous dispersion onto Xerox paper using a Meyer Rod deposition technique and sheet resistances of 10 Ω/sq have been achieved [16]. These composites were shown to be able to be bent to a radius of 2 mm and still retain their low sheet resistance, which is ideal for flexible electrode devices [17]. These composites have also shown use for supercapacitors as specific capacitances of up to 200 F/g have been measured in a sulfuric acid electrolyte [16].

A SWNT-coated cotton paper supercapacitor electrode has been fabricated using the dipcoating technique [18]. The SWNTs were acid treated and then dispersed in water to create a stable suspension of SWNTs without surfactant. To fabricate the electrode, the cotton paper was dipped in the suspension and then dried at 120°C on a hot plate. These steps were repeated until a sheet resistance of 10 Ω/sq was achieved. Using a solid state electrolyte, specific capacitances of 13.15 F/g and specific energies of 5.54 Wh/kg were measured [18].

Vacuum filtration of graphene nanosheets (GNS) of < 2 μm in length into paper has been used previously to make flexible supercapacitors [2]. In this study conducted by

Weng et al., the GNS suspension was filtered through a sheet of filter paper (pore size = 10 μm) from both sides of the paper and the GNS content deposited into the paper was controlled by varying the suspension concentration. Figure 1.3 shows the areal energy vs. areal power graph for these composites in different electrolytes and stackings/configurations showing that these composites could be useful for power sources in microelectromechanical systems [2].

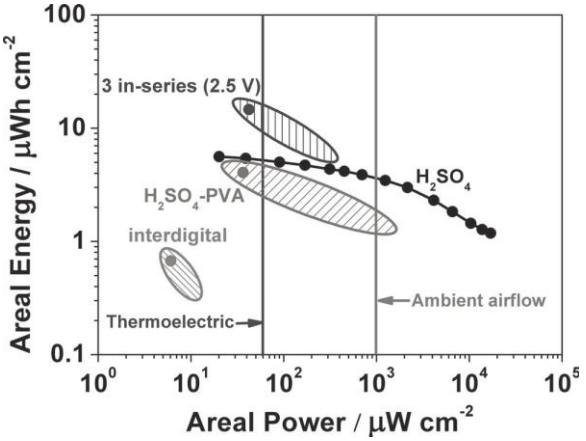

Figure 1.3: Areal energy vs. areal power for various GNS-paper composites using a variety of stacking arrangements and electrolytes [2].

1.2.2 Properties of Carbon Nanotubes

While there are many filler materials that could be added to paper to improve its electrical properties, the filler material used in this thesis is the carbon nanotube (CNT). The discovery of multiwalled carbon nanotubes (MWNTs) [19] and single walled carbon nanotubes (SWNTs) [20] has led to an increased interest in research and publications due to their exceptional theoretical properties: electrical mobility above 100,000 $cm^2/(V*s)$, a conductivity approaching 200,000 S/cm, and a current carrying capacity of 10^9 A*cm [21-23], thermal conductivities between 3000 and 6600 W/(m*K) at room temperature [24], and specific surface areas between 50 and 1315 m^2/g have been calculated for CNTs and bundles of CNTs [25].

1.2.2.1 Electrical Properties of Carbon Nanotubes

The properties of the CNT arise because of its tubal structure. The SWNT can be described as a sheet of graphene which is then folded into a cylindrical tube. The MWNT is made up of concentric SWNTs. Each carbon atom in the CNT contains three sp^2 bonds in plane with the tube and 1 unsaturated π-orbital perpendicular to the surface [26]. The sheet of graphite can be rolled in a variety of directions which results in different chiralities (armchair, metallic, zigzag) and radii which impact the properties of the tube. All armchair tubes are metallic, and zigzag tubes are metallic under specific folding conditions. If these conditions are not met or the SWNT is designated as achiral, the SWNT is semiconducting [27]. Each nanotube is uniquely defined by its $\mathbf{C_h}$, the chiral or roll-up vector (also sometimes labeled as **r**), which is the circumference of the tube when rolled and can be defined as shown in Equation 1.1. n and m are magnitude integers as shown in Figure 1.4 [28].

$$\mathbf{C_h} = n\mathbf{R_1} + m\mathbf{R_2} \tag{1.1}$$

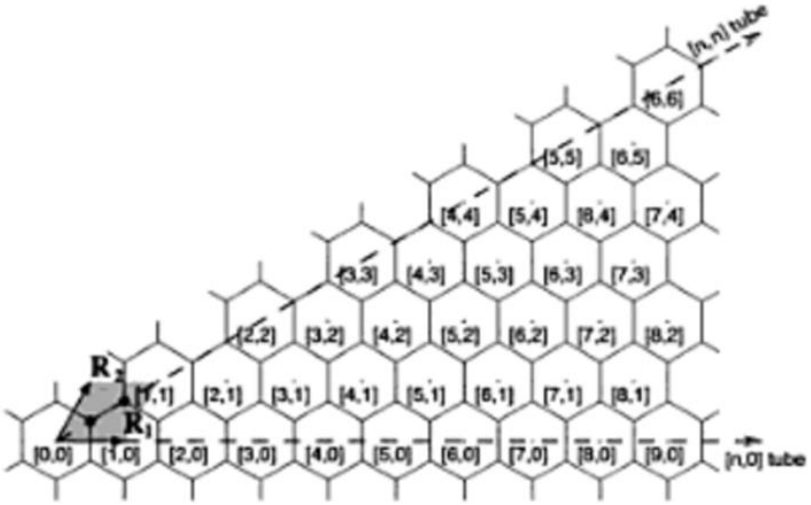

Figure 1.4: Schematic showing the determination of n,m with respect to the graphene lattice vectors, R_1 and R_2 [28]

A single CNT should behave as a quantum wire due to the confinement effect on the tube circumference. Perfect quantum wire behavior, however, is rare since the type, diameter, and curvature of CNTs cause a deviation of properties from ideality. In addition, CNTs tend to group together and form bundles rather than exist as a single wire, further impacting the properties of the CNT [29]. For SWNTs, resistance increases nonlinearly with the length of the tube (from 350 to 2100 nm) [30]. Computational modeling confirmed the outcome of this experiment, suggesting that the nonlinear resistance behavior is an intrinsic property of SWNTs [31]. Intertube coupling which arises from having either bundles of SWNTs or MWNTs also impacts the properties of the CNT. When the π clouds of different types of CNTs overlap, metallic CNTs can have an induced band gap while the band gap in semiconducting CNTs can be reduced by up to 40% [29].

In the case of MWNTs, the band structures from each SWNT that makes up the MWNT contribute to the overall band structure of the tube. Double-walled carbon nanotubes (DWNTs) are MWNTs with only two components: an inner tube and an outer tube. The tube is described by the chiral vector of each tube as $(n_1, m_1)@(n_2, m_2)$ where 1 describes the inner tube and 2 describes the outer tube. Figure 1.5 shows what happens to the band structures of 2 SWNTs when they are combined to make a DWNT [32]. As shown on the left of Figure 1.5, when a metallic and a semiconducting SWNT are combined to create a DWNT, the Fermi level of the combined DWNT falls within the band structure, indicative of metallic electronic conduction. Electrons flow preferentially through the metallic SWNT. As is shown to the right of Figure 1.5, when two

semiconducting tubes are put together to make a DWNT, the Fermi energy remains between the valence and conduction bands, although the band gap decreases [32].

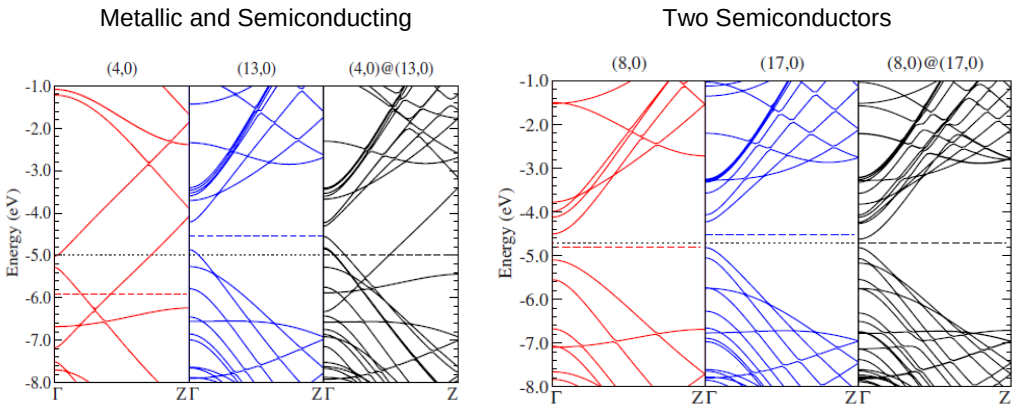

The band structures calculated by LDA for (4,0) SWNT (red) , (13,0) SWNT (blue), and (4,0)@(13,0) DWNT

The band structures calculated by LDA for (8,0) SWNT (red) , (17,0) SWNT (blue), and (8,0)@(17,0) DWNT

Figure 1.5: Band structures for a DWNT made up of metallic and semiconducting SWNTs (left) and two semiconducting SWNTs (right) [32].

The transition from SWNT to DWNT helps to understand how the addition of more tubes would impact the electronic structure and why MWNTs are often described as zero band-gap semiconductors. It is suggested that at least one of the tubes within the MWNT will be metallic-conducting- dropping the Fermi energy within the band structure [32]. The properties of the MWNT are type-dependent, diameter-dependent, and curvature-dependent. Measuring the electrical properties of a single MWNT showed that as diameter increased, the resistance decreased for tubes of similar curvature [33]. Alternatively, as the curvature increased, the resistivity of the tubes increased which is likely due to defects created during bending [33].

1.2.2.2 Properties of Carbon Nanotube Networks- Thin Films

While it is important to understand the behavior of individual CNTs, most deposition methods for CNTs from solution/dispersion, including those used in this thesis, result in randomly oriented arrangements of CNTs, wherein the tubes lie directly on the substrate and interact with one another [34]. When two tubes come together on a substrate, the CNT-substrate attraction results in a force which presses one tube against another [35]. As a result, the random network of CNTs has two structural components: (1) bundles of CNTs and (2) the junctions between different bundles of CNTs. Figure 1.6 depicts the structure of a CNT network including the bundles of CNTs (blue rods) and the junctions between CNTs (green circles).

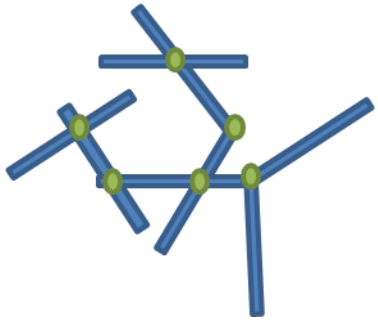

Figure 1.6: Bundles of CNTs (blue rods) and the junctions (green circles) between bundles for a randomly oriented CNT network.

When the density of CNTs on a substrate is low, the overlap between CNTs results in an interaction of the delocalized π clouds of each CNT, and electrons can tunnel from one tube to the next. Electrical conduction occurs across a single tube or bundle following the ballistic conduction mechanism. In ballistic conduction, the mean free path of the electron is longer than the length of medium of transport due to lack of scattering mechanisms. For CNT networks, there are two different mechanisms of electronic transport in the CNT network: ballistic conduction along the tube and tunneling between tubes. Electrical conductivity is limited by the high resistance transport mechanism. At

low CNT film densities, the high resistance regime is the CNT-CNT junction where tunneling rather than ballistic conduction is occurring.

When junction resistance > bundle resistance, the conductivity of the CNTs networks varies due to the bundle length and bundle diameter of the CNT. In a study comparing the conductivity of a CNT film to CNT bundle length, L_b, it was shown experimentally that the DC conductivity scales proportionally to $L_b^{1.46}$ [36]. Also of note is that when the length of the tubes approaches 20-30 μm, the resistance along the tube becomes comparable to the resistance of the junctions, likely due to an increased number of defects in the CNT [36]. A molecular modeling approach obtained similar results. As a function of tube length (up to L_b = 10 μm), conductivity was found to scale proportionally to $L_b^{2.32}$. As a function of tube diameter, d, conductivity was found to scale proportionally to $d^{-3.15}$ [37].

The diameter-dependency and junction-dependency of the electronic behavior of SWNT films could be confirmed using current-AFM (I-AFM) [38]. Figure 1.7 shows the impact of the junction between SWNTs on the electrical resistance through the SWNT film. In Figure 1.7a, a single SWNT with a diameter of 1.65 nm interacts with a SWNT bundle with a diameter of 2.3 nm. Figure 1.7b shows the increase in resistance at this junction: there is a 2 times increase in resistance after the SWNT-SWNT junction. Similarly, Figure 1.7d shows the junctions between multiple bundles of CNTs of different diameters while Figure 1.7e shows the jump in resistance at each junction. The junctions between tubes cause an increase in resistance of 2 to 4 times depending on the pathway taken. However, resistance increases of up to 1000x have been detected depending on tube diameter [38].

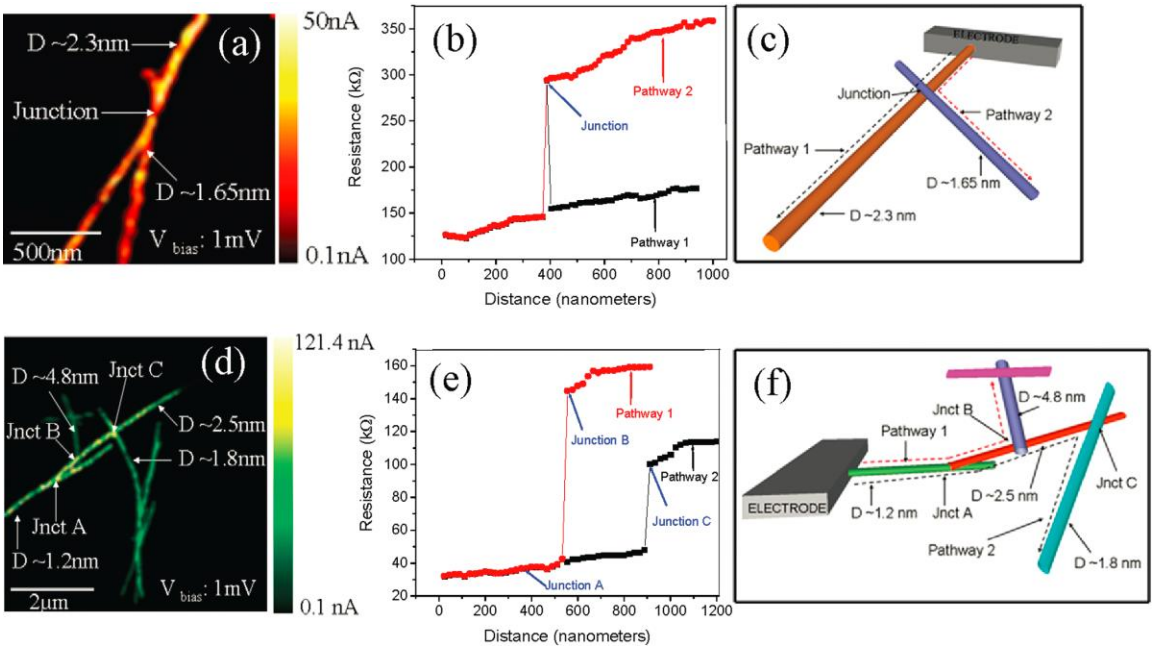

Figure 1.7: I-AFM study on SWNTs of different bundle diameters and corresponding junction resistances. a) I-AFM image of a junction between a single SWNT and a bundle of SWNTs; b) Resistance vs. Distance graph describing the differences between conducting pathways; c) Stick model describing the different pathways and tube diameters for the system in part (a); d) I-AFM for multiple SWNT bundle junctions; e) Resistance vs. Distance graph describing the differences in the multiple current pathways; f) Model describing the different pathways and tube diameters in this system in part (d) [38].

Impedance spectroscopy, which is an AC electrical measurement technique, has been done on low density thin films of SWNTs [39]. It was possible to separate the resistance of the bundles from the resistance of the junctions [39], and the difference in resistance values measured matched that which was determined by the I-AFM study [38]. In that study, the measured impedance spectra exhibited two semicircles in the 1st quadrant of the Nyquist plot. Each semicircle was found to correspond to one of the components of the thin film: the carbon nanotube bundles and the junctions between the bundles. For a film with a density of 0.4 μg/cm^2, the resistances extracted from the data were 6.607 ± 0.108 kΩ for the bundles and 24.392 ± 0.205 kΩ for the junctions. For the film with a density of 1.6 μg/cm^2, the resistances determined were 0.498 ± 0.011 kΩ for

the bundles and 1.066 ± 0.013 kΩ for the junctions [39]. The junction resistance is 2 to 4 times larger than the bundle resistance as expected for low density films.

1.2.2.3 Properties of Carbon Nanotube Networks- Buckypaper

At high densities of CNTs, the junction resistance no longer dominates the properties of the CNT network [40, 41]. The CNT network is three-dimensional in structure, and the overlap of π clouds is so dense that the CNT network forms, essentially, a large ballistic conductor. This type of CNT network is called 'buckypaper.' When the buckypaper is formed by randomly oriented CNTs, the properties of the network are isotropic in all directions, resulting in a highly electrically conductive mat of CNTs [40]. While the electrical resistance of the buckypaper is extremely low, defects in the mat due to defects in the individual tubes as well as a result of processing conditions still limit the material from reaching the theoretical level of properties [41].

1.2.3 Impedance Spectroscopy

AC impedance spectroscopy will be the main electrical technique used to characterize the wide range of paper-CNT composite materials developed in this thesis. While DC electrical characterization techniques are more widely used to obtain electrical properties, the response which is measured by DC techniques describes only the overall response of the sample. The overall response of the sample is a sum of the responses of many different electrical processes in the sample [42]. AC electrical techniques, such as impedance spectroscopy, are frequency dependent, allowing for the measurement and separation of each individual electrical process in the material that contributes to the overall electronic behavior [43, 44].

The impedance of a material, *Z**, is the total resistance (both real, *Z'*, and imaginary, *Z''*) to current flow in a material system. Equation 1.2 is the mathematical definition of impedance: the ratio between applied sinusoidal voltage (Equation 1.3) and its current response (Equation 1.4). The parameter θ is defined as the phase angle or the angular lag between voltage and current, ω is defined as the angular frequency ($\omega = 2\pi f$), and t is time.

$$Z^*(\omega) = \frac{V(\omega)}{I(\omega)} = Z' + jZ'' \tag{1.2}$$

$$V(\omega) = V_m \sin(\omega t) \tag{1.3}$$

$$I(\omega) = I_m \sin(\omega t + \theta) \tag{1.4}$$

The resulting experimental data can be presented in a variety of frequency-implicit and –explicit graphs, all of which are important in gaining a complete understanding of the behavior of the sample. The frequency-implicit Nyquist plot shows imaginary vs. real impedance, -Z'' vs. Z', and its shape offers an abundance of visual clues to aid in understanding the electrical behavior of the measured samples. Frequency-explicit graphs or Bode Plots are also commonly used to present impedance behavior. Presenting the different impedance parts (Z', Z'', θ, and |Z*|, where |Z*| is the impedance magnitude) as function of frequency allows for the determination of what frequency different processes occur at, how wide of a frequency range each process covers, and where transitions between different electrical behavior happens [43-45].

Through careful data analysis and model construction, circuit elements are used to fit the impedance data and describe the electrical processes occurring in the sample. The more common circuit elements and element arrangements as well as their impedance equations are shown in Figure 1.8 [44]. These circuit elements (1.8a) and arrangements (1.8b) are used as 'building blocks' as many materials systems that are measured by this technique often require more complex arrangements to fully understand the system [5, 44-46].

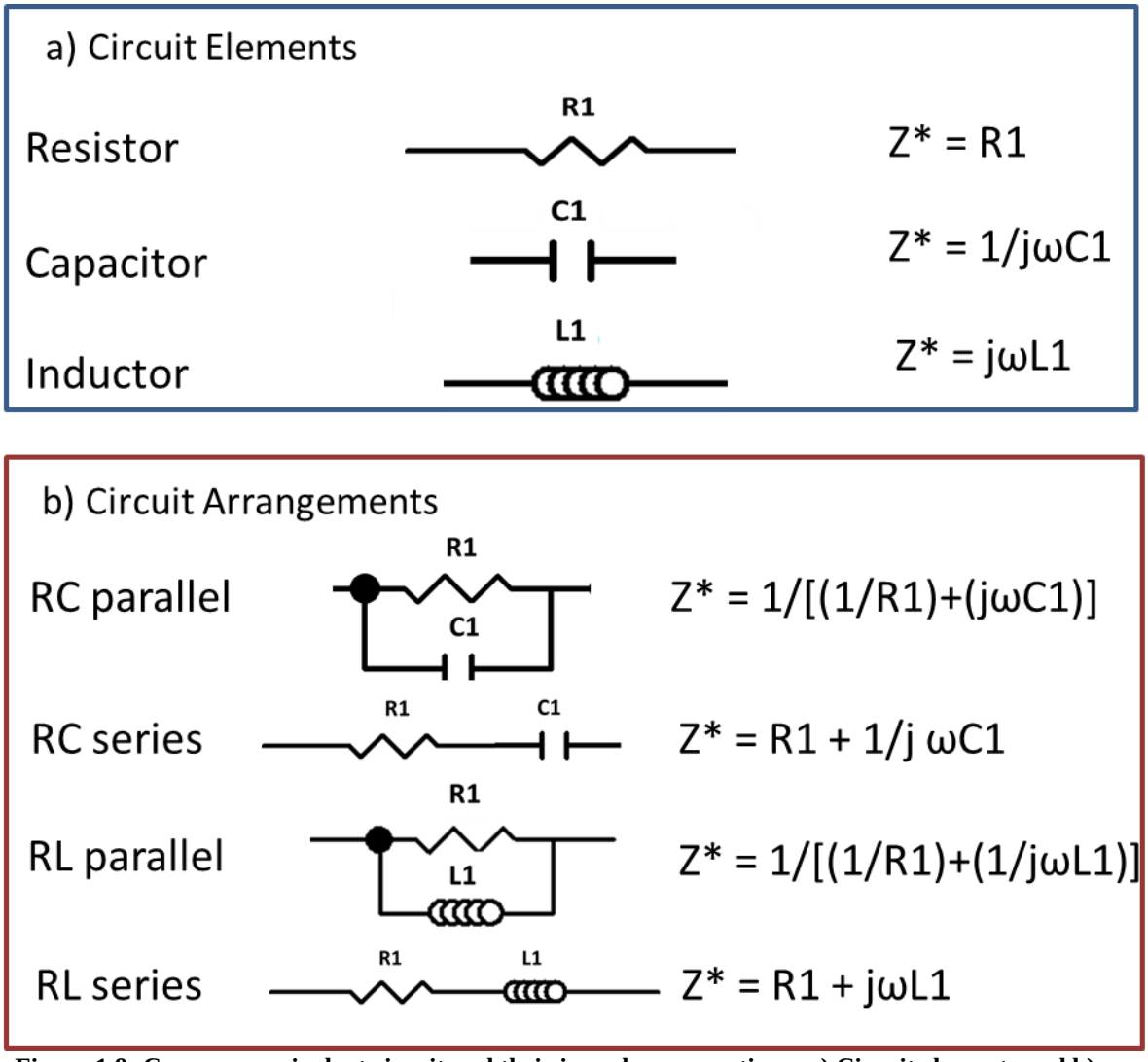

Figure 1.8: Common equivalent circuit and their impedance equations; a) Circuit elements and b) Circuit element arrangements. Figure adapted from ref [44].

In order to understand how the more complex circuits are built, it is important to be able to visualize the behavior of individual circuit elements. Figure 1.9 shows the Nyquist plot (a), log(|Z*|) vs. log(f) (b), and θ vs. log(f) (c) showing the impedance results of a single resistor (R) circuit element (R = 1000 Ω). In the Nyquist plot, the resistor is a single point at (Z',Z") = (1000, 0), its impedance magnitude and phase angle (θ = 0°) is constant across the entire frequency range.

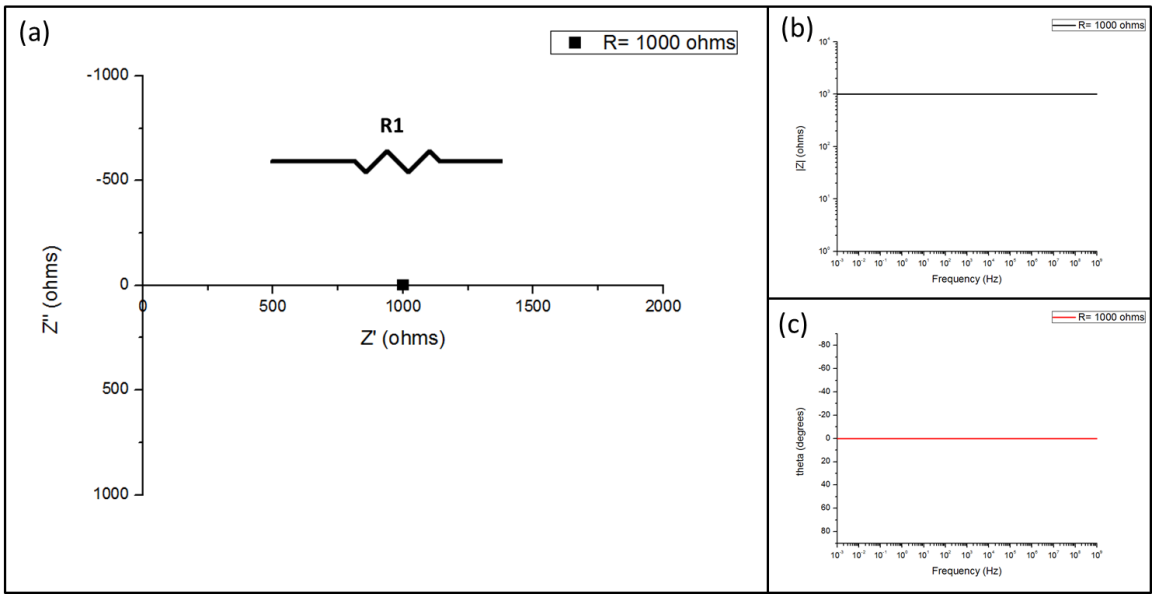

Figure 1.9: Impedance properties of a pure resistor with R = 1000 Ω.

Figure 1.10 shows the Nyquist plot (a), log(|Z*|) vs. log(f) (b), and θ vs. log(f) (c) showing the impedance results of a single capacitor (C) circuit element (C = $1x10^{-9}$ F). In the Nyquist plot, the capacitor is a straight line in the 1st quadrant. Its impedance magnitude decreases with increasing frequency while its phase angle (θ = -90°) is constant across the entire frequency range.

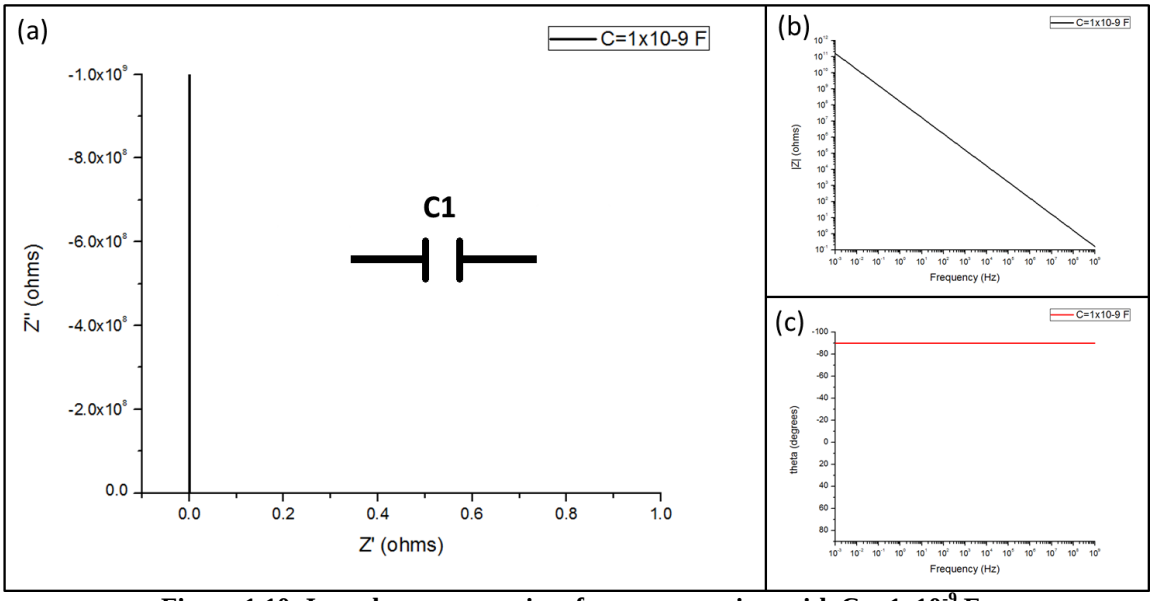

Figure 1.10: Impedance properties of a pure capacitor with C = 1x10^{-9} F.

Figure 1.11 shows the Nyquist plot (a) log(|Z*|) vs. log(f) (b), and θ vs. log(f) (c) showing the impedance results of a single inductor (L) circuit element (L = 1x10^{-5} H). In the Nyquist plot, the inductor is a straight line in the 4th quadrant. Its impedance magnitude increases with increasing frequency while its phase angle (θ = 90°) is constant across the entire frequency range.

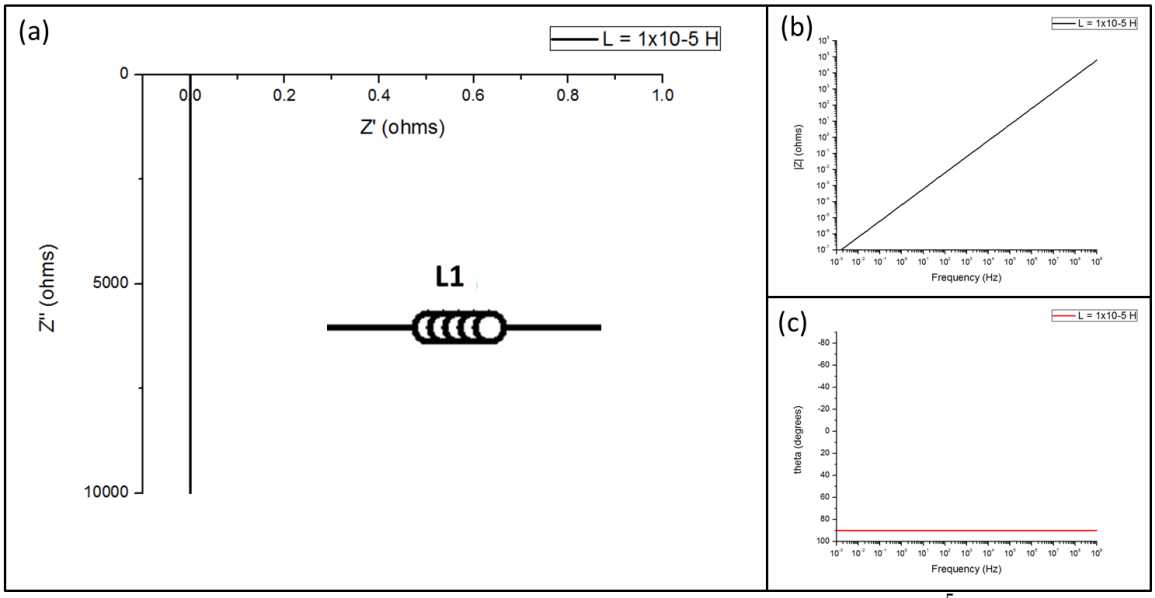

Figure 1.11: Impedance properties of a pure inductor with L = 1x10^{-5} H.

Arrangements of these circuit elements result in impedance spectra with combined responses from each element. Figure 1.12 shows the Nyquist plots for the 4 circuit arrangements given in Figure 1.8b: a) RC Parallel; b) RC Series; c) RL Parallel; d) RL Series. In all cases R = 1000 Ω, C = $1x10^{-9}$ F, and L = $1x10^{-5}$ H. The RC Parallel circuit fits impedance behavior which plots as a semicircle in the 1st quadrant (1.12a) with a diameter equal to R = 1000 Ω. The RC Series circuit fits impedance behavior which plots as a straight line in the 1st quadrant which is shifted from the y-axis by a value of R = 1000 Ω (1.12b). The RL Parallel circuit fits impedance behavior which plots as a semicircle in the 4th quadrant (1.12c) with a diameter equal to R = 1000 Ω. The RL series circuit fits impedance behavior which plots as a straight line in the 4th quadrant which is shifted from the y-axis by a value of R = 1000 Ω (1.12b). This exercise was adapted from Ref [47].

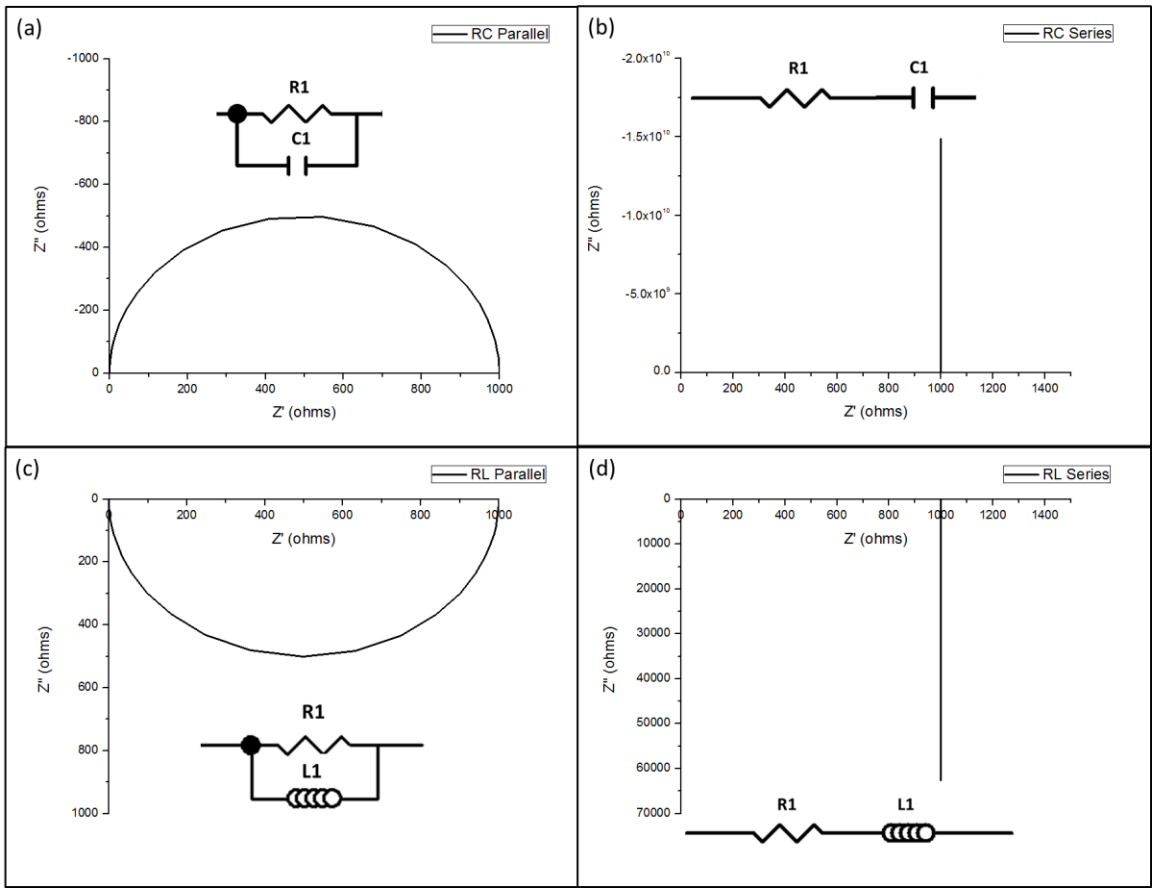

Figure 1.12: Nyquist plots requiring the different circuit arrangements presented in Figure 1.8 to fit the presented data. a) RC Parallel; b) RC Series; c) RL Parallel; d) RL Series. R = 1000 Ω, C = $1x10^{-9}$ F, and L = $1x10^{-5}$ H

In combination with other characterization techniques, each of the elements or arrangements can be used to describe a distinct electronic behavior or mechanism within the material being studied. Additionally, since many materials have multiple mechanisms which contribute to their electronic behavior, multiple element and arrangement 'building blocks' may be required to fit a single impedance spectrum. Figure 1.13 shows a Nyquist plot which requires two RC parallel circuits in series with each other to fit the data (R1 = 10000 Ω, C1 = $1x10^{-9}$ F; R2 = 10000 Ω, C2 = $1x10^{-12}$ F) [48, 49].

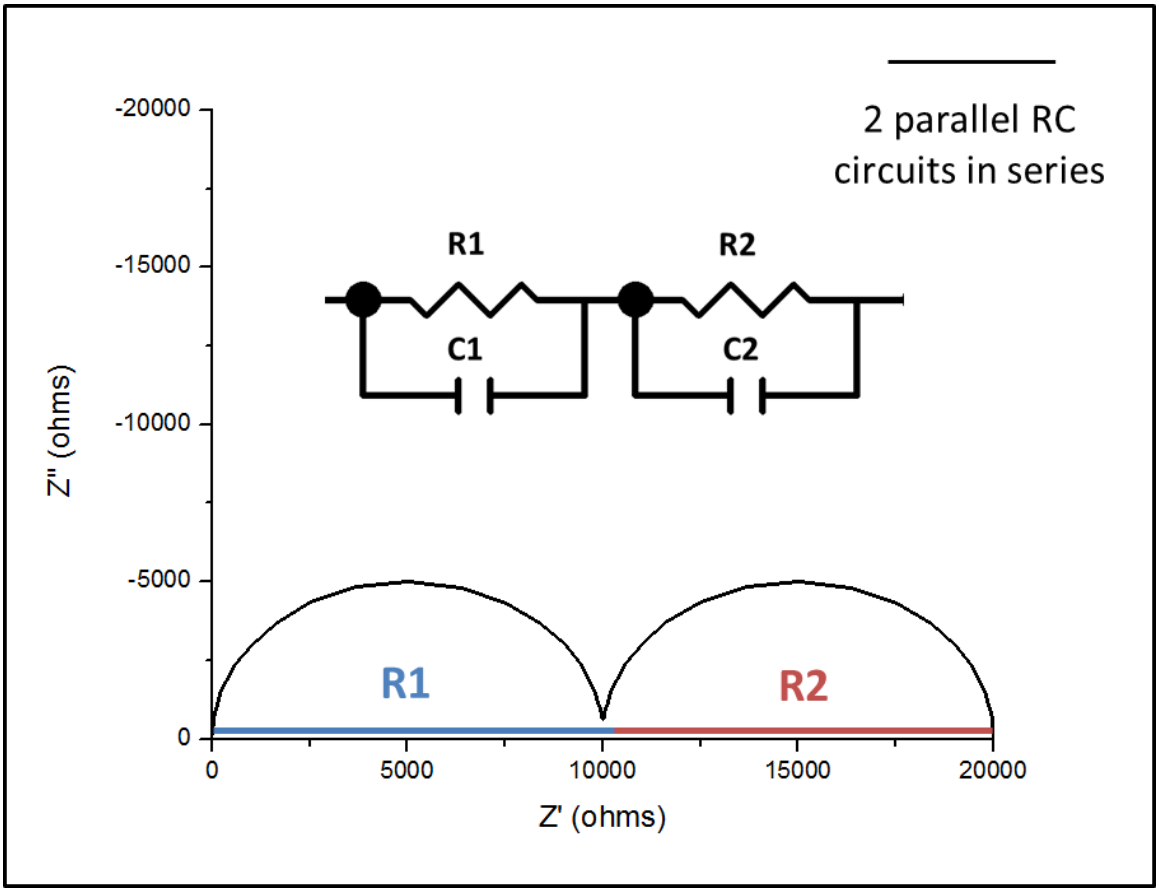

Figure 1.13: Nyquist plot requiring two RC parallel circuits in series with each other to fit the impedance data. (R1 = 10000 Ω, C1 = $1x10^{-9}$ F; R2 = 10000 Ω, C2 = $1x10^{-12}$ F)

There are three other functions, referred to as immittance functions, which can be used along with impedance to describe the AC electronic properties of the material [50-52]. These functions are electrical modulus, M*, permittivity, ε*, and admittance, Y*. Multiple circuits can be used to fit the same impedance data so it is important to simultaneously study all of the immittance behaviors in order to develop an equivalent circuit model which is actually representative of the material being studied [46, 50-52]. Equations 1.5-1.7 describe the equations for the different immittance functions while equations1.8-1.10 describe the relationship between each function. C_0 is the geometrical capacitance.

$$M^* = M' + jM'' \tag{1.5}$$

$$\varepsilon^* = \varepsilon' + j\varepsilon'' \tag{1.6}$$

$$Y^* = Y' + jY'' \tag{1.7}$$

$$Y^* = \frac{1}{Z^*} \tag{1.8}$$

$$M^* = \frac{1}{\varepsilon^*} \tag{1.9}$$

$$\varepsilon^* = \frac{1}{j\omega C_0 Z^*} \tag{1.10}$$

In addition to the vast earlier literatures, the recent PhD dissertations of two classmates (SM Joshi and TL Pruyn) show additional detailed examples of how impedance spectroscopy can be used to relate the structure of the material to the measured impedance spectra [45, 46].

CHAPTER 2

EXPERIMENTAL PROCEDURES

The goal of this chapter is to provide a basic outline of the materials used and their properties along with the methodologies employed to fabricate and characterize the MWNT-paper composite materials. It will not include the specifics of the different experimental procedures employed in this dissertation: those procedures will instead be described in their respective Chapters.

2.1 Materials

Figure 2.1 shows low magnification scanning electron microscopy (SEM) images of the three filter papers used as composite backbone materials. These filter papers are cellulose-based qualitative filter papers purchased from VWR.com and, from left to right in Figure 2.1, have pore sizes of 1, 5, and 25, µm (labeled 410, 413, and 415, respectively). Table 2.1 gives structural and flow rate details about the filter paper materials.

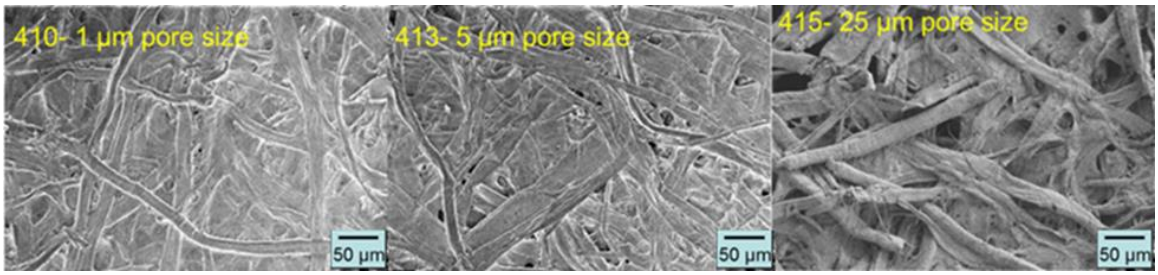

Figure 2.1: SEM images of the three filter papers used as backbone materials in this study: left) 410 filter paper with 1 µm pore size; middle) 413 filter paper with 5 µm pore size; right) 415 filter paper with 25 µm pore size. The scale bar for each micrograph is 50 µm.

Table 2.1: Filter Paper Specifications and Properties

	410 filter paper	**413 filter paper**	**415 filter paper**
Pore Size	1 µm, fine	5 µm, medium	25 µm, coarse
Fiber Diameter	~25 µm	~20 µm	~30 µm
Flow Rate	Slow	Medium	Fast
Thickness	0.182 mm	0.144 mm	0.206 mm

MWNTs obtained from cheaptubes.com with the following specifications were used as the conductive material: 0.5-2.0 μm in length, 8-15 nm in diameter, >95 wt% purity with <1.5 wt% ash. Images of the pure powder, a high resolution SEM image of the MWNT bundles, and two high resolution transmission electron microscopy (HR-TEM, JEOL 100Cx-2 TEM, 100 kV accelerating voltage) images are available in Figure 2.2. The HR-TEM images show both a group of MWNTs (c) and an example of the number of walls for a single tube (d).

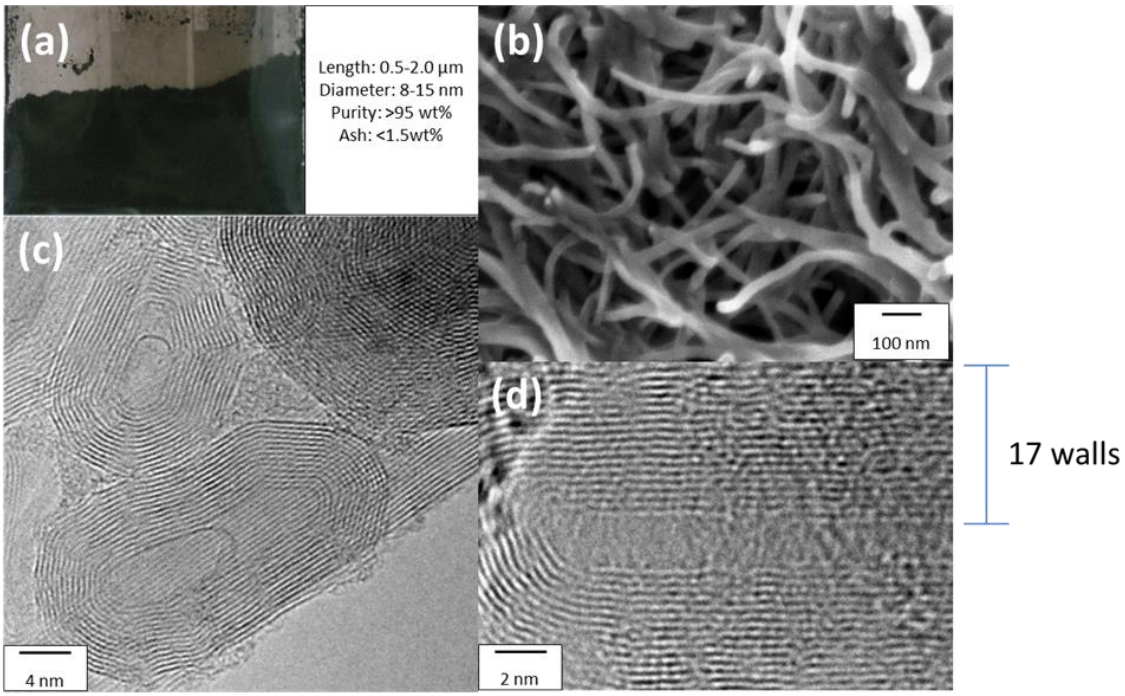

Figure 2.2: Multiscale images of the MWNTs used in this thesis. a) Photograph of the MWNT powder along with the powder specifications from cheaptubes.com; b) SEM micrograph (with a scale bar reading 100 nm) of the MWNT bundles; c) HR-TEM image (scale bar reads 4 nm) of the MWNTs; and d) HR-TEM image (scale bar reads 2 nm) of a single MWNT such that the number of walls can be counted.

2.2 Dispersion Synthesis

Aqueous based dispersions containing 1 mg/mL of MWNTs and 10 mg/mL of the surfactant material sodium dodecylbenzenesulfonate (SDBS) were made. First, a known volume of DI water was added to a vial or flask. Next, the MWNTs were added to the

water, and the water-MWNT mix was ultrasonically mixed for ten minutes to help break apart the MWNT powder and begin the dispersing process. For the next ten minutes, while the water-MWNT mixture was still undergoing sonication, the SDBS was slowly added. Adding too much surfactant too quickly caused the surfactant material to clump up at the bottom of the container, greatly increasing the time required to create a stable dispersion. Finally, once all of the surfactant material had been added, the MWNT-SDBS-water mixture was ultrasonicated for an additional hour. Following sonication, a stir bar was placed in the dispersion, and the dispersion was magnetically mixed for at least 12 hours before use to ensure that the MWNTs were not aggregated [5, 53].

If the entirety of the MWNT dispersion was not used during the experiment, the dispersion was placed back on the magnetic mixer to be continuously mixed. This ensured that agglomeration of the MWNTs would not occur between experiments and allowed for a single dispersion to be used over a period of three to six months without the MWNTs falling out of dispersion and collecting at the bottom of the glassware.

2.3 Justification for Dispersion Contents

SDBS was chosen as the surfactant material as previous studies have shown that anionic surfactants showed the best ability to break up agglomerates into individual or small bundles of CNTs [54]. Furthermore, the presence of the phenol group in the SDBS helps promote the separation of agglomerates even further than other anionic surfactants and stabilized the dispersions for up to 3 months (no re-aggregation of CNTs occurred), likely due to π-π interactions between SDBS and the CNTs [55, 56]. 1 mg/mL of MWNTs was chosen as the concentration for the majority of this thesis as it is the lowest concentration from which an interconnected network could be formed on the 410 filter

paper (1 μm pore size). Lower concentrations could not form an interconnected network on the surface of the smallest pore size paper, even after multiple layers were deposited.

2.4 Composite Fabrication

MWNTs were deposited from aqueous dispersion onto paper substrates to form the composites using a deposition methodology referred to as a "modified-dropcasting" technique. 150 μL of MWNT dispersion was dropcasted on the surface of the paper backbone and dried using vacuum filtration. Each completed dropcast-dry step will be referred to as "1 layer" in this dissertation. Therefore, multilayered composites will be denoted based on the number of dropcast-dry steps used to deposit the material along with the paper backbone pore size. Because of the hydrophilic nature of the paper, the dropcast step results in a spread area and a splash distance of the dispersion which increases with increased height. In order to minimize any methodological error associated with the dropcasting step, it is important that the distance of the pipette above the paper substrate (approximately 1.5 cm in this thesis) is always the same.

Vacuum filtration has been a popular methodology for forming CNT films on filter membranes as the process is quick and forms repeatable CNT networks given the same materials and formation conditions since the report given in Reference [57]. Because drying occurs through the membrane, this drying technique allows for the easy removal of all material which is smaller than the pores of the membrane by pulling it through the thickness of the paper material. While this is generally thought as a way to remove water and surfactant from the surface film, it is not the only implication of this technique. If the pore size of the filter paper is larger than or comparable to the length of

the MWNT bundles, they too will be pulled through the paper material resulting in a variety of composite morphologies that can have very different properties even while using the same dispersion [5]. An image of the vacuum filtration set up used in this dissertation is shown in Figure 2.3.

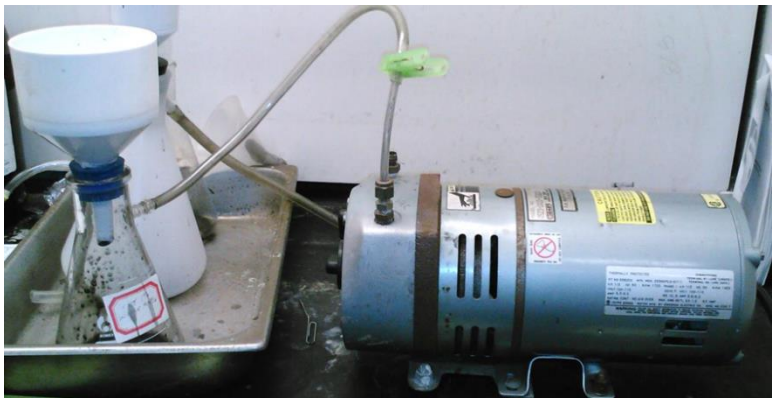

Figure 2.3: Photograph of the vacuum filtration setup.

2.5 Materials and Composite Characterization Techniques

2.5.1 Structure Analysis

Both the surface and the internal structure of the composite must be visualized to gain the greatest understanding of how the MWNT-paper composite formed. The surface structure was imaged at multiple length scales using both optical microscopy (OM) and scanning electron microscopy (SEM) as materials properties arise from interactions at the different length scales. Optical photomicrographs of the surface were taken using an ARI XSB411 Optical Microscope with a Digital Camera USB hook-up and PhotoLib 3.03 software. The light source is positioned above the composite to image the top-most layer in order to determine both how widespread MWNT deposition is across the entire surface of the composite. In-lens SEM images were taken with a Zeiss SEM Ultra-60 at 1-2 kV

and at a variety of magnifications to get detailed images of the MWNT-paper composite surface formation as well as how the MWNT network formed.

Because the MWNTs and the paper are not covalently bonded together, slicing the paper and imaging the cross-section in the same manner as the surface does not allow for an accurate depiction of the deposition within the thickness of the paper. Instead, a more indirect method of imaging was used to gain an understanding of the internal structure of the composite: current atomic force microscopy (I-AFM) [12, 58]. I-AFM is a contact mode form of AFM meaning that during a scan, a cantilever containing the measurement probe (tip) rasters across a given surface area while maintaining contact with the surface during the entire scan. By setting up I-AFM such that the tip is one electrode and the metal support attached to the back of the composite is the second electrode, regions of current flow through the sample can be detected and measured. Determining the location of current flow through the composite effectively shows where in the composite the MWNTs are interconnected from the top to bottom surfaces [12]. I-AFM was done using a Park Systems XE-100E AFM in the external I-AFM mode with an NSC18 Ti/Pt coated AFM tip and an applied voltage of 2 V to the bottom of the sample.

2.5.2 Surface Chemistry Characterization

As a way to determine what materials were on the surface of the composites and whether the surfactant was truly pulled into the material during drying, the surface chemical structure was determined using Fourier Transform Infrared Spectroscopy (FTIR). A Thermo Scientific Nicolet iS 5 FT-IR Spectrometer in ATR mode using the Thermo Scientific iD5 ATR Accessory with a ZnSe window was used to determine what

types of chemical bonds were available on the material surface, and this setup is shown in Figure 2.4. The wavelength range scanned was 4000 cm^{-1} to 400 cm^{-1}.

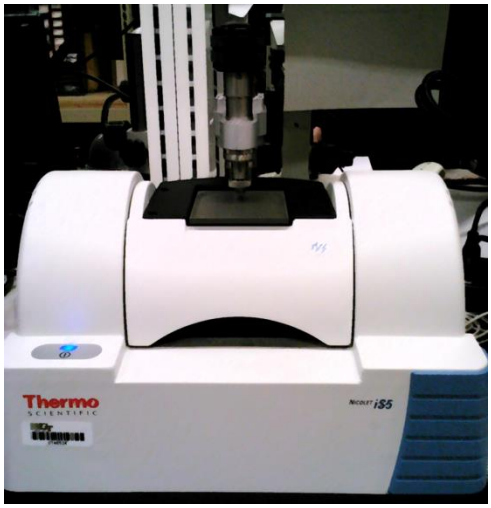

Figure 2.4: Photograph of Thermo Scientific Nicolet iS 5 FT-IR Spectrometer in ATR mode using the Thermo Scientific iD5 ATR Accessory with a ZnSe window.

2.5.3 Electrical Properties Characterization

AC electrical characterization was done across the surface and through the thickness of the composite by impedance spectroscopy. Impedance spectroscopy was performed using a Solartron 1260 Impedance Analyzer connected to a Solartron 1296 dielectric interface as shown in Figure 2.5. For the in-plane measurements, a two probe measurement technique was used to determine the surface behavior, and the measurements were carried out by scanning the frequencies from 21 MHz to 0.01 Hz using an AC voltage of 0.1 V. For the thru-plane measurements, the samples were placed in a parallel plate arrangement and measured using the high resistance impedance setup with an AC voltage of 4 V. The experimental arrangements can be seen in Figure 2.5 for both the in-plane (Figure 2.5b) and the thru-plane (Figure 2.5c) measurements. In the cases where the sample is very conducting, only the Solartron 1260 was used to carry out

the impedance measurement as the machine is more capable of handling low resistance materials.

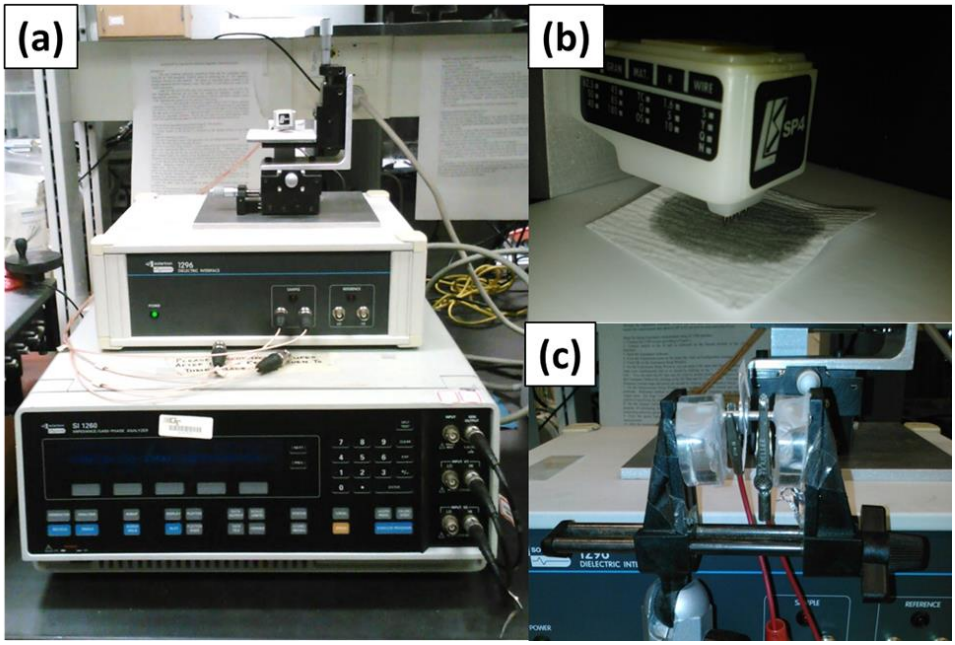

Figure 2.5: Photographs of the impedance setups used in this study. a) Solartron 1296 dielectric interface connected to the Solartron 1260 for impedance scans; b) Composite material loaded under a probe stand for in-plane impedance measurements; c) Composite material loaded between two electrodes for thru-plane impedance measurements.

For DC electrical characterization, a Keithley 6430 Sub-Femtoamp Remote SourceMeter in the auto ohms measurements setup and connected to a four-point probe stage with a probe spacing of 1.016 mm was used to measure the in-plane properties of the composites. For the DC thru-plane measurement, the sample was placed in the parallel plate setup and a Keithley 2000 multimeter with two probes was used to contact each side of the composite.

2.5.4 Thermal Properties Characterization

Thermal properties of the powders (MWNT and surfactant), filter papers, and the paper-MWNT composites were found using a TA Instruments SDT Simultaneous Q600 DSC/TGA (differential scanning calorimeter/thermogravimetric analysis). Samples were

loaded into an alumina pan and scanned from room temperature to 900°C (600°C maximum for the paper only sample) in an air environment using a 20°C/min heating rate. At maximum temperature, the samples were held isothermally for 5 min before the machine was cooled. Using the DSC/TGA dual measurement technique allowed for the determination of what temperature different weight loss (%) and/or heat flow (W/g) events occurred in the materials. By determining the properties of the base materials as well as the composite materials, the cause of each thermal event was determined and used to help form the structural models presented in this thesis. An image of the DSC/TGA is shown in Figure 2.6 while a sample pan and a composite sample used for the scan is shown in the inset.

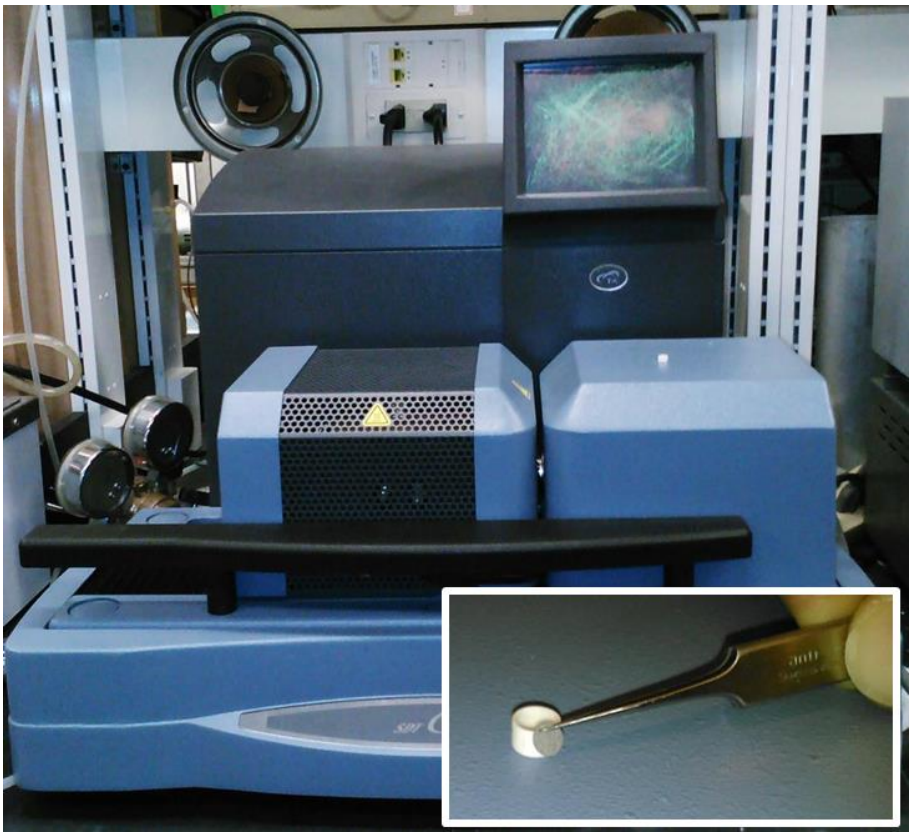

Figure 2.6: Photograph of a TA Instruments SDT Simultaneous Q600 DSC/TGA. The inset shows an alumina sample pan and a composite sample which are loaded into the DSC/TGA for thermal characterization.

CHAPTER 3

EFFECT OF PAPER PORE SIZE ON THE MORPHOLOGY AND PROPERTIES OF MWNT-PAPER COMPOSITE MATERIALS FORMED USING VACUUM FILTRATION

3.1 Introduction

Vacuum filtration of dispersions containing CNTs has been a widely used method in the fabrication of freestanding CNT films due to the ease and repeatability of the methodology. In this technique, a volume of a CNT dispersion is dropcasted onto a filter membrane, and under the presence of the vacuum force, the dispersion is pulled unidirectionally through the pores of the filter membrane [59]. In most cases, the filter membrane has a much smaller pore size than the length of the CNT and the solvent and any other small molecule contents (e.g. surfactants) can be pulled through the filter and removed from the surface of the membrane. However, when the CNTs are much larger than the filter membrane pores, the CNTs remain on the surface and interact with one another. In the absence of any other stimuli, the CNTs form a rigid and randomly oriented network on the membrane surface (with some CNT loss through the thickness due to the small diameter of the tubes) [57, 60]. Typically, the membrane material used is something which the CNTs have a low affinity for, resulting in easy removal of the deposited film from the membrane [60].

Thin, transparent films of CNTs are often deposited from dilute CNT dispersions onto an alumina filter membrane and transferred from the filter membrane to substrates

such as glass or plastic for optoelectronic applications. Thick films of highly conductive networks of CNTs can be peeled off of the filter membrane and used as a standalone material, commonly known as buckypaper [59]. The properties of the CNT films are dependent upon the characteristics of the dispersion, but as long as the films are made using the same dispersion and processing characteristics, repeatable structures and properties are found across multiple samples [5, 39, 57, 60, 61]. However, while the deposition methodology looks to be an additive form of processing, the removal of the film from the membrane results in a subtractive step. Excess waste occurs in the form of used filter membranes and from the leftover CNTs which are not removed from the filter membrane. Rarely does the vacuum filtration-fabricated film remain on the filter membrane for applications or even for testing.

In this work, rather than the filter membrane being a throwaway part of the fabrication step, it will serve as the backbone material for the multiwalled carbon nanotube (MWNT)-paper composites. Since deposition using vacuum filtration has been used to form thin films and buckypapers on other filter membranes, these types of networks should be achievable on the surface of paper membranes as well. This dissertation will determine the processing conditions required to form conducting CNT networks on the various papers used during processing as well as any other types of networks which may form during the experiments.

Additionally, unlike the previous research in vacuum filtration-aided CNT network formation wherein the CNT length is always significantly greater than the pore size of the filter membrane, this dissertation focuses on different MWNT bundle length (L_b) to pore size (d_p) ratios: (1) MWNT bundle length is slightly greater than the pore

size, (2) MWNT bundle length ≈ pore size, and (3) MWNT bundle length << pore size. These ratios coupled with the affinity of CNTs for paper should result in CNT deposition on the surface of the paper, within the thickness of the paper, or in a combination of both locations, resulting in a large number of unique composites which can be made while employing the same methodology.

Because of the potential dual nature of this deposition, in this Chapter, the structures and properties on both the surface of the composite (in-plane) as well as the through the thickness of the composite (thru-plane) are measured and presented to provide a complete understanding of the formation of the composites. Understanding the conditions required for specific composite structures and properties to form will allow for the usage of these composites for applications and future application-based research.

3.2 Experimental Details

MWNT-paper composites were made with the materials and via the dropcast-dry methodology described in Chapter 2. One to twenty (1-20) layers of the MWNTs were deposited onto each filter paper material to determine the impact that the pore size of the paper has on the formation of the composite material with increasing MWNT loading (multilayered deposition). In addition, 1-20 layers of a 1 mg/mL dispersion containing long-MWNTs (L-MWNT obtained from cheaptubes.com) which differed from the other MWNTs only in length (10-50 μm) were deposited on the 410 filter paper. Further, 1 layer films were deposited onto each filter paper material from dispersions containing 1, 2, 5, and 10 mg/mL MWNTs to compare the properties of composites formed from multilayer deposition to composites formed from different dispersion concentrations.

Table 3.1 shows the different deposition conditions (paper materials and the number of layers deposited from different MWNT dispersion concentrations) for the composites fabricated and tested in Chapters 3 and 4. Unless otherwise labeled with L-MWNT, the dispersion used to make the composite materials contained the MWNTs described in Chapter 2.

Table 3.1: MWNT dispersion concentration, paper material, and number of deposited layers used to form the different composite materials tested in Chapters 3 and 4. Shading denotes composites which are only discussed in Chapter 4.

	1 mg/mL	2 mg/mL	5 mg/mL	10 mg/mL
410 (1 µm pore size)	1-20 layers	1 layer	1 layer	1 layer
	1-20 layers (L-MWNT)			
413 (5 µm pore size)	1-20 layers	1 layer	1 layer	1 layer
415 (25 µm pore size)	1-20 layers	1 layer	1 layer	1 layer

3.3 Results

3.3.1 Structural Analysis of Multilayered Composites

3.3.1.1 In-Plane Structural Analysis

In order to determine how the surface structure develops with increasing layer number, low magnification SEM images were taken of all surfaces for all of the paper backbones. Figure 3.1 shows the surfaces of the MWNT-410 paper composites for the deposition of (a) 1 layer; (b) 4 layers; (c) 8 layers; (d) 12 layers; (e) 16 layers; and (f) 20 layers of the MWNT dispersion. At 1 deposited layer (Figure 3.1a), MWNTs deposit along paper edges and pore edges, coating the regions underneath the topmost layer of paper fibers. In addition, deposition occurs on some of the fiber surfaces. At 4 layers (Figure 3.1b), the topmost surfaces of the fibers are coated in MWNTs and large pockets of MWNTs are observable in the underlying structure; however, there are still regions on

the surface which are uncoated. At 8 layers and beyond (Figure 3.1c-f), nearly the entire surface is coated in MWNTs, and by 20 layers, MWNT surface deposition is so prevalent that the underlying paper substrate is completely undetectable. MWNT deposition began at pore and fiber edges, expanded across the fiber surfaces, and eventually, coated the entire paper surface. In addition, there is no visual evidence for the presence of surfactant on the surface.

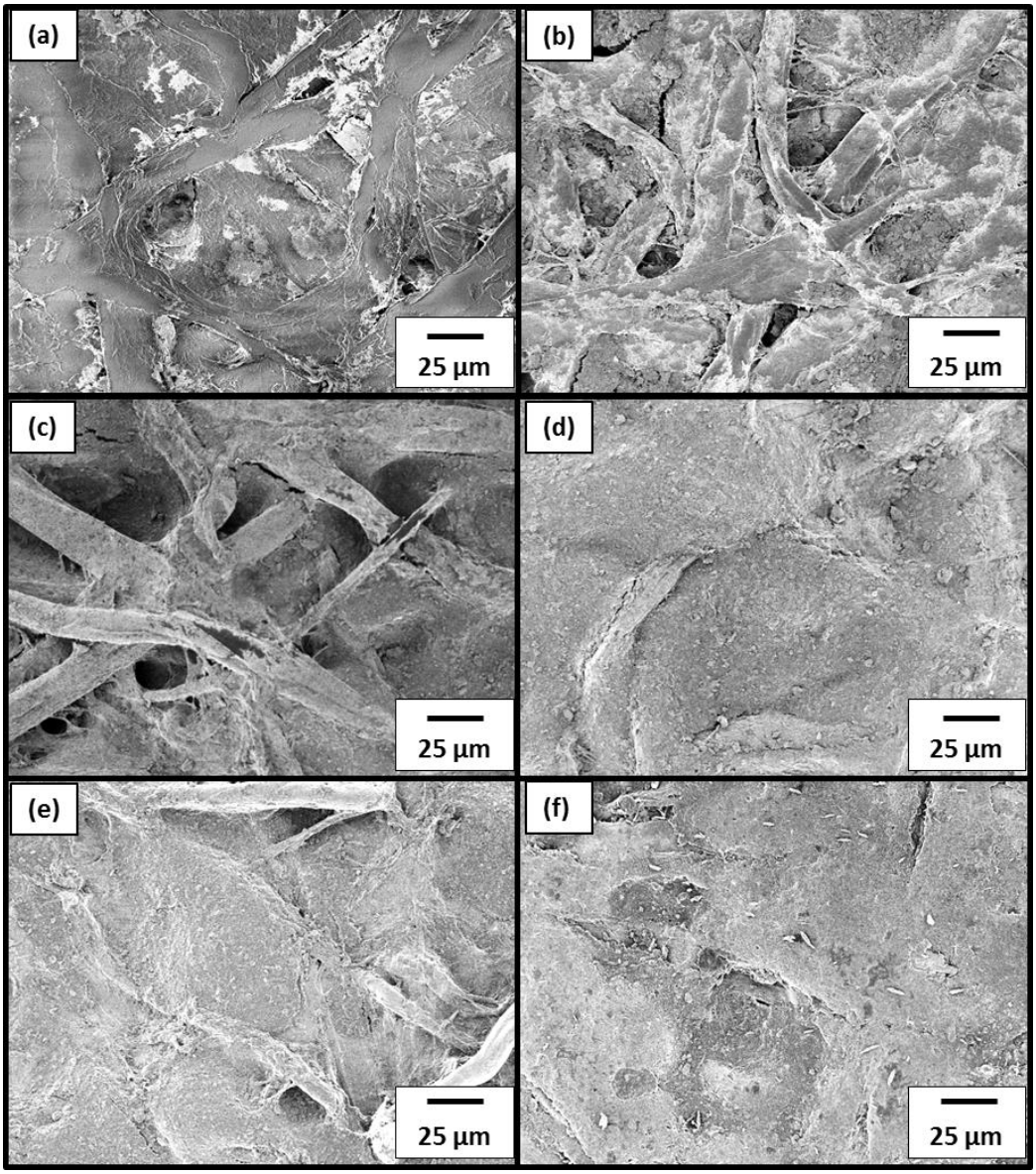

Figure 3.1: Low magnification SEM images of the surfaces of the composites made from 1-20 deposited MWNT layers on the 410 (1 µm) pore size paper. a) 1 layer; b) 4 layers; c) 8 layers; d) 12 layers; e) 16 layers; f) 20 layers.

Figure 3.2 shows how the MWNTs deposit on the 413 paper surface. At 1 deposited layer, shown in Figure 3.2a, MWNTs are located in a single pocket on the surface along some fiber and pore edges. This deposition does not extend in either direction of the image: it was localized to a single area. At 4 layers, shown in Figure 3.2b, the pockets of MWNTs have extended across the image, interconnected across the surface, and begun covering fiber surfaces. At 8 layers, shown in Figure 3.2c, coverage of the MWNTs over the surface paper fibers began; however, the paper backbone still has regions which are not entirely coated. Finally, at 12-20 layers, shown in Figures 3.2d-f, the entire surface region is coated by MWNTs.

Figure 3.3 shows the deposition of MWNTs on the 415 paper surfaces. Very small amounts of MWNTs are seen in Figures 3.3a-c for 1, 4, and 8 layer composites, respectively. In all cases, the MWNTs are found as agglomerated clumps along the edge of a pore and below the surface. For further MWNT loadings (Figure 3.3d-f), MWNT agglomeration within the pores increased, suggesting deposition occurs mostly below the surface. MWNTs are observed on the surface fibers in Figures 3.3d-f; however, deposition was minimal and the MWNTs which deposited were highly disconnected.

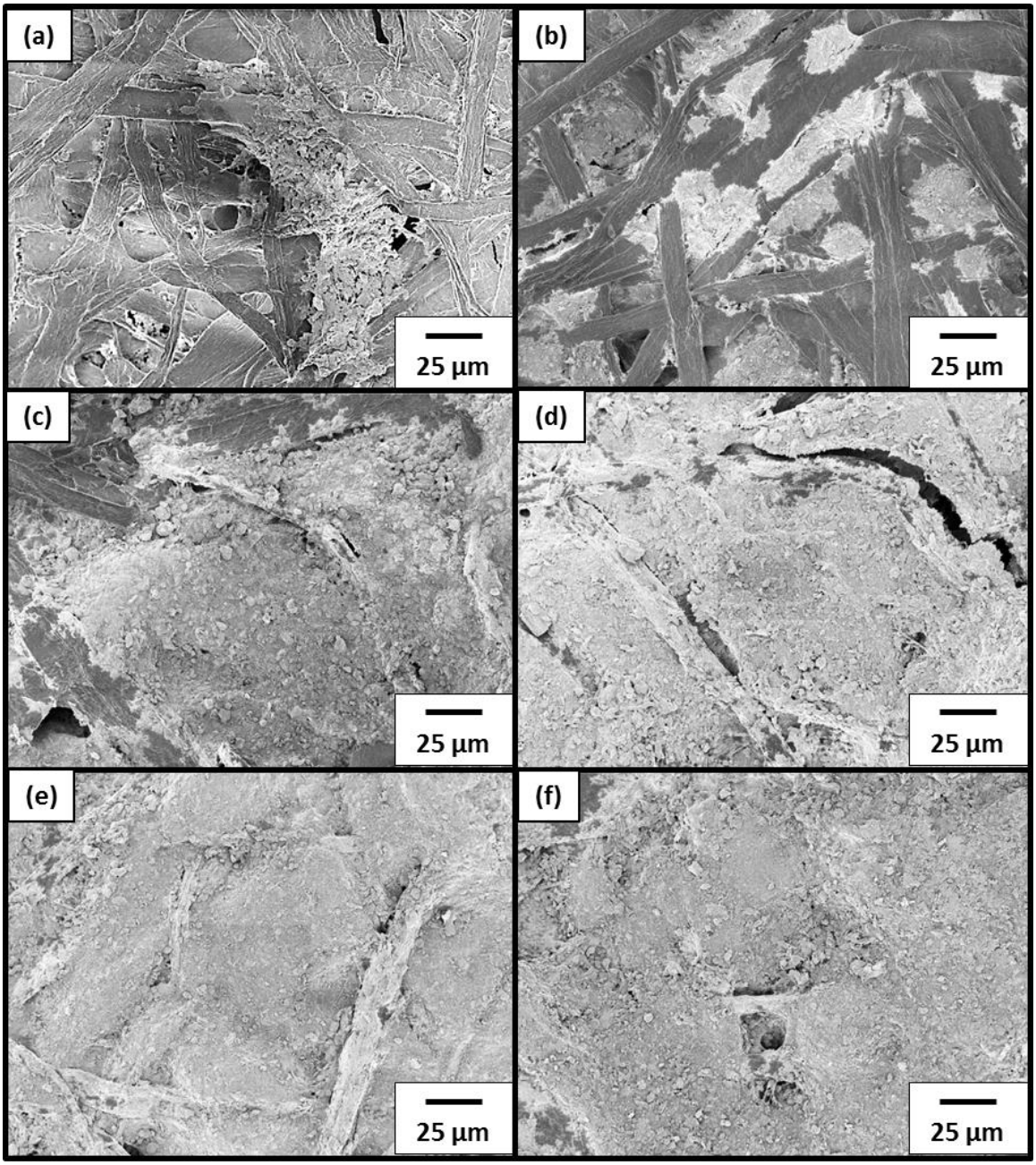

Figure 3.2: Low magnification SEM images of the surfaces of the composites made from 1-20 deposited MWNT layers on the 413 (5 µm) pore size paper. a) 1 layer; b) 4 layers; c) 8 layers; d) 12 *la*yers; e) 16 layers; f) 20 layers.

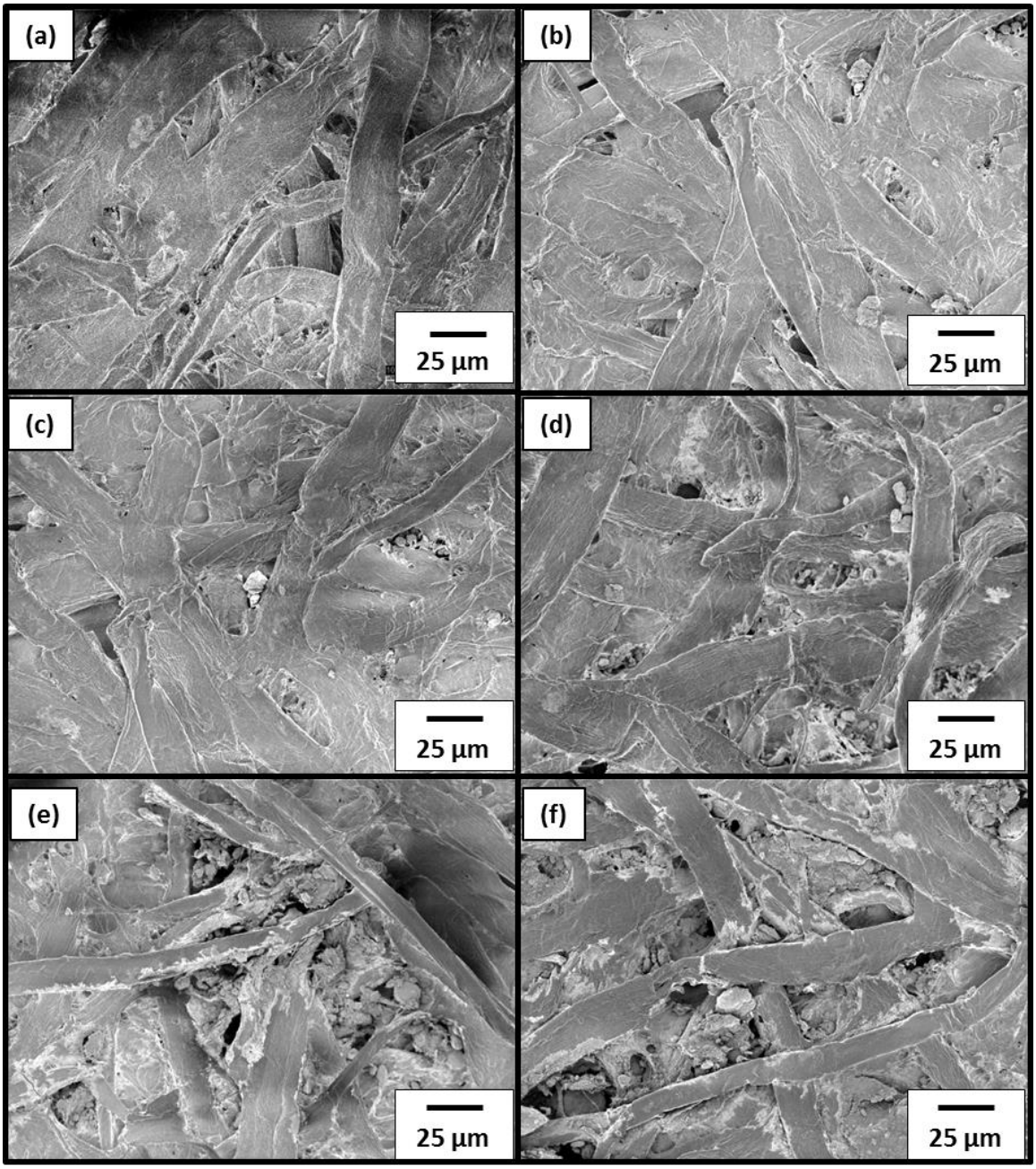

Figure 3.3: Low magnification SEM images of the surfaces of the composites made from 1-20 deposited MWNT layers on the 415 (25 µm) pore size paper. a) 1 layer; b) 4 layers; c) 8 layers; d) 12 layers; e) 16 layers; f) 20 layers.

3.3.1.2 Thru-Plane Structural Analysis

Since the composite materials are not chemically bonded together, cutting the composite causes the movement and removal of MWNTs. Because the composites could not be sectioned without distorting their structure, imaging the thru-plane of the composite materials directly using SEM (as was done with the in-plane) was not possible. However, it was possible to gain information about thru-plane structure of the composite with I-AFM: it was possible to measure current flow through the thickness of the composite. The detection of current flow implies that MWNTs are interconnected from the top to bottom surface of the paper. While this is not the best way to image the thru-planes, it gives some indication of interconnection of MWNTs within the paper thickness.

Figure 3.4 shows 10 μm x 10 μm I-AFM images showing current flow through the thickness of the a) 1 layer and b) 20 layered MWNT-410 composite materials. For both images, current flow is detected, suggesting that the MWNTs are interconnected within the composite thru-plane for all layer numbers. Since current is detected at 1 layer, the composites have percolated with only a single deposition step. For both composites, the region of current is segregated to small regions in the image with diameter of 1 μm: the MWNTs are interconnecting through the thickness along the pore edges of the paper. While the size of the regions where current flows through composite does not seem to change as layer number increases, the current is better defined and slightly greater in magnitude in the 20 layer image.

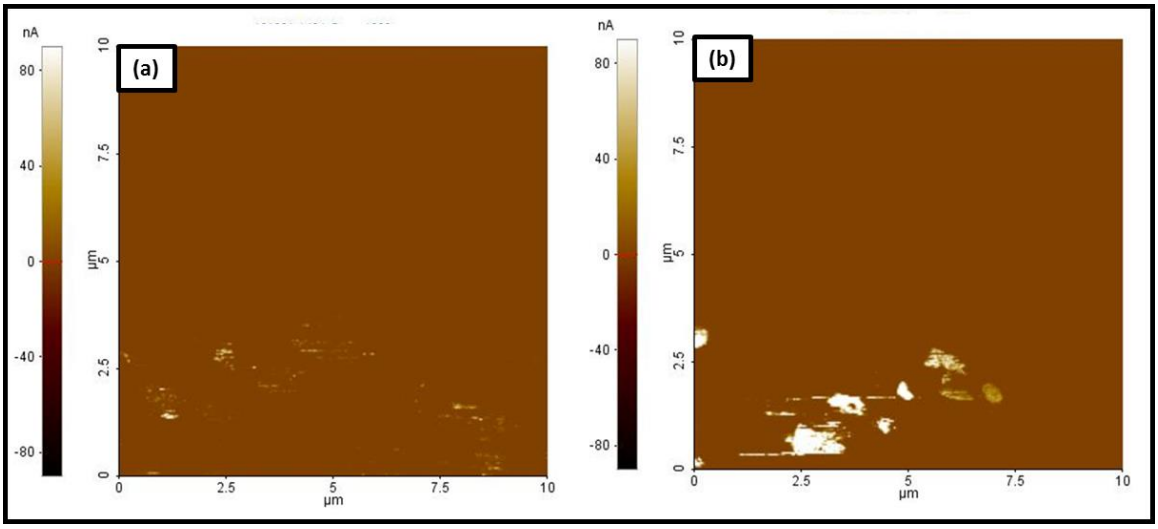

Figure 3.4: 10 µm x 10 µm I-AFM images showing current passing through the thickness of the MWNT-410 paper composite materials at a) 1 deposited layer (maximum current 80 nA) and b) 20 deposited layers (maximum current of 80 nA) of MWNTs.

Figure 3.5 shows 10 µm x 10 µm I-AFM images showing current flow through the thickness of the a) 1 layer and b) 20 layered MWNT-413 composite materials. For the 1 layer image (Figure 3.5a), current flow is detected, suggesting that the MWNTs are already interconnected through the composite thickness, and the percolation threshold for the thru-plane is 1 layer. At 1 layer, the region where current flows is segregated to a single location of the image which has a diameter of 5 µm: the MWNTs are interconnecting through the thickness along the pore edges of the paper. The maximum current detected in this composite is 80 nA. Conversely, the 20 layer image (Figure 3.5b) shows current which is more randomly distributed throughout the 10 µm x 10 µm image. The MWNTs are not just interconnected in the pore network but throughout the entire thickness of the paper. Additionally, the maximum current detected was 400 nA, a 5x increase from the 1 layer sample. As more MWNTs deposit in the thru-plane of the 413 paper, current flow through the thickness changes from a segregated location to randomly located, and the intensity of the current flow increases.

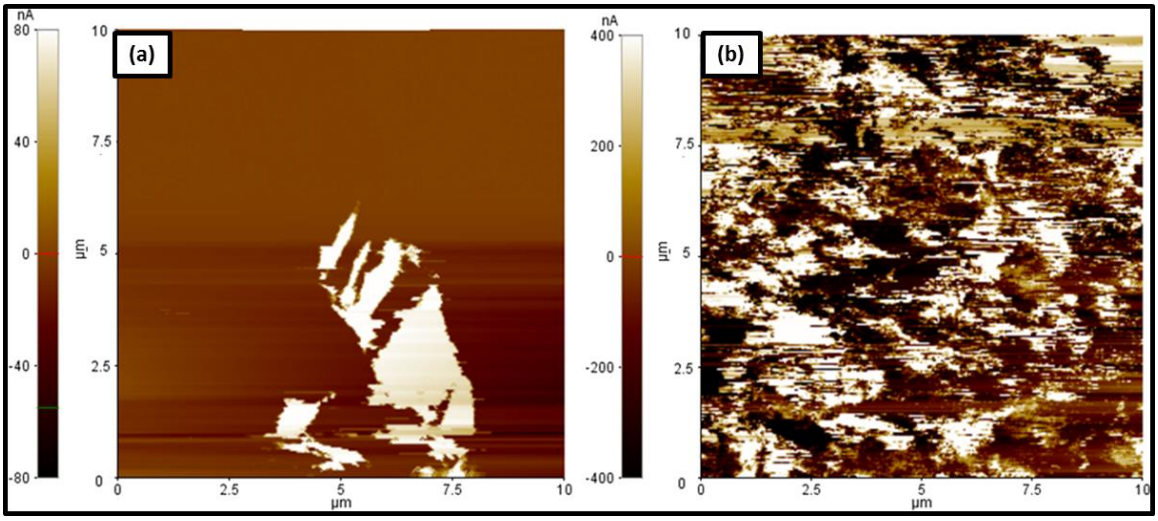

Figure 3.5: 10 μm x 10 μm I-AFM images showing current passing through the thickness of the MWNT-413 paper composite materials at a) 1 deposited layer (maximum current 80 nA) and b) 20 deposited layers (maximum current of 400 nA) of MWNTs. The images show the difference in current flow between a thru-plane where the MWNTs a) segregate in their deposition or b) randomly deposit.

I-AFM could not be used to detect how current flows through the thickness of the MWNT-415 paper samples. The sample roughness was too great to maintain tip contact with the surface, and the paper pore size (25 μm) was approaching the maximum scan size of the machine (40 μm x 40 μm).

3.3.2 Chemical Analysis: FTIR of Multilayered Composite Surfaces

Surface chemistry of the pure papers and the composite materials was determined using FTIR to confirm the presence of MWNTs and surfactant material on the surface of the composite. Figure 3.6 shows the FTIR spectra for the uncoated filter paper materials along with the average peak positions present in each spectrum. The three papers show nearly identical peak positions (< 5 cm^{-1} difference from paper to paper) suggesting that they are chemically invariant. Peaks are labeled at 3700 cm^{-1}, 3375 cm^{-1}, 2850 cm^{-1}, 2340 cm^{-1}, 1650 cm^{-1}, 1160 cm^{-1}, 1100 cm^{-1}, 1050 cm^{-1}, and 1030 cm^{-1}.

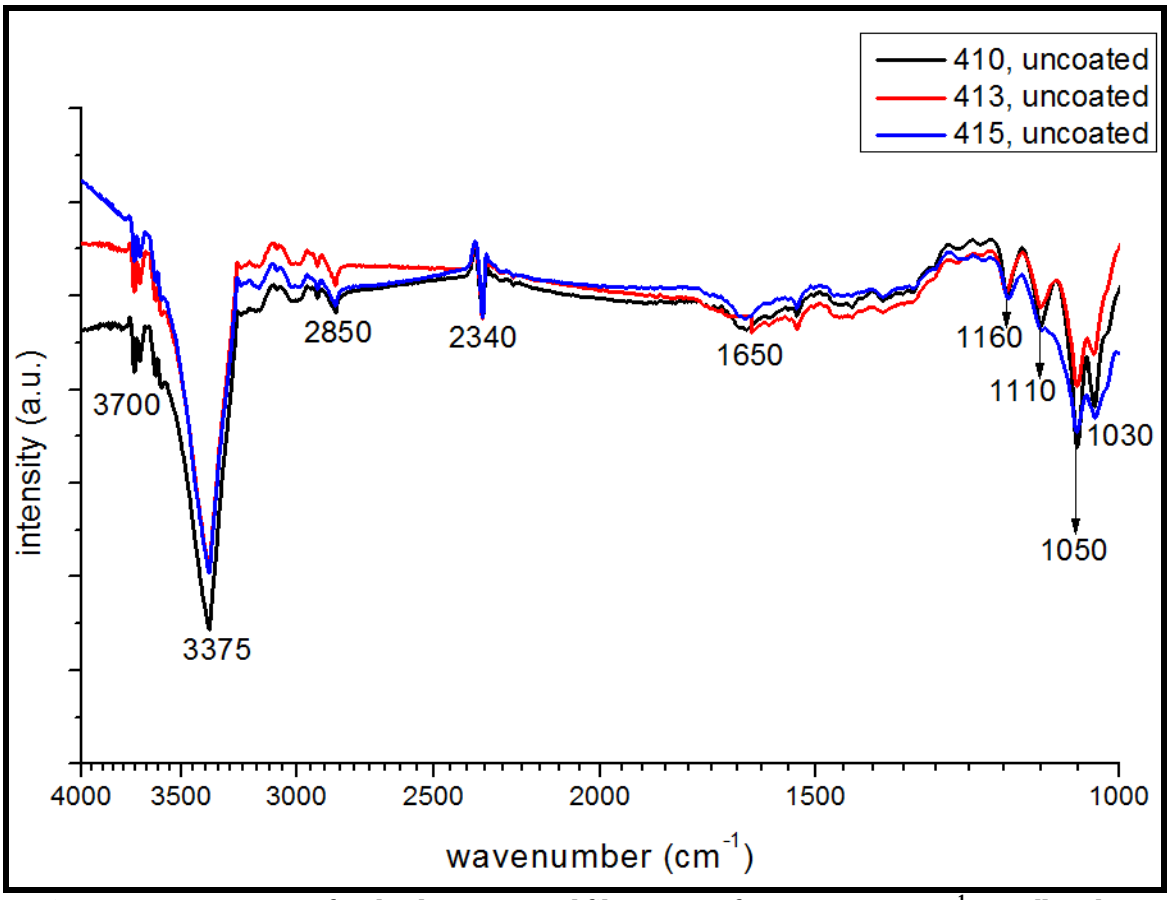

Figure 3.6: FTIR spectra for the three uncoated filter papers from 4000-1000 cm^{-1} as well as the average peak positions.

Figure 3.7 shows the FTIR spectra for the a) MWNT-410, b) MWNT-413, and c) MWNT-415 paper composite sets as well as labeling of the location of three potential peaks that can detect MWNT or SDBS deposition: 3380-3370 cm^{-1}, 1650 cm^{-1}, and 1450 cm^{-1}. MWNTs have characteristic FTIR peaks at ~3500 cm^{-1} and 1650 cm^{-1} [62]. Since these peaks overlap with paper peaks, the confirmation of the presence of MWNTs on the composite surface will be detected by a change in intensity and/or shape in the peak structure.

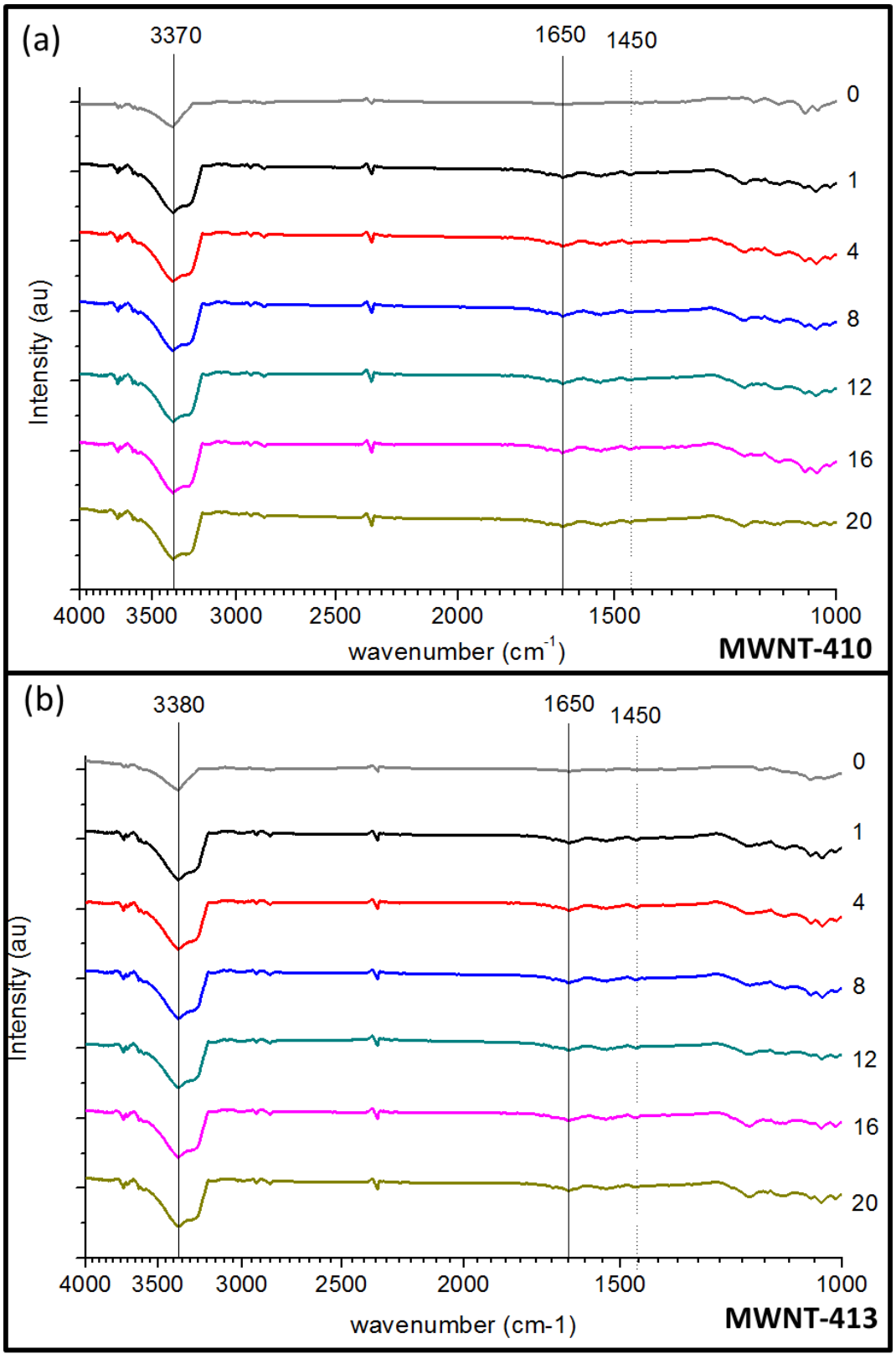

Figure 3.7: FTIR spectra for the a) MWNT-410, b) MWNT-413, and c) MWNT-415 composite sets for 0 to 20 deposited MWNT layers. Potential peak locations of 3370/3380 cm^{-1}, 1650 cm^{-1}, and 1450 cm^{-1} are denoted by a solid line, solid line, and dotted line, respectively.

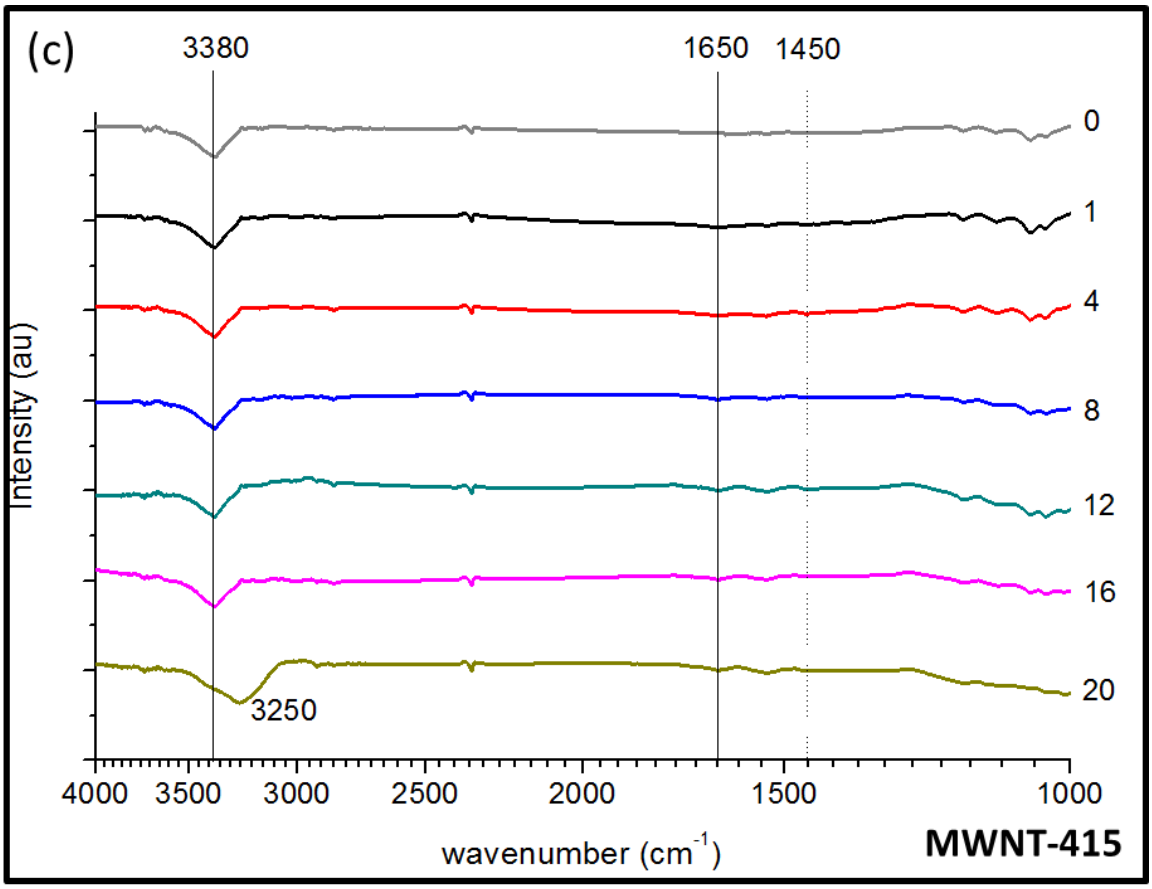

Figure 3.7 continued: FTIR spectra for the a) MWNT-410, b) MWNT-413, and c) MWNT-415 composite sets for 0 to 20 deposited MWNT layers. Potential peak locations of 3370/3380 cm^{-1}, 1650 cm^{-1}, and 1450 cm^{-1} are denoted by a solid line, solid line, and dotted line, respectively.

Figure 3.7a shows the FTIR spectra for MWNT-410 composites starting at the top with 0 layers and ending at the bottom with 20 layers. The peak at 3370 cm^{-1} changes in both shape and intensity for 1-20 layers of MWNTs as compared to the 0 layer peak. In addition, the peak at 1650 cm^{-1} shows an increase in intensity for 1-20 layers as compared to the 0 layer peak. From the FTIR spectra and as predicted by the SEM images in Figure 3.1, MWNTs are indeed present on the surface of the 410 paper material for all layer numbers.

The FTIR spectra for the MWNT-413 composite set given in Figure 3.7b shows the same trends as the MWNT-410 composites: there is an increase in magnitude and

change in peak shape at 3380 cm^{-1} and an increase in magnitude for the peak measured at 1650 cm^{-1}. MWNTs should be present on all the surfaces of the MWNT-413 layered composites. This is confirmed by the series of SEM images in Figure 3.2.

The FTIR spectra shown in Figure 3.7c for the MWNT-415 composite series do not present in the same manner as the other composite surfaces. The peak at 3380 cm^{-1} remains unchanging in shape and intensity until the 20 layer surface. At 20 layers, the peak shifts to 3250 cm^{-1} and also increases in intensity and changes in shape. In addition, the peak at 1650 cm^{-1} remains unchanged in intensity until the 12 layer MWNT-415 composite surface. As was shown in Figure 3.3, the surfaces of the MWNT-415 composite materials are not at all coated with MWNTs until 12 deposited layers (Figure 3.3d). At that point, there were enough MWNTs on the surface to vary the behavior of the FTIR spectra, and at 20 layers, the size and shape of the peak changed, and location of the peak shifted from 3380 cm^{-1} to 3350 cm^{-1}.

A third peak is labeled on all three parts in Figure 3.7 at 1450 cm^{-1} using a dotted line. For the range of 4000 cm^{-1} to 1200 cm^{-}1, the SDBS surfactant material has peaks in the FTIR scan at 3450 cm^{-1}, 2930 cm^{-1}, 2850 cm^{-1}, 1600 cm^{-1}, 1450 cm^{-1}, and 1380 cm^{-1} [63]. Peaks found at and less than 1200 cm^{-1} are not given as this region is very heavily dominated by the paper structure, as shown in Figure 3.6, making it difficult to decide which peaks are caused by the paper and which peaks are caused by the surfactant. For the same reason, the surfactant peaks at 3450 cm^{-1}, 2930 cm^{-1}, 2850 cm^{-1}, and 1600 cm^{-1} cannot be used to detect surfactant material. None of the spectra presented in Figure 3.7 show enough variation at 1380 cm^{-1} to use that peak as an indicator for surfactant on the surface, leaving only the potential peak at 1450 cm^{-1} (S=O) to be used as a marker for the

presence of the SDBS surfactant. Both Figures 3.7a and 3.7b show the presence of a small peak at 1450 cm^{-1} for the 1-20 layer samples which does not appear for the 0 layer sample. Conversely, Figure 3.7c does not show the presence of any peak at 1450 cm^{-1}. Even though it could not be seen in the SEM images, for the MWNT-410 and MWNT-413 multilayered surfaces, surfactant is not removed completely from the surface during vacuum filtration. For the MWNT-415 multilayered composite surfaces, SDBS surfactant is never detected on the surface.

3.3.3 Thermal Properties Characterization using DSC/TGA

Thermal properties characterization was done using DSC/TGA. Differential Scanning Calorimetry, DSC, allows for the detection of events causing thermal fluctuations in the material as well as the temperature at which these temperatures happen. If the thermal fluctuation has to do with a weight loss or gain event at a critical temperature, the amount of weight loss/gain can also be measured by thermal gravimetric analysis (TGA).

For these composites, this means that critical temperatures for the burning of the MWNT-paper material can be found, but also, the amount of weight loss which occurs at each critical temperature can be measured. By comparing the location of the weight loss peaks to those of the pure materials, the weight loss event can be described as a function of the material being lost [64]. Figure 3.8 shows the results of the DSC (Figure 3.8a) and the TGA (Figure 3.8b) runs for the three different uncoated papers. For all cases, exothermic events point upward in the heat flow vs. temperature graphs. The DSC results in Figure 3.8a show that the three papers have two characteristic exothermic peaks: a

broad peak around 370°C and a sharp peak around 505°C. Likewise, the TGA results in Figure 3.8b show two separate weight loss events at those temperatures.

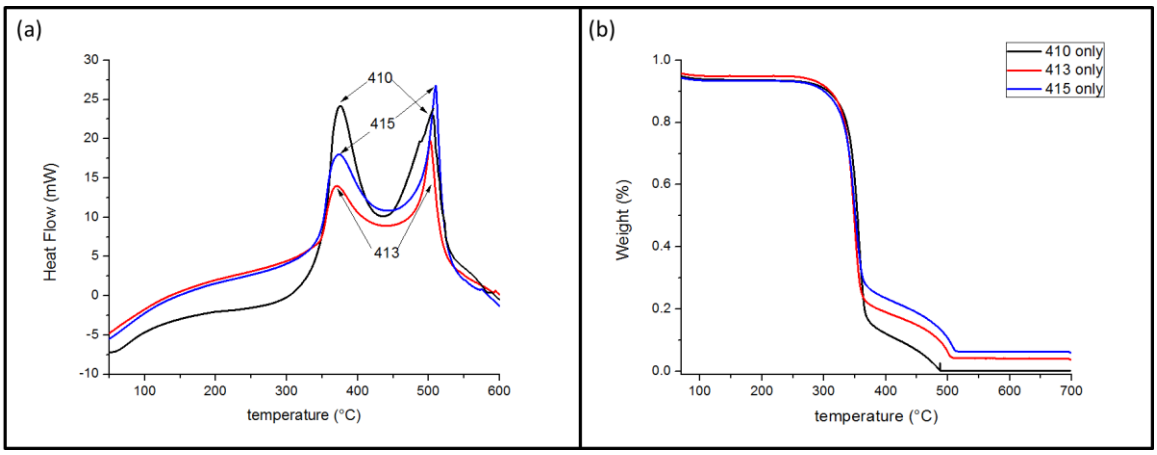

Figure 3.8: DSC/TGA results showing a) Heat flow vs. temperature and b) weight % vs. temperature for the three uncoated filter papers. Two different weight loss events are detected for each paper at approximately the same temperature.

Similarly, Figure 3.9 shows the DSC/TGA results for the different powder materials: a) MWNT and b) SDBS. For each powder, the left axis corresponds to the TGA results (weight % vs. temperature) and the right axis corresponds to the DSC results (heat flow vs. temperature). The MWNT powder shows a single weight loss event around 670°C, as shown in Figures 3.9a. As there is still weight being detected by the TGA, there is still remnant MWNT powder after the end of the final weight loss event in the alumina pan. Figure 3.9b shows the DSC/TGA results for the SDBS surfactant material. Two exothermic peaks are shown at approximately 360°C and 405°C in the heat flow vs. temperature graph which correspond to two overlapping weight loss events in the weight loss vs. temperature plot. 100% of the SDBS powder has been burned off after the second exothermic event. The temperature corresponding to each heat flow peak maximum for the uncoated paper and the powder materials is given in Table 3.2. Average values will be presented for the temperature data. Standard deviations are not included as the sample to sample difference in all cases for all peaks was less than 1°C.

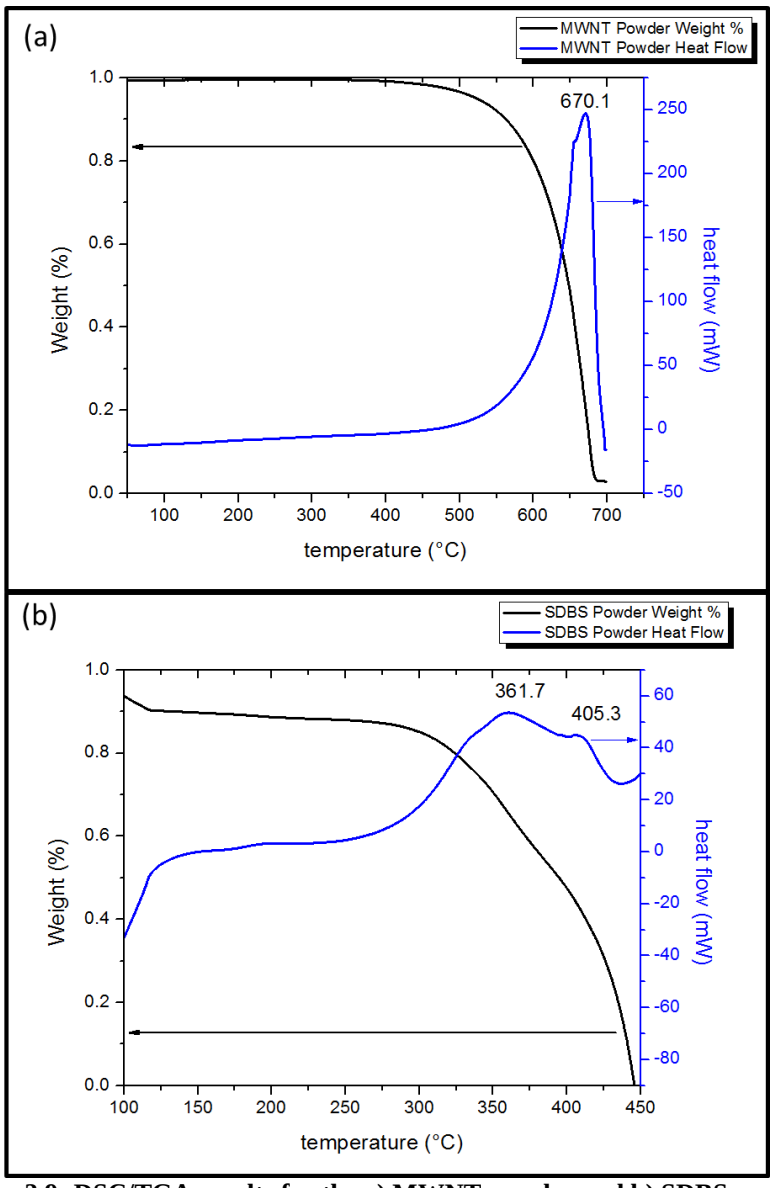

Figure 3.9: DSC/TGA results for the a) MWNT powder and b) SDBS powder.

Table 3.2: Average heat flow peak temperature corresponding to weight loss events for the powders and uncoated papers.

	Peak 1 (°C)	Peak 2 (°C)
MWNT	670.1	
SDBS	361.7	405.3
410 Paper	374.6	506.3
413 Paper	369.6	504.2
415 Paper	371.6	509.7

The results of the DSC scans for the multilayered composites are shown in Figure 3.10. For each image, the order of the stacked data is 1, 4, 8, 12, 16, and 20 deposited layers from bottom to top. Figure 3.10a shows the behavior of the MWNT-410 composite materials. Two peaks are detected for the 1 and 4 layered composites while three peaks are detected for the 8 to 20 layered composites. Figure 3.10b shows the thermal behavior of the MWNT-413 composite materials. Two peaks are detected for the 1 to 8 layered composites while three peaks are detected for the 12 to 20 layered composites. For 12 and 16 deposited layers, the third peak is small and hard to detect in the stacked image, but at 20 deposited layers, the third peak can be easily resolved. Figure 3.10c shows the thermal behavior of the MWNT-415 composite materials. Two peaks are detected for the all of the composite materials.

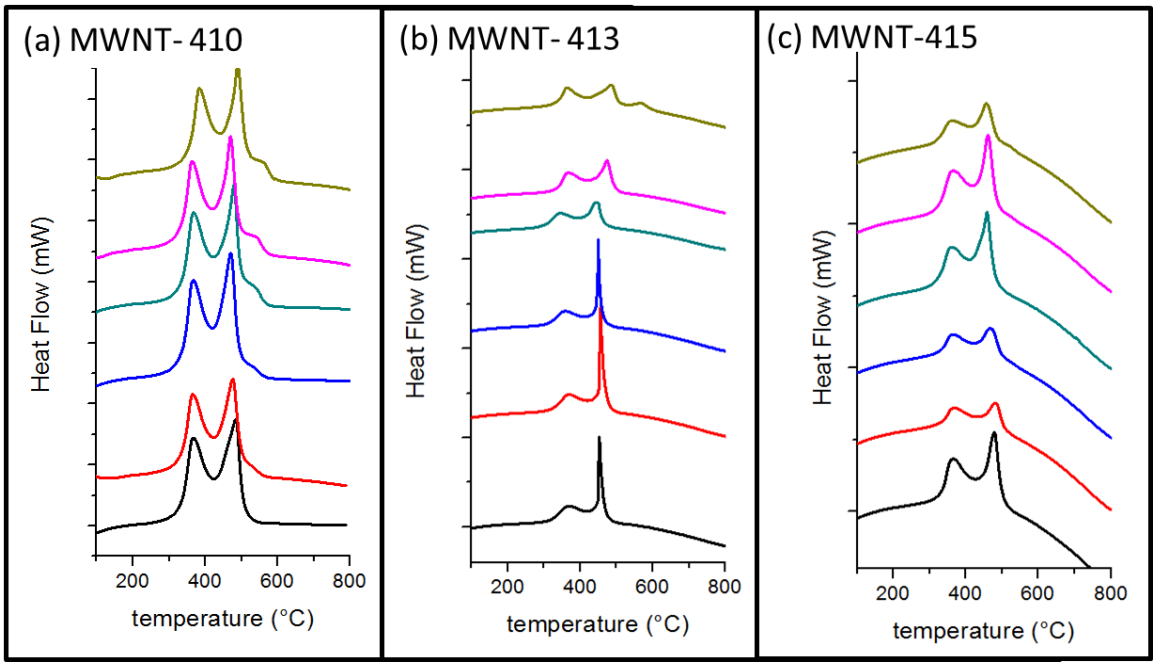

Figure 3.10: Heat flow vs. temperature graphs for the a) MWNT-410; b) MWNT-413; and c) MWNT-415 multilayered composites. For each image, the order of the stacked data is 1, 4, 8, 12, 16, and 20 deposited layers from bottom to top.

Figure 3.11 shows a summary of the peak position (temperature) vs. the number of deposited layers for each composite material. As was shown Figure 3.10, there are a

maximum of three exothermic peaks which appear at different temperatures in the heat flow vs. temperature graphs. At each of these peak temperatures, there is a weight loss event simultaneously detected by the TGA. “Peak 1” describes the exothermic event which happens around 365°C for all composites. “Peak 2” corresponds to the exothermic event which happens around 470°C for all composites. “Peak 3” denotes the exotherm which appears around 550°C for some of the composites.

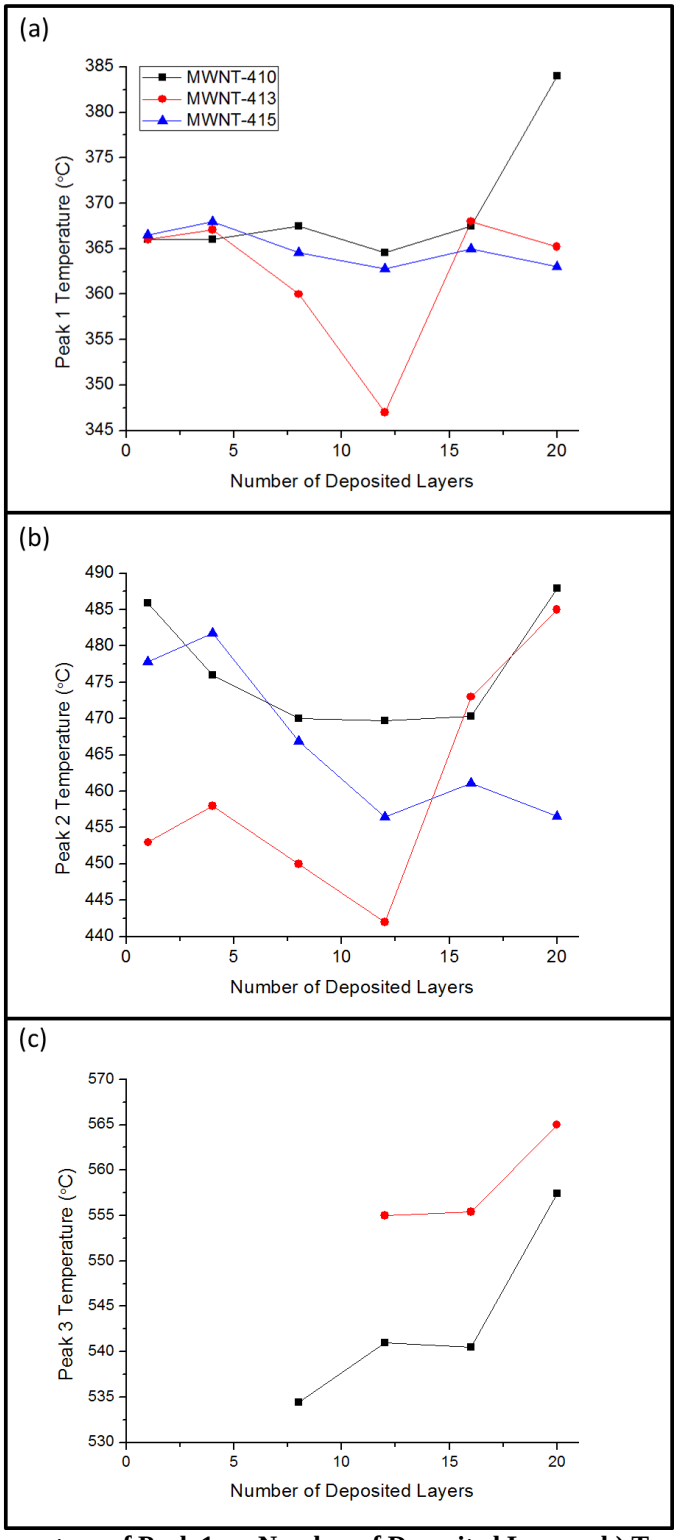

Figure 3.11: a) Temperature of Peak 1 vs. Number of Deposited Layers; b) Temperature of Peak 2 vs. Number of Deposited Layers; c) Temperature of Peak 3 vs. Number of Deposited Layers for all composite sets. Black square data points refer to the MWNT-410 composites. Red circle data points refer to the MWNT-413 composites. Blue upward pointing triangle data points correspond to the MWNT 415 composites.

Figure 3.11a shows the temperature corresponding to peak 1 for the different composite sets. Generally, as layer number is increased, the peak temperature decreases, shifting left in Figure 3.10. The majority of the temperatures are centered around 365°C, which is right between the temperatures of the first paper weight loss event and the first SDBS weight loss event. As the peak appears for all of the composites, it is likely that this peak corresponds to the burning of the paper and the surfactant material. The decrease in peak temperature toward the pure SDBS powder first peak as the number of deposited layers increases suggests that additional surfactant is being deposited within the composite materials.

Figure 3.11b shows the temperature corresponding to peak 2 for the different multilayered composite sets. The temperature for the peak ranges from a minimum of 442°C to a maximum of 490°C, which falls between the 2nd peak temperatures for the SDBS and paper materials. Typically, as layer number increases, the peak temperature decreases before beginning to increase again. This is true except for the MWNT-415 composites which show a decreasing peak temperature with increasing number of deposited layers. The decreased temperature suggests that the SDBS has an influence on this second event for the MWNT-415 composites which did not show SDBS from the FTIR of the surfaces (see Figure 3.7c). SDBS is indeed present in these composites and is located within the paper structure.

As temperature increases with increased MWNT loading, it is possible that the second peak also encompasses the beginning of the MWNT burn off. The high thermal conductivity of MWNTs (up to 3000 W/m*K for a single MWNT at room temperature [24]) would result in localized heating caused by the transfer of heat from the paper to the

MWNT network. Localized heating would cause the MWNT networks to be at a higher temperature than the equipment, decreasing the equipment-measured temperature for which the MWNT burn off starts.

As shown in Figure 3.11c, the third peak appears for only some of the composites, all of which contain a large number of deposited layers of MWNTs. This peak never appears for the MWNT-415 samples. Comparing these results with the SEM images in Figures 3.1-3.3, it is likely that the third peak is detecting the burn-off of MWNTs which are not interacting with the paper material. The MWNT burn off detected by the second peak, therefore, describes the burn-off of MWNTs which do interact with the paper material. The temperature of the third peak is always above 530°C (beyond any paper or surfactant material behavior) and increases with increasing layer number toward the temperature detected for the MWNT powder weight loss event. However, the third peak temperature is much lower than the temperature predicted by the DSC scan of the pure MWNT powder (see Table 3.2). Once again, the high thermal conductivity of the MWNTs as well as their dense packing (which can be seen in Figures 3.1c-f and 3.2d-f) allows localized heating to occur. The temperature which is measured by the DSC/TGA may not actually be the local temperature at the MWNT network.

The TGA is sensitive enough to determine the amount of the composite material which is MWNT. By always measuring samples of the same dimension, the weight of the composite material can be compared back to the weight of the pure paper material. Assuming that the weight of the surfactant is negligible as most of it is pulled through with the water during filtration, the weight difference between composites is the amount of MWNT in the sample. To determine the weight percent (wt%) of the composite, the

amount of MWNT in the composite is divided by the total weight of each composite. The weight percent estimated for each composite studied is given in Table 3.3. All indicate that the amount of MWNT deposited increases with the number of deposited layers. While samples deposited on the 410 and 413 are similar, the amount of MWNT deposited onto the 415 paper is much lower as already demonstrated by the SEM images in Figure 3.3.

Table 3.3: wt% MWNT in each composite material.

	MWNT-410	**MWNT-413**	**MWNT-415**
	wt % MWNT	**wt % MWNT**	**wt % MWNT**
1 layer	17.1 ± 1.51	11.9 ± 1.12	0.079 ± 0.011
4 layers	20.3 ± 2.89	14.2 ± 0.99	5.05 ± 1.01
8 layers	22.6 ± 0.94	16.8 ± 1.04	5.62 ± 0.66
12 layers	27.9 ± 1.83	24.1 ± 3.42	7.16 ± 0.88
16 layers	30.6 ± 3.55	29.5 ± 2.18	9.30 ± 1.76
20 layers	34.8 ± 4.68	32.1 ± 0.85	9.43 ± 0.99

3.3.4 DC Electrical Properties Characterization

Figure 3.12 shows DC resistance vs. number of deposited layers for both the in-plane (3.12a) and the thru-plane (3.12b) of the MWNT-410 (squares), MWNT-413 (circles), and MWNT-415 (triangles) composite materials plotted on a log-log scale. The y-axis for the in-plane measurements spans from 10^1 Ω to 10^{11} Ω, while the y-axis for the thru-plane measurements only spans from 10^3 Ω to10^7 Ω. Error is plotted for all composites; however, because these graphs are presented in log-log format and span such a wide range of values, it is difficult to see the error for all data points. The error does tend to be larger for the thru-plane measurements than the in-plane measurements.

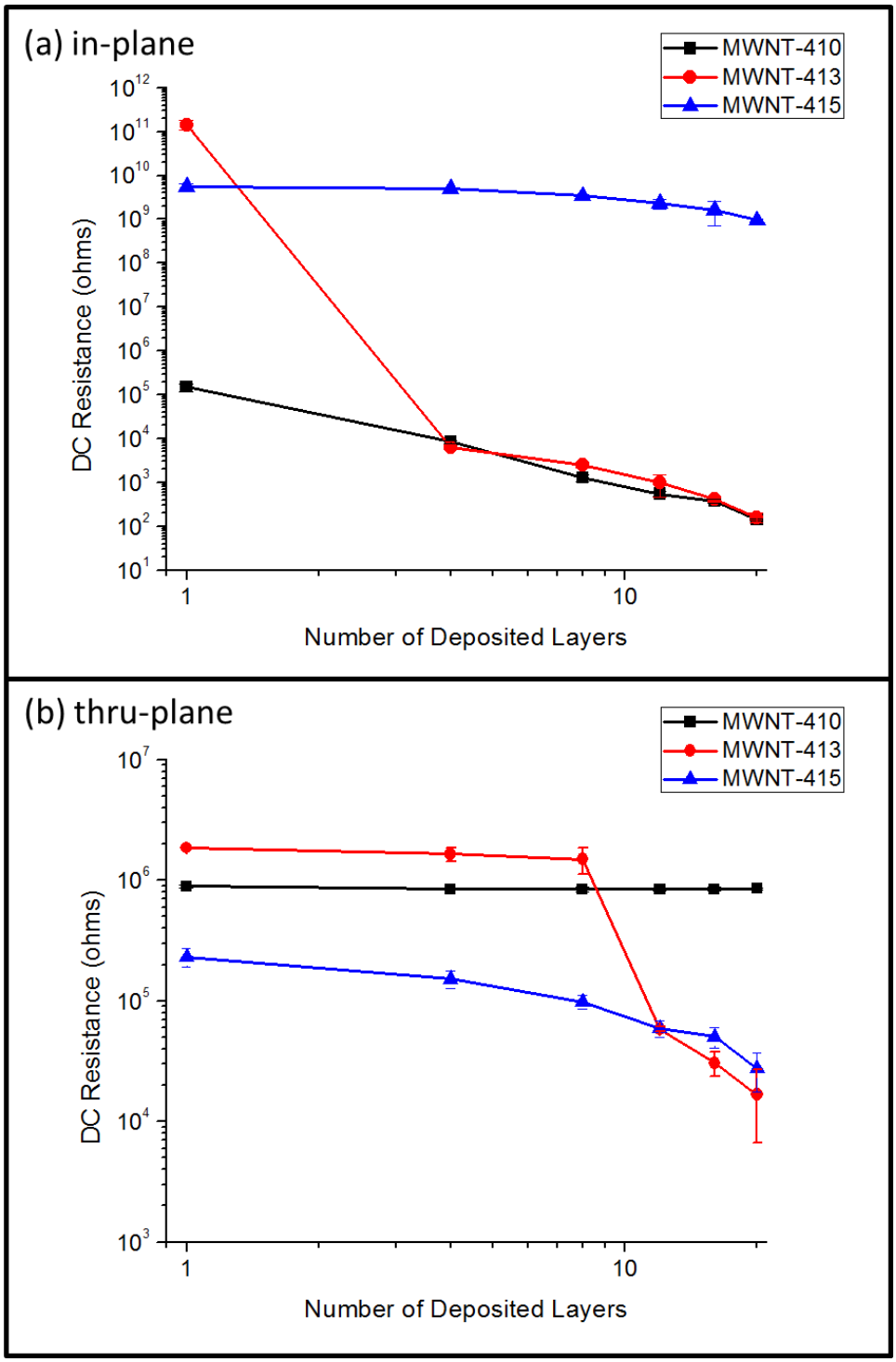

Figure 3.12: DC resistance vs. number of deposited layers for the (a) in-plane and b) thru-plane for the MWNT-410 (squares), MWNT-413 (circles), and MWNT-415 (triangles). These graphs are plotted in the log-log scale.

3.3.4.1 In-Plane DC Resistance Trends

From the DC resistance vs. number of deposited layers graphs for the in-plane of the composite materials in Figure 3.12a, a number of trends are apparent. In order to inform these trends further, it is important to first note that the resistance of the uncoated paper surface measured $8.00 \times 10^{11}\ \Omega \pm 1.50 \times 10^{11}\ \Omega$. The MWNT-410 composite surfaces are always conducting and continually drop in resistance (from $\sim 10^5\ \Omega$ to $\sim 10^2\ \Omega$) as the number of deposited layers is increased from 1 to 20. The SEM images in Figure 3.1 show an interconnected MWNT network across the entire in-plane of the paper for all layer numbers. As layer number increases, the MWNT network becomes thicker and denser resulting in a decrease in resistance.

The MWNT-410 and MWNT-413 composite in-plane resistances have a similar shape, except at 1 layer. At 1 layer, the in-plane resistance for the MWNT-410 composite measures slightly above $10^5\ \Omega$, 6 orders of magnitude lower than that of the 1 layer MWNT-413 composite. It is the difference in the degree of MWNT deposition on the 1 layer composite in-planes which leads to the much lower electrical resistance on the 410 paper. The difference in deposition can be seen in Figure 3.1a and 3.2a for the 1 layered MWNT-410 and 1 layered MWNT-413 composites, respectively. Even at 1 deposited layer, MWNT interconnection occurs across the entire 410 paper surface, allowing for conduction to occur across the in-plane through the MWNT network rather than through the paper fibers.

The MWNT-413 composite materials show the most drastic decrease in resistance, dropping 8 orders of magnitude from 1 to 20 deposited layers. There is a

distinct transition from insulating behavior to conducting behavior on the 4 layered surfaces which measure ~10^4 Ω. The difference in the SEM images shown in Figures 3.2a and 3.2b help inform the transition which is detected. At 1 layer (Figure 3.2a), a single region containing MWNTs is found. The high resistance value is approaching that of the uncoated paper surface suggesting that the MWNTs are not aiding in the in-plane electrical transport. The electrical properties are overwhelmingly dominated by the paper.

However, at 4 deposited layers (Figure 3.2b), the MWNTs show both a massively increased surface deposition as well as interconnection across the surface of the 413 paper. With this increase in interconnection and deposition comes a large decrease in resistance: in-plane electrical properties are dominated by the MWNTs rather than the paper. This is further confirmed by continuing to increase the number of deposited MWNT layers. Similar to the MWNT-410 composite in-plane properties, as the MWNT deposition increases further and covers the entire 413 paper backbone, as shown in Figures 3.2c-f, the resistance continues to decrease.

Conversely, the in-plane behavior of the MWNT-415 composite materials shows the least variation in DC resistance and the highest overall resistance at ~10^9 Ω. There is no transition from insulating to conducting as all samples remain insulating from 1 to 20 deposited layers. As was shown in Figure 3.3, MWNT deposition tends to occur below the surface or in very small pockets on the surface. The small amount of MWNT deposition on the surface of the 415 paper results in primarily paper-dominated electrical properties and the high resistance for the in-plane even after a large number of deposition steps.

3.3.4.2 Thru-Plane DC Resistance Trends

For the electrical properties of thru-plane of the composites which was given in Figure 3.12b, the MWNT-413 composites once again show the greatest change in DC resistance, spanning 2 orders of magnitude between 1 and 20 deposited layers. The MWNT-410 composites show little to no change, exhibiting a resistance slightly under 10^6 Ω for the entire composite set. The MWNT-415 composite materials have the lowest resistance at 1 layer (~$2x10^5$ Ω), and the resistance of the multilayered composites continuously decreases with increasing layer number. Interestingly, the MWNT-413 composites show behavior which mirrors the other two composite sets depending on the number of deposited layers. At low number of deposited layers (1-8), a constant value of ~10^6 Ω was measured for the resistance, similar to the behavior of the MWNT-410 composites. Between 8 and 12 deposited layers the MWNT-413 composites show an order of magnitude drop in resistance and then continuously decrease in resistance like the MWNT-415 composites.

For all composites, the DC resistance at 1 layer is much lower than the DC resistance of the thru-plane of the uncoated papers ($2.1x10^7$ Ω ± $6.4x10^6$ Ω) suggesting that all of the composites are at least partially conducting at 1 layer. However, the MWNT-410 composites remain at about the same level of partially conducting from 1 to 20 deposited layers. There is a small decrease in thru-plane resistance between the 1 and 4 layered composites. However, after 4 deposited layers of MWNTs, the resistance value remains static for the rest of the measurement range. In studying the I-AFM derived current maps presented in Figure 3.4, the current flow is almost identical between the 1 layered composite, shown in Figure 3.4a, and the 20 layered composite, shown in Figure

3.4b. A slight increase in current flow is detected from 1 to 20 layers; however the shape of the current map is exactly the same. The nearly identical current flow suggests that a limited amount of MWNTs penetrate the internal structure and then a barrier for deposition occurs. This barrier is the growth of the thick MWNT networks on the in-plane of the 410 paper.

Comparing the electrical data to the wt% data presented in Table 3.3 yields some interesting trends. The MWNT-415 paper composites contain the lowest wt% of MWNTs which is expected given the large size of the pores as compared to the length of the MWNTs. The 1 layer MWNT-415 paper composite sample has a wt% of 0.079%. From Figure 3.12b, the 1 layer MWNT-415 composite shows a fairly low electrical resistance across the thru-plane. Therefore, a conducting network can form in the thru-plane of the paper materials with a very small amount of MWNTs. For in-plane conduction to occur, a much larger weight percent is required, however. The minimum MWNT wt% found for a conducting composite in-plane was 14.2% (4 layered MWNT-413 composite) for composites with mostly surface deposition and a small amount of internal deposition.

3.3.5 Percolation Models

Percolation theory is a useful tool for describing transport properties of heterogeneous materials, such as composites. A filler material is added to a continuous matrix material, and at a critical amount, the filler material comes together to form a completely interconnected network [65]. At this critical threshold, the complete connectivity of the filler material causes the measured properties of the system to switch from properties of the matrix or backbone material to the properties of the filler material.

In this thesis, percolation behavior is studied for the electrical behavior of the composite materials by determining the critical number of deposited MWNT layers (similar to composite filler) required to form a percolated network of MWNTs on the surface and within the thickness of the paper materials (insulating matrix). From the percolation behavior, equations can be developed which can be used to predict the resistances of the composite materials.

Using power law curve fitting to the experimental data in Figure 3.12a (for a detailed explanation of how the equations for both the in-plane and thru-plane were developed, see Appendix A), Equation 3.1 was built to describe the resistance of the in-plane of the composite materials. $R_{percolation}$ is the resistance at in-plane percolation, (L_b/d_p) is the rod bundle length to pore size ratio, n is a deposition constant, L is the layer number, and L_c is the critical number of layers required for percolation. Figure 3.13 shows the experimentally determined DC data as well as the model predicted resistance for the conductive surfaces of the MWNT-410 and MWNT-413 composite materials. For the MWNT-410 composites, $R_{percolation} = 1.5x10^5\ \Omega$, $L_b/d_p = 5$, n = 1, and $L_c = 1$. For the MNWT-413 in-plane, $R_{percolation} = 6400\ \Omega$, $L_b/d_p = 1$, n = 2, and $L_c = 4$. The in-plane of the MWNT-415 surfaces never percolated and is therefore not shown.

$$R_{in-plane} = \frac{R_{percolation}}{(L_b / d_p)} n\pi (L - L_c)^{-2.08} \quad \textbf{(3.1)}$$

Unlike most percolation models wherein the critical threshold value is guessed and tested along with the curve fit constants, using a layered deposition method results in an exact value for the critical threshold. For the MWNT-410 paper composites that value

was 1 (when $L_b/d_p > 1$, in most cases, the surface will be percolated at 1 layer). For the MWNT-413 paper composites, that value was 4. For the MWNT-415 paper composites, percolation did not happen for the number of layers investigated. The equation (3.1) used to predict the in-plane resistance is a function of the resistance at percolation, the L_b/d_p, and the directionality of deposition (surface only (n=1) or surface and internal (n=2), which can be estimated using L_b/d_p).

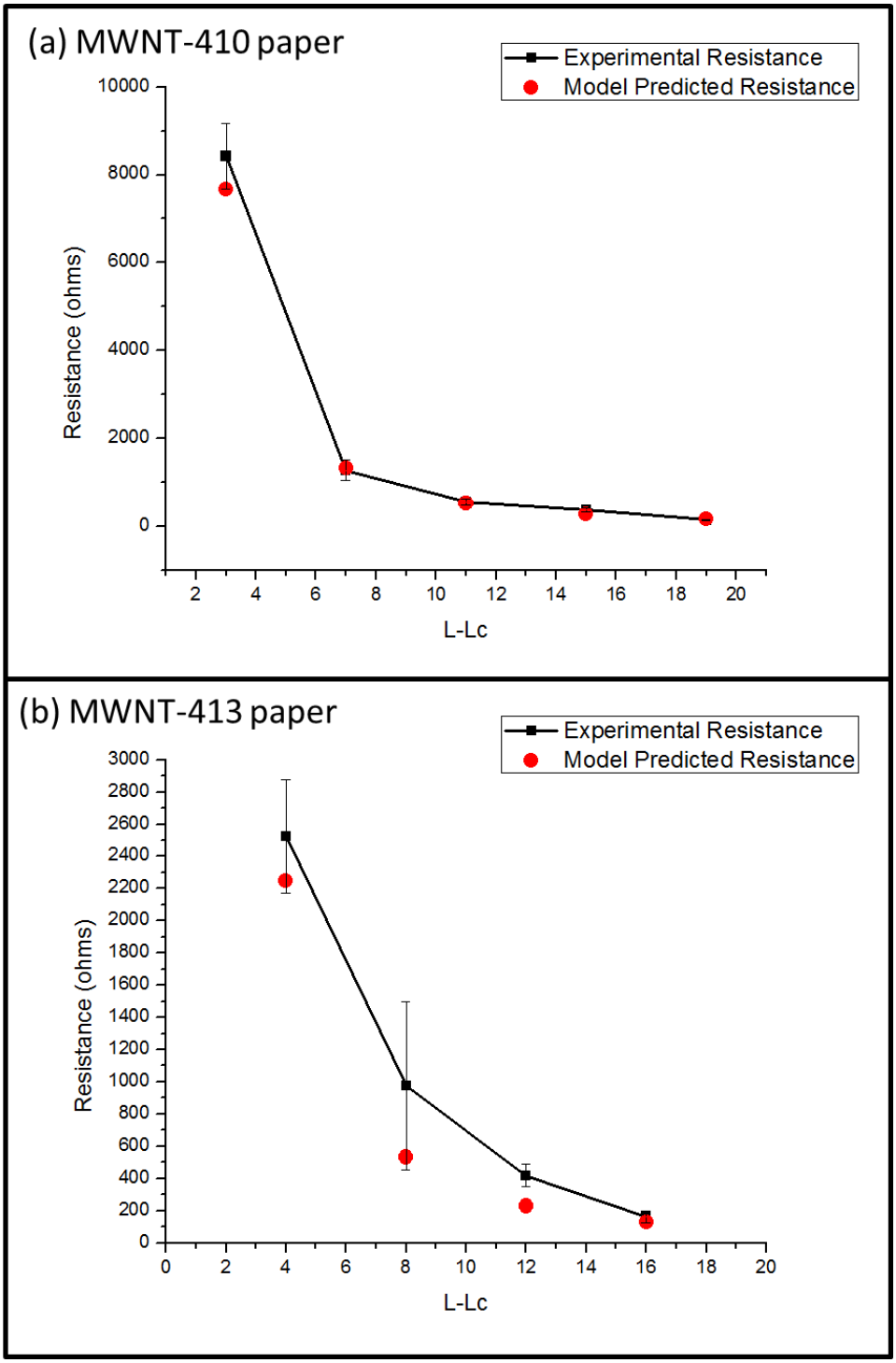

Figure 3.13: The measured DC resistance values and the model predicted resistance values for the in-plane of the a) MWNT-410 paper and b) MWNT-413 paper composite systems.

Equation 3.2 was built to describe the resistance of the thru-plane of the composite materials and only depends on $R_{percolation}$ and L_c (see Appendi A for more details). The experimentally measured DC resistance values are plotted with the predicted values in Figure 3.14. For the MWNT-415 paper composites, $R_{percolation}$ = $2.3x10^5$ Ω and L_c = 1. For the MWNT-413 paper composites L_c = 10 and $R_{percolation}$ = $7.5x10^4$ Ω. In both cases, the model predicted values fall within the experimentally determined resistance, with the exception of one data point in each system.

$$R_{thru-plane} = R_{percolation} \frac{\pi}{2} (L - L_c)^{-0.85} \quad \textbf{(3.2)}$$

For the thru-plane, the model describes the resistance within the pore for instances where *continuous deposition* of the MWNTs is occurring through the thickness of the composites. This model does not describe the thru-plane where the resistance value is unchanged after percolation (MWNT-410 composite thru-planes and 1-8 layered MWNT-413 composite thru-planes). Because of this constraint, the model does not have L_b/d_p as an explicit variable, although this variable is implicit. When $L_b/d_p < 1$, this model always applies, when $L_b/d_p > 1$, the model never applies, and when $L_b/d_p = 1$, the model only applies after a second percolation event occurs. Equation 3.2 can be used to predict the resistance within the pore structure.

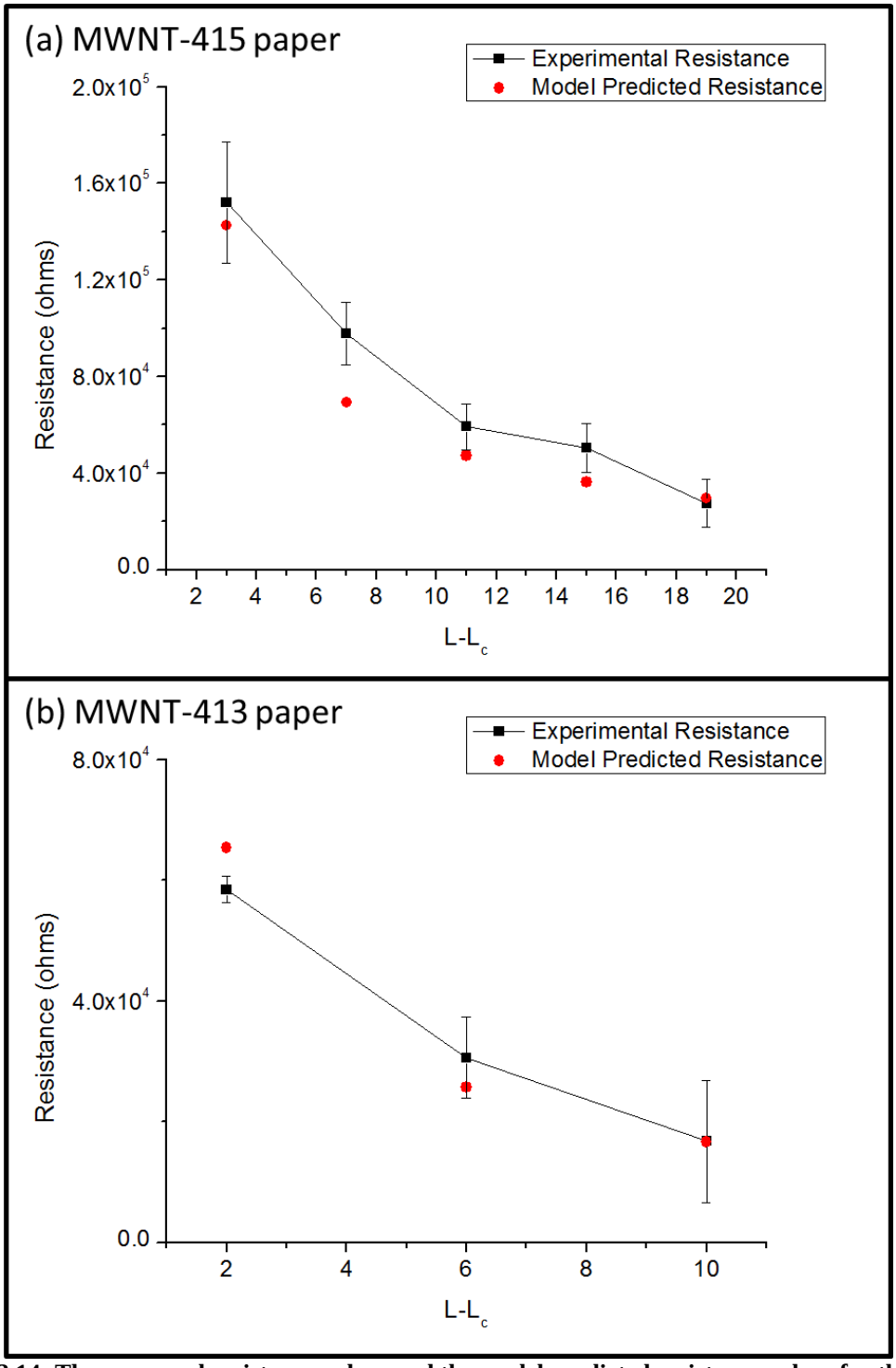

Figure 3.14: The measured resistance values and the model predicted resistance values for the thru-plane of the a) MWNT-415 paper and b) MWNT-413 paper composite systems.

Like the equation for the in-plane, the thru-plane equation also requires knowledge of the percolation threshold value and the resistance at percolation. However,

those values are all provided in this thesis. With close inspection, a few trends can be made for estimation purposes such that these equations can be used outside of the composites presented here.

(1) Both the in-plane and the thru-plane show a maximum value for $R_{percolation}$ of $\sim 10^5\ \Omega$. If $R_{percolation}$ is unknown, this value would be a good estimate.

(2) If $L_b/d_p > 1$, assume only surface deposition is occurring and $L_c = 1$ for the in-plane. If $L_b/d_p < 1$, assume only internal deposition and $L_c = 1$ for the thru-plane.

(3) When $L_b/d_p = 1$, the widest array of properties can be found as materials simultaneously deposit in both planes. However, this also means L_c is harder to predict. In this study, $L_c = 4$ for the in-plane and 10 for the thru-plane.

3.4 Conclusions

1 to 20 layered MWNT-paper composite materials were fabricated by vacuum filtration-aided drying of dropcasted MWNT dispersions on paper substrates with pore sizes less than, equal to, and greater than the length of the MWNT bundles. The layered methodology for depositing the MWNTs as well as the pore size variation of the paper backbone led to a vast number of composite structures. Each composite structure resulted in its own unique set of properties and behaviors- physical, chemical, thermal, and electrical- which were measured and described. The structures and properties presented in this Chapter will be used as a guide in developing the mathematical and structural models detailed in Chapter 4.

CHAPTER 4

IMPEDANCE SPECTROSCOPY AND EQUIVALENT CIRCUIT MODELING FOR MWNT-PAPER COMPOSITE MATERIALS FABRICATED USING VACUUM FILTRATION

4.1 Introduction

Impedance spectroscopy is a powerful tool for characterizing the behavior of materials systems. Unlike their DC-based counterparts, AC electrical techniques, including impedance spectroscopy, are more sensitive to individual electrical processes present due to the dependence of frequency on the measurement [43]. Since impedance is measured over a wide range of frequencies, it is possible to detect and separate the response of different electronic, ionic, and dielectric processes which are active from the overall behavior of the material. As was discussed in Section 1.2.3, through the use of equivalent circuit analysis on the data provided by impedance spectroscopy as well as the other immittance functions (see Appendix B), it is possible to determine which impedance process is active at different frequencies as well as describe the properties of that process [44]. In this Chapter, the impedance behavior of the in-planes (surfaces) and the thru-planes (through the thickness of the paper) of the composite materials are presented. Equivalent circuit fitting is done for each impedance behavior, and an overall equivalent circuit for each plane of measurement is proposed.

4.2 In-Plane

Figure 4.1 shows a schematic describing the measurement of the in-plane properties using a view parallel to the in-plane of the material with an exaggerated paper backbone thickness. Both probes were placed on the surface of the paper backbone material (uncoated or coated with MWNTs) and connected to an AC voltage source for the impedance measurements.

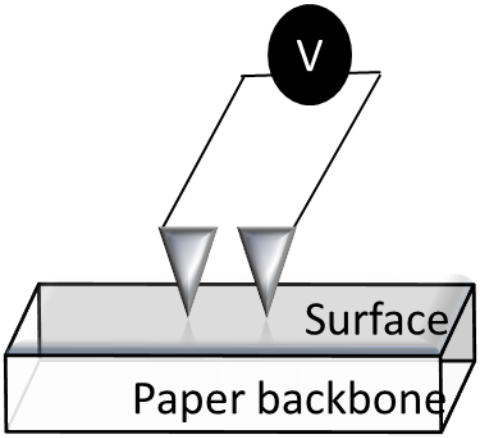

Figure 4.1: Schematic describing the measurement of the surface of the paper/composite from a view parallel to the in-plane of the material.

4.2.1 Presentation of In-Plane Frequency-Explicit Plots

While a number of trends were detectable using DC resistance data, as shown in Figure 3.12, impedance spectroscopy offers even more information about the electrical behavior of the composite materials. From just the frequency-explicit impedance data, information about the DC resistance, resistance drops between samples, and electrical behavior can be obtained. Figure 4.2 plots frequency-explicit impedance data for the in-plane of the different composite sets in the form of impedance magnitude vs. frequency, log(|Z|) vs. log(f) (Figures 4.2a,c,e) and phase angle vs. frequency, θ vs. log(f) (Figures 4.2b,d,f).

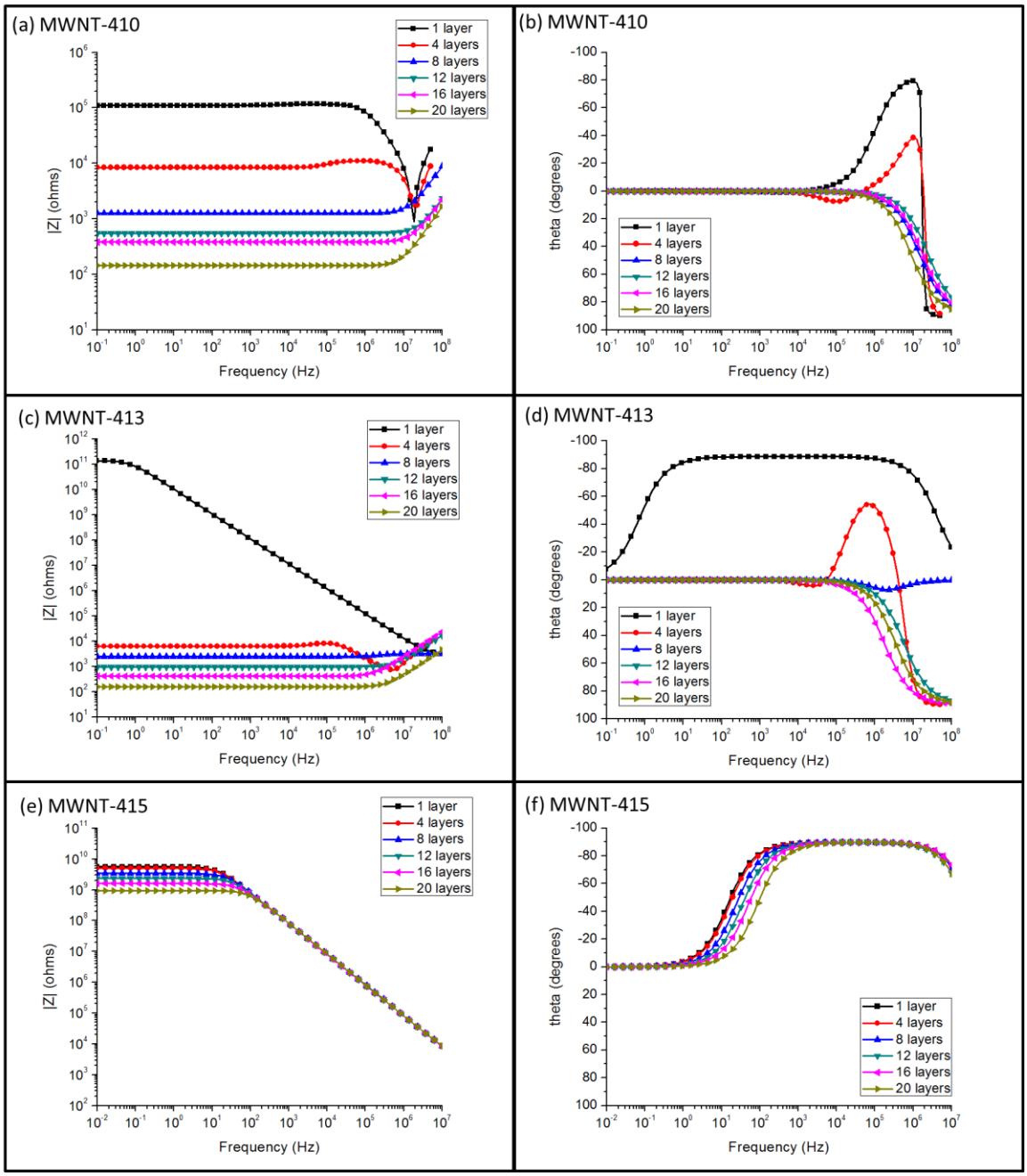

Figure 4.2: Frequency explicit impedance graphs for the multilayered composite materials. The impedance behavior for the MWNT-410 paper composites can be seen in the a) log(|Z|) vs. log(f) and b) θ vs. log(f) graphs. The impedance behavior for the MWNT-413 paper composites can be seen in the c) log(|Z|) vs. log(f) and d) θ vs. log(f) graphs. The impedance behavior for the MWNT-415 paper composites can be seen in the e) log(|Z|) vs. log(f) and f) θ vs. log(f) graphs.

The low-frequency impedance value in the log(|Z|) vs. log(f) graph is analogous to the DC resistance value. In all cases, the measured DC resistance and the extracted low frequency AC impedance matched within one standard deviation. Also, the degree

of change for the DC resistance (low frequency impedance) for each sample can be gathered from the log(|Z|) vs. log(f) graph. In Figure 4.2a, the three orders of magnitude decrease in low frequency impedance from the 1 layer sample to the 20 layer sample for the MWNT-410 composite surfaces can be measured. In Figure 4.2c, the 8 order of magnitude decrease from 1 to 4 deposited layers for the MWNT-413 composite surfaces can be seen. There is a much smaller rate of change for the impedance of the samples made with 4-20 deposited layers of MWNTs. Finally, Figure 4.2e shows a very small variation for the low frequency impedance, within a single order of magnitude, for the 1-20 layer MWNT-415 composite surfaces. These trends agree with the DC values reported in Figure 3.12a.

In addition to providing information about the steady-state behavior of the composites, studying the shapes of the log(|Z|) vs. log(f) and θ vs. log(f) graphs gives some indication about the number of electrical behaviors present for the in-plane of these materials. Each curve shape corresponds to a different electronic behavior. For the MWNT-410 composite materials, as shown in Figures 4.2a and 4.2b, there are two distinct impedance behaviors which are observed. For the MWNT-413 composite materials, as shown in Figures 4.2c and 4.2d, there are four distinct impedance behaviors observed. For the MWNT-415 composite materials, as shown in Figures 4.2e and 4.2f, a single impedance behavior is observed. It is worth noting that the two behaviors present for the MWNT-410 composite materials and the one behavior present for the MWNT-415 composite materials are also exhibited by the MWNT-413 composite materials.

4.2.2 Presentation of In-Plane Nyquist Plots

Another way to present the data found using impedance spectroscopy is using frequency-implicit Nyquist plots. Real impedance, Z', is plotted on the x-axis while imaginary impedance, Z", is plotted on the y-axis. It is typical that the impedance Nyquist plots have a 1st quadrant which corresponds to –Z" vs. Z' [43, 44]. Figure 4.3 shows the four different Nyquist plots which describe the four different impedance behaviors exhibited by the MWNT-413 composite surfaces [66]. For Figures 4.3a-c, measurement frequency increases in the direction of the y-axis while for Figure 4.3d, frequency increases away from x-axis. Figure 4.3a shows the behavior of the surface formed by depositing 1 layer of MWNTs onto the 413 filter paper. There is a single semicircle in the first quadrant of the Nyquist plot. At 4 layers, the electrical behavior of the surface switches to that presented in Figure 4.3b. At both low and high frequencies, the Nyquist plot shows impedance values in the 4th quadrant. At mid-range frequencies, the Nyquist plot shows impedance values in the 1st quadrant. At 8 layers, the electrical behavior of the MWNT-413 composite surface switches yet again and is plotted in Figure 4.3c. A single semicircle is detected in the 4th quadrant. Finally, as shown in Figure 4.3d, at 12 deposited layers and beyond, the impedance behavior presents as a straight line in the 4th quadrant.

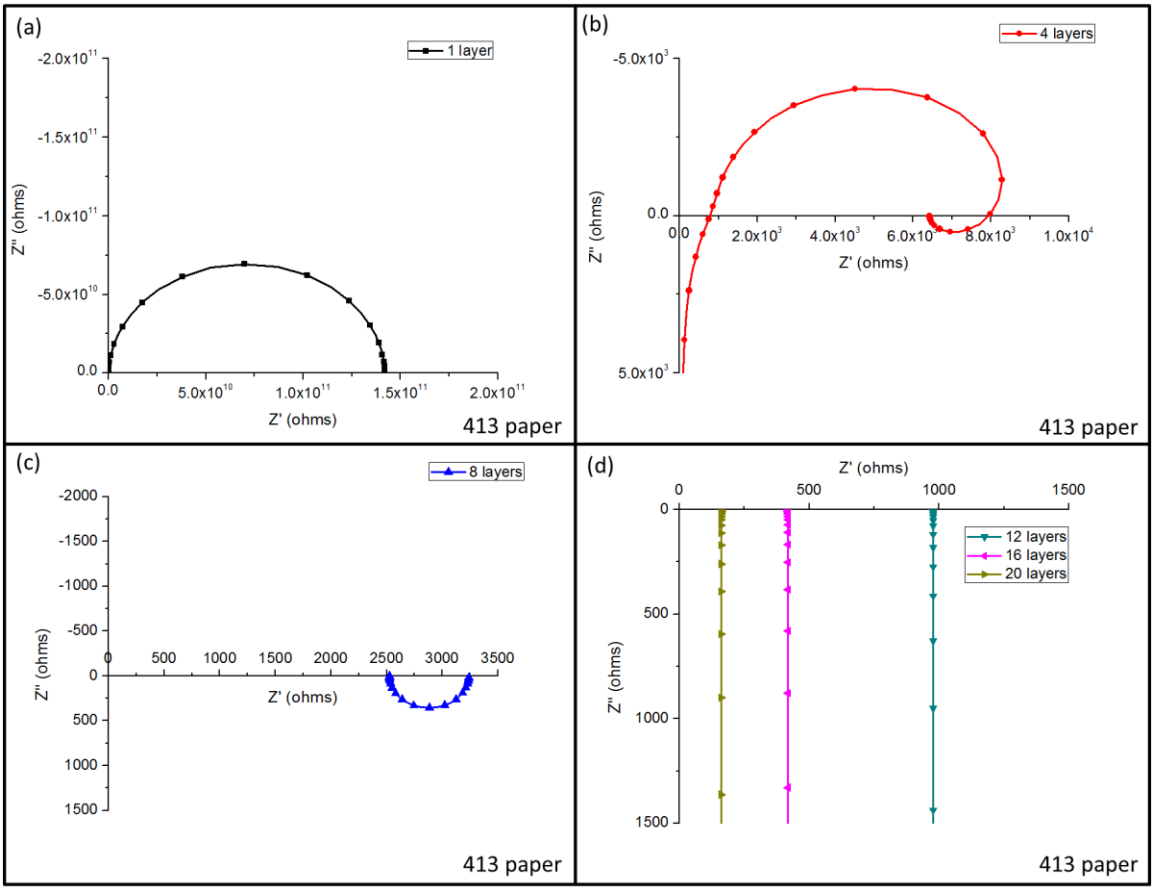

Figure 4.3: Impedance data presented as Nyquist plots for the surfaces of the MWNT-413 composite materials formed by depositing a) 1 layer; b) 4 layers; c) 8 layers; and d) 12-20 layers of MWNTs.

Figure 4.4 shows the two different impedance behaviors exhibited by the MWNT-410 composite surfaces [64]. Figure 4.4a shows the Nyquist plots for the impedance behavior of the surfaces formed by depositing 1 (square data points) and 4 (circle data points) layers of MWNTs on the 410 paper. This same behavior was seen for the 4 layer MWNT-413 composite surface (Figure 4.3b). For 8-20 deposited layers, the second impedance behavior is active for the MWNT-410 surfaces switches and is shown in Figure 4.4b. This behavior was seen previously for the 12-20 layered MWNT-413 composite surfaces (Figure 4.3d).

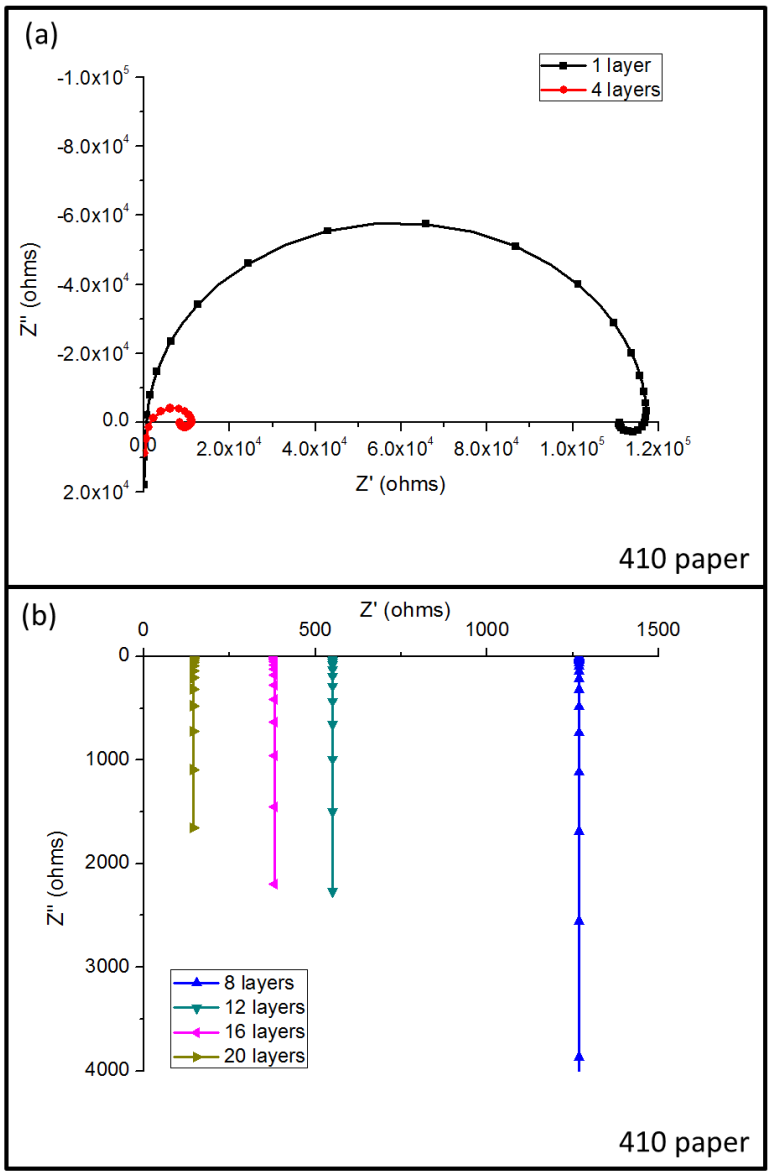

Figure 4.4: Impedance data presented as Nyquist plots for the surfaces of the MWNT-410 composite materials formed by depositing a) 1 and 4 layers; and b) 8-20 layers of MWNTs [64].

Figure 4.5 shows the Nyquist plots for the single impedance behavior exhibited by the 1-20 layered MWNT-415 paper composite surfaces. A single semicircle is present in the first quadrant which decreases in size with increasing number of deposited layers. This impedance behavior was also exhibited by the 1 layer MWNT-413 composite surface, as shown in Figure 4.3a.

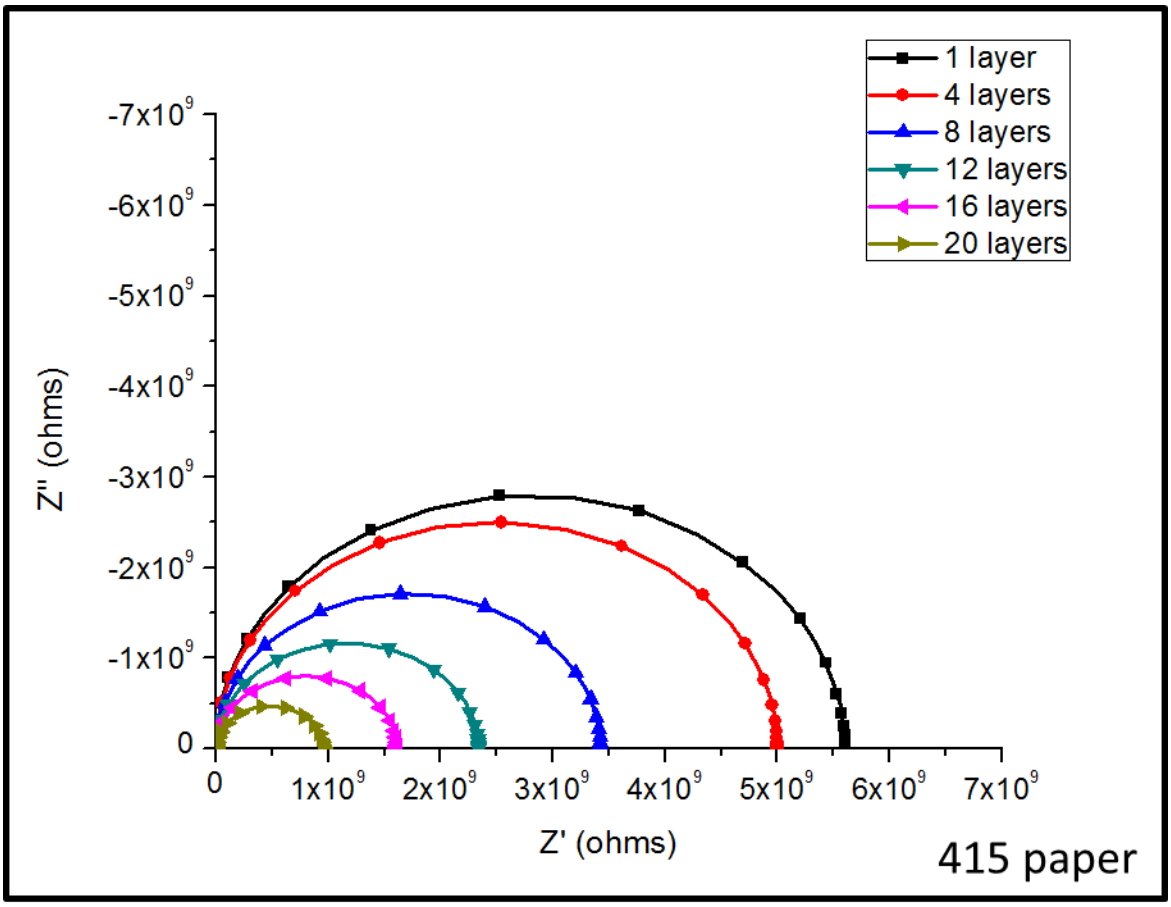

Figure 4.5: Impedance data presented as Nyquist plots for the surfaces of the 1-20 layered MWNT-415 composites.

4.2.3 In-Plane Equivalent Circuit Modeling

As was discussed in Chapter 1, mathematic models can be built to fit impedance curves using circuit elements (resistors, capacitors, and inductors) and arrangements of those circuit elements. The arrangements can be basic, such as two circuit elements in series or in parallel; however, as the shape of the impedance curve becomes more complex, the arrangement of circuit elements required to fit that curve also becomes more complex. Through careful analysis and understanding of the structure of the material being studied, the different conduction processes present in the material can be described by the arrangement of the elements in its equivalent circuit [43, 44]. In this section,

equivalent circuits for the different impedance behaviors shown for the in-planes of the composite materials in Figures 4.2-4.5 will be presented. In addition to the presentation of each equivalent circuit, the electronic behaviors described by each circuit will also be described and justified. The fits discussed in each section were already shown for the data presented in Figures 4.2-4.4

4.2.3.1 Paper-Dominated Transport

The impedance spectra in Figure 4.3a and Figure 4.6 present as a single depressed semicircle shifted away from the y-axis in the first quadrant of the complex impedance plane. The results are fit with the circuit presented in Figure 4.6. This circuit contains a resistor (R) and a constant phase element (CPE) arranged in parallel, $(R_1\text{-}CPE_1)_p$, in series with a relatively small series contact resistance, R_s. The values for the circuit elements for each surface whose impedance response was fit by this circuit are available in Table 4.1.

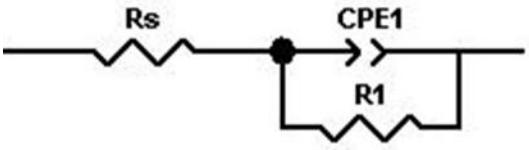

Figure 4.6: Equivalent circuit used to fit the impedance response for the in-plane of the 1 layer MWNT-413 composite and the entire MWNT-415 composite series shown in Figures 4.3a and 4.5, respectively.

Table 4.1: Circuit element values for the composite surfaces described by the equivalent circuit in Figure 4.6.

	R_s (kΩ)	R_1 (GΩ)	CPE-τ pF	CPE-β
1 layer, 413	3.0 ± 0.12	140 ± 45	1.61 ± 0.34	0.985 ± 0.01
1 layer, 415	2.33 ± 0.76	5.6 ± 0.82	1.98 ± 0.55	0.963 ± 0.012
4 layers, 415	2.46 ± 3.8	5.0 ± 0.31	1.97 ± 0.30	0.966 ± 0.008
8 layers, 415	2.77 ± 2.9	3.4 ± 0.29	1.93 ± 0.44	0.959 ± 0.011
12 layers, 415	3.33 ± 1.6	2.3 ± 0.69	1.96 ± 0.29	0.971 ± 0.006
16 layers, 415	2.34 ± 2.2	1.6 ± 0.93	1.98 ± 0.26	0.978 ± 0.009
20 layers, 415	3.34 ± 0.99	0.98 ± 0.07	1.95 ± 0.64	0.969 ± 0.011

For the 1 layer MWNT-413 composite surface, the value of R_1, $1.42 \times 10^{11}\ \Omega \pm 3.48 \times 10^{10}\ \Omega$, is on the same order of magnitude as the resistance of the uncoated paper ($8.00 \times 10^{11}\ \Omega \pm 1.50 \times 10^{11}\ \Omega$). The pockets of CNTs present in Figure 3.2a are too spread apart to contribute to the behavior of the measured spectrum, although they do aid slightly as the resistance does drop. The resistance values for the MWNT-415 composite materials are two orders of magnitude lower than that of the uncoated paper. The SEM images for these composite surfaces in Figure 3.3 showed that MWNT deposition occurred mostly as aggregates in the large pores. It is likely that the MWNT agglomerates along the pore edges helped promote conduction by providing a conductive pathway around the pores causing the resistance to decrease. However, surface conduction was overwhelmingly dominated by the paper fibers. This equivalent circuit describes paper-dominated electrical transport.

Paper-dominated transport is further confirmed by the presence of the CPE rather than a capacitor (C). A CPE, defined mathematically in Equation 4.1, is similar to a capacitor except that it takes into account electrical processes which occur either due to a distribution of current density on an inhomogeneous electrode surface or with a distribution of relaxation times for the conduction process [43, 67, 68]. τ has units of $(\Omega * F)^{\beta}/\Omega$. When $\beta = 1$, τ is equivalent to capacitance (units = F) [68]. Since the CPE is very similar to a capacitor, for simplicity τ will be presented with the units of F in this thesis.

$$Z_{CPE} = \frac{1}{\tau(j\omega)^{\beta}} \qquad \textbf{(4.1)}$$

As shown previously in Figures 3.2a and 3.3, the surfaces of these composites are highly inhomogeneous. The 1 layer MWNT-413 composite surface contains both scattered, unconnected pockets of MWNTs and open pores between paper fibers. The MWNT-415 composite materials shows agglomerates within the pore network, although at higher layer numbers also show some scattered, unconnected coating of the surface fibers. The exponent β determines the degree of depression of the semicircle [67] and can be used to determine the degree of homogeneity of the surface. The further β decreases from 1, the less homogenous the surface. While the equivalent circuit for paper-dominated transport requires a CPE over a capacitor, the value of β is very close to 1 suggesting that the presence of the MWNT pockets/agglomerates contribute only to a slight deviation from ideality.

4.2.3.2 Thin Film-Dominated Transport

When a sufficient amount of MWNTs are deposited on the surface, an interconnected network of MWNTs is formed across the paper. The paper fibers are no longer the dominant conduction mechanism, and the shape and magnitude of the impedance behavior changes to that shown in Figures 4.3b and 4.4a. The equivalent circuit which fits this behavior is shown in Figure 4.7 and has four major components: a high frequency inductor, (L_1), a high-mid frequency, $(R_1\text{-}C_1)_p$, a mid-low frequency, $(R_2\text{-}C_2)_p$, and a low frequency, $(R_3\text{-}L_2)_p$. Because the low frequency element $(R\text{-}L)_p$ is nested within the second element $(R\text{-}C)_p$, this circuit will be referred to as the "Nested-RL" equivalent circuit. The values for the circuit elements for each surface whose impedance response was fit by the "Nested-RL" circuit are available in Table 4.2.

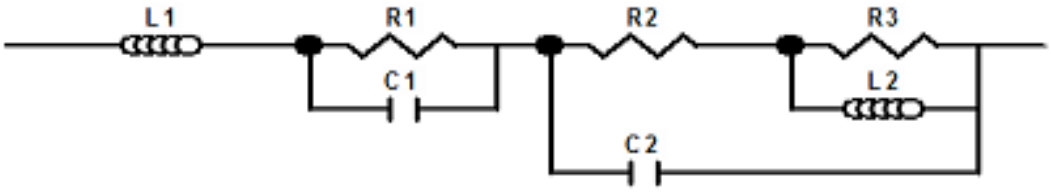

Figure 4.7: Equivalent circuit used to fit the impedance response for the in-plane of the 1 and 4 layered MWNT-410 composites and the 4 layered MWNT-413 composite shown in Figures 4.3a and 4.2b, respectively.

Table 4.2: Circuit element values for the composites whose in-plane impedance response can be fit by the "Nested-RL" equivalent circuit.

	L_1 (H)	R_1 (Ω)	C_1 (F)	R_2 (Ω)	C_2 (F)	R_3 (Ω)	L_2 (H)
1 layer, 410	$6.50\text{x}10^{-5}$ ± $9.26\text{x}10^{-6}$	900 ± 3.21	$3.21\text{x}10^{-11}$ ± $1.29\text{x}10^{-11}$	$1.57\text{x}10^{5}$ ± $2.21\text{x}10^{4}$	$1.34\text{x}10^{-11}$ ± $1.85\text{x}10^{-12}$	$6.41\text{x}10^{4}$ ± $1.21\text{x}10^{4}$	$2.00\text{x}10^{-4}$ ± $4.00\text{x}10^{-5}$
4 layers, 410	$3.35\text{x}10^{-5}$ ± $3.50\text{x}10^{-6}$	895 ± 9.90	$4.93\text{x}10^{-11}$ ± $1.91\text{x}10^{-12}$	$7.53\text{x}10^{3}$ ± 242	$1.98\text{x}10^{-12}$ ± $1.06\text{x}10^{-13}$	$2.78\text{x}10^{3}$ ± 554	$3.95\text{x}10^{-4}$ ± $3.01\text{x}10^{-5}$
4 layers, 413	$3.08\text{x}10^{-5}$ ± $3.54\text{x}10^{-6}$	908 ± 4.24	$1.96\text{x}10^{-11}$ ± $4.95\text{x}10^{-12}$	$5.53\text{x}10^{3}$ ± 504	$8.50\text{x}10\text{-}^{11}$ ± $1.13\text{x}10^{-11}$	$2.73\text{x}10^{3}$ ± 233	$7.40\text{x}10^{-4}$ ± $1.55\text{x}10^{-5}$

At high frequencies (~10 MHz), pure inductive behavior is measured, L_1, which is likely an artifact of the wiring and instrument used to measure the sample. At low frequencies, another inductive response is measured although this time the response occurs in parallel with a resistor. In addition to these composites [5, 64], the low frequency element $(R\text{-}L)_p$ has been detected on MWNT thin films deposited via inkjet printing on paper substrates and was suggested to be a result of coiled MWNT bundles [13]. This coiling can be seen in Figure 4.8 which, in the foreground, shows the wrapping of MWNTs around a single paper fiber. In order for the coiling to be a detected part of the electronic behavior of this composite, there must be a sufficient number MWNTs on the surface that are interconnected but in a way such that the paper fibers still have an impact on the electronic behavior of the surface. This suggests that the filter paper surface is coated with a thin film of MWNTs and that this circuit describes thin film behavior of the MWNT network.

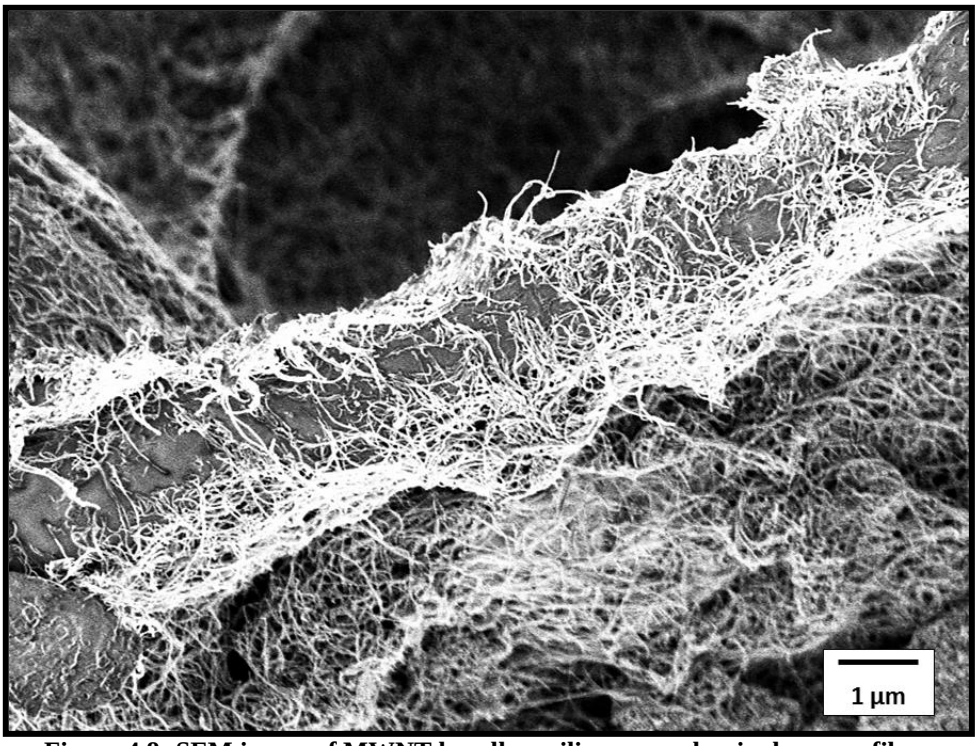

Figure 4.8: SEM image of MWNT bundles coiling around a single paper fiber.

Thin film behavior is further verified by the presence of the two $(R\text{-}C)_p$ in series with each other, $(R1\text{-}C1)_p$ and $(R2\text{-}C2)_p$, which appear in the middle frequency range. Previous research in using impedance spectroscopy to measure the properties of SWNT thin films determined that it was possible to extract both the resistance from the SWNT bundle as well as the resistance of the SWNT-SWNT junctions [39]. Using equivalent circuit fitting, the impedance data collected could be fit by a circuit arrangement of two $(R\text{-}C)_p$ in series with each other. It was suggested that the high frequency $(R\text{-}C)_p$ described conduction across the SWNT bundles while the low frequency $(R\text{-}C)_p$ corresponded to conduction through the junctions [39]. In addition, a study of conduction along SWNT bundles and junctions using conductance-atomic force microscopy showed that at the junction between two bundles of SWNTs resistance generally increases 2 to 10 times, but an increase of up to 3 orders of magnitude was also

observed. The degree of the increase in resistance depends upon the diameters of the bundles which make up the junction: the larger the diameter, the larger the junction resistance [38].

As is shown in Table 4.2, the high frequency resistance, R_1, is fairly consistent across the thin film samples with an average value of 901 Ω ± 22 Ω. The low frequency resistance, R_2, varies, depending on both layer number and paper pore size. R_2 is 2 orders of magnitude, 8.4 times, and 6.1 times higher than R_1 for the 1 layer MWNT-410 surface, the 4 layered MWNT-410 surface, and the 4 layered MWNT-413 surface, respectively. R_1 is the bundle resistance for these MWNTs while R_2 is the junction resistance. The bundle resistance is fairly constant from sample to sample, regardless of the fabrication parameters, suggesting that R_1 is a materials property. Junction resistance, however, is influenced by the processing conditions and varies from sample to sample due to changes in film structure. It is also worth noting that the value of the resistance assigned to the coiled bundles (R_3) exceeds that of the predicted MWNT bundle resistance (~900 Ω) and also varies with processing conditions. The increase in resistance is likely caused by defects in the bonding structure required to accommodate coiling: a greater degree of coiling leads to a greater resistance value [69].

In a study done to determine the conduction properties of MWNT bundles at room temperature, Berger et al. concluded that for MWNT bundles with a length longer than 400 nm, the upper limit for the intrinsic resistance of a MWNT bundle per unit length could be predicted by the slope of the conductance vs. MWNT bundle length graph: 180 Ω/μm [70]. Using impedance spectroscopy, the MWNT bundle resistance was found to be ~900 Ω which corresponds to a bundle length of 5 μm. However, the

individual MWNTs used in this thesis have a reported length of 0.5 to 2 µm, which is smaller than the predicted value.

Due to Van der Waals forces, MWNTs tend to aggregate together. While the mixing steps and use of the surfactant material help break up that aggregation on a macroscopic scale, the tubes are still somewhat aggregated at the microscopic level [71]. The aggregated MWNTs have a larger diameter and length than the single MWNT would. Figure 4.9 shows an image of a very low density MWNT network deposited onto the 413 filter paper (5 µm pore size). The MWNTs appear as the high contrast/bright areas of the image and are shown bridging a pore between two paper fibers but not extending past the pore. From this image, the bundle length for these MWNTs is estimated to be approximately the diameter of the pore, 5 µm. This is also the length predicted using the relationship determined by Berger et al. and the measured bundle resistance for these MWNTs.

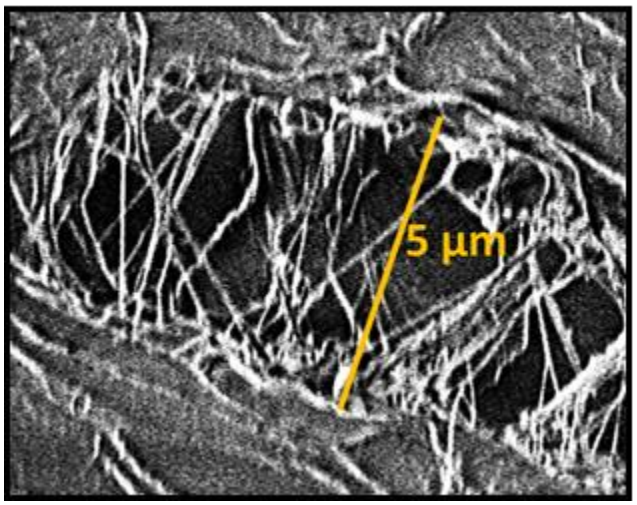

Figure 4.9: A 5 µm pore from the 413 qualitative filter paper and MWNT bundles bridging neatly across the pore diameter. The MWNT bundles are estimated to have a length of approximately 5 µm.

The Nested-RL equivalent circuit describes electronic processes which are all a function of the MWNT network but are influenced by the underlying paper structure.

Prior to the appearance of this impedance spectrum and equivalent circuit fit, the MWNT film is too disjointed to have much of a contribution to the electronic properties of the surface: the conduction behavior for the in-plane is dominated by the paper fibers. As discussed earlier in the Chapter, there is a large drop in resistance found between the 1 and 4 layered MWNT-413 composite surfaces. This large decrease in resistance is also found between 0 and 1 layer MWNT-410 composite surfaces. Therefore, the loading/layer number at which the impedance behavior fit using the Nested-RL circuit first appears is also the in-plane percolation threshold for the multilayered composites. For the MWNT-410 composites, the percolation threshold is 1 layer. For the MWNT-413 composites, the percolation threshold is 4 layers. The MWNT-415 composite series does not percolate in-plane.

4.2.3.3 Transitional Behavior

As MWNT loading on the in-plane continues to increase with an increasing number of deposited layers, the MWNT network eventually reaches a point where it can no longer be considered a thin film. However, a surface structure can form like the one in Figure 3.2c which shows a thick MWNT network that does not extend across the entire paper surface. This impedance behavior of this surface can be seen in Figure 4.3c for the 8 layered MWNT-413 composite in-plane. It can be described as a single semicircle in the 4^{th} quadrant of the complex impedance plane which is shifted away from the y-axis. This impedance behavior can be fit with an $(R_2\text{-}L_1)_p$ in series with a resistor, R_1, as shown in Figure 4.10.

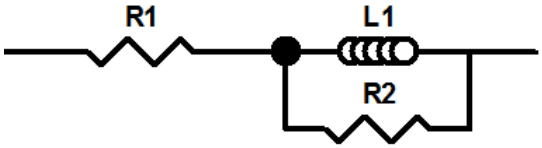

Figure 4.10: Equivalent circuit used to fit the impedance response for the in-plane of the 8 layered MWNT-413 composite in-plane shown in Figure 4.2c.

No impedance behavior is detected in the 1st quadrant which suggests that the thin film behavior is lost; however, the semicircle in the fourth quadrant remains, suggesting that the paper still has an impact on the electronic behavior of these materials. R_1 measures 2525 Ω ± 350 Ω, which falls between the bundle and junction resistances determined for the MWNT thin film surfaces. R_1 contains information about the MWNT network; however, the network is too dense to separate out the individual contributions of each structural component of the network. The fourth quadrant $(R\text{-}L)_p$ remains at low frequencies, suggesting that the coiled bundle frequency response, with a resistance of 713.2 Ω ± 202.6 Ω and an inductance of 4.78×10^{-5} H ± 1.35×10^{-5} H, can still be detected. However, the resistance of the coiled bundles has dropped significantly, likely due to the pressure exerted by the increased amount of MWNTs on the surface compressing the existing coiled bundles. (This effect will be studied in more detail in Chapter 5.) This circuit describes the MWNT network behavior which is transitioning from thin film to bulk but is not dense enough to completely remove the effect of the underlying paper substrate.

4.2.3.4 Bulk, Metallic MWNT Network Transport

Increasing the number of deposited layers will eventually form a thick, dense MWNT network on the surface which covers the entirety of the paper. As is shown in the SEM images of Figures 3.1c-f and 3.2d-f for the 8-to-20 layered MWNT-410 composites

surfaces and the 12-to-20 layered MWNT-413 composite surfaces, respectively, the paper surfaces are nearly completely coated in this thick layer of MWNTs. Measuring the impedance behavior of the thick layer of MWNTs gives the spectrum shown in Figures 4.3d and 4.4b: a straight line in the 4th quadrant of the complex impedance plane and shifted away from the y-axis. This impedance shape can be fit with an equivalent circuit consisting of a resistor and inductor in series with each other, $(R1\text{-}L1)_s$. This circuit describes conduction through the bulk, metallic MWNT networks [64, 66]. The series RL circuit is shown in Figure 4.11, and the values of the circuit elements for the composite surfaces exhibiting this behavior are given in Table 4.3. For each paper material, as the number of deposited layers increase, the bulk network resistance decreases. In addition, at 16 deposited layers and beyond, the resistance of the MWNT-410 surfaces and the MWNT-413 surfaces for the same layer number are statistically equivalent.

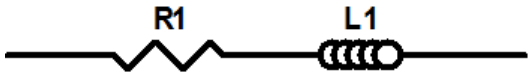

Figure 4.11: Equivalent circuit used to fit the impedance response for the in-plane of the 8-to-20 layered MWNT-410 composite surfaces and the 12-to-20 layered MWNT-413 composite surfaces shown in Figures 4.3b and 4.2d, respectively.

Table 4.3: Circuit element values for the composites whose in-plane impedance response can be fit by the $(R\text{-}L)_s$ equivalent circuit.

	R_1 (Ω)	L_1 (H)
8 layers, 410	1270 ± 240	$1.41\text{x}10^{-5} \pm 4.0\text{x}10^{-6}$
12 layers, 410	550 ± 59	$3.61\text{x}10^{-6} \pm 4.6\text{x}10^{-7}$
16 layers, 410	382 ± 32	$3.50\text{x}10^{-6} \pm 2.2\text{x}10^{-7}$
20 layers, 410	143 ± 9.0	$2.63\text{x}10^{-6} \pm 5.5\text{x}10^{-7}$
12 layers, 413	977 ± 520	$1.49\text{x}10^{-5} \pm 3.5\text{x}10^{-6}$
16 layers, 413	419 ± 70	$1.55\text{x}10^{-5} \pm 6.3\text{x}10^{-6}$
20 layers, 413	160 ± 37	$1.52\text{x}10^{-5} \pm 9.9\text{x}10^{-7}$

4.2.4 Overall In-Plane Equivalent Circuit Model

While the four different equivalent circuits discussed in this section appear very different, Figure 4.12 shows all four Nyquist plots for the MWNT-413 composite surfaces in log-log form. These four very different shapes actually have some degree of shape overlap as the composite surfaces evolve with increasing MWNT loading [66].

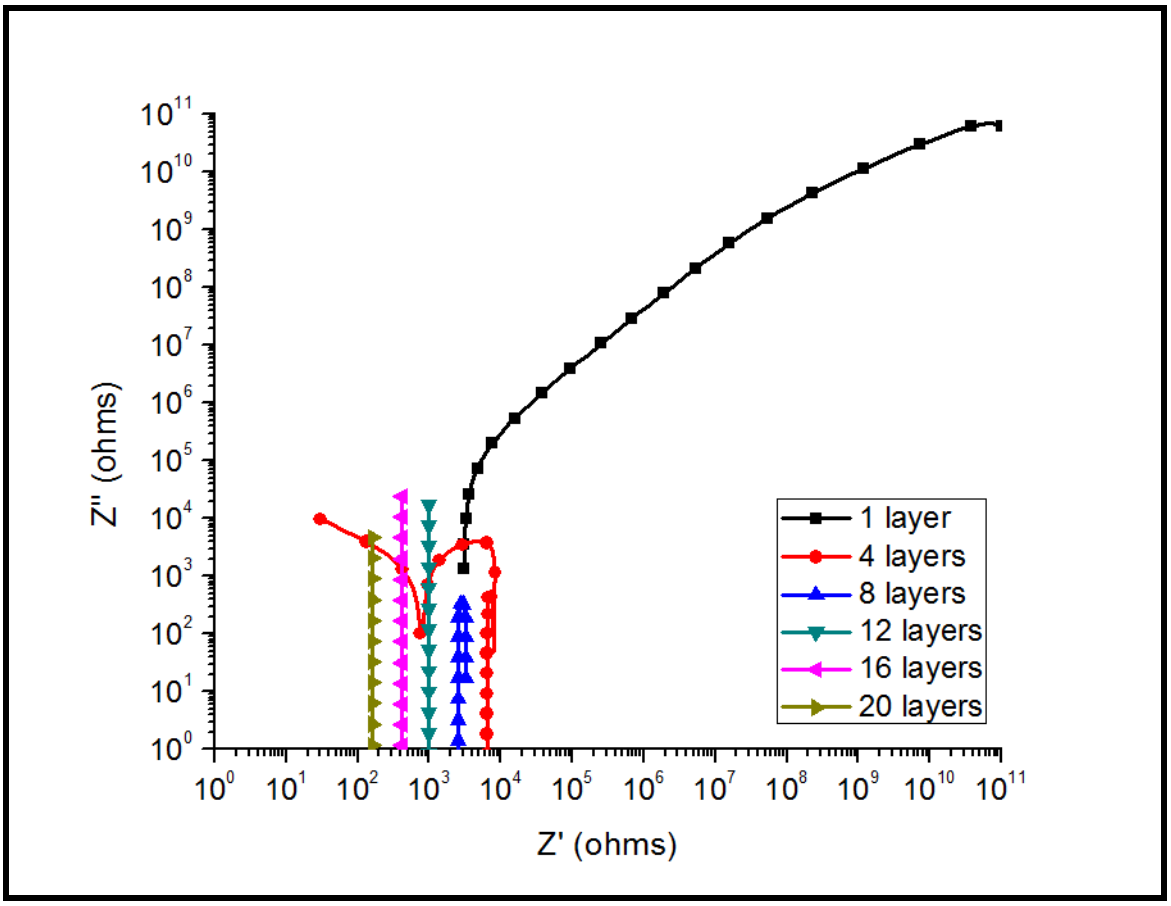

Figure 4.12: Impedance Nyquist plots presented in log-log form in order to show all 4 behaviors exhibited by the MWNT-413 filter paper composite surfaces in one plot [66].

The overlap in the shape of the different Nyquist plots suggests that the behaviors of the different composite surfaces are not completely independent from one another. A single equivalent circuit, as shown in Figure 4.13, can be used to fit all of the in-plane behaviors of the composite material. This circuit contains information about the paper backbone and the MWNT network which may coat it. In this circuit, R_p and C_p are the

resistance and capacitance of the uncoated paper surface. The other circuit elements arise due to MWNT deposition. R_b and C_b are the resistance and capacitance of the MWNT bundles, R_j and C_j are the resistance and capacitance of the MWNT-MWNT junctions, and R_{cb} is the curved bundle resistance. L does not have a subscript as its role in the MWNT network changes. Depending on the nature of the surface of the material, different elements of the overall circuit are active and dominate the in-plane electrical response. This circuit does not take into account any contact resistances or machinery effects- it only describes the material behavior.

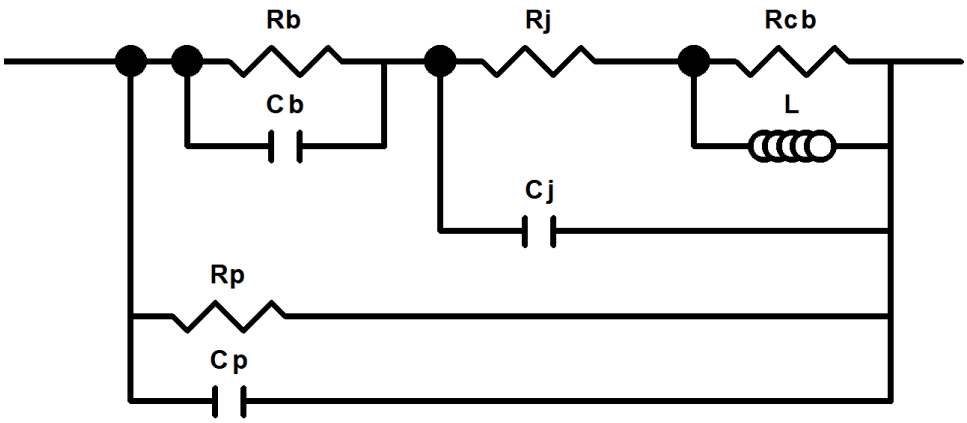

Figure 4.13: Equivalent circuit which can be used to fit all impedance behaviors outlined in Chapter 4 for the in-plane of the MWNT-paper materials.

Figure 4.14 shows schematics detailing the MWNT network structure for the different electronic transport behaviors. The elements of the overall equivalent circuit which are active for each electronic behavior are also shown. Figure 4.14a describes the two different cases where paper-dominated transport is active: no surface deposition or a disconnected MWNT network on the surface. When no MWNTs are deposited on the surface, the only circuit elements present are R_p and C_p, (no surface deposition). When MWNTs are present but are not interconnected (disconnected MWNT network), the properties of the surface are still dominated by the paper but are influenced by the

disconnected coating (R_j, C_j, R_b, C_b, R_{cb}, and L_{cb}). The influence of the disconnected MWNTs results in the decreased resistance exhibited by the MWNT-415 and the 1 layered MWNT-413 composite surfaces. Figure 4.14b shows the MWNT thin film network. In this network, all of the circuit elements are active and fully describe the impedance response (R_p, C_p, R_j, C_j, R_b, C_b, R_{cb}, and L_{cb}). Figure 4.14c shows as schematic describing the transitional MWNT network. The MWNT surface is thick enough to obscure the underlying paper properties: R_p and C_p are no longer measureable.

The transitional MWNT network is also highly dense, resulting in the combination of R_b and R_j into a single resistance R_t ($R_{transitional}$), and highly conducting such that it no longer contains any capacitive behavior. The curved bundle response, however, is still detected. The only elements required to describe the transitional network are R_t, R_{cb}, and L_{cb}. Finally, Figure 4.14d shows a bulk MWNT network. The curved bundle resistance is no longer detectable and R_t becomes the bulk MWNT network resistance (R_B). Only two elements are required to describe the network: R_B and L_B (B= bulk).

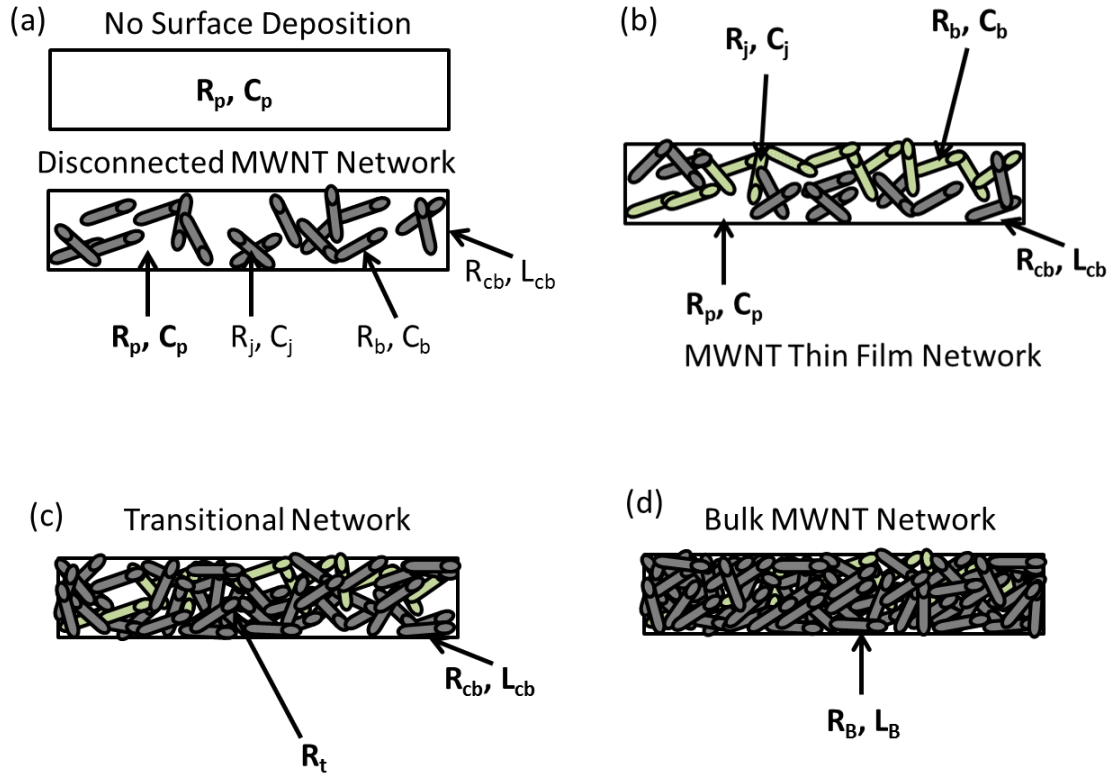

Figure 4.14: Schematics detailing the view perpendicular to the in-plane/surface of the paper for the different electronic transport behaviors as well as the active equivalent circuit elements: a) Paper-Dominated; b) MWNT thin film; c) Transitional Network; d) Bulk MWNT Network transport. The green MWNTs highlight the first percolated network which spans the paper surface while the rest of the MWNTs are gray in color.

4.3 Thru-Plane

Figure 4.15 shows a schematic describing the measurement of the thru-plane properties using a view perpendicular to the thru-plane of the material with an exaggerated paper backbone thickness. Probes were placed on the top and bottom surfaces of the paper and connected to a voltage source.

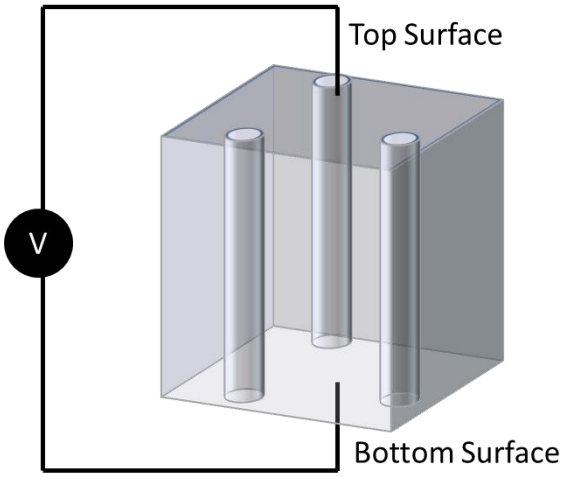

Figure 4.15: Schematic describing the measurement of the thru-plane electrical properties of the paper/composite from a view perpendicular to the thru-plane of the material.

As was shown in Figure 3.12b, all of the layered composite materials show some degree of conduction in their thru-plane; however, each composite set shows a very different shape in their DC Resistance vs. Number of Deposited Layers curves. The MWNT-410 composite thru-planes show a relatively constant resistance for all layer numbers while the MWNT-415 composite thru-planes show a consistently decreasing resistance as deposited layer number increases. The MWNT-413 composite thru-planes show a combination of the other two behaviors. The thru-planes of the 1-to-8 layered MWNT-413 composites show a constant resistance value. After 8 deposited layers, resistance decreases continuously with increasing deposition. As was done in the previous section, a combination of impedance spectroscopy and imaging was used to

determine the conduction mechanisms present in the composites and how the conduction behavior is related to the structure of the thru-plane.

4.3.1 Presentation of Thru-Plane Frequency-Explicit and Nyquist Plots

Figure 4.16 shows both the frequency-explicit, log(|Z|) vs. log(f) (a) and θ vs. log(f) (b), and the Nyquist plots presented in both linear (c) and log-log (d) form for the impedance behavior of the multilayered MWNT-410 composite thru-plane measurements. While the frequency-explicit plots presented previously in this Chapter were useful for determining the number of different impedance behaviors of the in-plane measurements, the curve shapes in Figures 4.16a and 4.16b are too similar to definitively provide the number of impedance behaviors occurring in the thru-plane. Similarly, the Z" vs. Z' linear plot in Figure 4.16c shows six impedance curves all overlapping and showing similar shapes and behavior. There are no apparent trends for increasing layer number. However, looking at the log-log version of the Nyquist plot in Figure 4.16d, two different behaviors can be discerned for MWNT-410 thru-plane. The first behavior is detected at 1 and 4 layers while the second behavior occurs at 8 layers and above.

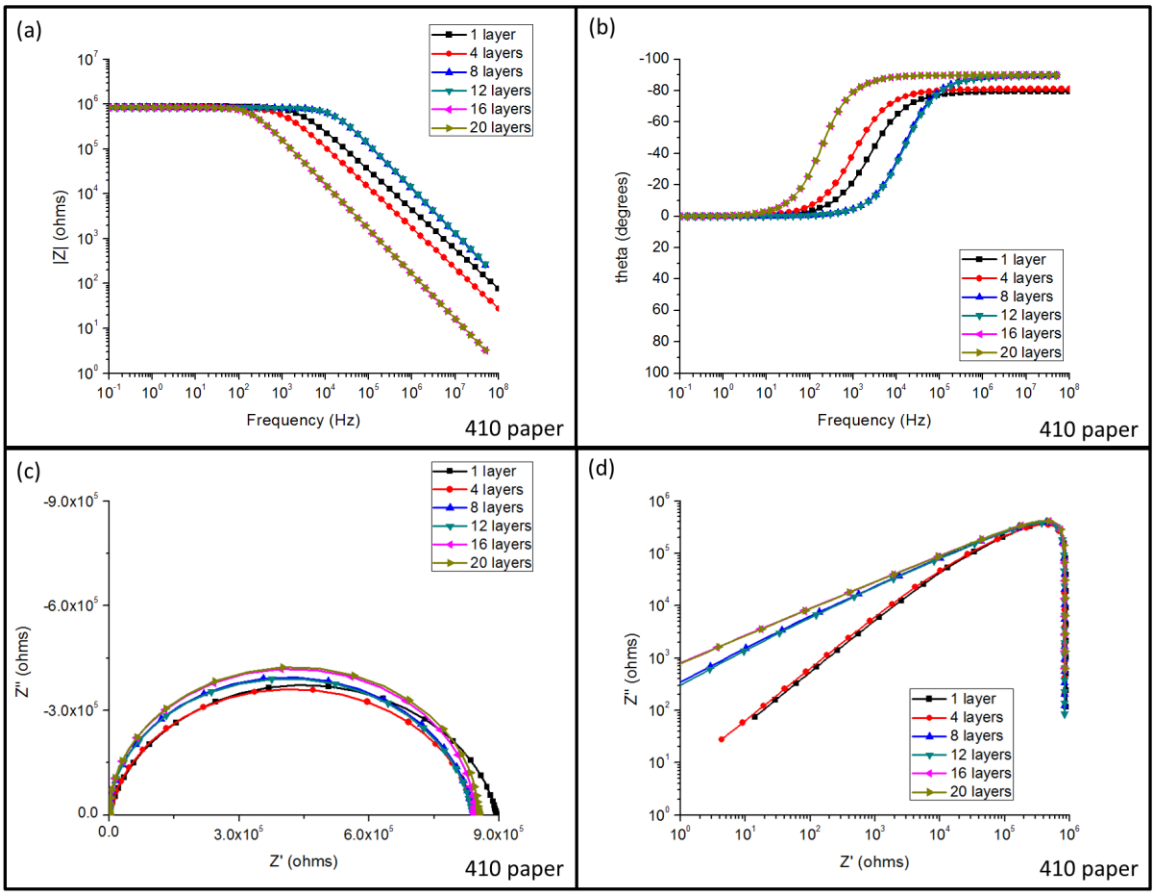

Figure 4.16: Frequency-explicit and –implicit impedance graphs for the MWNT-410 composite thru-planes. a) log(|Z|) vs. log(f); b) θ vs. log(f); c) Z" vs. Z' on the linear scale; d) Z" vs. Z' on the log-log scale.

Figure 4.17 shows the impedance curves for the thru-planes of the MWNT-413 composite materials. Unlike the MWNT-410 composites, both the frequency-explicit (Figures 4.17a and 4.17b) and the linear Nyquist plots (Figures 4.17c and 4.17d) show two distinct impedance behaviors. The first behavior is exhibited by the 1-to-8 layered MWNT-413 composite thru-planes while the second behavior is exhibited by the 12-to-20 layered MWNT-413 composite thru-planes.

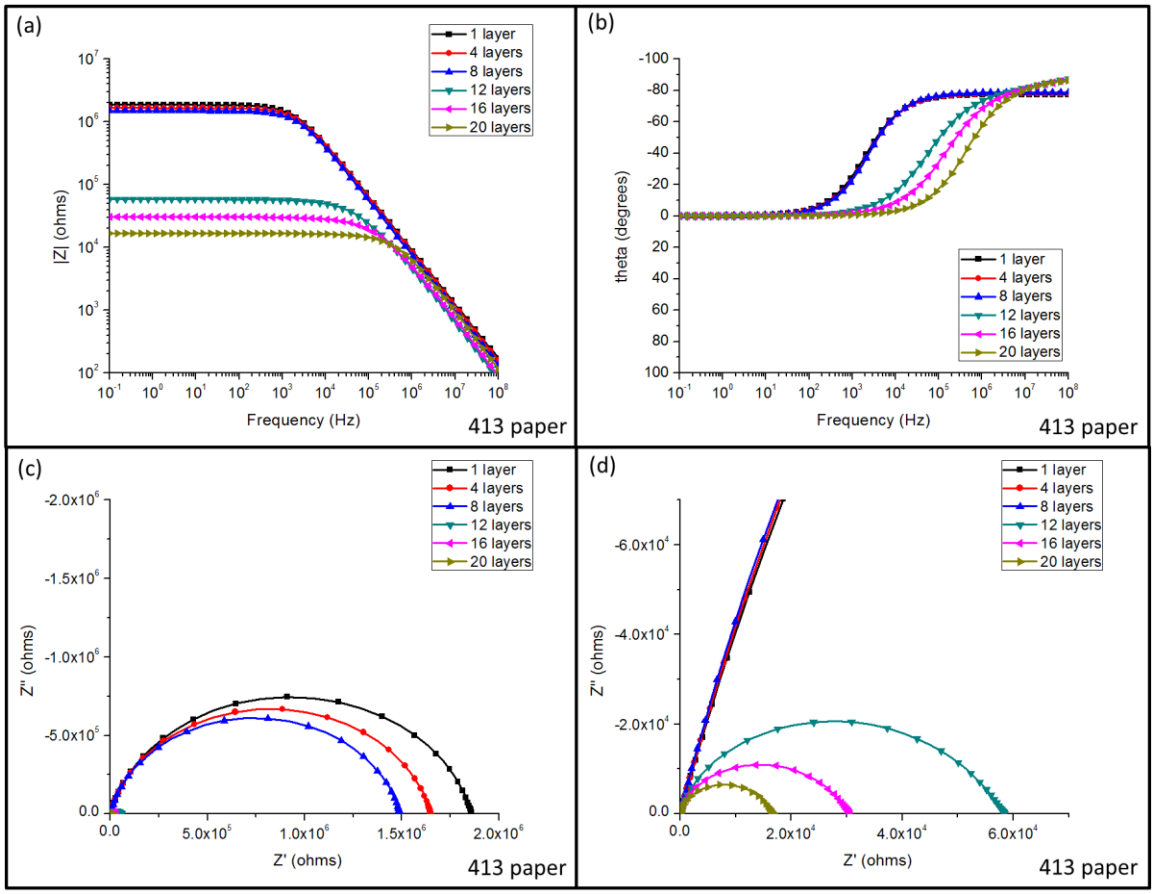

Figure 4.17: Frequency-explicit and –implicit impedance graphs for the MWNT-413 composite thru-planes. a) log(|Z|) vs. log(f); b) θ vs. log(f); c) Z" vs. Z' with the y-axis extending from 0 Ω to -2x10^6 Ω and the x-axis extending from 0 Ω to -2x10^6 Ω; d) Z" vs. Z' with the y-axis extending from 0 Ω to -7x10^4 Ω and the x-axis extending from 0 Ω to 7x10^4 Ω.

Figure 4.18 shows the impedance curves for the thru-planes of the MWNT-415 composite materials. All three plots indicate that there is a single impedance response for these materials which decreases in magnitude with an increasing number of deposited layers.

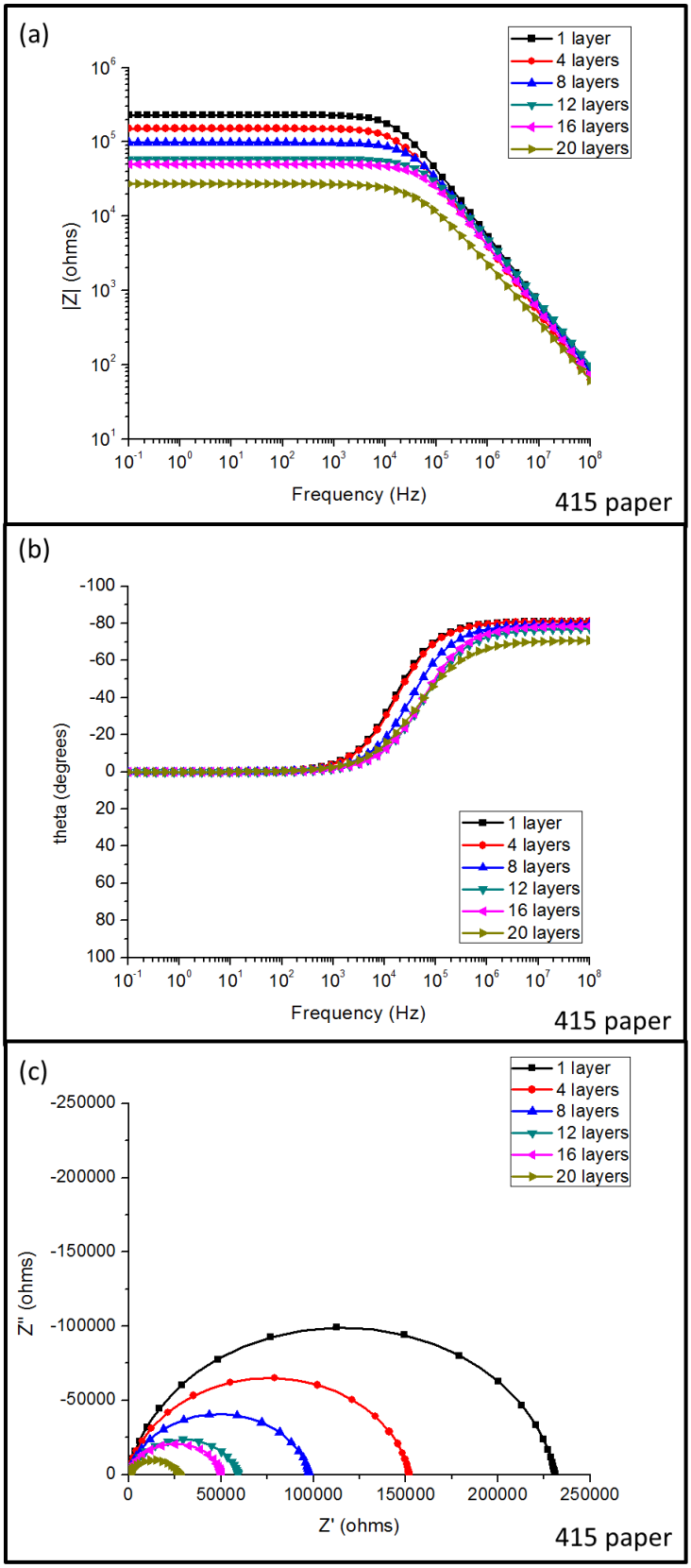

Figure 4.18: Frequency-explicit and –implicit impedance graphs for the MWNT-415 composite thru-planes. a) log(|Z|) vs. log(f); b) θ vs. log(f); c) Z" vs. Z' on the linear scale.

4.3.2 Thru-Plane Equivalent Circuit Modeling

4.3.2.1 Internal Deposition Only

The impedance spectra for the MWNT-415 composites in Figure 4.18 can all be described as a single semicircle in the 1st quadrant of the impedance plane which is not shifted away from the y-axis. The magnitude of the semicircle decreases as layer number increases. In addition, the amount of depression of the semicircle increases as layer number increases. The impedance of the thru-planes of the MWNT-415 composites can be fit with a resistor in parallel with a CPE, $(R\text{-}CPE)_p$, as shown in Figure 4.19. The values of the circuit which fit the impedance of each MWNT-415 composite are given in Table 4.4.

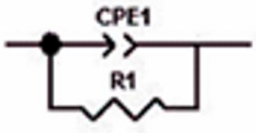

Figure 4.19: Equivalent circuit used to fit the impedance response for the thru-plane of the MWNT-415 composite materials.

Table 4.4: Circuit element values for the thru-planes of the MWNT-415 composites whose impedance response can be fit by the $(R\text{-}CPE)_p$ equivalent circuit.

	R_1 (Ω)	CPE-τ (F)	CPE-β
1 layer	$2.31x10^5 \pm 4.0x10^4$	$1.31x10^{-10} \pm 3.6x10^{-11}$	0.904 ± 0.032
4 layers	$1.52x10^5 \pm 2.5x10^4$	$1.89x10^{-10} \pm 7.1x10^{-11}$	0.901 ± 0.008
8 layers	$9.79x10^4 \pm 1.3x10^4$	$2.04x10^{-10} \pm 1.1x10^{-11}$	0.884 ± 0.027
12 layers	$5.92x10^4 \pm 9.5x10^3$	$2.89x10^{-10} \pm 4.9x10^{-11}$	0.858 ± 0.061
16 layers	$5.05x10^4 \pm 1.0x10^4$	$2.76x10^{-10} \pm 3.9x10^{-11}$	0.875 ± 0.015
20 layers	$2.74x10^4 \pm 9.8x10^3$	$1.85x10^{-9} \pm 0.98x10^{-10}$	0.789 ± 0.099

It was previously discussed that the surfaces of the MWNT-415 composites show very little MWNT deposition, even at high layer numbers. Additionally, the resistances of the thru-planes for these composites are two to three orders of magnitude smaller than the resistance measured for the thru-plane of the uncoated paper. Nearly all deposited MWNTs deposit within the pore network of the 415 paper. As layer number increases,

the connection of the MWNTs within the pore network improves and the impedance/resistance of the material drops. The $(R\text{-}CPE)_p$ circuit describes the electrical behavior of the thru-plane of a composite which contains only MWNT coated paper fibers within the thickness of the material.

Figure 4.20 shows an SEM image focused within a single pore (25 µm) of the 20 layered MWNT-415 composite further confirming the density of the MWNT network within the pore as well as the lack of surface deposition. Three sample characteristics can be elucidated from this image. First, the top of the pore shows large MWNT agglomerates which were detectable from the low magnification surface images in Figure 3.3. Second, the paper fibers near the bottom of the pore are covered in a fairly dense MWNT network. Third, for the paper fibers which are in the foreground of the image, a small amount of MWNTs can be seen where the fibers overlap with other fibers.

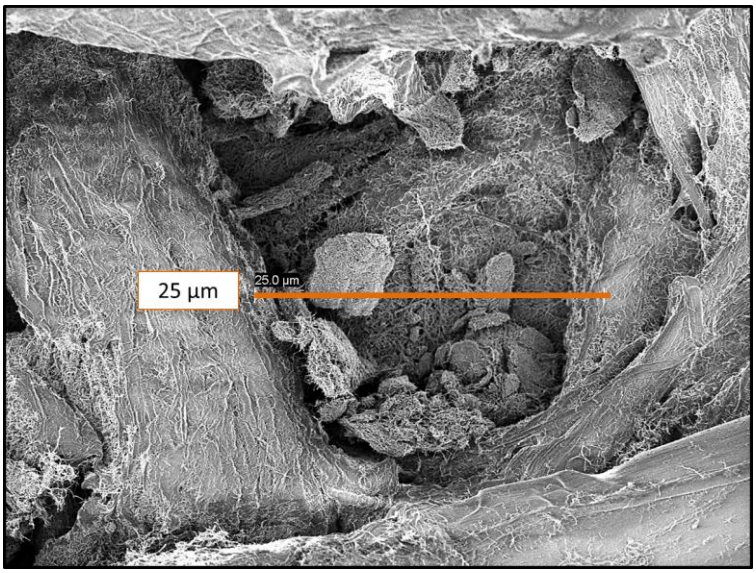

Figure 4.20: SEM images of MWNTs within a 25 µm pore for the 20 layered MWNT-415 composite. Large MWNT agglomerates are seen close to the surface and small regions of coated paper fibers are observed.

4.3.2.2 Combined Internal and Surface Deposition

As was shown in Figures 4.16 and 4.17, the thru-planes for both the MWNT-410 and MWNT-413 composites show two impedance behaviors. The first impedance behavior, which was exhibited by the 1-4 layered MWNT-410 and the 1-8 layered MWNT-413 composites, was fit using the $(R\text{-}CPE)_p$ circuit from Figure 4.18. The values of the $(R\text{-}CPE)_p$ circuit elements are given in Table 4.5. For both filter papers, as the number of deposited layers increases, the resistance of the thru-plane slightly decreases. The thru-plane of these composites has only the single impedance process corresponding to the coating of the pore network.

Table 4.5: Circuit element values for the thru-planes of the 1-4 layered MWNT-410 and 1-8 layered MWNT-413 composites whose impedance response can be fit by the $(R\text{-}CPE)_p$ equivalent circuit.

	R_1 (Ω)	CPE-τ (F)	CPE-β
1 layer, 410	$8.85\text{x}10^5 \pm 2.3\text{x}10^4$	$2.20\text{x}10^{-10} \pm 4.4\text{x}10^{-11}$	0.883 ± 0.047
4 layers, 410	$8.45\text{x}10^5 \pm 9.5\text{x}10^3$	$4.26\text{x}10^{-10} \pm 4.4\text{x}10^{-11}$	0.901 ± 0.062
1 layer, 413	$1.86\text{x}10^6 \pm 7.7\text{x}10^4$	$1.59\text{x}10^{-10} \pm 5.4\text{x}10^{-11}$	0.860 ± 0.023
4 layers, 413	$1.65\text{x}10^6 \pm 2.2\text{x}10^5$	$1.49\text{x}10^{-10} \pm 5.6\text{x}10^{-11}$	0.867 ± 0.012
8 layers. 413	$1.49\text{x}10^6 \pm 3.2\text{x}10^5$	$1.52\text{x}10^{-10} \pm 5.6\text{x}10^{-11}$	0.874 ± 0.041

The second impedance behavior appears for the 8-20 layered MWNT-410 and 12-20 layered MWNT-413 composite thru-planes. The shape of the data in the complex impedance plane, as shown in Figures 4.16c,d and 4.17d, is that of two semicircles which overlap. The equivalent circuit which fits the shape of this data is a two part circuit containing an outer $(R_1\text{-}C_1)_p$ and an inner $(R_2\text{-}CPE_1)_p$ which is nested within the first part of the circuit. This circuit, which will be called 'Nested-RC', is shown in Figure 4.21. The values of the circuit elements for the composites whose impedance behavior is fit with the Nested-RC circuit are given in Table 4.6.

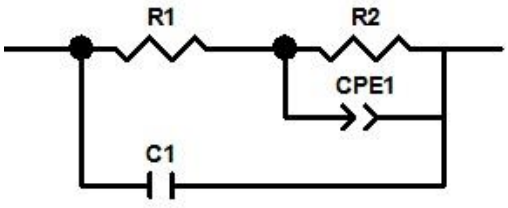

Figure 4.21: Equivalent circuit used to fit the impedance response for the thru-plane of the 8-20 layered MWNT-410 and 12-20 layered MWNT-413 composite materials.

Table 4.6: Circuit element values for the thru-planes of the 8-20 layered MWNT-410 and 12-20 layered MWNT-413 composites whose impedance response can be fit by the Nested-RC equivalent circuit.

	R_1 (Ω)	C_1 (pF)	R_2 (kΩ)	CPE-τ (nF)	CPE-β
8 layers, 410	1023 ± 281	12.4 ± 8.11	844 ± 42.7	0.189 ± 0.066	0.571 ± 0.051
12 layers, 410	852 ± 333	11.6 ± 7.5	843 ± 21.2	0.186 ± 0.078	0.583 ± 0.009
16 layers, 410	661 ± 104	986 ± 53.8	843 ± 33.4	0.188 ± 0.034	0.572 ± 0.033
20 layers, 410	192 ± 77.2	973 ± 89.9	853 ± 19.3	0.189 ± 0.011	0.588 ± 0.012
12 layers, 413	1130 ± 405	39.3 ± 6.4	57.3 ± 2.2	4.20 ± 0.773	0.657 ± 0.053
16 layers, 413	902 ± 227	34.7 ± 6.6	29.7 ± 6.7	5.17 ± 0.921	0.639 ± 0.088
20 layers, 413	235 ± 44.4	25.8 ± 9.0	16.5 ± 10	3.42 ± 0.102	0.637 ± 0.012

Aside from the thru-plane impedance behavior being fit with the Nested-RC circuit, the 8-20 layered MWNT-410 and the 12-20 layered MWNT-413 composites share another commonality. When studying the in-plane behavior, these composites all exhibit bulk, metallic MWNT behavior, and their surfaces are fully coated in MWNTs. R_1 in Table 4.6 matches the value of the corresponding composite's bulk resistances given in Table 4.3. R_1 in the Nested-RC circuit describes conduction through the bulk surface of MWNTs. For these samples, current flowing either through the surface layer or across the surface layer experiences the same resistance.

R_2, therefore, measures the resistance through the thickness of the paper material. For the 8-20 layered MWNT-410 composites, R_2 remains static and equivalent to the thru-plane resistance of the 4 layered MWNT-410 sample. When a bulk MWNT film formed on the surface of the 410 paper, the film remained rigid and obstructed the addition of any more MWNTs into the thickness of the paper. Once the pores were

covered completely, all further deposition steps resulted in only surface deposition. This is confirmed by I-AFM, shown in Figure 3.4. The current flow through the thickness of the MWNT-410 composite materials increases only slightly between the 1 and 20 layer samples.

In comparison, R_2 for the 12-20 MWNT-413 composite thru-planes continues to decrease with the increasing number of deposited layers. Deposition of the MWNTs is occurring simultaneously on the surface and through the thickness of these composites, suggesting that the larger pore size of the paper results in a less rigid bulk surface network. This structure accommodates MWNTs continually being pulled into the thickness of the 413 paper. In fact, the I-AFM image shown in Figure 3.5b suggests that the MWNTs deposit throughout the thickness of the paper, rather than just in the pores, as was the case for the MWNT-415 composites.

4.3.3.3 Surface Deposition Only

As was shown in the previous section, when the MWNTs are larger than the pore size of the paper, the pores are eventually covered, which eliminates any further deposition within the paper thickness. This occurs even between two materials which have a high affinity for one another and with a processing method which promotes the pulling of the second material into the filter paper. It should stand to reason, then, that if the MWNT filler material were much larger than the pore size of the paper, only surface deposition would occur [64]. The L-MWNT material was used to test this hypothesis through the fabrication of 1-20 layered L-MWNT-410 composite materials. Figure 4.22 shows low magnification SEM images for the a) 1 layer and b) 20 layered L-MWNT-410

composite surface. Figure 4.22a shows the L-MWNT agglomerates capping the pores on the surface at 1 deposited layer. Figure 4.22b shows inconsistent surface deposition of 20 deposited L-MWNT layers.

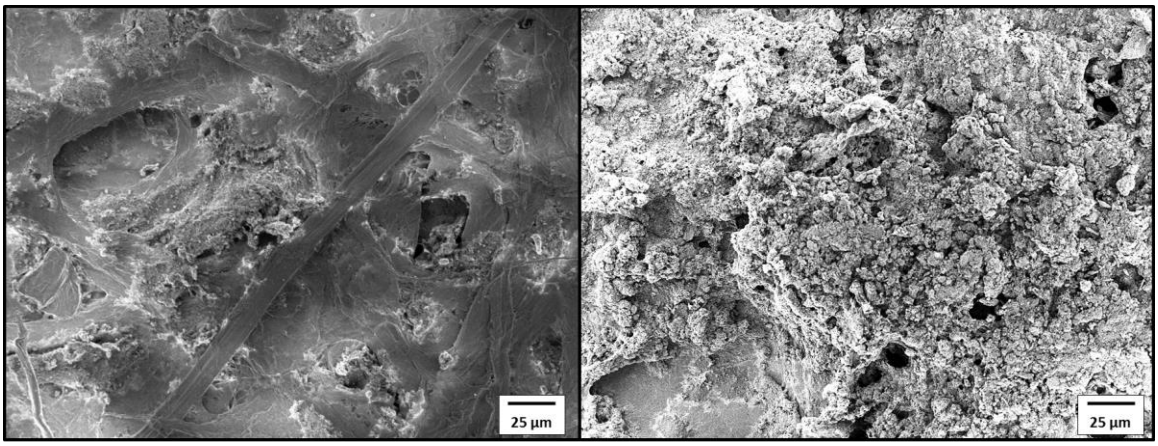

Figure 4.22: Low magnification SEM images of a) 1 layer of L-MWNTs depositing near and over pores and b) 20 layers of L-MWNT agglomerates forming a dense network on the 410 paper surface.

Figure 4.23 shows the in-plane and thru-plane DC resistance values for the L-MWNT-410 paper composite materials. The resistance of the in-plane decreases to approximately ~250 Ω at 20 deposited layers from a maximum of $1.4x10^{11}$ Ω at 1 deposited layer. The in-plane behavior of the L-MWNT-410 composites mirrors that of the MWNT-413 composite surfaces except that percolation (Nested-RL circuit) occurs later at 8 deposited layers. The thru-plane behavior of the L-MWNT-410 composites mirrors that of the MWNT-410 composites (Nested-RC circuit) except that the resistance value is an order of magnitude higher (~$2x10^7$ Ω).

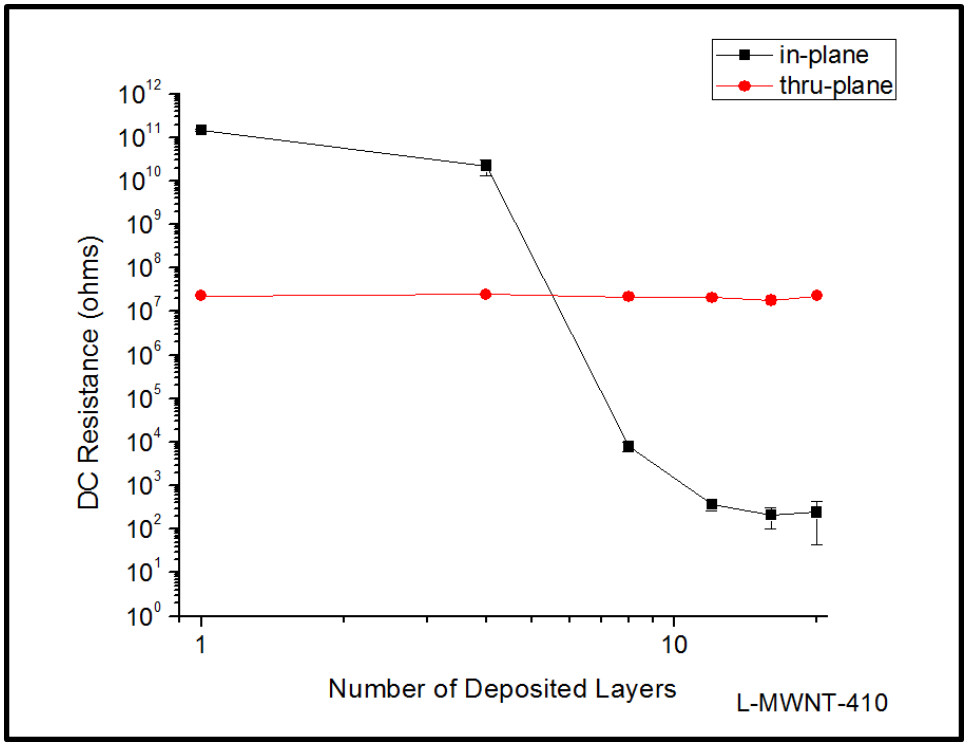

Figure 4.23: DC Resistance vs. Number of Deposited Layers for the in-plane and the thru-plane of the L-MWNT-410 composite materials.

Figure 4.24 shows the frequency-explicit and implicit thru-plane behavior of the L-MWNT-410 paper composite materials. The graph of log(|Z|) vs. log(f) in Figure 4.24a shows the flattening of the data at approximately the same frequency value (~10^2 Hz) and to the same impedance value (>10^7 Ω). Similarly, the data shown in Figure 4.24b for θ vs. log(f) shows only one behavior for all of the composite samples. The Nyquist plots for these samples (Figure 4.24c) also all show the same shape, indicating the same electronic behavior across composites, and are fit with the Nested-RC equivalent circuit given in Figure 4.21. The equivalent circuit values (average and standard deviation) are available in Table 4.7.

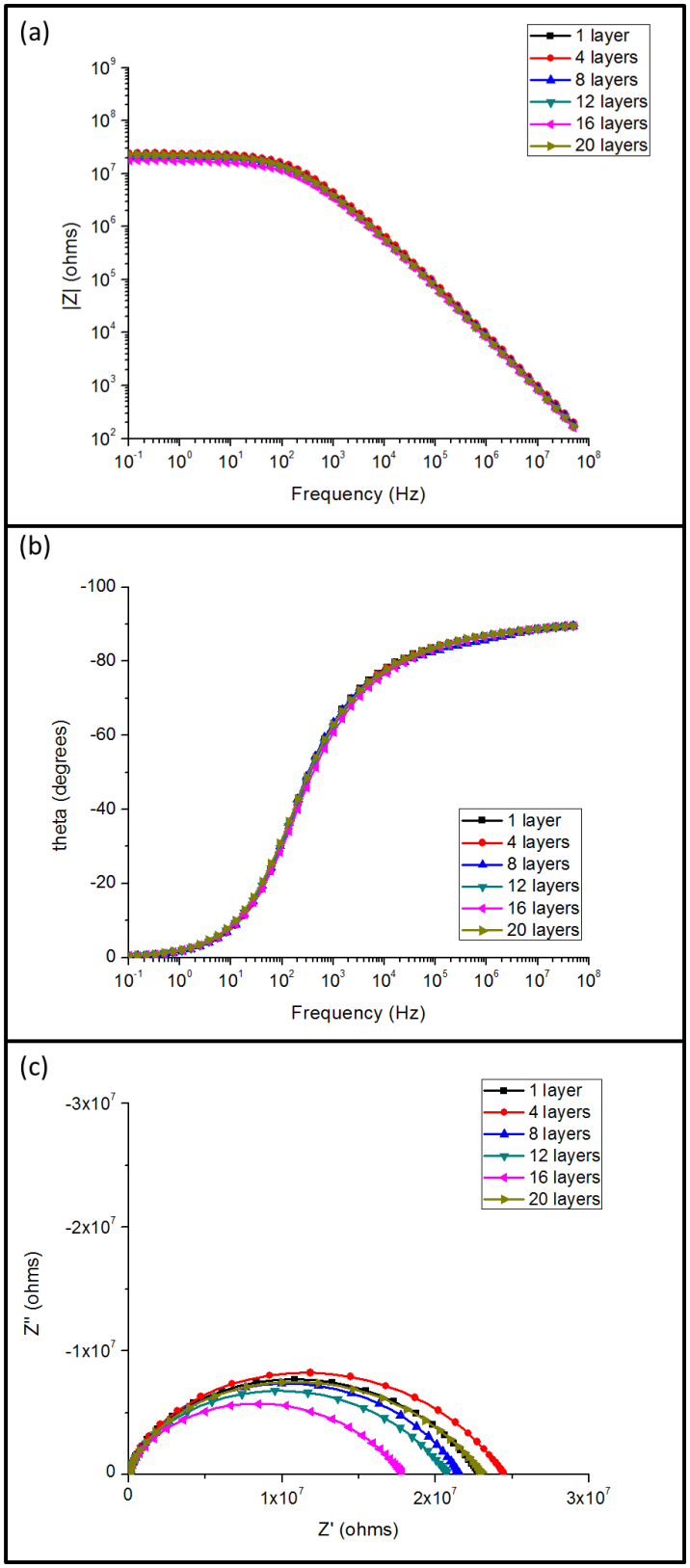

Figure 4.24: Impedance data presented as frequency explicit a) log(|Z|) vs. log(f) and b) θ vs. log(f) as well as the frequency implicit C) Z" vs. Z' Nyquist plots for the thru-plane measurements of the L-MWNT-410 multilayered composites.

Table 4.7: Circuit element values for the impedance response of the thru-planes of the L-MWNT-410 composites fit by the Nested-RC equivalent circuit which shows a constant R_2 value.

L-MWNT	R_1 (kΩ)	C_1 (pF)	R_2 (MΩ)	CPE-τ (nF)	CPE-β
1 layer	25.7 ± 8.3	17.7 ± 2.3	22.9 ± 7.1	43.0 ± 8.7	0.647 ± 0.011
4 layers	23.8 ± 4.3	15.8 ± 3.8	24.5 ± 3.2	38.9 ± 9.2	0.648 ± 0.020
8 layers	22.3 ± 1.1	17.6 ± 2.9	21.6 ± 2.9	40.7 ± 7.4	0.672 ± 0.009
12 layers	21.8 ± 7.0	18.6 ± 1.6	20.8 ± 3.7	54.5 ± 9.4	0.638 ± 0.008
16 layers	20.6 ± 3.5	19.8 ± 2.2	17.9 ± 1.2	65.9 ± 10	0.629 ± 0.011
20 layers	19.2 ± 1.9	18.6 ± 0.99	23.1 ± 2.3	54.1 ± 6.5	0.632 ± 0.007

Unlike the MWNT-410/413 paper composites which transition to this circuit upon reaching bulk, metallic behavior in the in-plane, this circuit appears for the L-MWNT-410 composites regardless of the in-plane behavior. The in-plane of this material actually begins as insulating (paper-dominated), transitions to thin film at 8 layers, and then becomes bulk, metallic at 12 layers. However, as MWNT deposition tends to occur in agglomerates on paper and pore edges, as is shown in Figure 4.22a, the pores are covered immediately. As loading increases from 1 to 20 layers, the value of R_2 remains that of the resistance of the thru-plane of uncoated paper, confirming that the L-MWNTs do not penetrate the paper pore structure. R_1 decreases slightly from 1 to 20 deposited layers but does not reach the value of R_B for these composites (~250 Ω which can be seen in Figure 4.23 for the composites made with 12-20 deposited layers). As was shown in Figure 4.22b, surface deposition is inconsistent due to the L-MWNT agglomerates, leading to a much larger degree of anisotropy in conduction for the surface film when measured across the film vs. through the film thickness.

4.3.3 Overall Thru-Plane Equivalent Circuit Model

Similar to the in-plane, it is possible to describe the different electronic behaviors measured for the thru-plane of these composites with a single equivalent circuit: the

Nested-RC circuit as shown in Figure 4.25. The Nested-RC circuit is comprised of two electronic behaviors. First, the nested part of the circuit is a $(R\text{-}CPE)_p$ arrangement which describes current flow through the internal structure of the paper. Second, the outer part of the circuit is a $(R\text{-}C)_p$ arrangement which describes the current flow through the surface of the composite. The behavior of these circuit elements depends on where the MWNTs deposit and how much of the MWNTs deposit at those locations.

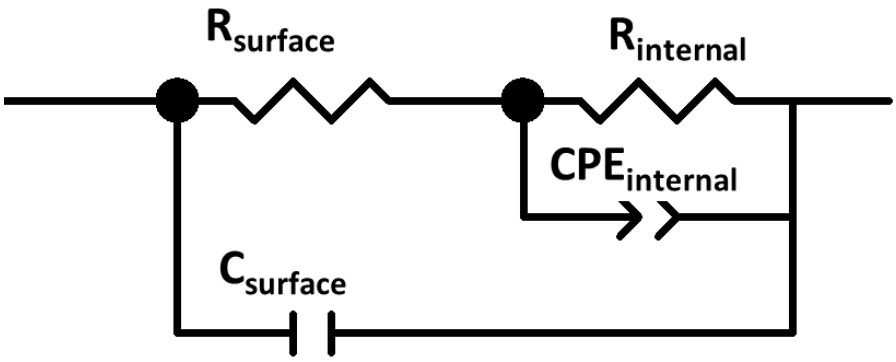

Figure 4.25: Equivalent circuit describing all behaviors outlined in Chapter 4 for the thru-plane of the MWNT-paper materials.

The response and activation of each circuit element describes the location of MWNT deposition within and on the paper. Each deposition condition is described schematically in Figure 4.26. These schematics describe an extremely idealized version of a pore within a filter membrane in order to easily show the deposition of MWNTs. Realistically, the pores are not purely cylindrical and have a tortuous pathway from top to bottom. However, in order to provide a visual clue to understand the deposition within the paper thickness, these simplified models are presented.

Figure 4.26a shows deposition within the pore structure of the paper only. As little or no MWNTs even deposit on the surface, the pore network controls the electrical transport and only $R_{internal}$ and $CPE_{internal}$ are activated. Figure 4.26b-d describes the three

different types of deposition which require all equivalent circuit elements to describe conduction across the thru-plane ($R_{surface}$, $C_{surface}$, $R_{internal}$, $CPE_{internal}$). For dual-deposition throughout the fabrication step, as shown in Figure 4.26b, both $R_{surface}$ and $R_{internal}$ decrease with increasing number of deposited layers. For dual deposition followed by only surface deposition as shown in Figure 4.26c, $R_{internal}$ remains constant once the pores are covered and only surface deposition can occur. $R_{surface}$ continues to decrease. For surface deposition only, as shown in Figure 4.26d, $R_{surface}$ decreases with increasing number of deposited layers. $R_{internal}$ always shows the same value as the uncoated paper resistance.

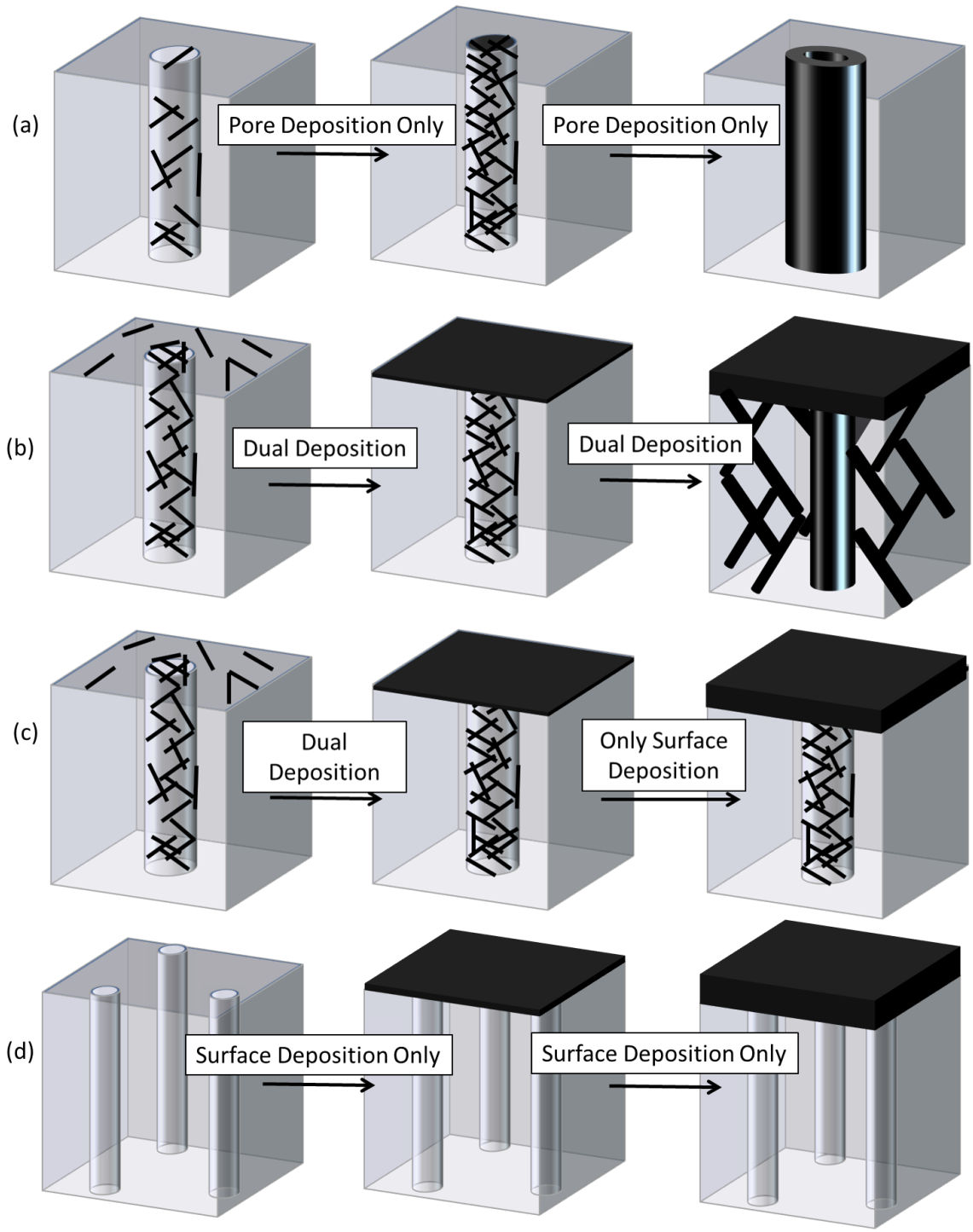

Figure 4.26: Idealized schematics describing the different MWNT deposition types which lead to the activation and behavior of the different circuit elements within the Nested-RC circuit in Figure 4.25 with increasing number of layers from left to right. a) Internal Deposition only; b) Dual Internal and Surface Deposition; c) Dual Internal and Surface Deposition followed by only Surface Deposition; d) Surface Deposition only.

4.4 Comparing Multilayered Deposition to Concentration Variation

Multilayer dropcasting of the MWNT dispersion was chosen as the method to add the MWNTs to the paper materials as it allowed the pore network to play a role during processing, especially when the dispersion concentration is optimized. The 1 mg/mL MWNT dispersion is dense enough to allow for network formation to occur throughout the paper material, including the on the paper surface and along the fibers exposed within the paper thickness. Smaller dispersion concentrations resulted in insulator behavior in both planes as the amount of MWNTs being deposited is not enough to form a complete coating over the surface area of exposed paper fibers [66]. In addition to utilizing the pore network, employing the multilayer drying methodology allows for the control over the properties by systematically adding more MWNTs to the composite until the desired properties are reached.

However, more MWNTs can also be added to the composites by utilizing dispersions with larger concentrations. MWNT dispersions containing 1, 2, 5, and 10 mg/mL were dispersed in DI water with 10 mg/mL SDBS surfactant as described in Chapter 2. 1 layer of the MWNT dispersion was dropcasted onto the three filter papers, and the electrical properties of the in-plane and thru-plane were measured and compared to the properties of the composites made by multilayered deposition. While it may seem that increasing layer number and increasing dispersion concentration should be analogous and interchangeable as both result in increased MWNT loading and coating, it turns out to only be the case for a few unique conditions which can be seen in Figure 4.27.

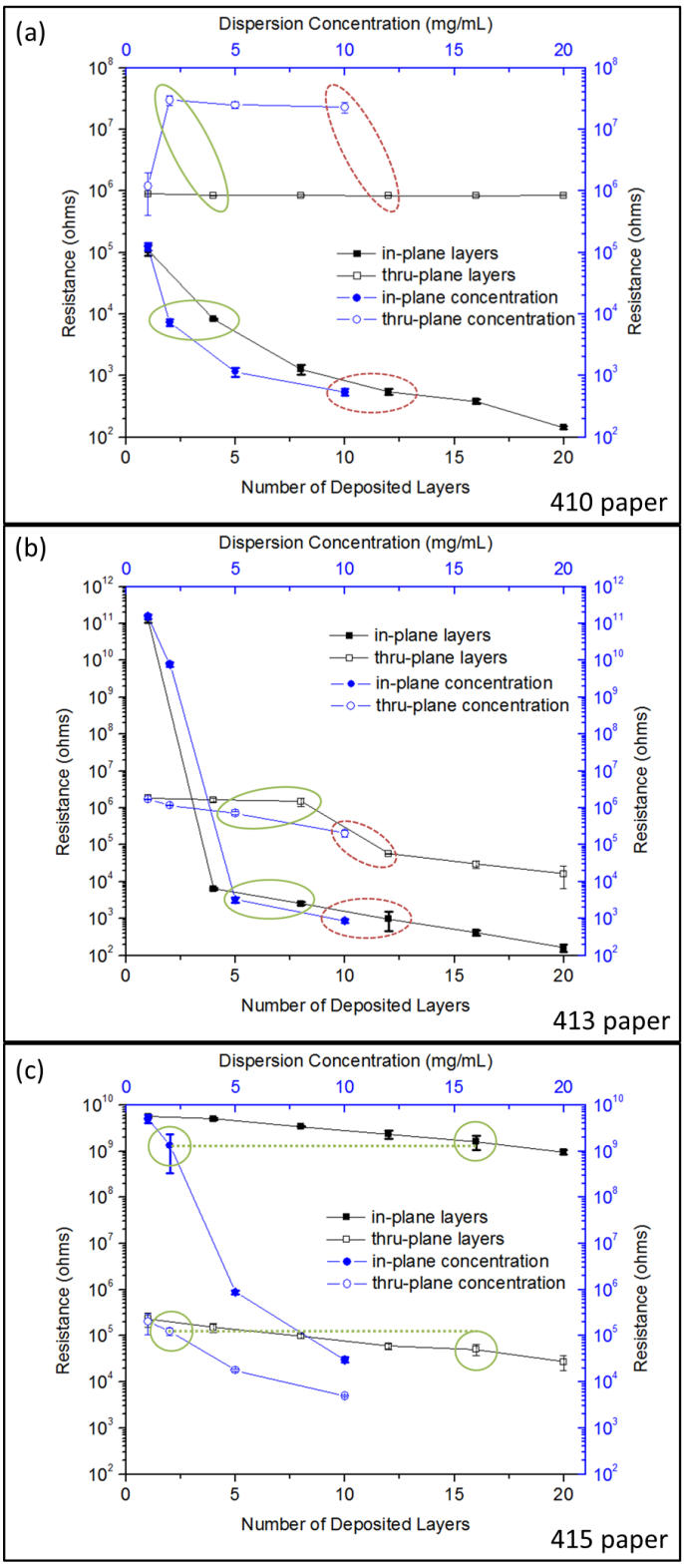

Figure 4.27: Resistance vs. number of deposited layers (left y-axis and bottom x-axis) plotted with Resistance vs. dispersion concentration (right y-axis and top x-axis) for the a) MWNT-410 paper composites; b) MWNT-413 paper composites; c) MWNT-415 paper composites. The green or red circles show conditions where one of the measured planes show a similarity between the layered and concentration deposition as well as the corresponding behavior in the other plane.

For the MWNT-410 composite materials, while a correlation can be made for layer number and dispersion concentration for the in-plane, the equivalent correlation cannot be made for the thru-planes. That is, while the 4 layer and 2 mg/mL composites, for example, may have the same structure and properties measured for their surfaces (thin film behavior), the properties that these two composites exhibit in the thru-plane are vastly different. These two materials are not the same. The resistance difference can be seen in Figure 4.27a. There are two sample sets whose in-plane resistances match directly: 2 mg/mL and 4 layer MWNT-410 composites, as shown by the solid circle, and the 10 mg/mL and 12 layer MWNT-410 composites, as shown by the dashed circle. In both cases, however, the thru-planes of the composites differ by an order of magnitude. Also, the resistance values measured for the 2-10 mg/mL MWNT-410 samples in the thru-plane are above 10^7 Ω, which is indicative of no or minimal internal deposition.

The impedance results confirm this assertion: for the 2, 5, and 10 mg/mL MWNT-410 composites, the thru-plane behavior is fit with the Nested-RC circuit where the internal part of the circuit has a resistance value above 10^7 Ω. Additionally, for the samples which show bulk metallic surface behavior (5 and 10 mg/mL), the value of the outer R_1 is two orders of magnitude larger than the bulk resistance. This behavior is similar to that of the L-MWNT-410 composite materials. While all of the MWNTs are depositing on the surface, they do not form a quality network and have a higher resistance through the thickness of the film. The multilayer deposition methodology improves surface deposition as the repeated number of steps pulling the dispersion downward seems to also pull the MWNTs closer together. The resistance of the surface film is the same in-plane as it is through the thickness of the film.

In the case of the MWNT-413 composite materials, there are two cases (excluding the 1 layer and 1 mg/mL samples) where the composite properties overlap perfectly in the in-plane and come much closer in the thru-plane, as shown by the circles in Figure 4.27b. In addition, the measured impedance behaviors of these two systems evolve in a similar manner. For the in-plane, the concentration MWNT-413 composites grow from paper-dominated (1 mg/mL and 2 mg/mL) to the transitional behavior (5 mg/mL) and then to bulk metallic behavior (10 mg/mL). While thin film behavior is not measured, from the behaviors presented in Chapter 4, Section 2, it is likely that either 3 or 4 mg/mL would show thin film surface conduction.

For the thru-plane, the impedance behavior also transforms in the same manner: the internal pore structure fills up at lower loadings, denoted by the $(R\text{-}CPE)_p$ circuit, and when sufficient MWNTs coat the surface, the Nested-RC circuit fits the impedance behavior (10 mg/mL). The impedance behavior of the thru-plane of the 8 layer and 5 mg/mL samples are both fit by the (R-CPE)p circuit. Likewise, the impedance behavior of the thru-plane of the 12 layer and 10 mg/mL composites are fit by the Nested-RC circuit where the inner resistance has continued to decrease with increased loading and the outer resistance is much closer to the bulk resistance of the sample. For the 10 mg/mL sample, the outer resistance is measured $2.53 \times 10^3\ \Omega \pm 402\ \Omega$ while the bulk resistance measured on the surface was $873\ \Omega \pm 104\ \Omega$. Once again, the multilayer methodology allows for the formation of a bulk network with isotropic properties while the network which forms from the high concentration dispersions does not.

The resistance value measured for the in-plane of the 5 mg/mL sample is statistically equivalent to the 8 layer composite; similarly, the resistance of the in-plane of the 10 mg/mL sample is statistically equivalent to the 12 layer composite. For the thru-planes, the resistance of the 5 mg/mL composite is half that of the 8 layer sample ($7.2x10^5$ Ω as compared to $1.49x10^6$ Ω) and the resistance of the 10 mg/mL composite is twice that of the 12 layer sample ($2.07x10^5$ Ω vs. $5.84x10^4$ Ω). While the thru-planes do not have the exact same electrical properties, the properties are much closer than those discussed for the MWNT-410 composites. Because the pore size and bundle length of the MWNTs are the same, fabrication of the composites on the 413 paper can be done fairly equally using either the multilayer technique or by varying the concentration of the dispersion as is shown by the similar curve shapes in Figure 4.27b.

For the MWNT-415 composite materials, using higher concentration dispersions vastly changes the deposition on the surface of the composites which can be seen in Figure 4.27c. For these large pore size materials, the increased concentration of the dispersion was a benefit rather than a hindrance. At 10 mg/mL, the impedance behavior measured for the composite was that of a thin film with a junction resistance nearing 29000 Ω. As a bulk film did not form, the thru-plane impedance could only detect electrical transport through the pore network. However, the resistance measured for this thru-plane was just below 5000 Ω, which is the lowest resistance achieved for the thru-plane of any of the multilayered samples in this chapter. Additionally, the resistances of the 16 layer composite and the 2 mg/mL composite were statistically equivalent for the surfaces.

However, the thru-plane of the 16 layer composite was 2 times more conducting than the 2 mg/mL composite (50500 Ω ± 13400 Ω vs. 1.25×10^5 Ω ± 22200 Ω). While equivalency in properties could be had when comparing the composites formed by multilayer deposition to those formed using concentration variation, it is more important to note that it is possible to form conducting networks on the large pore size paper by varying conditions during fabrication. This will be explored in more detail in Chapter 6.

4.5 Conclusions

1 to 20 layered MWNT-paper composite materials were fabricated by vacuum filtration-aided drying of dropcasted MWNT dispersions on paper substrates with pore sizes less than, equal to, and greater than the length of the MWNT bundles. Using the knowledge of the composite structures gained in Chapter 3 as well as an extensive literature review, the structures and electronic behaviors of each composite material could be described using equivalent circuit modeling from the results obtained from impedance spectroscopy. The circuit elements from each model were assigned to different electronic behaviors present due to the structure of the material.

It was determined that there are four possible electronic equivalent circuits which can describe the in-plane behavior of these samples. Each circuit provides unique knowledge about both surface deposition of the MWNT and surface conduction. From equivalent circuit analysis, the electronic behavior on the surface can either be paper-dominated (low surface deposition), MWNT thin film dominated, a transitional surface bridging thin film and bulk behavior, or bulk metallic (very high surface deposition). When thin film dominated behavior is detected, it is possible to determine the electrical

properties of specific characteristics of the MWNT film, including the resistance of the MWNT bundle, the resistance of the junctions between bundles, and the resistance of the coiled MWNT bundles. The resistance of the coiled bundles and the junctions of the bundles can be manipulated by varying processing, and this will be the focus of Chapter 5. The resistance of the MWNT bundles is constant throughout all composites meaning that impedance spectroscopy can be used to determine both materials properties and fabrication properties. In addition, there are two different equivalent circuits which can be used to fit the thru-plane impedance data. One of these circuits provides information on whether MWNT deposition is occurring within the thickness of the composite and to what degree that is happening while the other describes samples where deposition is only occurring in the thru-plane.

Overall equivalent circuits were built and simulated to describe the in-planes and the thru-plane behaviors of the composites. These overall circuits showed that, although the composites exhibited seemingly discrete electronic behaviors, these behaviors are actually all related to one another. At different composite morphologies, different parts of the circuit become more dominant and other parts of the circuit are shrouded by the dominant elements. The circuit can be used simultaneously to determine the electrical properties of the composites and the structural mechanisms which lead to the measured electrical properties.

CHAPTER 5

ALTERING THE JUNCTION RESISTANCE OF MWNT THIN FILM NETWORKS DEPOSITED ON PAPER SUBSTRATES USING VACUUM FILTRATION

5.1 Introduction

This chapter will explore fabrication parameters which can be changed or altered in order vary the in-plane properties of the MWNT-410 paper thin film-behaving composites. It has been shown that the DC resistance of the MWNT thin film network (deposited on paper substrates [5] and on hard substrates [39]) is a summation of the resistance of the MWNT bundle (R_b) and the resistance of the junctions between bundles (R_j). As was shown in Chapter 4, Section 2, R_b is a constant value for the MWNT-paper composite materials presented in this thesis. Therefore, junction resistance dominates the DC resistance of the thin film MWNT-paper surfaces [5, 35, 39] and can be predicted by $R_j = R_{dc} - R_b$. Also from Chapter 4, Section 2, the MWNT-410 paper composite materials exhibit MWNT thin film conduction behavior between 1 and 7 deposited layers, resulting in a large range of values for junction resistance which can be achieved by changing only the number of deposited layers. Rather than alter the junction resistance by changing layer number, layer number will be held constant and changes will be made to the MWNT deposition parameters to demonstrate how junction resistance can be varied by processing choices.

5.2 Impacts on MWNT Thin Film Junction Resistance: Varying Surfactant Charge during Fabrication

5.2.1 Introduction

Throughout the MWNT-paper composite fabrication technique employed in this dissertation, there are many experimental variables which can influence the final properties of the composite. The very first processing step that has an impact on the final properties of the composite is creating the MWNT-containing dispersion. In this study, water is used as a solvent for the MWNTs as it is low cost, non-toxic, and will not chemically alter the paper or the MWNTs; however, water cannot break up the agglomerates of MWNTs nor keep them from re-agglomerating. Depositing agglomerated MWNTs onto the paper surface lowers the electronic properties as the surface which forms is highly non-homogeneous. (See Section 4.3.3.3 on the electrical properties of the L-MWNT-410 composites for an example.)

In order to break up the agglomerates of the MWNTs, a surfactant is added to the aqueous dispersion. In most of the work, SDBS has been used as the surfactant as it had been shown in the literature to form very high quality dispersions of MWNTs [55, 56]. However, there are many other surfactant materials which could be used to disperse the MWNTs. Using other surfactant materials in the dispersions used to deposit MWNTs on the 410 paper surface will allow for the physical assignments of the circuit elements given by the Nested-RL circuit described in Section 4.2.3.2 to be checked, reinforcing the analysis done in Chapters 3 and 4.

5.2.2 Dispersion Fabrication Details

Three different aqueous dispersions consisting of 1 mg/mL of MWNTs and 10 mg/mL of one of three surfactant materials were made using the same methodology described in Chapter 2. 10 mg/mL was chosen as the surfactant concentration as it was found to create the most stable MWNT dispersions with SDBS and had been used for the rest of the thesis. This concentration was used for the other surfactants in order to make one-to-one comparisons; however, this concentration may not be the ideal micelle concentration condition for the other surfactant materials which could have an impact on the final results. Figure 5.1 shows the chemical structure of the three surfactants used in this study: a) SDBS (anionic), b) Triton X-100 (non-ionic), and c) CTAB, cetyl trimethylammonium bromide, (cationic). All three surfactants were purchased from sigmaaldrich.com.

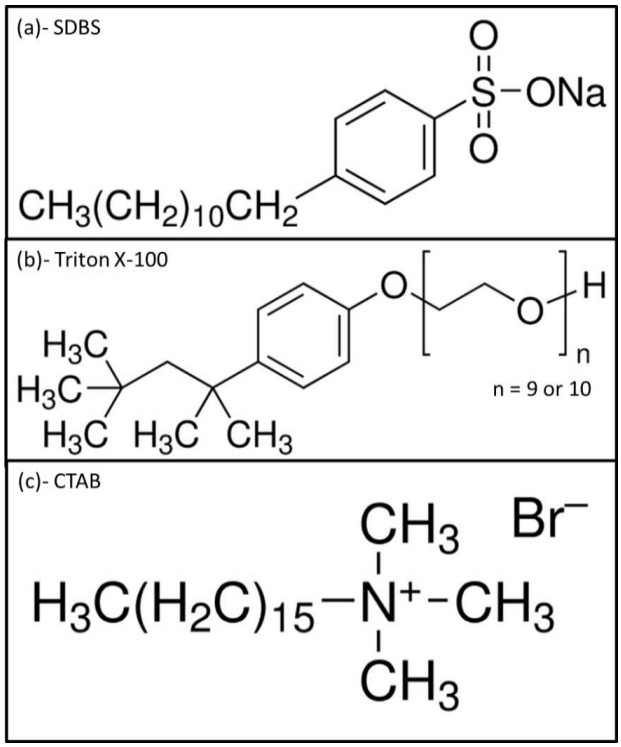

Figure 5.1: Chemical structure of the three different surfactant materials employed in this study: a) SDBS (anionic); b) Triton-X100 (non-ionic); c) CTAB (cationic).

The surfactant is a particle or molecule which is adsorbed onto the surface of the CNT. Surface adsorption inhibits the CNTs from interacting and promotes the breakage of bundles into smaller MWNT bundle or into single tubes. A schematic of this is shown in Figure 5.2 [56]. In step i, a large bundle of CNTs is shown. In step ii, the surfactant particles (circles) begin to diffuse into the bundle, and the tubes start moving apart. In step iii, the surfactant particles adsorb onto the tube which is shown in greater detail in the expanded view. By step iv, the surfactant adsorption has caused a CNT to separate from the bundle [56].

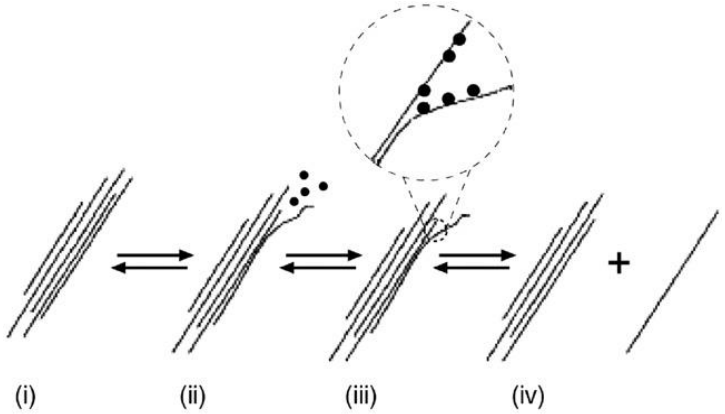

Figure 5.2: Surfactant adsorption breaking up a bundle of CNTs [56].

In addition to breaking up the bundles of CNTs, surfactants also function to increase the dispersion of CNTs in water. Surfactant molecules have a tendency to concentrate at interfaces rather than in the bulk of either phase. This occurs because the surfactant particle has one portion that is soluble in the medium and one portion which is incompatible with that medium. Since water is the media for dispersion, the surfactant must contain a hydrophobic region and a hydrophilic region. The surfactant can have a hydrophobic head with a hydrophilic tail or the inverse structure. Both types of structure are shown adsorbed onto a particle schematically in Figure 5.3.

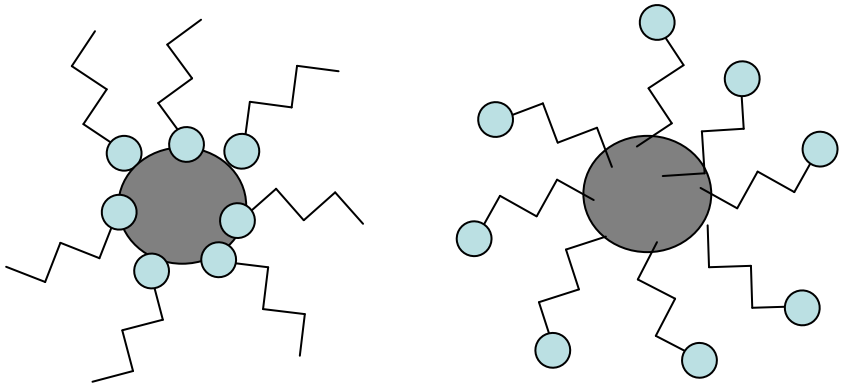

Figure 5.3: Interaction of surfactant molecules (round head, line tail) with a particle (gray). The interaction can be head to particle (left) or tail to particle (right) depending on the interactions of the surfactant molecule with the particle and the solvent.

The hydrophobic region of the surfactant will want to limit its interaction with water by adsorbing to the surface of the CNT. If this part of the surfactant also contains a pi-bond, the interaction will increase and further aid in the dispersion of the CNT [72]. This portion of the surfactant may be charged (positively or negatively) which will give the CNT an effective charge on its surface. Electrostatic repulsion is used to keep the CNTs from re-agglomerating. The hydrophobic head may also be uncharged and rely on steric repulsion or separation using long chains to keep the CNTs from interacting. The hydrophilic portion of the surfactant will interact with the water solvent, promoting dispersion of a phase (CNT) which would not usually disperse in water

5.2.3 Layer-by-Layer Composite Fabrication

Since the surfactant adsorbs onto the CNTs, the surfactant properties alter the CNT properties. If the surfactant is charged, the CNTs will have an effective charge. If the surfactant is uncharged, the CNTs will be effectively neutral. By alternating the charge of each deposited layer, electrostatic and steric repulsion and attraction can be used to manipulate the interaction between each deposited layer and change the in-plane electrical properties.

Figure 5.4 shows the layer-by-layer deposition schemes used in this study. 4 layers of the MWNT containing dispersions were deposited using vacuum filtration on the 410 filter paper. As was discussed in Chapter 4, Section 2, 4 deposited MWNT layers on the 410 filter paper result in a MWNT-paper in-plane whose conduction behavior is MWNT thin film dominated [5]. Each deposited layer is described using a circle with either an X, +, or – where X is Triton X-100 (neut), + is CTAB (pos), and - is SDBS (neg). Impedance spectroscopy of the layer-by-layer in-planes was done to extract the junction resistance of each film to determine how the alternating charges impact film formation through the alterations in MWNT-MWNT and MWNT-paper interactions.

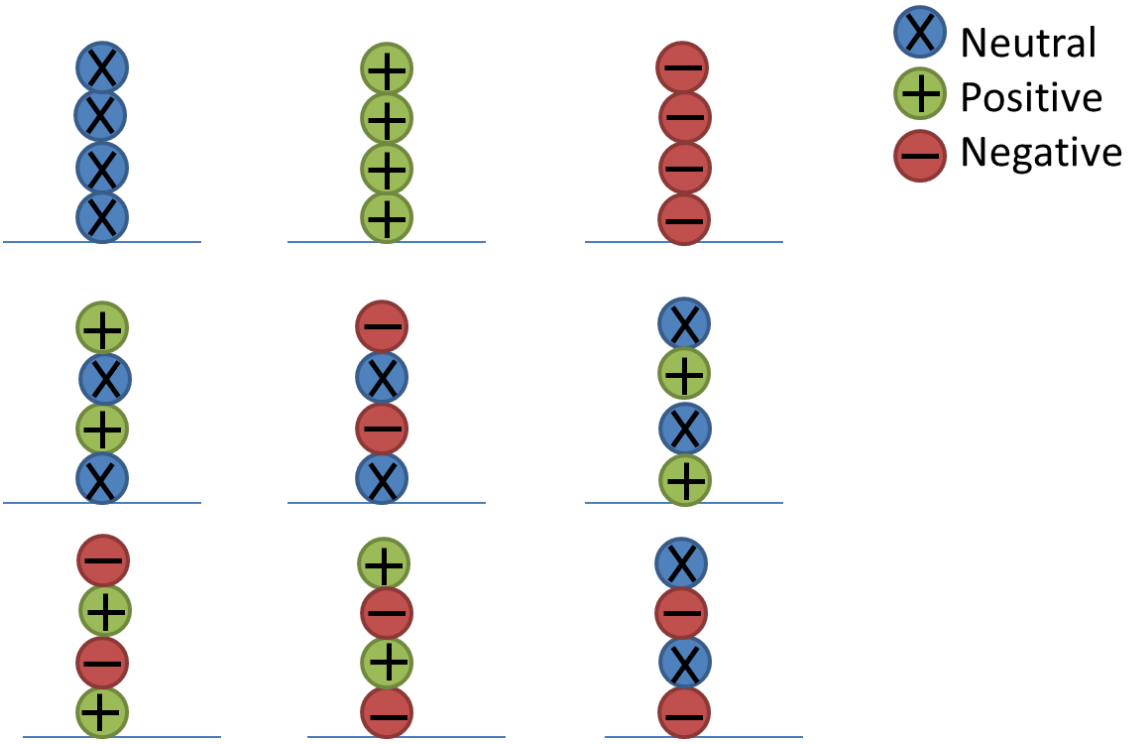

Figure 5.4: Deposition schemes for this surfactant variation study. Each circle corresponds to 1 deposited layer, and the symbol within the circle describes which surfactant is being deposited: X = Triton X-100; + = CTAB; - = SDBS.

5.2.4 Results

It was shown in Chapter 4, Section 2 that the electronic behavior of 1 layer of MWNTs deposited on the 410 filter paper show MWNT thin film conduction. In order to determine the quality of the thin film as a function of the interaction between the paper and the first deposited layer, 1 layer was deposited from each of the dispersions on the 410 filter paper. Using impedance spectroscopy and curve fitting, the bundle resistance (R_b) and junction resistance (R_j) were extracted. For all 1 layer in-planes, R_b measured approximately 900 Ω, suggesting that the surfactants created CNT bundles of approximately the same size.

However, R_j showed some variation depending on the surfactant material. For 1 layer films deposited using the SDBS, Triton X-100, and CTAB containing dispersions, $R_j = 1.39x10^5\ \Omega \pm 1.58x10^4\ \Omega$, $2.46x10^5\ \Omega \pm 5.23x10^4\ \Omega$, and $1.82x10^5\ \Omega \pm 4.11x10^4\ \Omega$, respectively. The 1 layer film deposited with Triton X-100 had the highest standard deviation and junction resistance, while the 1 layer film deposited with SDBS had the lowest standard deviation. Figure 5.5 shows medium magnification SEM images of the 1 layer films deposited with a) SDBS (neg), b) Triton-X100 (neut), and c) CTAB (pos). For the 1 layer film deposited with CTAB, surfactant material is still largely present on the surface.

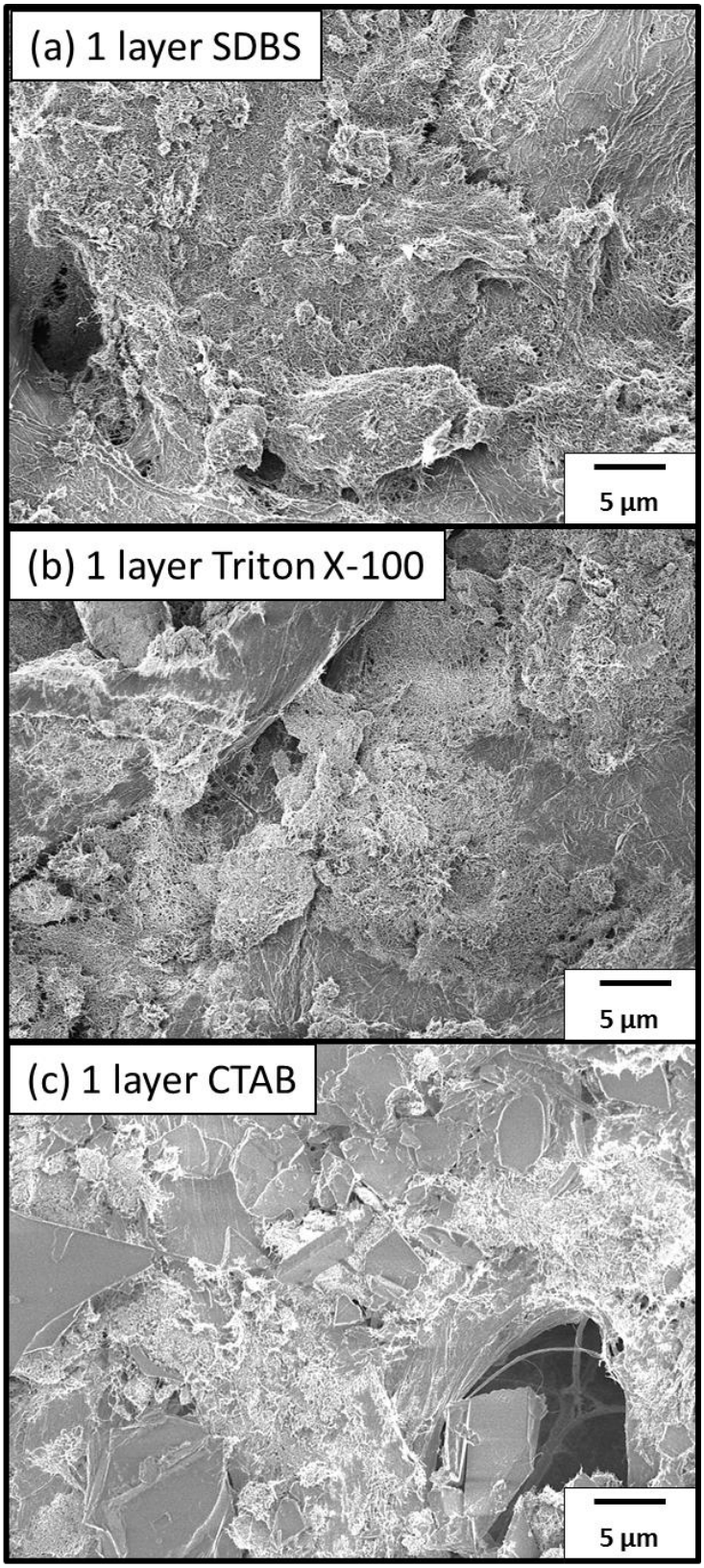

Figure 5.5: SEM images of 1 layer films deposited on the 410 paper with dispersions containing a) SDBS; b) Triton X-100; c) CTAB.

Figure 5.6 shows junction resistance plotted vs. each deposition scheme from highest to lowest R_j for the layer-by-layer in-planes. The dashed line shows R_j of a 4 layered film deposited using only the dispersion containing Triton X-100. The dotted line shows R_j of a 4 layered film deposited using only the dispersion containing SDBS. The dashed-dotted line shows the resistance of the 4 layered film deposited using only the dispersion containing CTAB. The denotation on the x-axis describes the deposition scheme for the layer-by-layer surfaces. For example, (Neg Neut)x2 corresponds to the deposition scheme wherein the surfactant in the dispersions used in each step alternated as negative (1st layer), neutral (2nd layer), negative (3rd layer), neutral (4th layer).

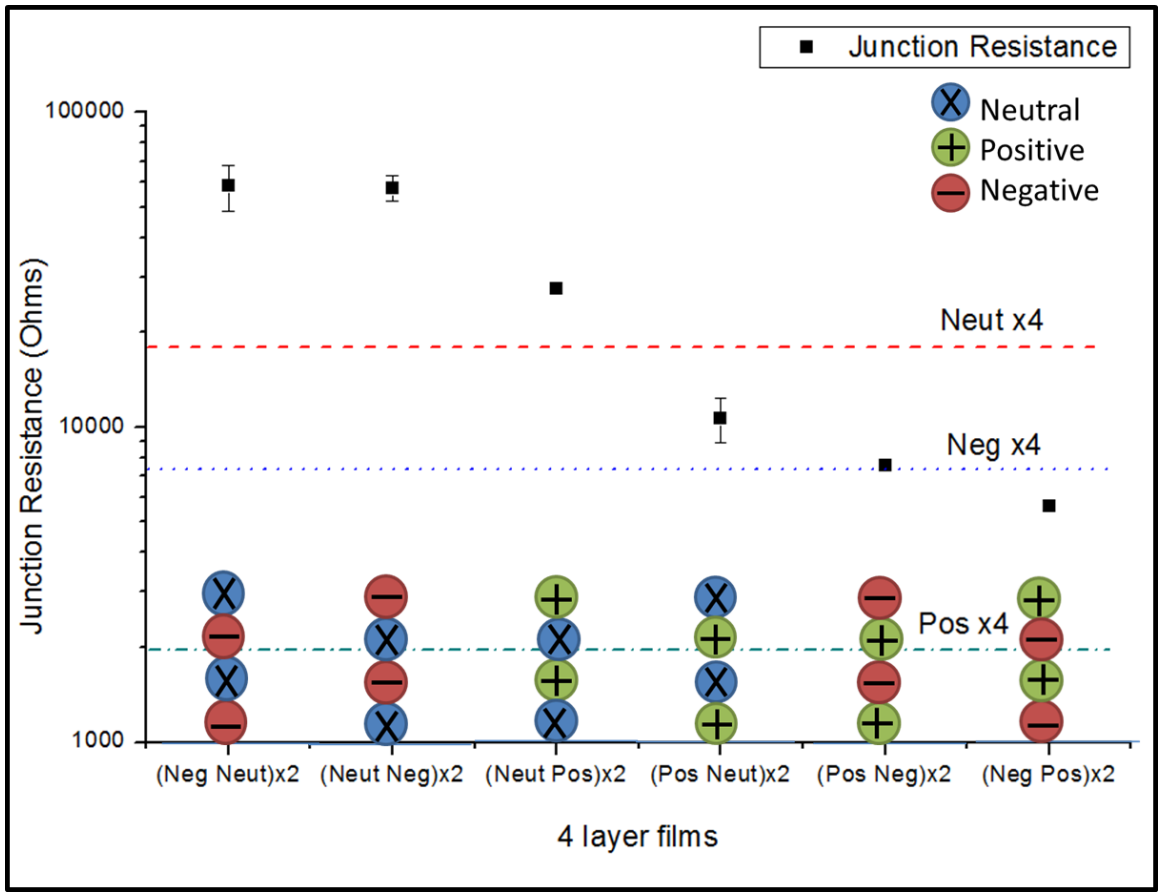

Figure 5.6: Junction resistance obtained from the samples that were made using the deposition schemes described in Figure 5.4.

SEM images of each 4 layer surface are shown in Figure 5.7. When the deposition scheme for the layer-by-layer films contains the neutral surfactant, the measured R_j's are much higher than for the film deposited from only the dispersion containing the neutral surfactant (Neut x4, dashed line in Figure 5.6). These networks can be seen in Figures 5.7a-c. For the two schemes where the neutral dispersion is deposited first (Figures 5.7b and 5.7c), the density of the MWNT film is fairly low, and the measured R_j is generally higher than its inverted deposition scheme (e.g. see (Neut Neg)x2 vs. (Neg Neut)x2 in Figure 5.6). The high R_j of the 1 layer film suggests that the Triton X-100 inhibits the initial interaction between the MWNTs and the paper fibers. The density of the MWNT film is impacted at the first layer, and subsequent deposition steps cannot overcome the low density of the first layer.

Conversely, Figure 5.7d details the surface of the (Pos Neut)x2 scheme which shows large pieces of surfactant dominating the image space with a fairly dense MWNT film between them. As shown in Figure 5.6, R_j for the (Pos Neut)x2 scheme is half the size of its inverted deposition scheme, (Neut Pos)x2. In addition, this is the first in-plane with an R_j lower than that of the Neut x4 sample (dashed line in Figure 5.6). The positive first layer seems to be aiding in film formation.

The layer-by-layer films deposited from the dispersions containing positive and negative surfactants have R_j's which fall between that of the purely negative dispersion (dotted line in Figure 5.6) and the purely positive dispersion (dashed-dotted line in Figure 5.6). The surfaces of the (Pos Neg)x2 and (Neg Pos)x2 samples are shown in Figures 5.7e and 5.7f, respectively. While it may be electrostatic interactions between the two surfactant materials aiding in the formation of the in-plane, the positive surfactant

remains on the surface. The film between the surfactant pieces is highly dense, but the surfactant is not drawn away during vacuum filtration. It is likely a combination the excess CTAB forcing the nanotubes into a smaller locations on the surface, and the interaction of the first layer with the paper surface which drives the R_j for the (Neg Pos)x2 in-plane down.

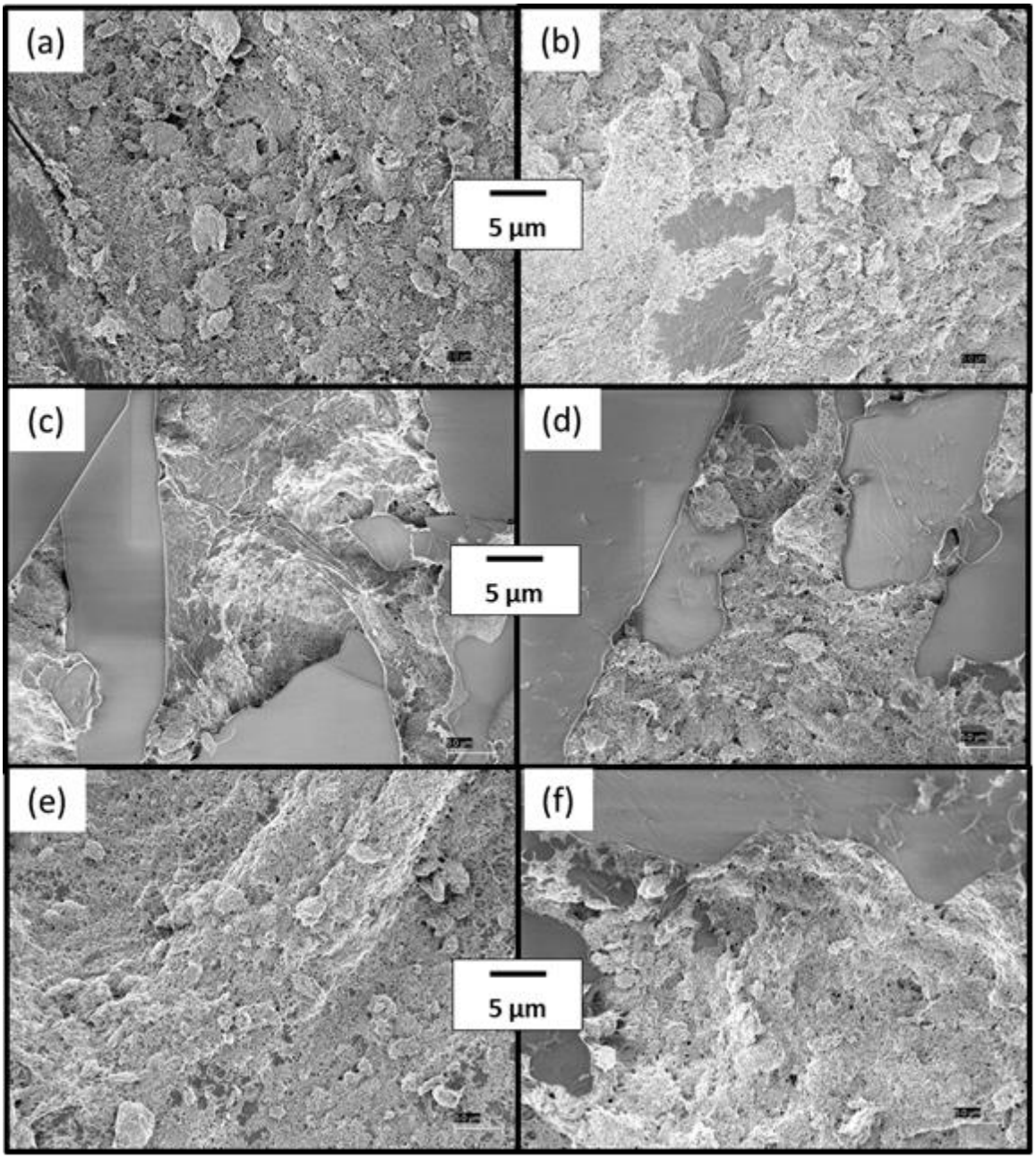

Figure 5.7: 4 layer surfactant charge varied surfaces for a) (Neg Neut)x2; b) (Neut Neg)x2; c) (Neut Pos)x2; d) (Pos Neut)x2; e) (Pos Neg)x2; and f) (Neg Pos)x2 deposition schemes.

5.2.4.1 Formation of Segregated Networks using CTAB Surfactant

As was shown in figure 5.7, the CTAB surfactant covers large areas on the surface; however, the CTAB molecule starts out the same size as the SDBS (similar molecular weight per molecule). It has been previously shown that CTAB containing solutions of CNTs formed large crystalline aggregates of the CTAB surfactant [54]. While the dispersion containing the MWNTs for this study did not have CTAB crystals which were macroscopically visible, aggregates of CTAB can be seen in the SEM micrographs. It is worth noting that if a solution of just water and 10 mg/mL of CTAB was made, the CTAB formed macroscopic crystals in the container within days. The MWNTs seem to temper some of the crystal growth but not completely, as evidenced by the presence of CTAB in the SEM images in Figures 5.5c and 5.7c,d,f.

However, the properties of the layer-by-layer MWNT thin films containing CTAB have much lower R_j's than those that were made with the other surfactants. The MWNT network which forms between the surfactant crystals is generally more densely packed than the MWNT networks which are deposited from dispersions containing just the negative and neutral surfactants. In addition, the impedance behavior of the 4 layered in-plane deposited from only the CTAB-containing dispersion was able to be fit with the equivalent circuit, $(R\text{-}L)_s$. This circuit was used previously in Section 4.2.3.4 to describe conduction through a bulk, metallic-like MWNT network.

Figure 5.8 shows SEM images of in-plane which formed after depositing 4 layers of the dispersion containing CTAB on the 410 paper at low magnifications (a) and

medium magnifications (b). The surfactant forms a flat surface structure while the MWNT deposition is pushed to the boundaries of the surfactant crystals. The segregated MWNT network contains the same amount of MWNTs as the other surfaces do, but all of the MWNTs are segregated to a much smaller surface region due to the large CTAB crystals. Therefore, the segregated MWNTs form a dense, bulk-behaving network rather than a thin film MWNT network, and that is why its resistances are so low.

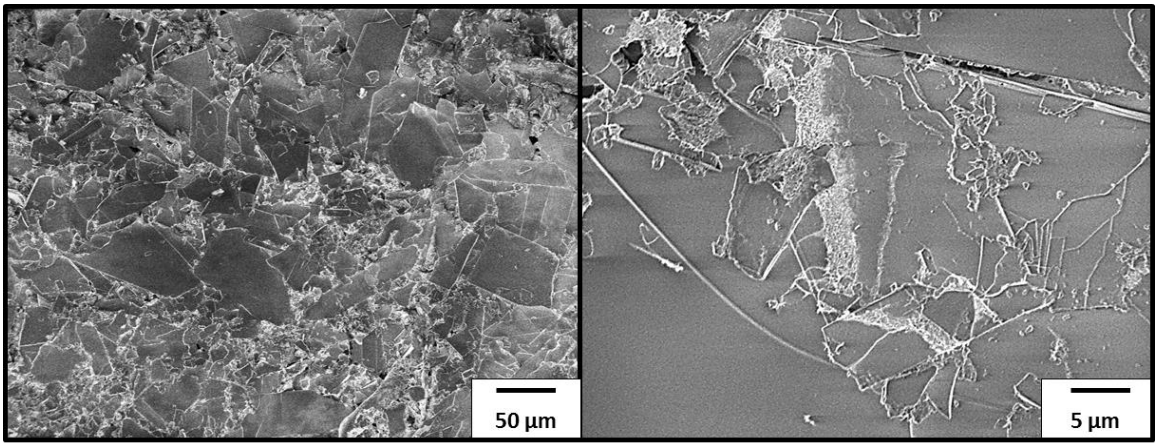

Figure 5.8: Segregated MWNT network formation between CTAB crystals on the surface of the 410 paper for the Pos x4 deposition scheme.

5.2.5 Conclusions

4 layers of MWNTs were deposited on the 410 paper surfaces from 1 mg/mL dispersions containing 10 mg/mL of three different surfactant materials: SDBS, CTAB, and Triton X-100. By varying only the surfactant in the dispersion being deposited, MWNT thin films could be formed with junction resistances spanning over an order of magnitude. Under the right conditions, even bulk network formation could be detected at 4 layers. This study shows both the importance of the surfactant material in the initial interaction between the MWNTs and the paper as well as how the interactions between MWNT layers contribute to the overall resistance of the film.

5.3 Impacts on MWNT Thin Film Junction Resistance: Post-Processing Application of Pressure

5.3.1 Introduction

In this section, a post-processing step is added after the established MWNT thin film fabrication technique in order to change the structure and properties of the original thin film composite surface on the 410 filter paper. There are a variety of post-processing techniques which have been employed previously to attempt to improve upon the resistance of the CNT thin film, and, more specifically, the junction resistance (R_j). Ion beam welding has been used to improve the electrical properties of CNT sheets [73]. MWNT sheets were exposed to argon and hydrogen beams with an energy of 70 KeV and irradiation dosages between 0 and $1x10^{18}$ ions/cm^2 at 800 K. It was found that at an irradiation dose of $4x10^{16}$ ions/cm^2 in the argon ion beam increased the electrical conductance of the MWNT sheet by 33%. Similarly, the electrical conductance of the MWNT sheet can be enhanced by 24% at a dosage of $1x10^{18}$ ions/cm^2 in a hydrogen ion beam. It was suggested that the ion beam covalently fuses MWNTs together at the junction, improving the contact between the tubes and decreasing the resistance. In both cases, excessive radiation dosages resulted in an increase to the resistance due to a large number of irradiation induced defects [73].

Similarly, electron-beam irradiation has been used to improve R_j in both SWNT and MWNT films [74]. For both film types, conductivity was improved by an order of magnitude when exposed to an electron beam with energy of 30 keV. However, at long exposure times, the MWNT film reaches a saturation point, and the properties no longer

improve. Conversely, the SWNT conductivity continues to improve with exposure time. Using Raman spectroscopy to probe the SWNT film, it was determined that the semiconducting SWNTs converted to metallic SWNTs over long radiation exposure times, and the decrease in the number of semiconductor-metallic junctions result in a continually increasing conductivity [74].

Both ion and electron beam irradiation methods are time consuming and costly procedures, drastically diminishing the attractiveness of these methods outside the laboratory. Any post-processing for the MWNT-paper materials should be simple and low cost just as the original processing methodology. Previously, a powder containing silicon carbide whiskers (10 μm in length, 0.65 μm in diameter) was uniaxially compressed to determine the impact of pressure on the electrical properties of the compacted powder [46]. The resistance of the compacted powder decreased 6 orders of magnitude with increasing pressure (from ~10^8 Ω at 5 MPa to ~10^2 Ω at 300 MPa) due to improved contact between whiskers [46]. As whiskers and nanotubes have a similar structure, uniaxial pressing of CNTs should lead to improved contact and a lower resistance. Unlike the previous research, however, the CNTs will be pressed not as a loose powder but instead after deposition on the 410 paper substrate.

5.3.2 Experimental Details

3 layers of MWNTs were deposited from the 1 mg/mL dispersion (containing 10 mg/mL SDBS) on the 410 filter paper using vacuum filtration. 3 layers were chosen to form the thin film network because the resistance of this network should be low enough that the deviation of the properties between each sample should be low. However, this

value should also be high enough that after the application of pressure, the in-plane should still be exhibiting thin film behavior. At 3 deposited layers, the R_j for the surfaces after fabrication was measured at 26000 Ω ± 5070 Ω, in line with the results presented in Chapters 3 and 4. This value also agrees and with the estimation provided by the model in Equation 3.1 (R_j = 21000 Ω). Figure 5.9 shows SEM images taken at a) low magnification, b) medium magnification, and c) high magnification for the 3 layered MWNT-410 paper composite in-planes after fabrication but before any pressure was applied to the surface.

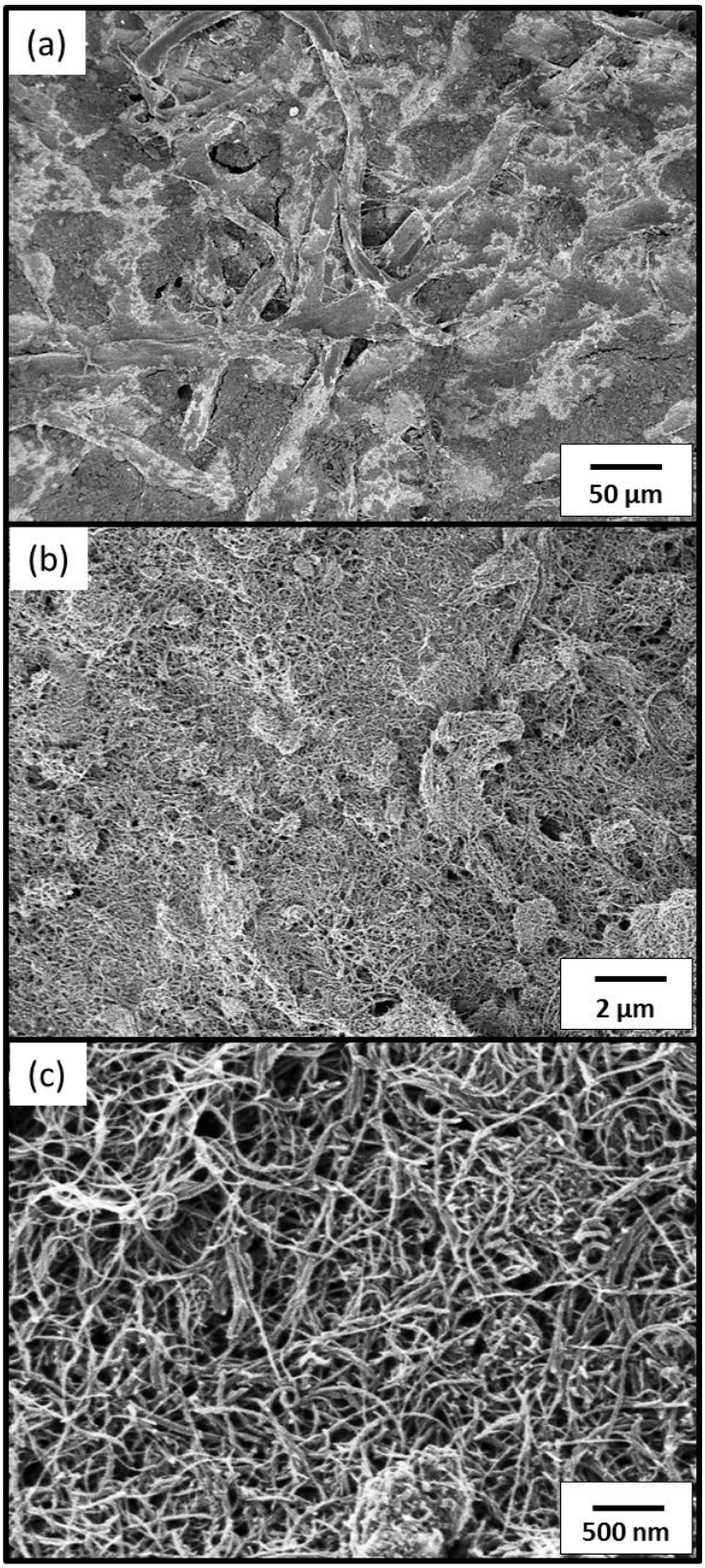

Figure 5.9: a) Low magnification, b) medium magnification, and c) high magnification SEM images of the 3 layered MWNT-410 paper composite in-planes before the application of pressure to the composite.

Pressing was done using a 12-ton model-C uniaxial Carver press (Carver In., Wabash, IN). Samples were punched into 3/8" round discs, and a barrier material (410 filter paper or aluminum foil) was placed over the surface of the MWNT film in order to prevent contamination from the equipment. The composite and the barrier were placed between two steel pins and loaded into the press. The press was then ramped up to the desired pressure and that pressure was held for two minutes before release. For the paper barrier, pressures of 6.2, 12, 31, and 62 MPa were used. For the aluminum foil barrier, pressures of 6.2, 12, 31, 47, 56, 59, and 62 were used.

Immediately following pressing, the sample was removed from the machine and, impedance spectroscopy was done to determine the impact of the pressure on the electrical properties of the MWNT thin film. For the samples pressed with the aluminum foil barrier, impedance spectroscopy was done again after 24 hours, 48 hours, and 14 days to determine whether the properties of the films deteriorated with time.

5.3.3 Results: Paper Barrier

Table 5.1 shows the R_j before pressing, after pressing, and the percent change (from the average value only) for the samples pressed with a paper barrier. At low pressures, while R_j decreased slightly after pressing, the change in resistance is less than 1%. At high pressures, R_j increased after pressing. Even at low pressures, and especially at high pressures, there was a transfer of MWNTs from the original paper substrate to the paper barrier. At low pressures, it seems that the least connected MWNTs moved between surfaces, and there was a statistically insignificant change in the R_j. The change trends downward only because the averages changed slightly. If the standard deviations

were factored into the calculation, there would be no change. For the high pressures, there was a statistically significant increase in junction resistance after pressing. Because of the affinity of MWNTs to paper, the use of paper as a barrier material leads to material transfer rather than improvements to the surface properties.

Table 5.1: Junction resistance (R_j) before and after the application of pressure for the samples pressed with a paper barrier.

Pressure	R_j before Ω	R_j after Ω	$\frac{R_j^{after} - R_j^{before}}{R_j^{before}} x100$
6.2 MPa	27000 ± 1200	27000 ± 650	0%
12 MPa	30500 ± 2400	29000 ± 2000	-0.36%
31 MPa	28000 ± 1800	37000 ± 4030	+3.3%
62 MPa	25000 ± 950	32000 ± 1100	+3.2%

5.3.4 Results: Aluminum Foil Barrier

After a variety of materials were tested to find the best barrier material which would promote compaction rather than material transfer, aluminum foil was chosen. The change in the MWNT network properties caused by the application of pressure is shown in Figure 5.10. Figure 5.10a shows the junction resistance of the thin films before the application of pressure (squares) and after the application of pressure (circles). For pressures between 6.2 and 47 MPa, R_j decreased by about 75% for all samples. At 56 MPa, the R_j values before and after pressing were statistically the same. For pressures beyond 56 MPa, R_j increased by ~6%.

Interestingly, R_j was not the only thin film property that was impacted by the post-processing addition of pressure. Three different electronic processes were detected and separated from the overall electronic behavior using impedance spectroscopy for the MWNT thin film networks deposited on paper (as discussed in Section 4.2.3.2): conduction through the MWNT bundles, conduction through curved MWNT bundles,

and conduction through MWNT-MWNT junctions. Figure 5.10b shows the curved bundle resistance (R_{cb}) of the MWNT thin film networks before (squares) and after (circles) the application of pressure. As pressure increases, R_{cb} decreases, and eventually, at high pressures, the curved bundle resistance disappears completely.

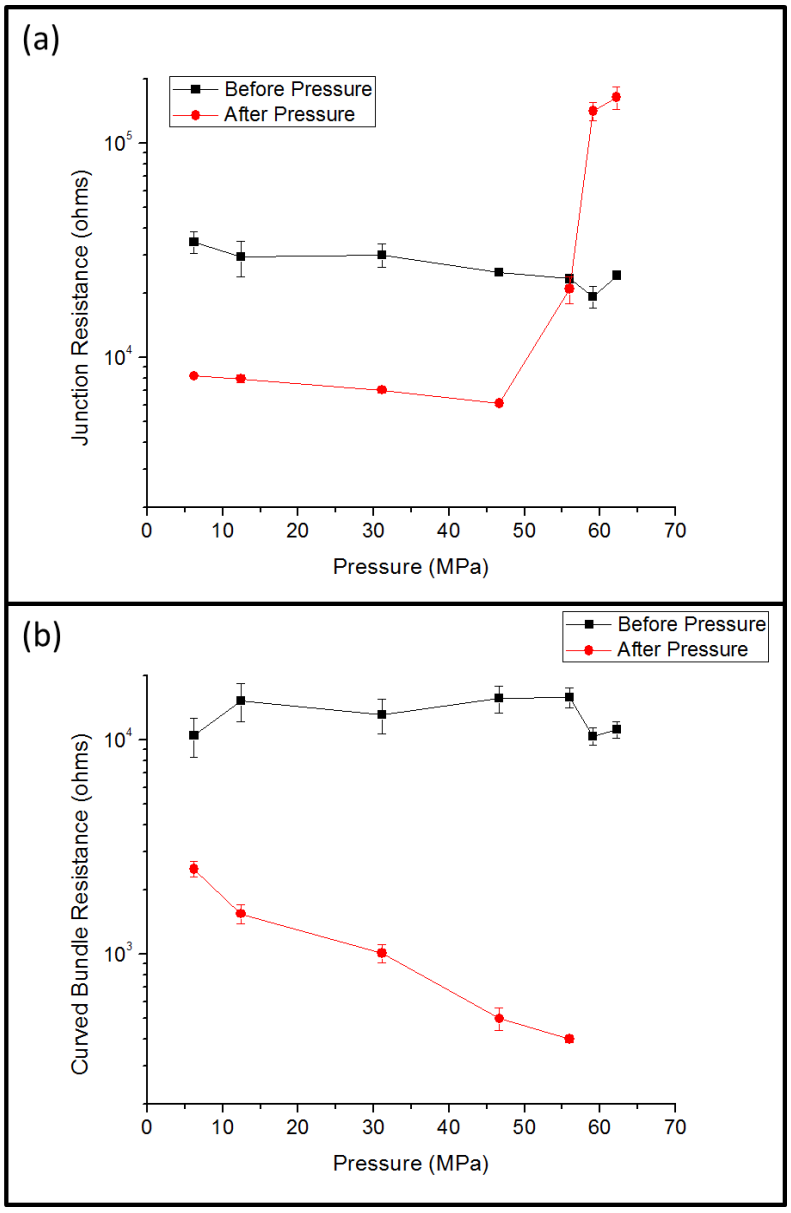

Figure 5.10: a) Junction resistance and b) curved bundle resistance before (squares) and after (circles) the application of pressure to the film surface.

In order to understand how the application of pressure changes the surface of the thin films, SEM images of the thin films were taken for the surfaces pressed at 6.2 MPa,

47 MPa, and 62MPa. Figure 5.11 shows three different SEM images taken for the film pressed at 6.2 MPa. Comparing these images to Figure 5.9 shows what only a small amount of pressure can do to the composite in-plane and helps explain the decrease in R_j and R_{cb}.

Figure 5.11a shows the low magnification SEM image for the film pressed at 6.2 MPa. The paper fibers sitting above the MWNTs are pushed downward and the regions of MWNTs interconnect to a further degree. The medium magnification image in Figure 5.11b shows a bunch of a large and highly flattened MWNT network regions which are connected to each other with normal MWNT network regions (similar to those seen in Figure 5.9b). At high magnifications, shown in Figure 5.11c, the tubes appear slightly flattened and pushed closer together compared to those in Figure 5.9c. The application of pressure pushes the MWNTs closer together and flattens them, leading to a decrease in R_j and R_{cb}.

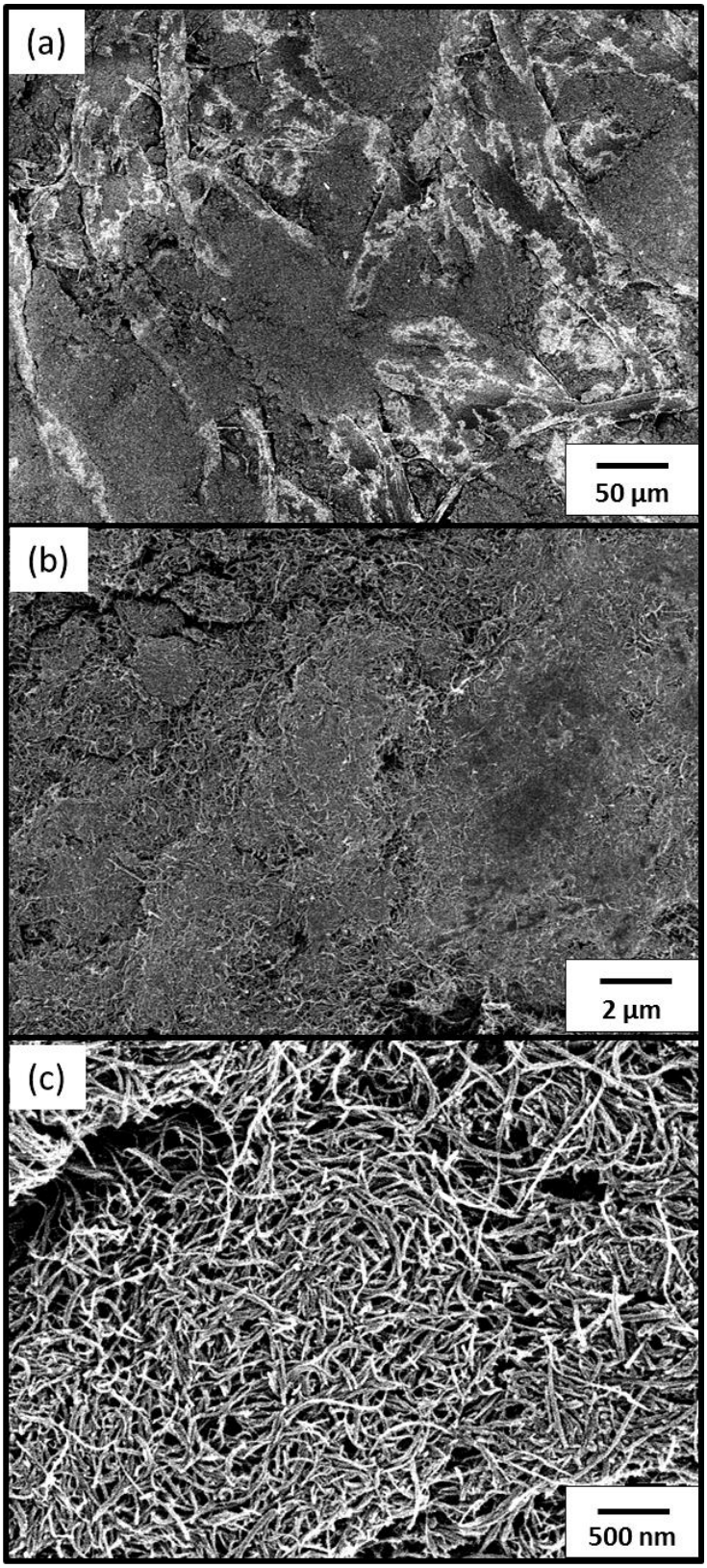

Figure 5.11: a) Low magnification, b) medium magnification, and c) high magnification SEM images of the 3 layered MWNT-410 paper composite in-plane after the application of 6.2 MPa pressure to the composite.

Figure 5.12 shows the a) low magnification, b) medium magnification, and c) high magnification SEM images for the film surface pressed at 47 MPa (low R_j and low R_{cb}). While the low magnification image (Figure 5.12a) shows a microstructure which does not vary all that much from that in Figure 5.11a (6.2 MPa pressure), both the medium and high magnification images offer some insight into the properties of the surface. Figure 5.12b shows both an increased degree of flattening in the MWNT network, the loss of the non-flattened MWNT regions, and the start of the formation of cracks on the surface. Figure 5.12c shows tubes which are highly flattened and pressed into one another. Nearly all MWNT curvature is lost to the pressing. Additional application of pressure continues to flatten out the curvature until the R_{cb} goes to zero (see Figure 5.10b).

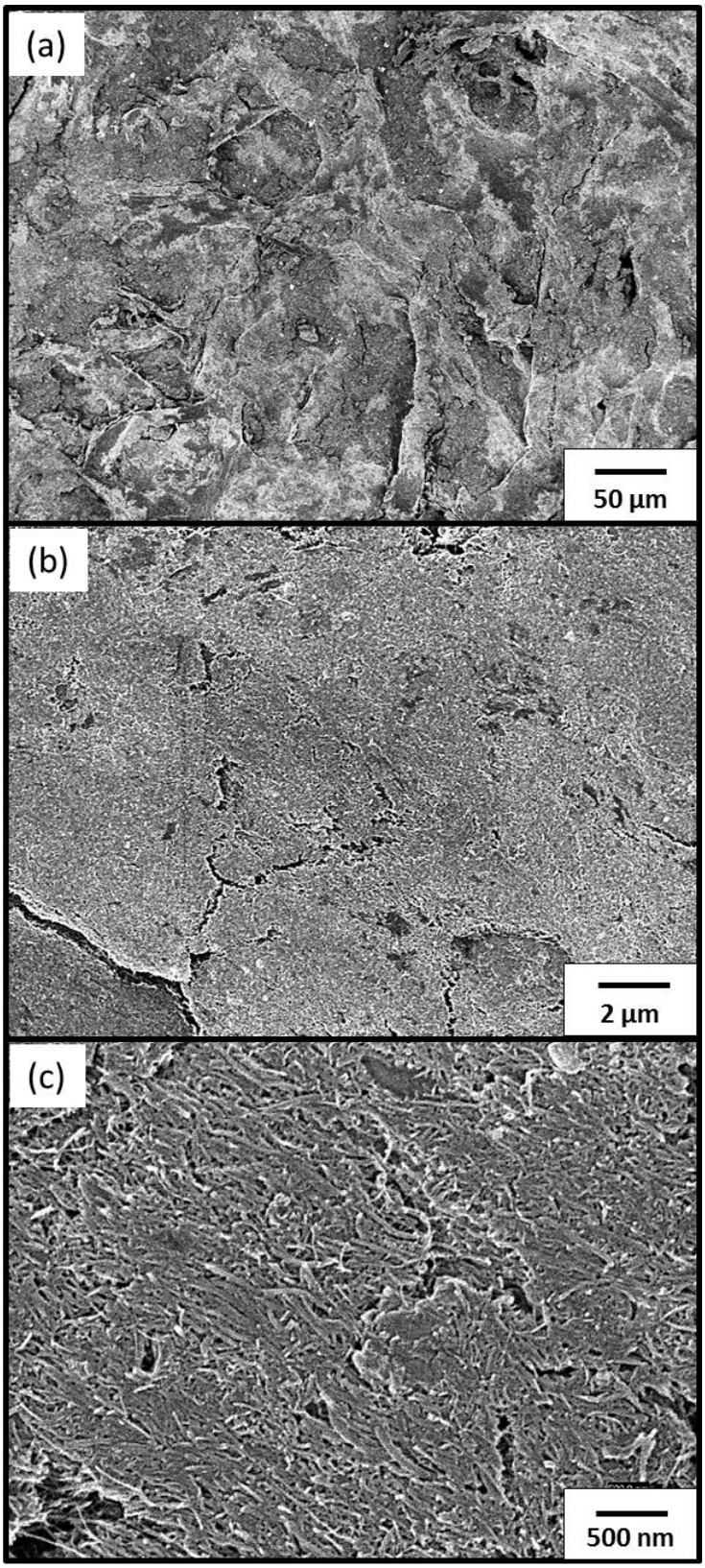

Figure 5.12: a) Low magnification, b) medium magnification, and c) high magnification SEM images of the 3 layered MWNT-410 paper composite in-planes after the application of 47 MPa pressure to the composite.

The application of pressure on the surface results in two competing mechanisms which alter R_j: (1) the pressing of the MWNT-MWNT junctions closer to one another and (2) the formation of surface cracks due to overpressing. At low pressures, the pressing mechanism dominates. As pressure is increased, more pressing of the MWNTs occurs, but the formation of surface cracks also begins. At 56 MPa, these mechanisms balance out, and while the surfaces appear completely different, the properties are similar before and after pressing. After 56 MPa, the cracking mechanism becomes dominant, and R_j increases, which can be seen in Figure 5.10a. Figure 5.13 shows low (a) and medium (b) magnification SEM images for the sample pressed at 62 MPa. Figure 5.13a shows the reemergence of the paper fibers on the surface as the MWNT containing regions are pushed under the highest paper fibers. In addition, Figure 5.13b shows the breaking apart of the pressed MWNT network and crack propagation which extends across the entire image.

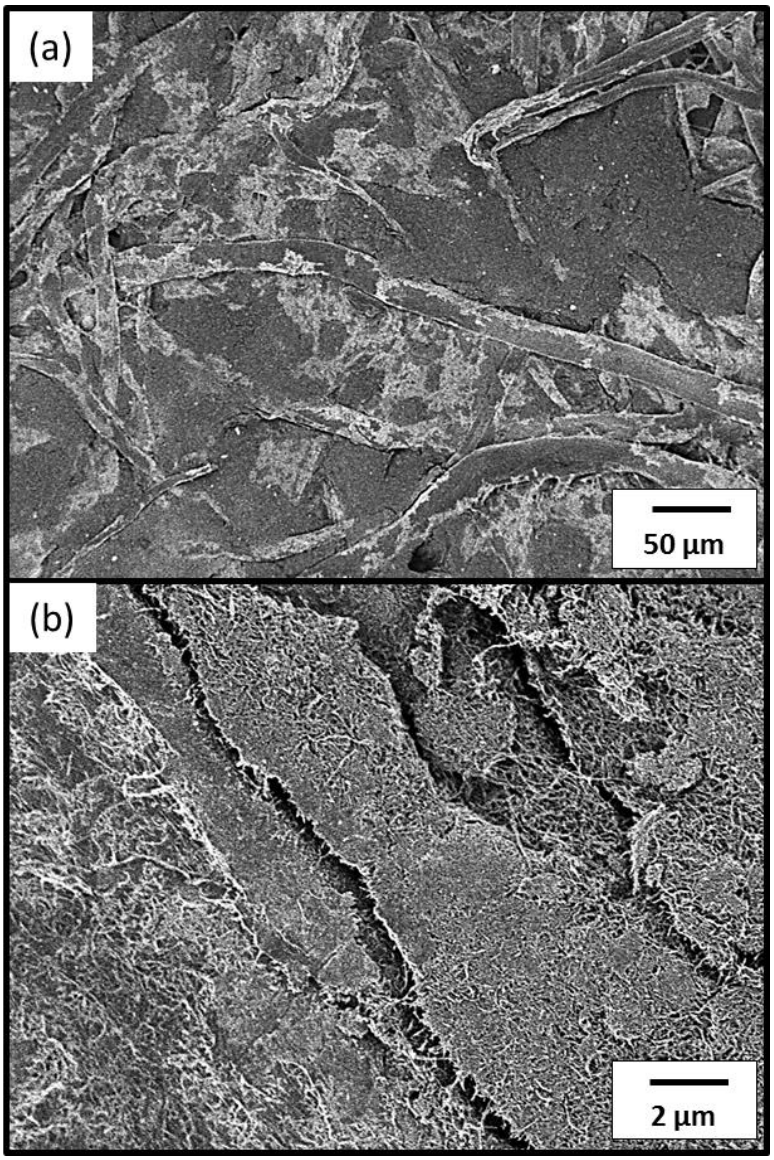

Figure 5.13: a) Low magnification and, b) medium magnification SEM images of the 3 layered MWNT-410 paper composite material after the application of 62.2 MPa pressure to the surface.

5.3.4.1 Stability of Pressed Surfaces over Time

Figure 5.14 shows the change in R_j (a) and R_{cb} (b) over time (measured in days) for the pressed samples. These samples were tested after 1, 2, and 14 days to determine whether the change in the surface architecture caused by the application of pressure remained or relaxed over time. As is shown in Figure 5.14a, the R_j of the samples pressed between 6.2 and 47 MPa remained constant over the time period being measured. The junction resistance for the surface pressed at 56 MPa increases slightly after one day but remains constant over the rest of the time interval. R_j for the surfaces pressed at 59 MPa and 62 MPa increases over the first two days but then remains constant over the rest of the time period. It seems that the surfaces which are highly cracked (high pressures) relax slightly with time; however, because these surfaces contain large defects, the relaxation actually causes more surface disruption and a greater increase of R_j with time. R_{cb}, shown in Figure 5.14b, remains relatively constant with increasing time. However, since the scale on this graph is linear, the degree of standard deviation for the curved bundles is much more visible. The standard deviation for R_{cb} is much higher at low pressures confirming what is shown in Figure 5.11b: the low pressure causes a higher variability in the flattening of the MWNTs (regions of flattened MWNT networks separated by regions of non-flattened MWNT networks).

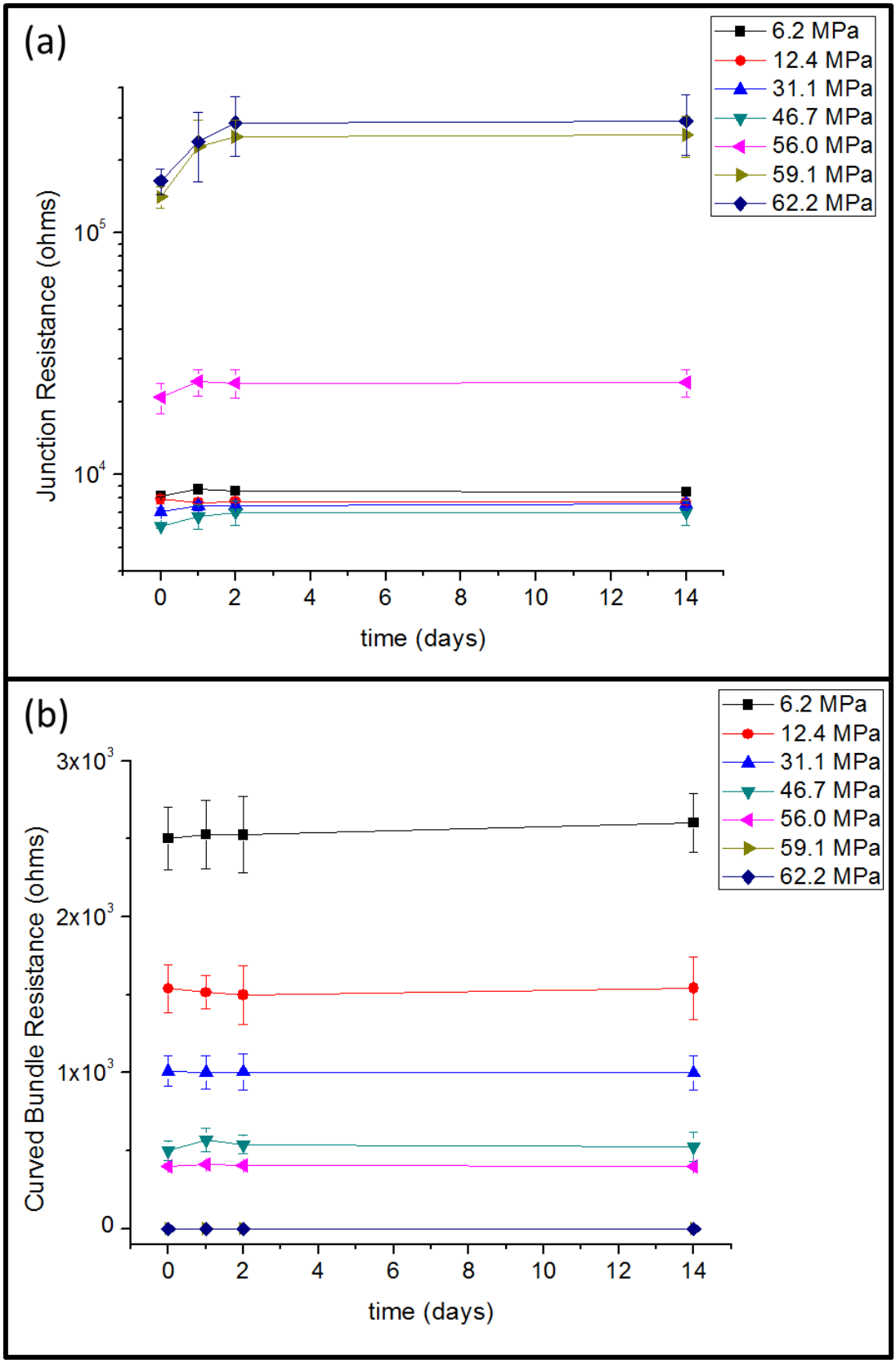

Figure 5.14: The impact of time (0-14 days) on the a) junction resistance and b) curved bundle resistance for all pressed samples.

5.3.5 Conclusions

The impact of compression by the addition of uniaxial pressure on the surface of a thin film MWNT-410 paper composite was determined by measuring the surface electrical properties as well as by imaging the surface structure of the films. Using the correct parameters during pressing (barrier material and pressure), it is possible to decrease both the junction resistance as well as the resistance of the curved bundles and form MWNT networks which are highly aligned and flattened. The easy alignment and flattening of the MWNT surfaces which decrease R_j provide a low cost method for making MWNT composite materials for advanced applications in electronics and energy storage.

5.4 Conclusions

The structures and properties of MWNT-paper in planes which show thin film conduction behavior can be easily varied through changes to the fabrication technique and through the addition of post-processing steps. 4 layers of MWNTs were deposited on the 410 paper surfaces from 1 mg/mL dispersions containing 10 mg/mL of three different surfactant materials: SDBS, CTAB, and Triton X-100. By varying only the surfactant in the dispersion being deposited, MWNT thin films could be formed with junction resistances spanning an order of magnitude. Under the right conditions, even bulk network formation could be detected at 4 layers. This study shows both the importance of the surfactant material in the initial interaction between the MWNTs and the paper as well as how the interactions between MWNT layers contribute to the overall resistance of the surface and junction resistance of the MWNT network.

The impact of the application of uniaxial pressure on the surface of a thin film MWNT-410 paper composite was determined by measuring the surface electrical properties as well as the surface structure of the films. Using the correct parameters during pressing (barrier material and pressure), it is possible to decrease both the junction resistance as well as the resistance of the curved bundles (and eventually eliminating their presence at high enough applied pressures). When pressure is applied to the film surface, two mechanisms result: (1) pressing and flattening of the MWNTs and (2) the cracking of the MWNT network. Both mechanisms are active during pressing as cracks form on the surface and the MWNTs are pushed into one another and flattened. Depending upon the dominant mechanism for each pressing condition, the junction resistance of the MWNT network can be decreased or increased. Regardless of the pressure used, curved bundle resistance decreases over the entire pressing range and with enough applied pressure goes to zero as the curvature is removed.

CHAPTER 6

MODIFYING THE PROPERTIES OF MWNT-PAPER COMPOSITES VIA ALTERATIONS TO THE DRYING METHODOLOGY

In the previous three chapters, the impacts of using vacuum filtration to dry MWNTs on and in the paper material using the layered fabrication methodology were determined. It was found that the bundle length to pore size ratio (L_b/d_p) coupled with the unidirectionality of drying under vacuum filtration determined the location of deposition and the composite properties. In this chapter, through changes in the composite fabrication process, the L_b/d_p constraints can be removed, and composites which are conductive across the surface or through the thickness regardless of pore size can be formed.

6.1 Introduction

The drying methodologies used in this chapter were adapted from Huang et al, shown in Figure 6.1 [53]. In that study, a paper material was coated with a polymer and CNT-containing dispersion using the Meyer-rod coating method [53, 75]. The coated paper was then placed into a heater and dried for 30 minutes. Figure 6.1a shows the placement of the coated paper in a 65°C heater. As the heater is the same temperature in all locations, there is no preferential direction for drying (described with the arrows pointing in all directions in the schematic). Figure 6.2a shows the placement of the paper in a 65°C heater on top of a ceramic heating board which is at 90°C. The authors suggested that the water is drawn toward the higher temperature heating board, leading to

unidirectional drying through the thickness of the paper. This was confirmed by measuring the thickness of the film surface: the thickness of the film made using a heating board was approximately 3x less than the film which was allowed to randomly dry in all directions [53].

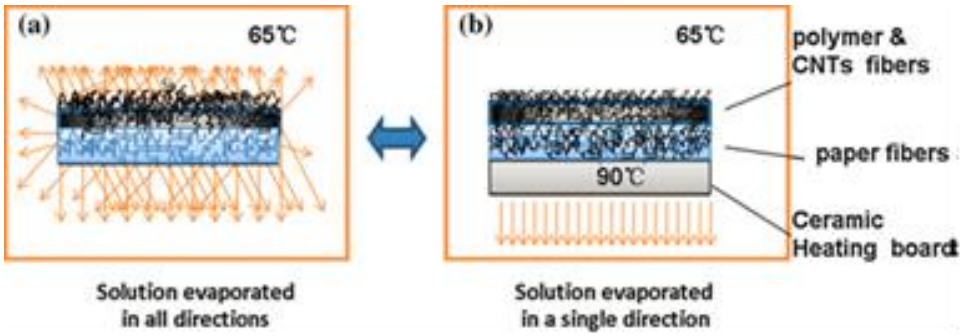

Figure 6.1: MWNT and polymer containing dispersions coated on paper and dried in a heater a) without a ceramic heating board, leading to randomized drying; and b) with a ceramic heating board, leading to unidirectional drying [53].

6.2 Experimental Details

1-20 layers of MWNTs were dropcast onto the different paper substrates (410 = 1 µm pore size; 413 = 5 µm pore size; 415 = 25 µm pore size) from the same 1 mg/mL aqueous dispersion (containing 10 mg/mL of SDBS) discussed in Chapter 2 and used to create the samples discussed in Chapters 3 and 4. However, while previously in this dissertation, each layer was deposited and dried using dropcast-vacuum filtration, in this section, the impact of two other drying methods on the properties of the in-plane and thru-plane of the multilayered composites will be discussed. A schematic of the three drying methods employed in this dissertation, including vacuum filtration, is shown in Figure 6.2.

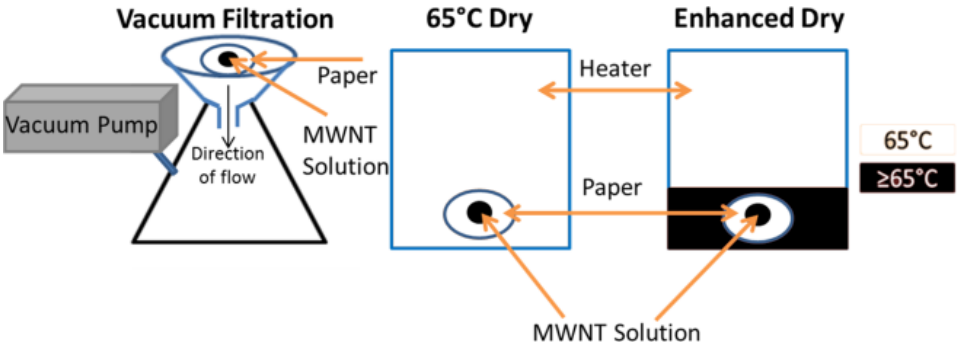

Figure 6.2: Schematics of drying techniques studied in this section: left) vacuum filtration; middle) 65ºC dry; right) enhanced dry where the heater was set to 65ºC and the base of the heater was kept at 95°C.

The other two drying methods presented in Figure 6.2 are heater-based methodologies. In 65°C dry (Figure 6.2 middle), the MWNT dispersion is dropcast onto the paper substrate and placed into a heater at 65°C for 10 minutes. The technique is repeated 1 to 20 times to form the multilayered composites. Enhanced dry (Figure 6.2 right) was adapted from the special dry technique described by Huang et al [53]. In enhanced dry, the heater was once again held at 65°C, but the heating board, placed at the bottom of the heater, can be set to any temperature above that. For this study, the heating board was warmed to 95°C, 30°C higher than the temperature of the furnace. The dispersion was dropcasted onto the paper which was sitting on the heating board and placed into the furnace for five minutes. The paper was removed from the heater and the heating board, and the heating board was reheated to 95°C before the next dropcast-dry step occurred. Once again, each dropcast-enhanced dry step corresponds to 1 deposited layer, and this process was repeated until the desired number of layers (1 to 20) was deposited. Such low dry times were chosen for this thesis compared to the previous study from which they were adapted in order to minimize the amount of penetration of the dispersion within the thickness of the paper to promote more surface located drying.

6.3 Results: Variations to In-Plane Properties

Low frequency AC in-plane resistance vs. the number of deposited layers as a function of drying methodology for each filter paper is plotted in Figure 6.3. A number of trends are apparent for each filter paper. On the 410 filter paper (1 μm pore size), as shown in Figure 6.3a, the data has the same shape, but there are clear differences between each drying method. In all cases, the resistance at 1 layer is ~10^5 Ω, indicating that a percolated network has already formed on the surface of these materials. For all layer numbers, regardless of layer number, the composites formed using 65°C dry have the highest in-plane resistance. The minimum resistance achieved is still an order of magnitude higher than it is for the other methods. The enhanced dry and vacuum filtered samples have in-plane properties which are more comparable. At 1 and 4 deposited layers, the vacuum filtered sample has a lower resistance than the enhanced dry sample; however, between 4 and 8 layers that behavior switches, and the enhanced dry composites have a lower resistance than the vacuum filtered composites of the same layer number. This trend holds until 20 deposited layers, at which point the resistance of the enhanced dry sample increases by a factor of 2, and the vacuum filtered sample again has a lower resistance value. This jump in resistance is seen across multiple sample sets made under the same conditions and is, therefore, not an anomaly to one data set.

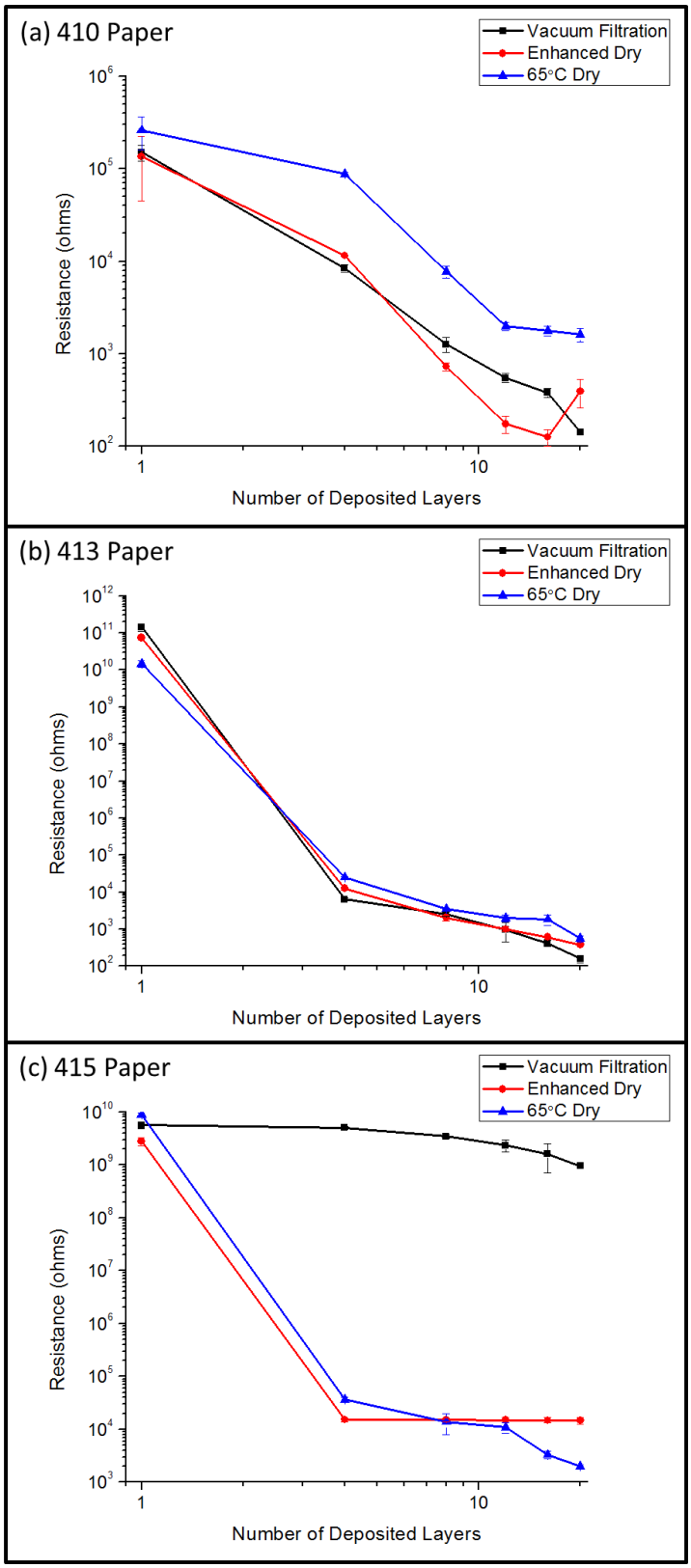

Figure 6.3: In-plane low frequency AC resistance vs. number of deposited layers for the multilayered composites fabricated on the a) 410, b) 413, and c) 415 filter papers using vacuum filtration (squares), enhanced dry (circles), and 65°C dry (triangles).

Figure 6.3b shows the in-plane resistance vs. number of deposited layers for the multilayered composites formed from each drying technique on the 413 filter paper (5 μm pore size). It seems that for this material, there is very little difference in the surface properties as a function of drying technique. At high layer numbers, the vacuum filtered sample set shows slightly lower resistance value than those made with the heater techniques. Additionally, for the heater techniques, the enhanced dry sample set also shows slightly better in-plane conduction than its counterpart formed by 65°C dry. However, the shape of the curves and the resistance values show only a small variation for each drying technique.

Figure 6.3c shows the in-plane resistance vs. number of deposited layers for the multilayered composites formed from each drying technique on the 415 filter paper (25 μm pore size). From these curves, a multitude of trends can be detected. First, for any layer number after 1, the heater drying method decreases the resistance of the surface by ~6 orders of magnitude as compared to the composites dried using vacuum filtration, indicating both surface deposition and conduction. Second, for films made with enhanced dry, after 4 layers, the in-plane electrical properties remain relatively constant with a resistance value slightly greater than 10^4 Ω. Lastly, while the in-plane properties of the 65°C dry samples have a higher resistance than the enhanced dry samples to begin with, after 8 layers, this trend reverses as the higher layer number samples show a continuous decrease in resistance all the way down to ~10^3 Ω.

Using the data present in Chapter 4, Section 2 as a guide, the electrical mechanisms present for the heater dried composite in-planes can also be detected and described using impedance spectroscopy. The frequency-explicit impedance plots for the

heater dried multilayered composites on the 410 filter paper are shown in Figure 6.4. Similar to the vacuum filtered composites (see Figures 4.2a,b), both the enhanced dry (Figure 6.4 top) and 65°C dry (Figure 6.4 bottom) sample sets show only two distinct in-plane behaviors, corresponding to thin film and bulk MWNT networks.

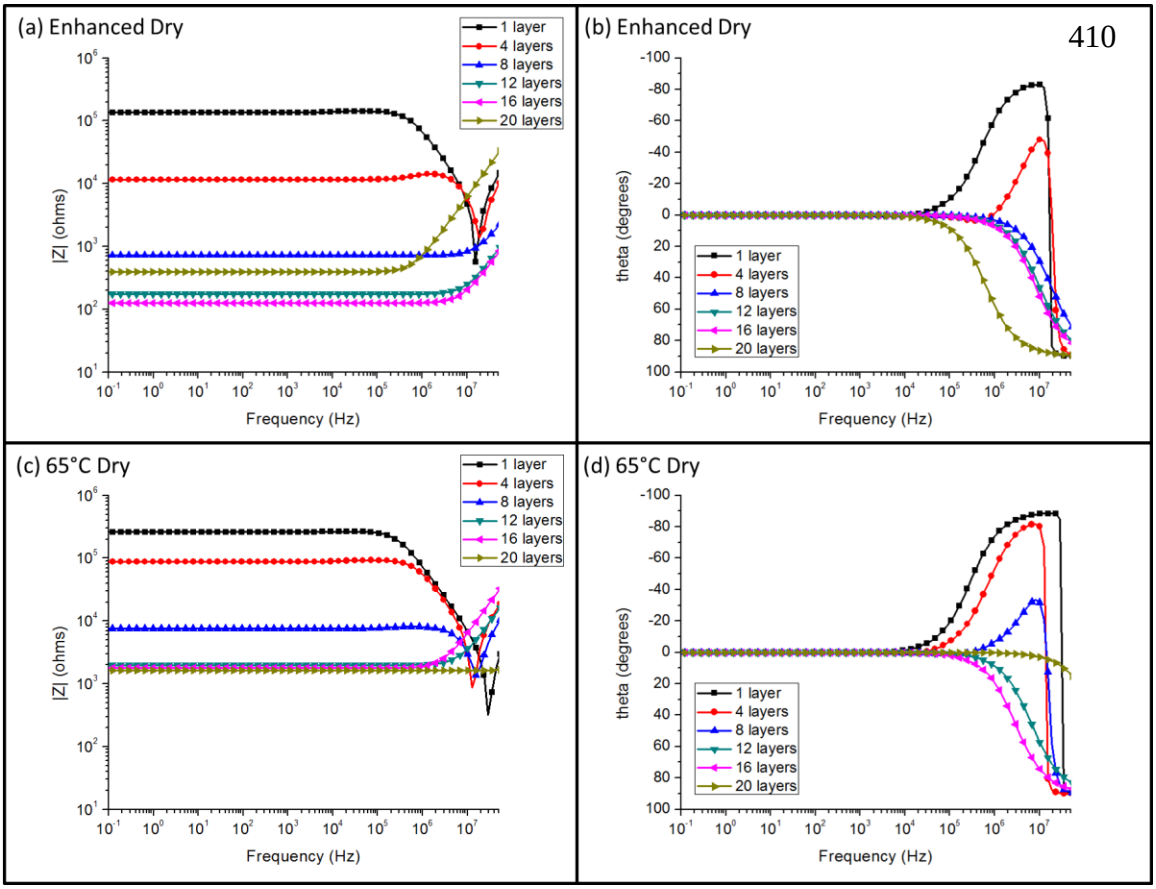

Figure 6.4: In-plane a) log(|Z|) vs. log(f) and b) θ vs. log(f) for MWNT-410 multilayered composite surfaces dried using enhanced dry and c) log(|Z)| vs. log(f) and d) θ vs. log(f) for MWNT-410 multilayered composite surfaces dried using 65°C dry.

For both unidirectional drying methodologies on the 410 filter paper (vacuum filtration and enhanced dry), the switch from thin film to bulk occurred at 8 deposited layers. When these surfaces are in the thin film regime, vacuum filtration leads to a lower junction resistance at the same layer number, and in the case of the 1 layer sample, a much smaller deviation from sample set to sample set. However, when these samples

move to bulk behavior, the resistance of the bulk surface of the enhanced dry sample is lower than the resistance of the bulk surface of the vacuum filtered sample of the same layer number (until 20 deposited layers). The 65°C dry sample set switches from thin film to bulk at 12 layers, further along during the deposition step than the other drying techniques.

Not surprisingly, the frequency-explicit impedance plots shown in Figure 6.5 for the heater dried multilayered composites formed on the 413 filter paper present nearly identically to the vacuum filtered samples (shown in Figures 4.2c,d). Only two differences arise when the heater dried techniques are compared to each other. One, all four impedance behaviors are detected for the 65°C dry sample set while only three are detected for the enhanced dry set (no transitional behavior). Two, the low frequency |Z| value of the bulk conducting samples is smaller for enhanced dry than it is for the comparable layer number for 65°C dry (12, 16, and 20 layers). For the 413 paper material, drying methodology has very little impact on the surface properties.

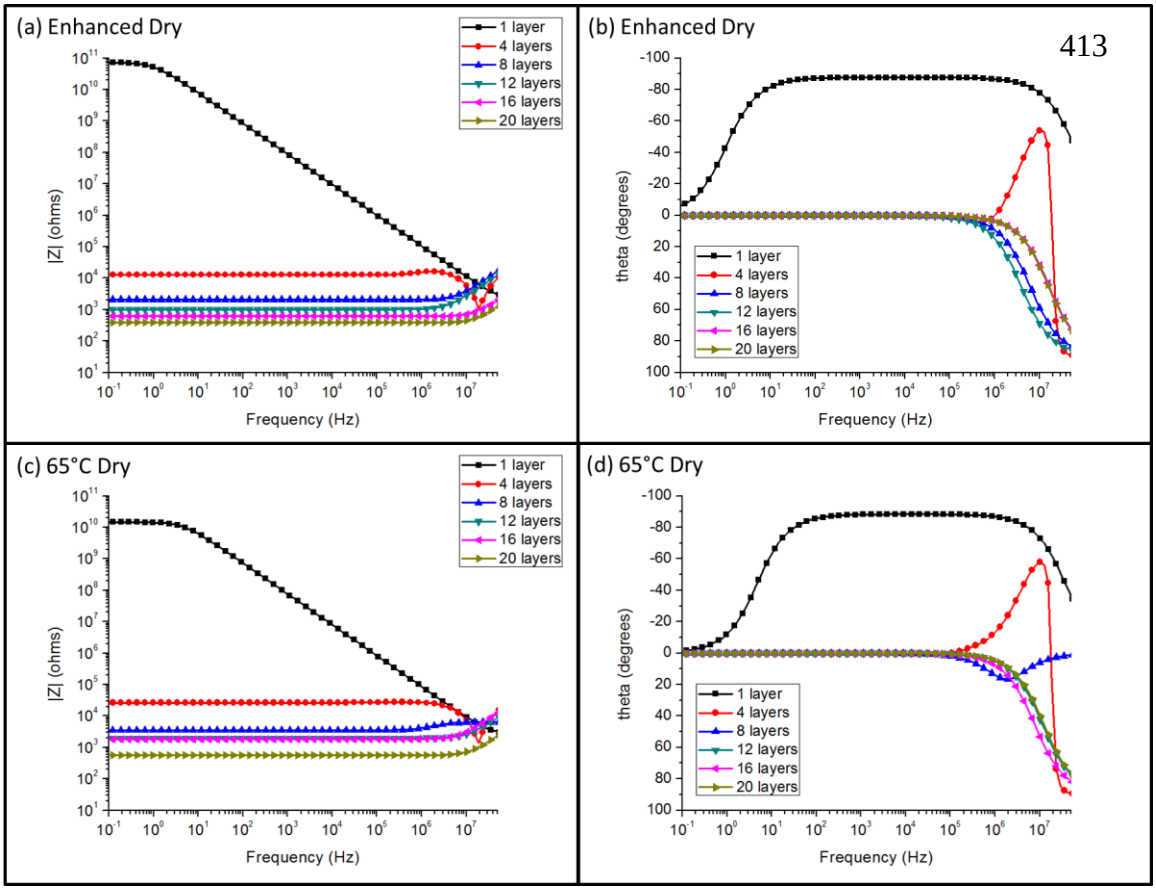

Figure 6.5: In-Plane a) log(|Z|) vs. log(f) and b) θ vs. log(f) for MWNT-413 multilayered composite surfaces dried using enhanced dry and c) log(|Z|) vs. log(f) and d) θ vs. log(f) for MWNT-413 multilayered composite surfaces dried using 65°C dry.

The frequency explicit impedance plots for the multilayered composites formed using the heater drying techniques on the 415 filter paper are shown in Figure 6.6. Figures 6.6a and 6.6b describe the in-plane behaviors given by the enhanced dry composite set. Only two different impedance behaviors are detected: paper-dominated electrical transport at 1 deposited layer and thin film-dominated for 4+ deposited layers. For samples created with 4 or more deposited layers, the impedance behaviors overlap over the entire frequency range. From curve fitting, the samples exhibiting thin film behavior have an R_b = 900 Ω ± 1.87 Ω, R_j = 14030 Ω ± 230 Ω, and R_{cb} = 9430 Ω ± 290 Ω. There is a very small spread in data between samples.

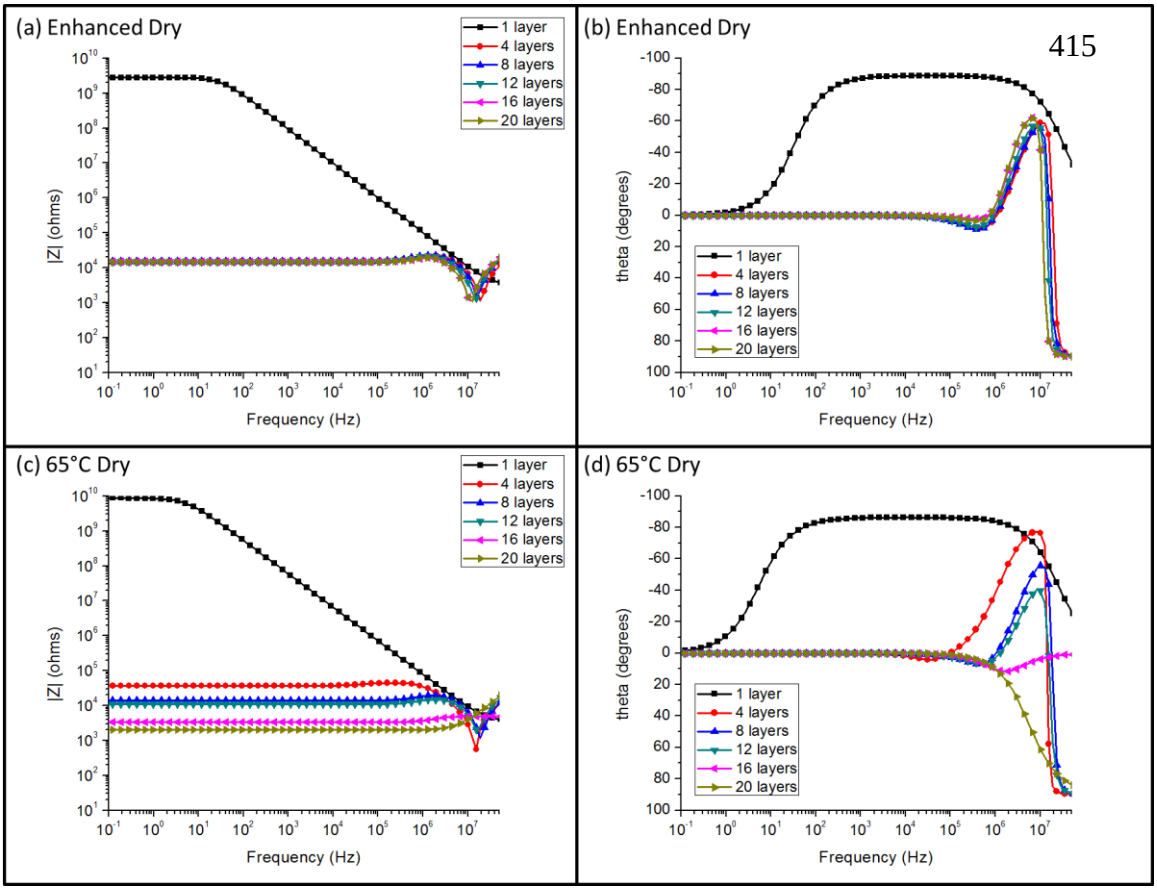

Figure 6.6: In-plane a) log(|Z|) vs. log(f) and b) θ vs. log(f) for MWNT-415 multilayered composite surfaces dried using enhanced dry and c) log(|Z|) vs. log(f) and d) θ vs. log(f) for MWNT-415 multilayered composite surfaces dried using 65°C dry.

The constant properties of the enhanced dry composites after 4 deposited layers suggests that the unidirectionality of the drying method, while not as extreme as vacuum filtration, still inhibits surface deposition on the large pore size paper. Figure 6.7 shows a low and a high magnification image of the 12 layered MWNT-415 composite formed using enhanced dry. At low magnifications (Figure 6.7a), it is apparent that the paper pores are still uncovered. However, the higher magnification image shows a fairly dense MWNT network on the paper surface (Figure 6.7b). An interconnected surface is formed, but never covers the paper pores, likely resulting in increased thru-plane MWNT deposition.

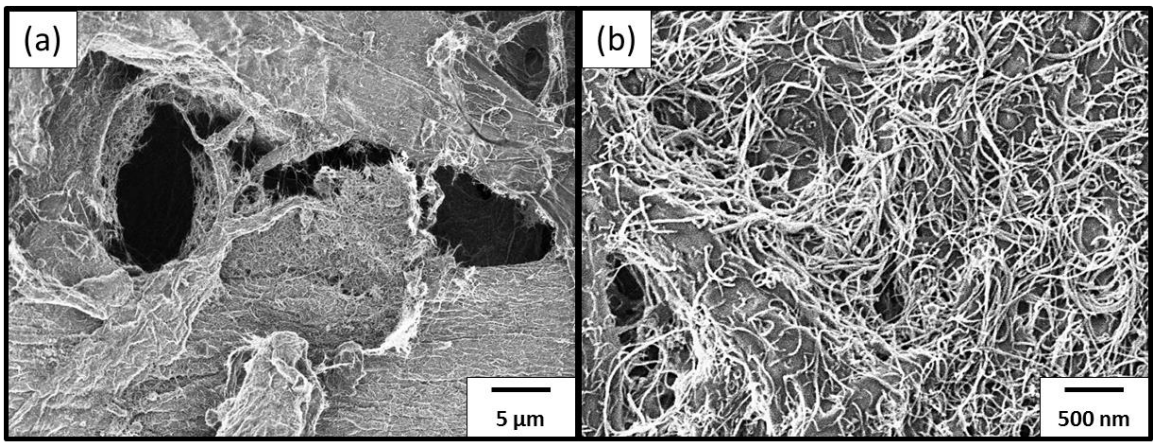

Figure 6.7: a) Low and b) high magnification SEM images of the 12 layered MWNT-415 paper composite material formed using the enhanced dry technique.

In comparison, the frequency explicit impedance plots (Figure 6.6c: log(|Z|) vs. log(f), Figure 6.6d: θ vs. log(f)) which describe the in-plane behavior of the 65°C dry composite series on the 415 filter paper show all four in-plane impedance behaviors discussed in Chapter 4, Section 2. At 1 layer, the in-plane response shows paper-dominated electrical transport. For layer number $4 \leq L < 16$, the in-plane shows MWNT thin film-dominated impedance behavior. At 16 layers, the thin film to bulk transitional behavior is measured for the in-plane. Finally, at 20 layers, bulk MWNT behavior is active. Since the resistance of the 65°C dry composites continues to drop over the entire deposited layer number range, surface deposition occurs continuously as MWNT content is increased. The randomness of the drying method to form these materials promotes rather than hinders surface deposition.

6.4 Results: Variations to Thru-Plane Properties

Since 65°C promotes random drying, the thru-plane propertiess of the composites made with this technique, regardless of the paper pore size, show very little MWNT deposition. For this reason, only thru-plane properties of the composites made using

enhanced dry will be compared to those which arise due to vacuum filtration in this section.

Thru-plane resistance vs. the number of deposited layers for the multilayered composites formed by vacuum filtration and enhanced dry on each filter paper is plotted in Figure 6.8. Regardless of the paper pore size, enhanced drying promotes internal deposition, and resistance continually decreases with an increased number of deposited layers. In fact, for all papers, the enhanced dry samples always have a lower resistance at the same layer number value than their corresponding vacuum filtered sample. This is especially true for the 410 and 415 filter papers, shown in Figures 6.8a and 6.8c, respectively. By 20 deposited layers, the resistance of the thru-plane created by enhanced dry for both the 410 and 415 filter papers is two orders of magnitude lower than the resistance of the thru-plane deposited by vacuum filtration. The thru-plane resistances measured for the 1 to 20 layered MWNT-415 composites formed via enhanced dry are the lowest measured for any deposition condition studied in this thesis (decreasing from $1.57 \times 10^5\ \Omega \pm 3.3 \times 10^4\ \Omega$ to $300\ \Omega \pm 150\ \Omega$ from 1 to 20 deposited layers).

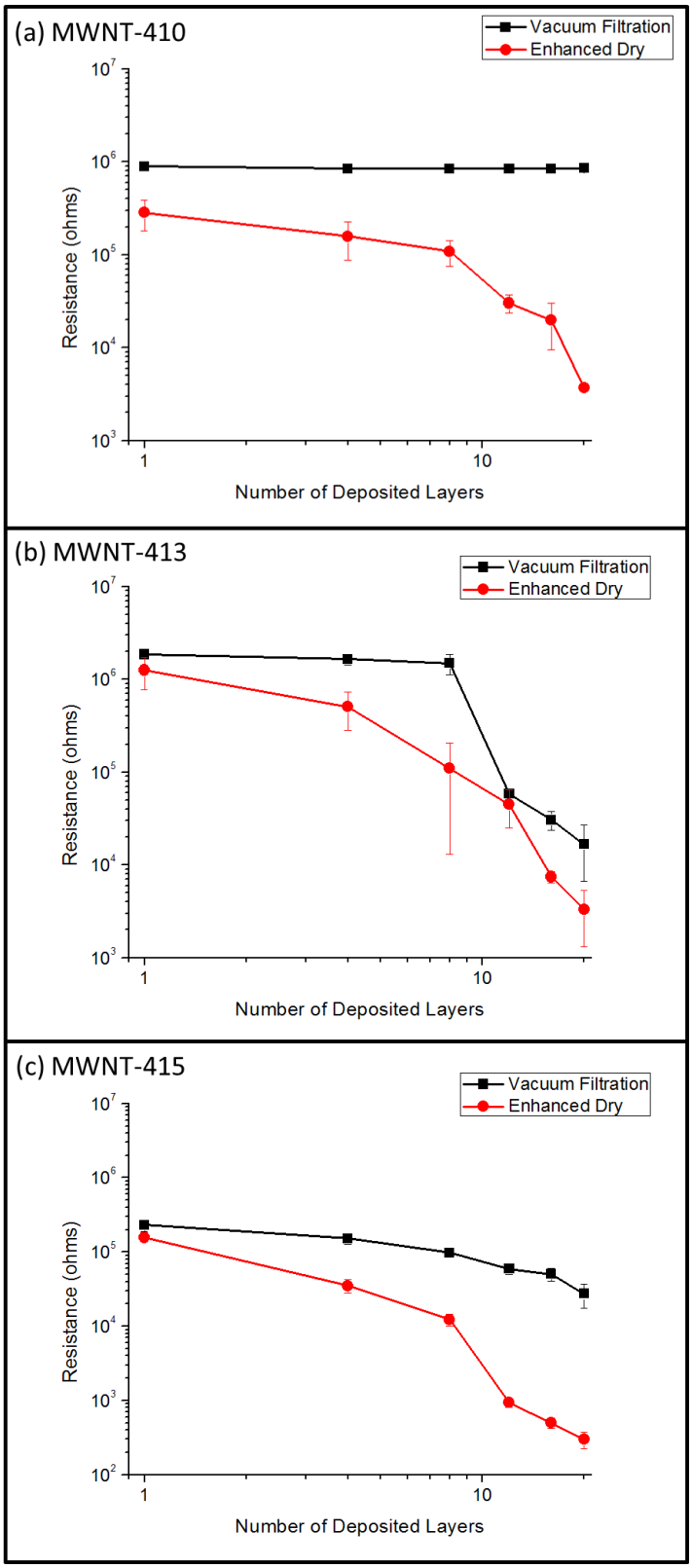

Figure 6.8: Thru-plane resistance vs. number of deposited layers for the multilayered composites fabricated on the a) 410, b) 413, and c) 415 filter papers using vacuum filtration (squares) and enhanced dry (circles).

Inspecting the thru-plane properties of these materials helps explain the low bulk surface resistance of the enhanced dry films on the 410 filter paper. The MWNT-410 enhanced dry sample set actually shows continuous deposition in the thru-plane. In contrast, the vacuum filtered sample set measured a nearly constant resistance value for all layer numbers. The MWNT surface network covered the pores and impeded further internal deposition. For the enhanced dry composites, the less rigid in-plane MWNT network allows for MWNTs to continually penetrate the paper pores throughout the deposition process. This leads to an increasingly conductive thru-plane as well as better bulk properties on the surface of the composite material. The enhanced dry technique is not without its challenges, however. The errors for the thru-plane resistance of each sample and overall sample set are considerably higher than the errors measured for the samples made by vacuum filtration. The less rigid surface film along with the lower degree of unidirectionality results in a larger variation in thru-plane deposition, and in return, a larger variation in thru-plane resistance.

Since the enhanced dry composite thru-plane resistance continually decreases with increased MWNT loading (layer number), it is unsurprising that the impedance behavior for all of the samples is the same. In all cases, the impedance curve for the thru-plane is fit with a single $(R\text{-}CPE)_p$, just like the MWNT-415 composites dried via vacuum filtration.

6.5 Issues with Techniques: Surface Homogeneity

Most of the DC and impedance measurements reported for the in-plane of all of these materials were done nearer to the center of the composite than the edge. While

multiple tests were done for each composite in different locations, the average position of the probes was still nearer the sample center than the edge. For a better understanding of the properties of the surfaces, the full range of the sample should be measured especially since the different drying methods result in a different degree of surface deposition. As the average and standard deviations for the more central parts of the composite are already known, surface homogeneity will be determined by measuring the properties of the sample from the sample center to the edge. Surface homogeneity will be quantified by dividing the diameter of the film which is within one standard deviation of the average sample resistance (quality film diameter) from the full diameter of the surface. The closer to 1 this value is, the more homogeneous the sample surface is.

When the dispersion is dropcasted onto the paper, the weight and wetness of the dispersion can cause the paper to buckle and pull the dispersion closer or push the dispersion away from the center of the dropcasting site. This leads to a macroscopically visible inner shell (high content of MWNT) and outer ring (low content of MWNT). Schematics describing the inner and outer shell with varying degrees of quality (decreasing from left to right) are shown in Figure 6.9. On the left of Figure 6.9 is a film with no outer ring and the film diameter is equal to the quality film diameter (surface homogeneity = 1). In the middle of Figure 6.9 is a film with a small outer ring where the total film diameter is only slightly larger than the quality film diameter (surface homogeneity < 1). On the right of Figure 6.9 shows a film where the outer ring is very large and the quality film diameter is much smaller than the total diameter of the film (surface homogeneity <<< 1).

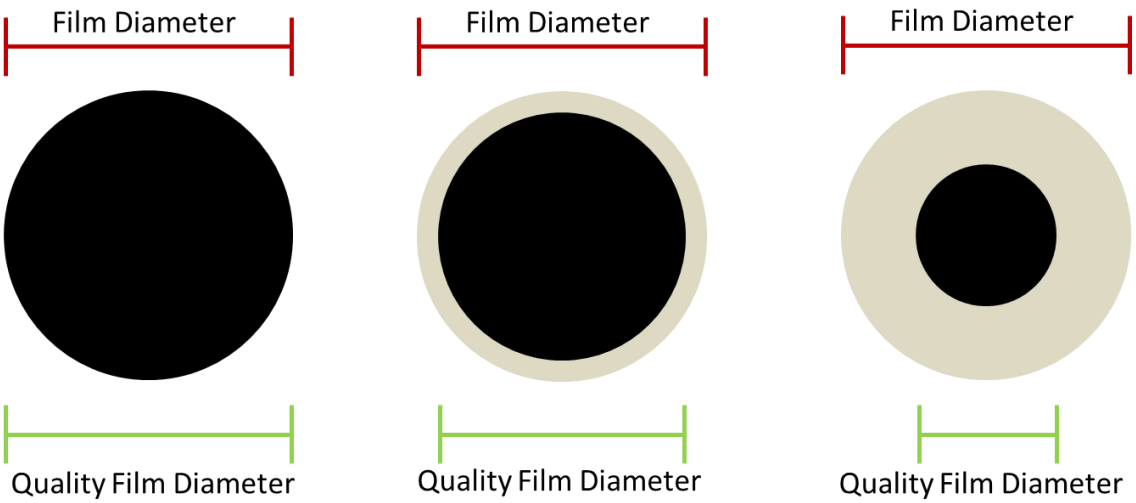

Figure 6.9: Inner shell of high MWNT deposition (black) surrounded by an outer shell of lesser MWNT deposition (light). As the size of the outer shell increases, the homogeneity of the in-plane properties decreases. Homogeneity of the MWNT-paper surface decreases from left to right in this Figure.

Figure 6.10 shows the quality film diameter/total film diameter vs. the number of deposited layers for the different drying methods on the 413 (a) and 415 (b) papers. The 410 papers are not presented in graphical form as the surfaces of these materials showed consistent properties (between 0.96 and 1 with minimal error <0.005) for all deposited layer numbers and all drying methods.

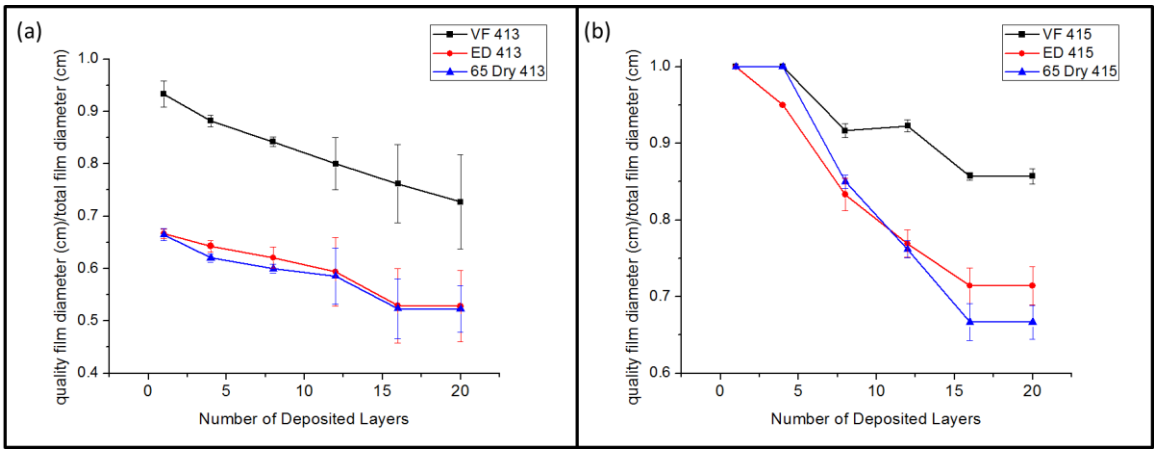

Figure 6.10: Surface homogeneity measured by dividing the quality film diameter by the total film diameter plotted vs. the number of deposited layers for the composites made on the (a) 413 and (b) 415 papers using vacuum filtration (squares), enhanced dry (circles), and 65°C dry (triangles).

From Figure 6.10a, it is immediately apparent that using the heater to dry the sample surfaces results in a much lower homogeneity than using vacuum filtration. The 413 paper is the least robust of the 3 filter papers. While there is a force pulling the paper flat during vacuum filtration, there is still enough localized buckling that this type of film forms, although to a much lower degree than the heater dried films. While weights were used to hold the paper flat in the heater, they needed to be far enough away from the center of the composite so as to not influence the drying: the quality film diameter is much lower from start to finish for these films. By 20 deposited layers, only slightly higher than 50% of the diameter of the surfaces formed using heater drying methods has properties within one standard deviation.

From Figure 6.10b, the heater drying also leads to less homogeneity on the surface of the 415 paper; however, a large portion of the surfaces are still within one standard deviation of the resistance of the sample. The 415 paper is thicker than the 413 paper and can hold up to wet deposition better than the 413 paper with regards to localized buckling, especially under vacuum filtration. For the 415 paper composites made under vacuum filtration, the homogeneity decreases from 1 to 0.85 from 1 to 20 deposited layers. For the composites made under heating drying, the homogeneity drops to a minimum of 0.67 under the 65°C dry conditions and 0.71 under the enhanced dry conditions.

6.6 Conclusions

It is possible to alter the location of deposition of the MWNT material, and ultimately the properties of the composite, by changing the drying technique used to form

the composite. Using heater drying instead of vacuum filtration removes the bundle length to pore size ratio constraints discussed in Chapters 3 and 4; instead, deposition can occur on any surface or within any paper thickness regardless of the pore size of the paper backbone. Through the change of one step in the fabrication of the MWNT-paper networks, entirely new composite materials and properties can be formed even when the chemistry of those materials are constant.

For the 415 paper, using heater drying allows for an interconnected MWNT network to form across the surface rather than all material being pulled into the paper backbone. In fact, increasing the randomness of the drying method can result in even bulk surfaces being formed on the surface of the 415 paper. For the 413 paper, there are no real differences between the surfaces formed under the different drying methodologies: the impedance behaviors and electrical resistance are similar for each layer when comparing different composite sets. However, these samples also have the least homogeneous surfaces due to paper buckling which occurs upon wet deposition of the MWNT material. Finally, for the 410 paper, unidirectionality in drying always results in a lower resistance than randomized drying. For thin film networks, vacuum filtration-aided drying results in a better MWNT-MWNT junction resistance than the heater-based enhanced drying and a lower overall film resistance. For bulk networks, enhanced drying leads to a lower bulk resistance than vacuum filtration. In addition, continuous deposition occurs in the 410 thru-plane for the heater dried films, resulting in resistances as low as ~$3x10^3$ Ω to occur through the paper thickness, even though the tubes are still much longer than the pore size of the paper. The removal of the vacuum force forms a

less rigid MWNT surface structure on all of the paper materials which allows for a large degree of MWNT penetration into the thickness of the paper during drying.

CHAPTER 7

MICROSTRUCTURE-RESISTANCE CORRELATIONS IN CARBON NANOTUBE NETWORK SURFACES: PREDICTING ELECTRICAL BEHAVIOR USING A DUAL LENGTH SCALE APPROACH

7.1 Introduction

Stereology combines geometric analysis with statistical sampling in order to quantify the structure of 3D materials using 2D cross-sections. 3D structural properties, including grain size and shape, can be extracted from 2D images of the cross-sections of materials [76]. For example, image analysis has been done to estimate parameters such as the volume fraction of inclusions or pores in 3D materials (bulk materials) from the 2D renderings obtained using low magnification optical microscopy (OM) [77]. In recent years along with the advent of nanomaterials and their unique architectures, techniques derived from traditional stereology have also been applied to the analysis of 2D microstructures. Images produced from high magnification imaging techniques such as SEM and AFM have been used to determine structural parameters for thin films and nanocomposite materials. These parameters include the size distribution of particles and second phases as well as area fraction at the microscale [78-81]. Important structural information can be derived at both length scales.

In this section, the analysis of the structure of the surfaces (in-plane) of the MWNT-paper materials is taken a step further. Rather than just measuring structural information using stereological techniques, the MWNT-paper surfaces will be quantified

by measuring macrostructural and microstructural densities simultaneously. These two densities will be compared directly to the measured electronic properties (both DC and AC) in order to determine the MWNT coverage and arrangements required to measure certain resistances and impedance behaviors.

7.2 Experimental Details

Images of the surfaces of the MWNT-paper composites were obtained using both optical microscopy (OM) and scanning electron microscopy (SEM) in order to determine overall film coverage and MWNT network density, respectively. Optical photomicrographs of the topmost layer of the composites were taken at 10x magnification with the light source positioned above the samples. The 10x magnification was chosen as it allowed for a fairly large region to be imaged in focus, which can be difficult to obtain given the surface roughness and height disparity of the paper fibers. In-lens SEM images of the MWNT networks were taken at 20,000x magnification as this magnification provided a focus on the MWNT network while still being able to observe the substrate material. For many of the insulating samples, this magnification was the maximum that could be achieved without charging taking over the image.

From the OM and SEM images, macrodensity and microdensity of the MWNT surfaces for the composites were calculated using a dual scale image analysis technique. In this technique, three images with a resolution of 1200 dpi were taken of each sample using both OM and SEM. Next, the pixels of each image were designated as either part of the substrate or as part of the film. After the pixel assignment process, the overall image was converted into black and white for simplicity. Using an in-house developed program

which counts pixels based on their hexadecimal color code, the number of pixels corresponding to the MWNTs was measured.

Macrodensity was estimated by counting the number of pixels corresponding to the MWNTs in the 10x optical images and dividing that by the total number of pixels in the image. Similarly, the microdensity was determined from the SEM images by counting the number of pixels which were associated with the MWNT network. The macrodensities and microdensities presented in this section are the average value from the three different surface images. For electrical property characterization and comparison to the densities, DC resistance and AC impedance were measured as reported in the previous Chapters.

In order to study the impact of layer number on the surface densities and the resulting electronic behaviors, the 1-20 layered MWNT-paper (410, 413, and 415) composites discussed in Chapters 3 and 4 were used. Samples made using the three different drying techniques and presented in Chapter 6 and shown in Figure 6.2 were also quantified.4 layers were deposited on the different paper substrates using the different drying methods since this layer number was shown to exhibit MWNT thin film behavior for majority of these processing conditions [5]. In addition, the MWNT thin films created using the layer-by-layer methodology by varying surfactant charge described in Chapter 5, Section 2 and shown schematically in Figure 5.4 were also quantified by this technique.

7.3 Results

7.3.1 Multilayered Samples

Figure 7.1 shows one of the original (left) and its digitized (right) macroscale OM image used to quantify 1-20 layered MWNT-413 surfaces. For the digitized images, white pixels correspond to the regions of the paper backbone while the colored/darkened pixels correspond to the MWNTs. As the number of deposited layers increase on the 413 paper, it can be seen that the number of pixels corresponding to MWNTs increases from 0.03% at 1 layer to 93.07% at 20 layers. The interconnectivity of the MWNTs over the imaged surface also increases with layer number. At 1 layer (Figure 7.1a and 7.1b), a few, disconnected dark spots are seen, but the image is overwhelmingly white in color, indicative of very little long range surface deposition. By 20 layers (Figure 7.1k and 7.1l), nearly the entire surface is coated in MWNTs, and interconnection between the MWNT regions is exhibited from both left to right as well as from top to bottom.

A similar trend is also observed at the microscale for these films which can be seen in Figure 7.2. For the digitized SEM images, black pixels correspond to the paper backbone while the colored/lightened pixels correspond to the MWNT network. At 1-layer (Figure 7.2a and 7.2b), the MWNTs are sporadically located across the microsurface which results in a surface density of 11.81%. At 4 deposited layers (Figure 7.2c and 7.2d), the microdensity rises dramatically to 68.19%. The MWNT network becomes increasingly interconnected with increasing layer number, and the microdensity continues to climb until 12 layers. Beyond 12 layers, the microdensity remains relatively constant, varying only from 76.14% at 12 layers to 77.78% at 20 layers.

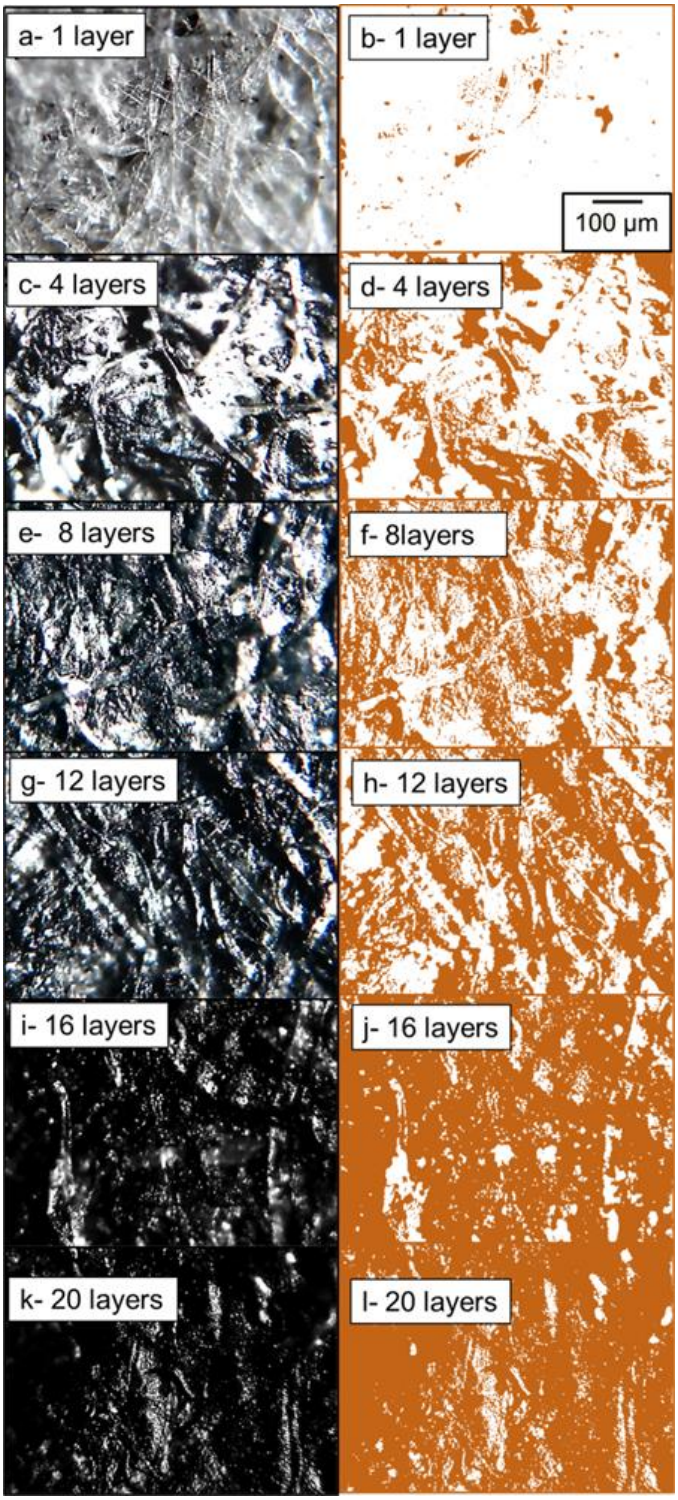

Figure 7.1: Original (left) and digitized (right) optical microscopy images used to determine macroscale surface coverage for the layered MWNT-413 composites made with a,b) 1 layer; c,d) 4 layers; e,f) 8 layers; g,h) 12 layers, i,j) 16 layers; and k,l) 20 layers of MWNTs. For the digitized images, white pixels correspond to the paper backbone while the dark pixels correspond to the MWNTs.

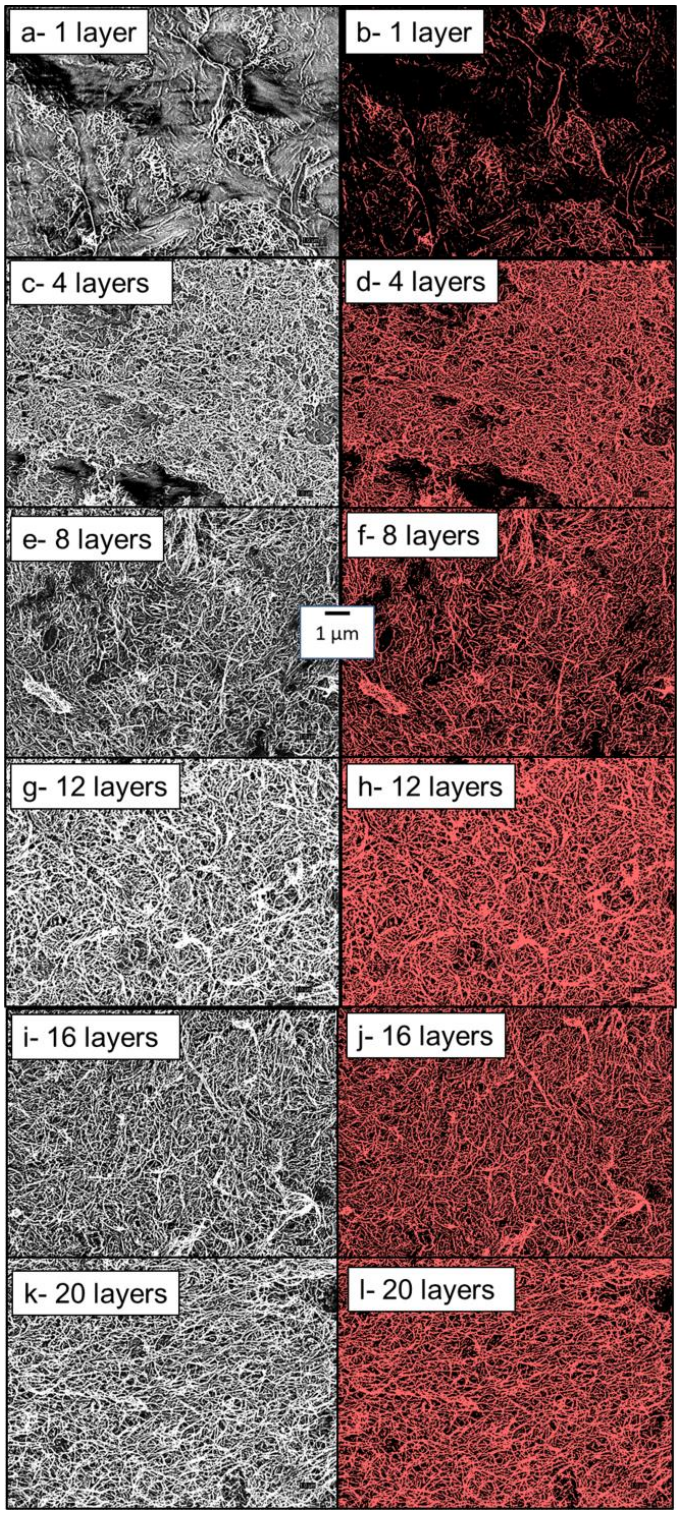

Figure 7.2: Original (left) and digitized (right) SEM images used to determine microscale surface coverage for the layered MWNT-413 composites made with a,b) 1 layer; c,d) 4 layers; e,f) 8 layers; g,h) 12 layers, i,j) 16 layers; and k,l) 20 layers of MWNTs. For the digitized images, black pixels correspond to the paper backbone while the colored pixels correspond to the MWNTs.

Figure 7.3 shows the digitized optical micrographs (left) and SEM images (right) for the 1-20 layered MWNT-410 composite surfaces. From the optical micrographs, it can be seen that, unlike the MWNT-413 composites, the MWNTs on the 410 paper interconnect across the surface in all directions at all layer numbers. In addition, the surface coverage of the MWNT network gradually increases with layer number starting at 53.5% at 1 deposited layer (Figure 7.3a) and ending at 94.6% at 20 deposited layers (Figure 7.3j).

The SEM images describing the microdensity of the MWNT-410 composite surfaces (Figure 7.3 right) show both how the MWNT surface evolves as well as how dense the MWNT networks are. At 1 deposited layer, MWNT network formation occurs on only the paper fibers (Figure 7.3b). The networks which form show a density gradient: the network is highly dense along the pore edges and decreases in density as it moves away from the pore edge. The dense MWNT network on the fiber surfaces are interconnected by a low density MWNT network which forms on the smaller paper fibers which span across open voids on the paper surface. A microdensity of 41.2% is measured for the 1 layer MWNT-410 surface. At 4 deposited layers, shown in Figure 7.3d, the MWNT network is dense and spans the entire area of the image. The density of the MWNT network increases to 71.1%. At 8 deposited layers and beyond, the microstructure remains relatively unchanged with increasing number of deposited layers, and the value of microdensity measures around 77%.

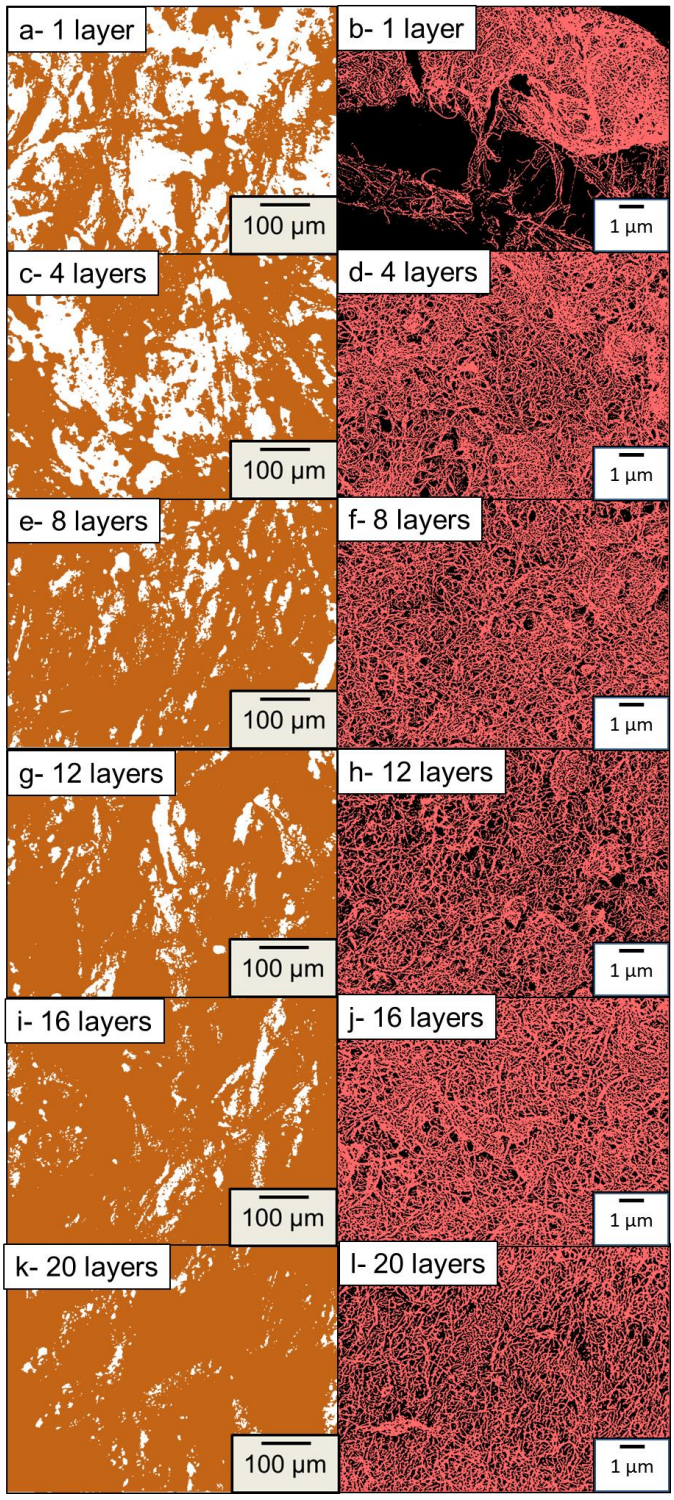

Figure 7.3: Digitized OM (left) and SEM (right) images used to determine macroscale and microscale surface coverage, respectively, for the layered MWNT-410 composites made with a,b) 1 layer; c,d) 4 layers; e,f) 8 layers; g,h) 12 layers, i,j) 16 layers; and k,l) 20 layers of MWNTs.

Figure 7.4 shows the digitized optical micrographs (left) and SEM images (right) for the 1-20 layered MWNT-415 composite surfaces. From the optical micrographs, macroscale MWNT coverage is extremely low and presents as tiny, disconnected regions. While the density of the disconnected regions increases with increasing layer number, full interconnection across the surface in any direction never occurs. In fact, there is very little interconnection of the deposited regions at all. The macrodensity for the 1 layer MWNT-415 composite surface, shown in Figure 7.4a, is so close to zero that an image could not be obtained in which the MWNT pockets were large enough to be detected. From 4 to 20 deposited layers, the macrodensity increases from 0.39% to 3.25%.

Only the 12, 16, and 20 layered MWNT-415 surfaces could be imaged under SEM at 20,000x magnification (Figures 7.4h,j,l). The large pore size coupled with no to low surface deposition (as discussed in Chapters 3 and 4) inhibited imaging until 12 deposited layers. At 12 deposited layers (Figure 7.4h), the MWNT network density is very low (8.85%) and individual bundles of MWNTs are found randomly across the surface. With increasing layer number, the individual bundles begin to interconnect as shown in Figures 7.4j,l; however, the networks are low density and, from their corresponding macrodensity images in Figures 7.4i,k, are scattered on the paper.

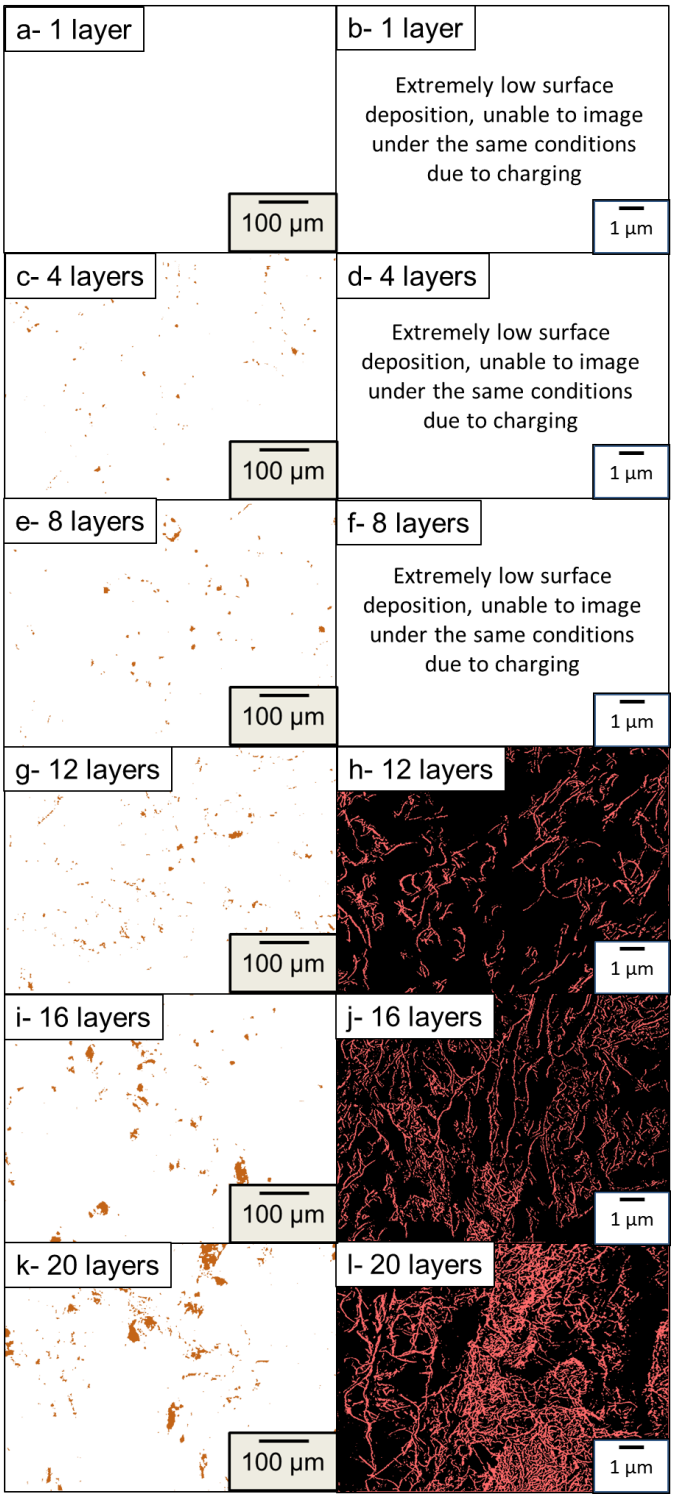

Figure 7.4: Digitized OM (left) and SEM (right) images used to determine macroscale and microscale surface coverage, respectively, for the multilayered MWNT-415 composites made with a,b) 1 layer; c,d) 4 layers; e,f) 8 layers; g,h) 12 layers, i,j) 16 layers; and k,l) 20 layers of MWNTs.

Table 7.1 contains the averaged DC resistance, macrodensity, and microdensity values for the multilayered MWNT-paper composite surfaces made using vacuum filtration. The measured DC resistance values and the densities of the surfaces are inversely related. This holds true both for each composite subset as well as across the entire sample set. The relationships between the number of deposited layers and the densities of the multilayered in-plane surfaces along with their corresponding resistance values are plotted in Figure 7.5 for each paper backbone.

Table 7.1: DC Resistance, Macrodensity, and Microdensity for the multilayered MWNT-paper composites obtained by vacuum filtration.

Number of Layers	DC Resistance (kΩ)	Macrodensity %	Microdensity %
410			
1	$1.50x10^{3} \pm 3.23x10^{2}$	53.5 ± 3.08	41.2 ± 7.08
4	8.43 ± 0.75	67.5 ± 1.11	71.1 ± 3.54
8	1.27 ± 0.24	87.8 ± 4.50	75.7 ± 1.15
12	0.55 ± 0.06	90.5 ± 1.24	76.7 ± 2.22
16	0.38 ± 0.04	92.5 ± 0.99	77.1 ± 1.09
20	0.14 ± 0.01	94.6 ± 1.01	77.4 ± 0.98
413			
1	$1.42x10^{8} \pm 3.48x10^{7}$	0.03 ± NA	11.8 ± NA
4	6.57 ± 0.61	72.0 ± 1.32	68.2 ± 2.33
8	2.53 ± 0.35	75.2 ± 5.66	74.9 ± 2.98
12	0.97 ± 0.52	90.9 ± 3.48	76.1 ± 0.87
16	0.42 ± 0.08	91.9 ± 1.67	77.7 ± 0.93
20	0.16 ± 0.04	93.1 ± 0.98	77.8 ± 1.11
415			
1	$5.61x10^{6} \pm 8.22x10^{5}$	NA	NA
4	$5.00x10^{6} \pm 3.00x10^{5}$	0.38 ± 0.12	NA
8	$3.43x10^{6} \pm 2.83x10^{5}$	0.55 ± 0.33	NA
12	$2.34x10^{6} \pm 6.43x10^{5}$	1.12 ± 0.91	8.85 ± 2.55
16	$1.61x10^{6} \pm 9.05x10^{5}$	1.73 ± 0.62	13.61 ± 1.79
20	$0.95x10^{6} \pm 0.06x10^{5}$	3.25 ± 1.12	24.75 ± 0.86

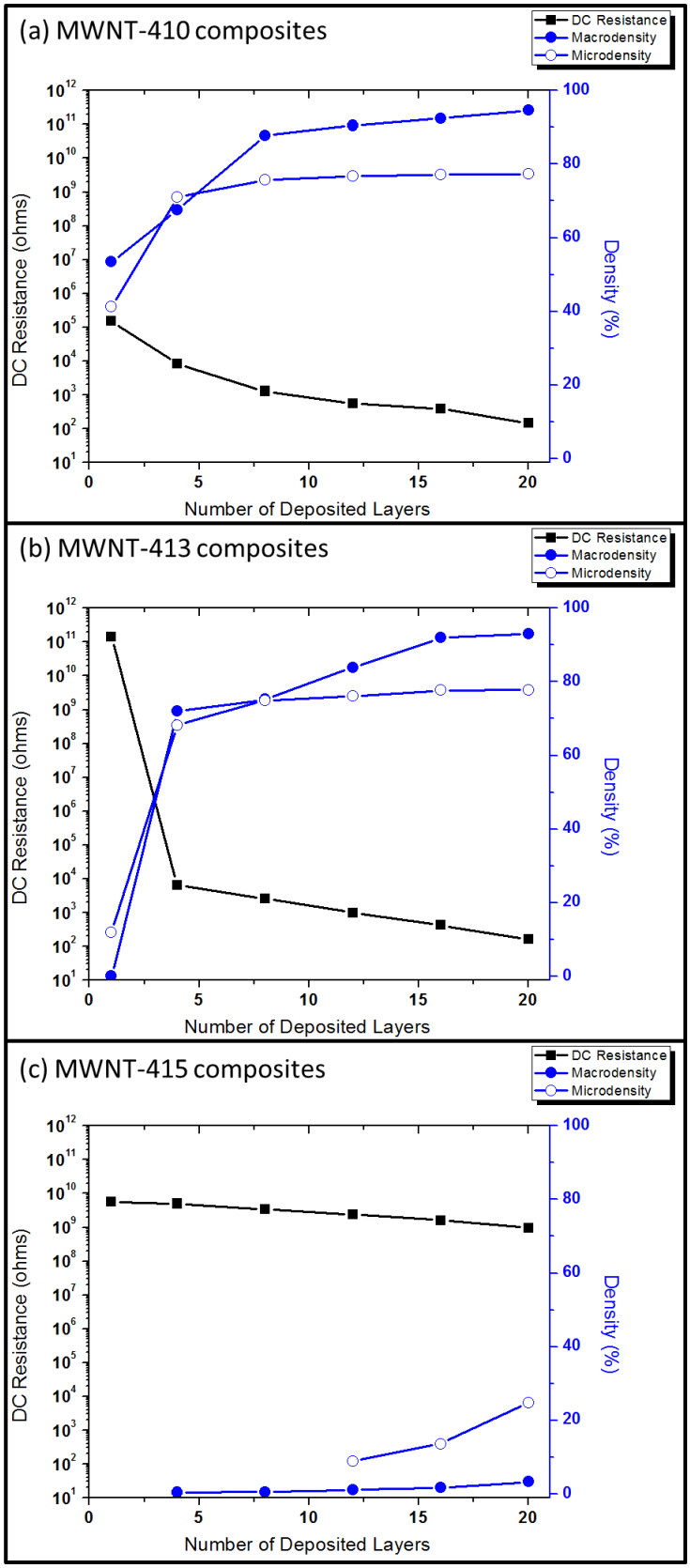

Figure 7.5: DC Resistance and Densities vs. Number of Deposited Layers for the layered a) MWNT-410; b) MWNT-413; and c) MWNT-415 composite sets.

7.3.2 Thin Film Samples: Variation in Drying Method

As was discussed in Chapter 6, a variety of drying methodologies can be used to create the composites. 4 layers were deposited and quantified on the three different papers using vacuum filtration, enhanced dry, and 65°C dry as thin film behavior was measured for the majority of these samples. Figure 7.6 shows the digitized OM (top) and the SEM (bottom) images for the 4 layered MWNT-410 composite surfaces dried using a,d) vacuum filtration; b,e) enhanced dry; and c,f) 65°C dry.

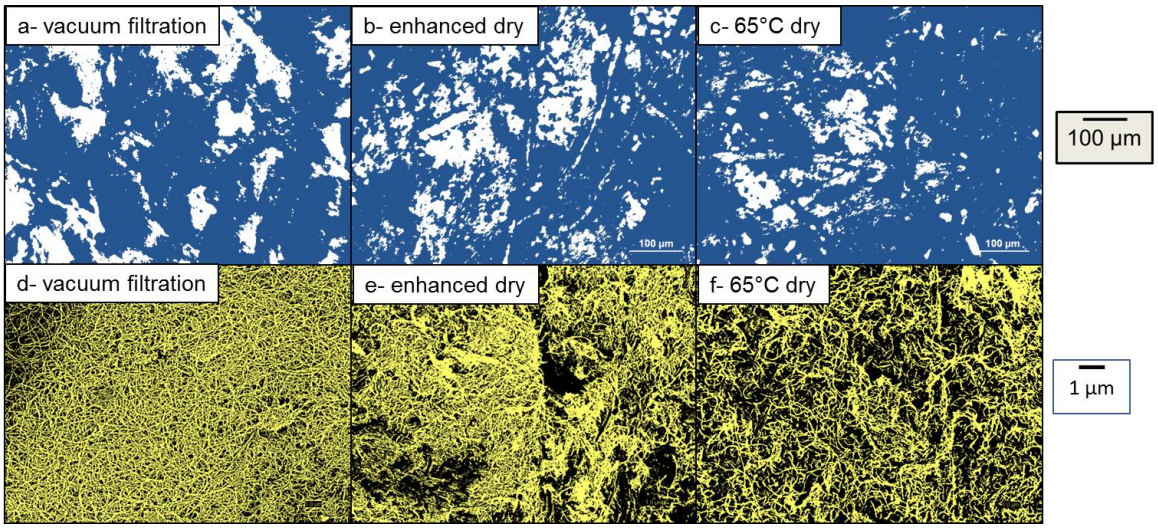

Figure 7.6: Digitized OM images (top) and digitized SEM images (bottom) for 4 layered MWNT-410 composites films deposited using the three different drying techniques: a,d) vacuum filtration, b,e) enhanced dry, c,f) 65°C dry.

From these differently dried samples, two trends can be seen which are exhibited by the 4 layered MWNT-paper in-plane images. First, the calculated macrodensity (Figures 7.6a-c) always increases with an increased degree of randomness during drying: macrodensity for 65°C dry > enhanced dry > vacuum filtration. Second, if a thin film can be formed on the surface of the paper material, microdensity (Figures 7.6d-f) increases with the increased unidirectionality in drying: microdensity for vacuum filtration > enhanced dry > 65°C dry.

Table 7.2 lists the average DC resistance values and the determined macrodensities and microdensities for the MWNT thin films made using the three different drying techniques on all of the paper substrates. Note, a thin film was not formed on the 4 layer MWNT-415 paper vacuum filtered composite as reported in the previous section (see Figure 7.4d), and microdensity could not be obtained for this sample. For thin films deposited using vacuum filtration, the DC resistance drops slightly from 8.3 ± 3.8 kΩ to 6.1 ± 0.9 kΩ between the 4 layered MWNT-410 paper composite and the 4 layered MWNT-413 paper composite. For the 4 layered MWNT-415 paper composite, the DC resistance is 6 orders of magnitude higher than the 4 layered MWNT-410 and -413 composites due to MWNT loss from the surface during deposition.

As is also shown in Table 7.2, for the heater drying techniques, DC resistance always increases with pore size; however, the impact of the pore size is minimized. All measured resistance values are on the same order of magnitude (10-40 kΩ).While there is directionality to the drying which pulls the tubes downward for the enhanced dry method, it is much smaller than the force provided by vacuum filtration. Surface deposition occurs on even the large pore sized paper. Similarly, for the composites fabricated using the 65°C dry method, the tubes are not preferentially dried in any direction, resulting in mostly surface deposition.

When pore size is held constant, enhanced drying always results in a higher microdensity than 65°C drying. This trend suggests that for the heater drying techniques having the higher temperature at the base of the heater promotes the pulling together of the film downward into the paper. The MWNTs form a much denser and less defective network at this length scale for the enhanced dry films. The randomness of the drying in a

heater at a constant 65°C did not cause any preferential direction for the dispersion to be pulled. The surface which forms is much more variable in density due to the randomness of the drying directions, causing the much higher DC resistance value for the 65°C sample set.

Table 7.2: DC Resistance, Macrodensity, and Microdensity for the 4 layered MWNT-paper composite materials fabricated using three different drying techniques. All of these composite surfaces exhibit thin film behavior, except under the condition of 415 paper and vacuum filtration. This sample is shaded to denote non-thin film behavior.

		DC Resistance (kΩ)	Macrodensity %	Microdensity %
Vacuum Filtration	410	8.35 ± 3.81	65.12 ± 6.11	72.70 ± 0.98
	413	6.12 ± 0.99	76.33 ± 10.02	68.77 ± 1.01
	415	$5.1x10^6 \pm 2.43x10^4$	0.27 ± 0.14	NA
Enhanced Dry	410	10.00 ± 0.65	78.41 ± 3.01	53.08 ± 1.22
	413	12.18 ± 1.13	76.80 ± 3.66	51.41 ± 1.03
	415	14.21 ± 1.26	75.72 ± 4.92	45.25 ± 0.87
65°C Dry	410	11.17 ± 1.85	86.31 ± 1.98	42.12 ± 1.00
	413	25.13 ± 3.72	85.76 ± 2.57	41.54 ± 0.94
	415	36.20 ± 2.17	76.57 ± 3.13	39.60 ± 1.53

7.3.3 Thin Film Samples: Surfactant Variation

MWNT thin film surfaces with variable junction resistances could also be created on the 410 filter paper by employing a layer-by-layer deposition method, as discussed in Chapter 5, Section 2. For fabrication of the surfaces using the layer-by-layer methodology, MWNT dispersions were made with three differently charged surfactant materials (SDBS = negative (neg); CTAB = positive (pos); Triton X-100 = neutral (neut)). 4 layers of MWNTs were deposited onto the 410 filter paper by alternating the charge of each deposited layer for each vacuum filtration dry step.

Figure 7.7 shows the digitized OM images for the 9 different deposition schemes described previously in Figure 5.4. The MWNT regions are darkened purple while the

paper remains white. It can be seen that when the dispersion containing the positive surfactant is used during deposition that the macrocoverage of MWNTs is much higher and tends to connect in all directions. For the other deposition schemes, the MWNTs are interconnected across the in-plane for all of the samples but the degree of interconnection is much smaller.

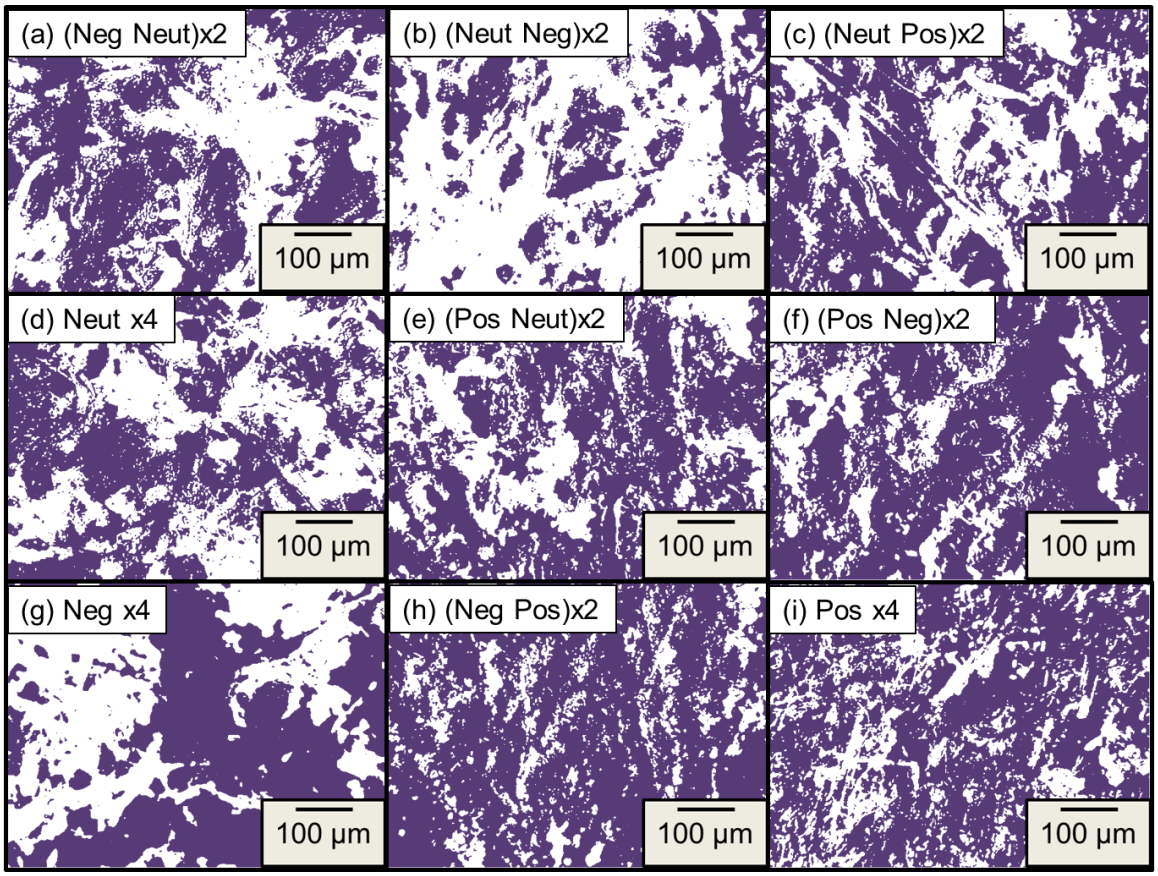

Figure 7.7: Digitized OM images for the layer-by-layer deposited 4 layered MWNT-410 composites with the deposition schemes of a) (Neg Neut)x2; b) (Neut Neg)x2; c) (Neut Pos)x2; d) Neut x4; e) (Pos Neut)x2; f) (Pos Neg)x2; g) Neg x4; h) (Neg Pos)x2; and i) Pos x4.

Figure 7.8 shows the digitized SEM images for the 9 different deposition schemes where the blue colored regions correspond to the MWNT network. The microdensities appear fairly consistent across all of the images in Figures 7.8a-g. However, in Figures 7.8h and 7.8i, the MWNT networks do not span the entire image space and are significantly less dense. In these images, blackened surface regions correspond to leftover

surfactant on the surface and the paper backbone. Excess surfactant on the surface decreases the amount of area available for the MWNTs to deposit, forcing MWNTs to form a network between the excess surfactant crystals. The decreased area for depositions results in much lower microdensities.

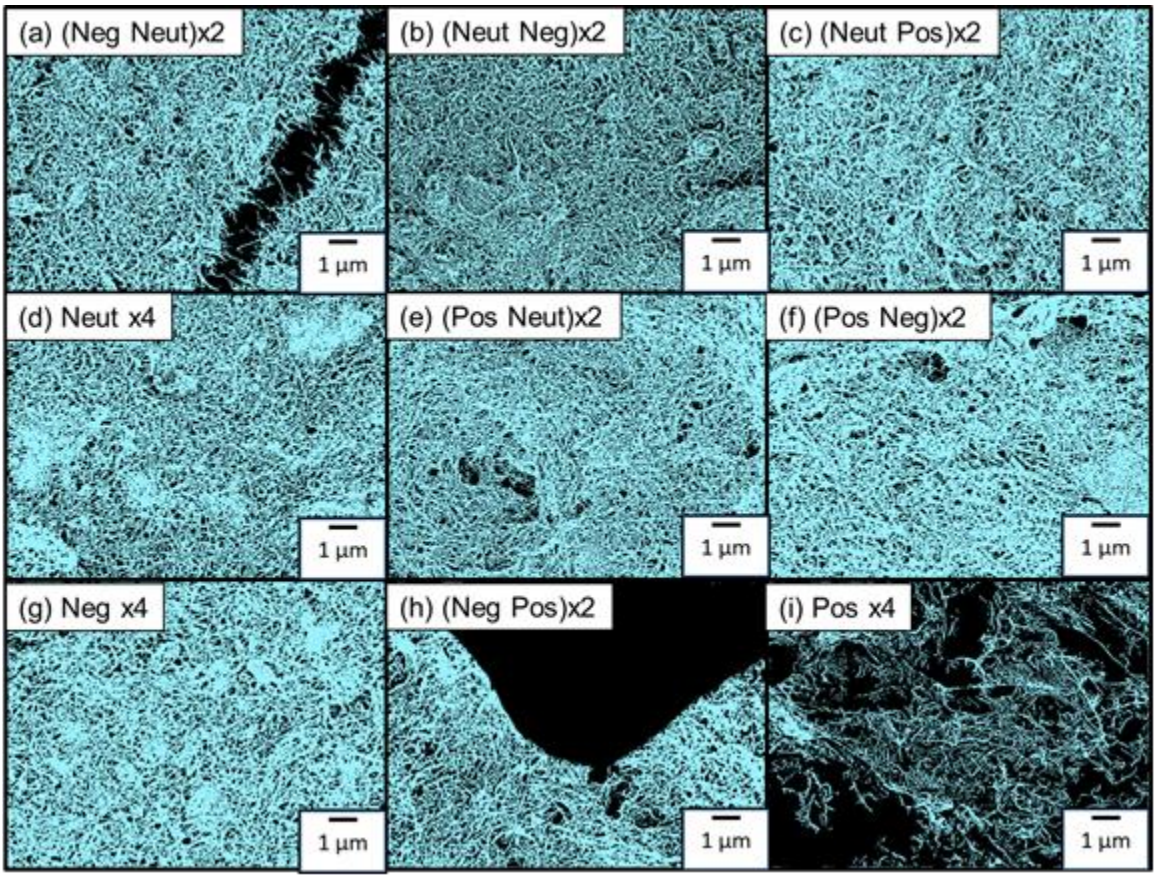

Figure 7.8: Digitized SEM images for the layer-by-layer deposited 4 layered MWNT-410 composites with the deposition schemes of a) (Neg Neut)x2; b) (Neut Neg)x2; c) (Neut Pos)x2; d) Neut x4; e) (Pos Neut)x2; f) (Pos Neg)x2; g) Neg x4; h) (Neg Pos)x2; and i) Pos x4.

Table 7.3 lists the measured DC resistance, macrodensity, and the microdensity values for the different 4 layered surfaces created by vacuum filtration-aided layer-by-layer deposition. Comparing Table 7.3 to 7.2 shows that the macrodensity of these thin film surfaces tend to be lower than the thin film surfaces created by using the different drying methodologies. The range of microdensities between the two sample sets is fairly similar; however, a new phenomenon is seen in this sample set which has not been

observed in any of the samples presented previously in this chapter but was discussed in Chapter 5, Section 2. For the (Neg Pos)x2 and the Pos x4 samples, a very low DC resistance value is measured along with a low microdensity. As shown in Figures 7.8h and 7.8i, the MWNT networks deposit at the region between the surfactant crystals. This type of surface is indicative of a "segregated network" of MWNTs- the MWNTs interconnect only at specific locations on the paper surface, separated by large surfactant crystals (see Figure 5.8 for SEM images). As the degree of segregation is increased (in this case due to more and more surfactant), the area in which the MWNTs deposit decreases which results in a lower microdensity locally but much more enhanced electrical properties.

Table 7.3: DC Resistance, Macrodensity, and Microdensity for the 4 layered MWNT-paper composite surfaces fabricated using the layer-by-layer deposition technique. All of these composite surfaces exhibit thin film behavior, except the Pos x4 sample. This sample is shaded to denote non-thin film behavior.

	DC Resistance (kΩ)	Macrodensity %	Microdensity %
(Neg Neut)x2	58.31 ± 9.64	51.73 ± 4.05	60.52 ± 0.22
(Neut Neg)x2	57.51 ± 5.33	31.73 ± 8.22	58.13 ± 1.47
(Neut Pos) x2	27.60 ± 0.85	57.82 ± 2.55	71.51 ± 0.19
Neut x4	18.99 ± 2.65	49.38 ± 3.09	71.52 ± 0.95
(Pos Neut) x2	10.64 ± 1.73	62.16 ± 1.44	72.11 ± 0.43
(Pos Neg) x2	7.56 ± 0.07	70.74 ± 2.55	75.92 ± 1.77
Neg x4	7.26 ± 0.33	62.37 ± 3.02	72.22 ± 0.81
(Neg Pos)x2	5.59 ± 0.14	76.88 ± 1.52	39.71 ± 1.22
Pos x4	1.99 ± 0.55	67.93 ± 1.87	25.01 ± 2.02

7.3.4 Predicting Electrical Transport Properties via Macrodensity and Microdensity Determination

Figure 7.9 plots DC resistance vs. macrodensity for all of the samples presented in this Chapter. As DC resistance decreases, the macrodensity increases, although not in a linear fashion. The data is clustered into three distinct groups, denoted by boxes around the data. In addition, a smaller dotted box is presented around one data point and a single filled diamond data point is not included in any of the groupings. As was discussed in Chapter 4, Section 2, four potential conduction mechanisms were found for the MWNT-paper surfaces using impedance spectroscopy: paper-dominated, MWNT thin film-dominated, a thin film to bulk transitional behavior, and bulk, metallic-like MWNT electrical transport. Combining the previous knowledge of the surface conduction behavior of these composites and the grouping of the data in Figure 7.9, macrodensity can be used to predict the conduction behavior of the MWNT-paper surface.

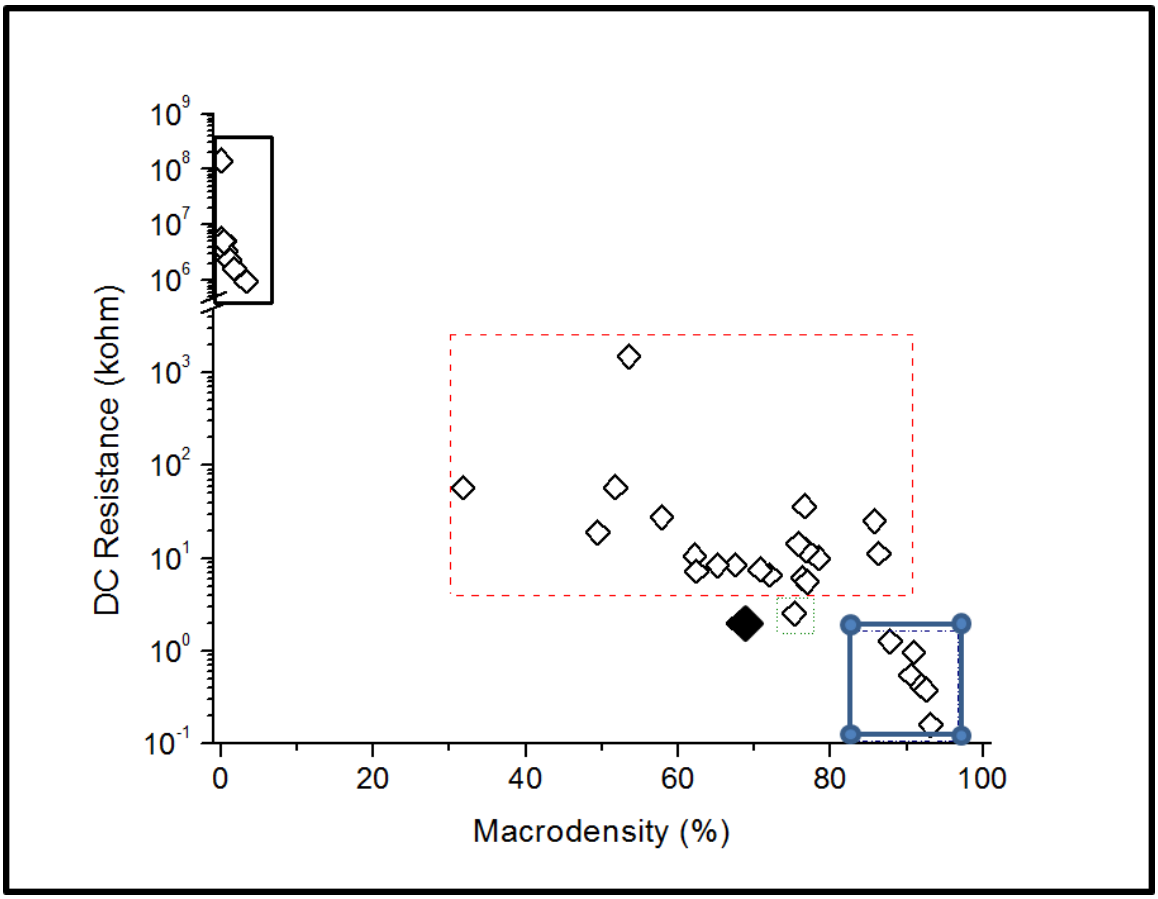

Figure 7.9: DC resistance vs. macrodensity for all of the samples presented in Chapter 7. The data shows four distinct groupings of points along with one data point (solid diamond) which does not fall into any of the groups. This data point corresponds to the Pos x4 sample. The y-axis is presented in log form and with a break in the axis to more clearly display the data.

The black solid box in Figure 7.9 groups together the data points which have high DC resistance values and very low macrodensities (<30%). These samples do not have a measurable microdensity or have microdensities of less than 25%. When these two conditions are met, paper-dominated electrical transport can be predicted by the density of the composite surface.

Macrodensities between 30 and 90% with DC resistances between 2.5 and 1000 kΩ are grouped in the dashed box in Figure 7.9 and correspond to the composites which exhibit thin-film MWNT network electrical transport in their in-plane direction. Thin film transport has the widest range of macrodensities as the MWNTs must form an

interconnected network across the surface. However, a large amount of uncoated paper backbone can still be present as long as the MWNTs are continuously interacting. As is shown in Figure 7.9, the DC resistance for the thin film regime does not necessarily decrease with increasing macrodensity.

For the samples displaying thin film behavior, DC resistance is more highly controlled by the quality of the MWNT network. The DC resistance value for thin film MWNT surfaces is the summation of the resistance of the bundles and the resistance of the junctions between MWNT bundles. Since bundle resistance is a constant value of 0.9 kΩ for all of the MWNT thin film networks presented in this study and all samples were made with the same MWNTs (see Chapters 4-6), the DC resistance value is overwhelmingly dominated by the MWNT-MWNT junction resistance. In order to elucidate some trends about the DC resistance for thin film samples, microdensity must also be considered. For thin film surfaces which are not in a segregated network structure, the determined microdensity is dependent upon fabrication parameters such as pore size, drying methodology, and layer number.

First, as is shown in Table 7.1, as the number of deposited MWNT layers via vacuum filtration on the 410 paper increases from 1 to 4, the measured microdensity increases from 31% to 71%. Higher layer numbers create more dense MWNT thin films. Next, as detailed in Table 7.2, when the number of deposited layers is held constant at 4, microdensity increases as the pore size of the paper backbone decreases. The film which forms on smaller pore size paper (410 and 413) is more rigidly pulled together on the surface, decreasing junction resistance. When pore size is larger (415), the thin film

develops around the pores rather than across them, creating a more loosely connected film. Junction resistance is increased.

In addition, when layer number is held constant at 4, as the unidirectionality of the drying technique increases (vacuum filtration > enhanced dry > 65°C dry), microdensity increases. Randomness in drying leads to a less homogenous surface structure which increases the junction resistance. The variation in surface density which arises during deposition also helps describe the behavior of the thin film networks formed by surfactant variation (for the in-planes which do not form segregated networks). As microdensity increases, DC resistance decreases. Figure 7.8 shows that the MWNT thin films which exhibit lower microdensities tend to have more defects, such as film height/thickness variation, pores, and cracks on their surfaces. The defects lead to a lower quality film which results in a higher junction resistance.

When macrodensity is > 90% and the DC resistance is < 2kΩ, conduction occurs through the bulk MWNT networks which have formed. In Figure 7.9, high macrodensities and very low DC resistance values are collected in the solid box with circles in the corners. In addition, as can be seen in Table 7.1, these bulk behaving composites exhibit a constant for microdensity of about 77% regardless of layer number or pore size. Bulk MWNT conduction behavior can be generally predicted by a macrodensity above 90% and a microdensity of 77%.

There are two data points which cannot be contained by the three major groupings in Figure 7.9. The first point is separated with a dotted box and corresponds to the 8 layered MWNT-413 composite. From Section 4.2.3.3, the impedance measured for this

composite in-plane exhibits both MWNT thin film and bulk electrical behaviors; therefore, it is not surprising that its macrodensity and DC resistance fall between the two data groupings for thin film and bulk MWNT networks. In addition, from the values presented Table 7.1 the macrodensity and microdensity of the 8 layered MWNT-413 composite overlap, suggesting that the transitional behavior arises when these two values are the same.

The second data point not contained by any of the three major groupings in Figure 7.9 is shown by the filled in diamond data point and corresponds to the Pos x4 composite. This sample measures a very low DC resistance which overlaps with the DC resistances of the bulk MWNT networks, but its macrodensity is in the range of the thin film composites. The macrodensity suggests an interconnected network has formed across the surface. However, as shown in Table 7.3, its microdensity is approaching that of the paper-dominated surfaces. A sample with a low resistance, thin-film macrodensity, and paper-dominated microdensity corresponds to a composite network which is bulk conducting but highly segregated, as was shown in Figure 7.7i and therefore cannot be interpreted in the same way.

7.4 Conclusions

A multiscale methodology derived from traditional and new stereology techniques was used to find bulk surface coverage (macrodensity) and MWNT film density (microdensity) from optical and scanning electron microscopy images, respectively. Comparing the structural parameters obtained at the two different length scales to the measured electrical properties of the MWNT-paper composite surfaces allowed for the

identification of trends in the structure-property relationships of these networks. It was shown that the conduction behavior of the MWNT could be predicted with the values of macrodensity and microdensity.

Surfaces which have both low macrodensities and microdensities have a surface structure where the interconnection of the MWNTs is not sufficient enough for electrical conduction to occur only across the MWNT network. Current instead flows through the paper fibers and a high DC resistance value is measured. While the addition of the MWNTs to the paper can decrease the electrical resistance slightly, the surface conduction is primarily paper-dominated transport. Surfaces which have a macrodensity between 30% and 90% are MWNT thin-film dominated. As the microdensity increases toward 77%, the DC resistance value/junction resistance decreases. Higher microdensities correspond to less defective thin film networks; therefore, microdensity for thin films can be used to quantify the quality of the network which forms. The higher quality films have higher microdensities and lower junction/DC resistances. When macrodensity is > 90% and microdensity is static at 77%, the surface is bulk MWNT conducting, and the DC resistance for the surface is very low.

Unexpected surface characteristics can also be predicted by this methodology. Low microdensities with thin film level macrodensities occur when the MWNTs are forced into a small area on the surface but still connect across the entire surface. This type of structure is indicative of a segregated network. As the microdensity value for the segregated network decreases, the DC resistance decreases and can even approach a value corresponding to a bulk MWNT conducting network.

CHAPTER 8

CONCLUSIONS AND FUTURE WORK

8.1 Conclusions

MWNT and filter paper composite materials with a huge variety in architectures and properties were fabricated by the combination of wet deposition of MWNTs via dropcasting and drying using vacuum filtration. Vacuum filtration is a popular technique in the formation of CNT films from dispersions as the CNT films which form are reproducible and high quality; however, rarely does the CNT film remain on the substrate on which it is created. In most cases, CNTs are deposited onto an expensive filter membrane and then transferred to other substrate materials for testing and applications. The methodology employed in this thesis takes advantage of the highly reproducible film formation techniques provided by vacuum filtration by keeping the deposited CNTs on the paper backbone.

By varying only the pore size of the paper backbone, the location of CNT deposition could be controlled. By varying the number of dropcasting steps (layer number), the properties of the composite materials could be varied and easily tailored. The combination of pore size and deposited layer number results in the unique architectures and properties which can be fabricated. This thesis provides the first look into the properties of the vacuum filtered MWNT-filter paper material system as well as the tailorability of those properties through fabrication step variations. Drying methodology, dispersion characteristics, and post-processing of the composites were

varied to determine the effect of processing on the established structure and properties of the composites.

The main contribution of this thesis was the demonstration that impedance spectroscopy can be used as a tool to simultaneously track the evolution of the structure and properties of the composite material. Using impedance spectroscopy as the main technique for electrical property determination allowed for the elucidation of the different electrical behaviors present in the composite system which came about due to the choice of MWNT deposition conditions. In addition, through the use of equivalent circuit analysis and curve fitting of the impedance data, the structural components of the composite material which contribute to the electronic behavior could be determined and their properties quantified. Overall equivalent circuit models were developed to describe all of the composite materials fabricated. The activity of the components present in the equivalent circuits could be used to determine what kind of structure was present in each composite material.

Structural models for composite formation were developed based on SEM and optical imaging as well as the impedance data which together described how and where the MWNTs deposited. This also allowed for the quality of the interaction between MWNTs as well as between the MWNT and paper structure to be determined. This was especially important for the thru-plane measurement of these materials which could not be directly imaged without severe distortion of the actual thru-plane and destruction of the composite material. The use of impedance spectroscopy and curve fitting in this thesis provides a detailed example of how to simultaneously determine both structure and properties using a non-destructive methodology.

This thesis also provided a new methodology to predict the electronic behavior of the surface of the different MWNT-paper composite materials using a combination of optical microscopy and scanning electron microscopy. The methodology relied on techniques derived from traditional stereology as well as new nanocharacterization techniques. Using the dual length scale imaging approach, the structural parameter of MWNT determined density was used predict the electronic behavior of the composite surface. The combination of density of MWNT coverage at the macroscale and the density of the MWNT network on the microscale were related to the impedance behaviors of the composite surfaces to provide a framework for predicting which behavior is active based on the two measured network density values.

8.2 Future Work

Throughout this thesis, a single methodology was used to develop the composite materials studied in each chapter. The process followed for the majority of this thesis was dispersion fabrication (1 mg/mL MWNT, 10 mg/mL SDBS surfactant in water), followed by dropcasting and drying using vacuum filtration (number of layers = number of dropcast-dry steps), and ending with property characterization of those materials. Figure 8.1 shows both the composite fabrication methodology as well as a breakdown for each variable changed at each point during processing in this thesis. The details provided in this chart allow for an immediate determination of what future work can be done to further build upon the results provided in this thesis.

This thesis did not focus on any pre-processing techniques. It may be possible to change the interaction between the paper and MWNTs through the addition of a pre-

processing step to the paper material. For example, it may be possible to form patterned or highly complex arrangements of MWNTs by first changing the properties of the paper material. If the paper can be patterned such that some of it is hydrophobic and some of it is hydrophilic, the dropcasted aqueous dispersion of MWNTs will segregate to the regions of hydrophilic paper. This will allow for the formation of macro-level segregated MWNTs.

In addition, as was determined in Chapter 3 and 4, if the deposited material is smaller than the pore size of the paper material, it will preferentially deposit within the paper pore network rather on the surface of the paper material. A chemical coating could be applied to the internal structure of the paper and not to the surface. If this coating and the MWNTs have a low affinity for each other, MWNT deposition will be entirely inhibited within the paper material, allowing only surface deposition regardless of the paper pore size.

This thesis did not focus on any specific applications, but for application development, the results provided by this thesis can act as a framework for obtaining the properties necessary to form a functioning device. An ample amount of information was gathered in this thesis on how to form certain structures with certain properties.

The majority of the changes to the fabrication step studied in this thesis were to the dispersion fabrication step and to the drying technique utilized. However, the deposition methodology used can also be altered. Other wet deposition techniques such as dipcoating, spraycoating, and spincoating (among many others) could be used to

deposit the MWNTs to the paper material in order to form different specimens with potentially different architectures.

Preliminary work has been done studying the properties of MWNT-paper materials which were formed by changing the dropcasting methodology from one-sided to two-sided. Using a 10 mg/mL dispersion of MWNTs and the 413 filter paper, a single layer was deposited on the top surface of the paper and dried using vacuum filtration. The paper was turned over and a single layer was deposited on the back surface of the paper and dried using vacuum filtration. Bulk MWNT network behavior was measured on both in-planes of the paper with an average resistance of 850 Ω ± 52 Ω. The thru-plane of the sample showed continuous deposition with a resistance value of 76 Ω ± 4.4 Ω. An extremely conductive thru-plane was formed. With additional work, the in-plane resistances should be able to be lowered even further. It may also be possible to remove the paper and further increase the conductivity of the sample, forming buckypaper structures cheaply and easily.

Finally, the results presented in this thesis provide a predictive capability of how to achieve certain network properties of the specific MWNTs and paper substrates used here. However, it is likely that these predictions will not hold for other CNT-type materials and more detailed experimentation of these CNTs will need to be done to get a complete understanding of network formation. This work may provide further refinement for the models presented here as well as provide an extended framework for property achievement.

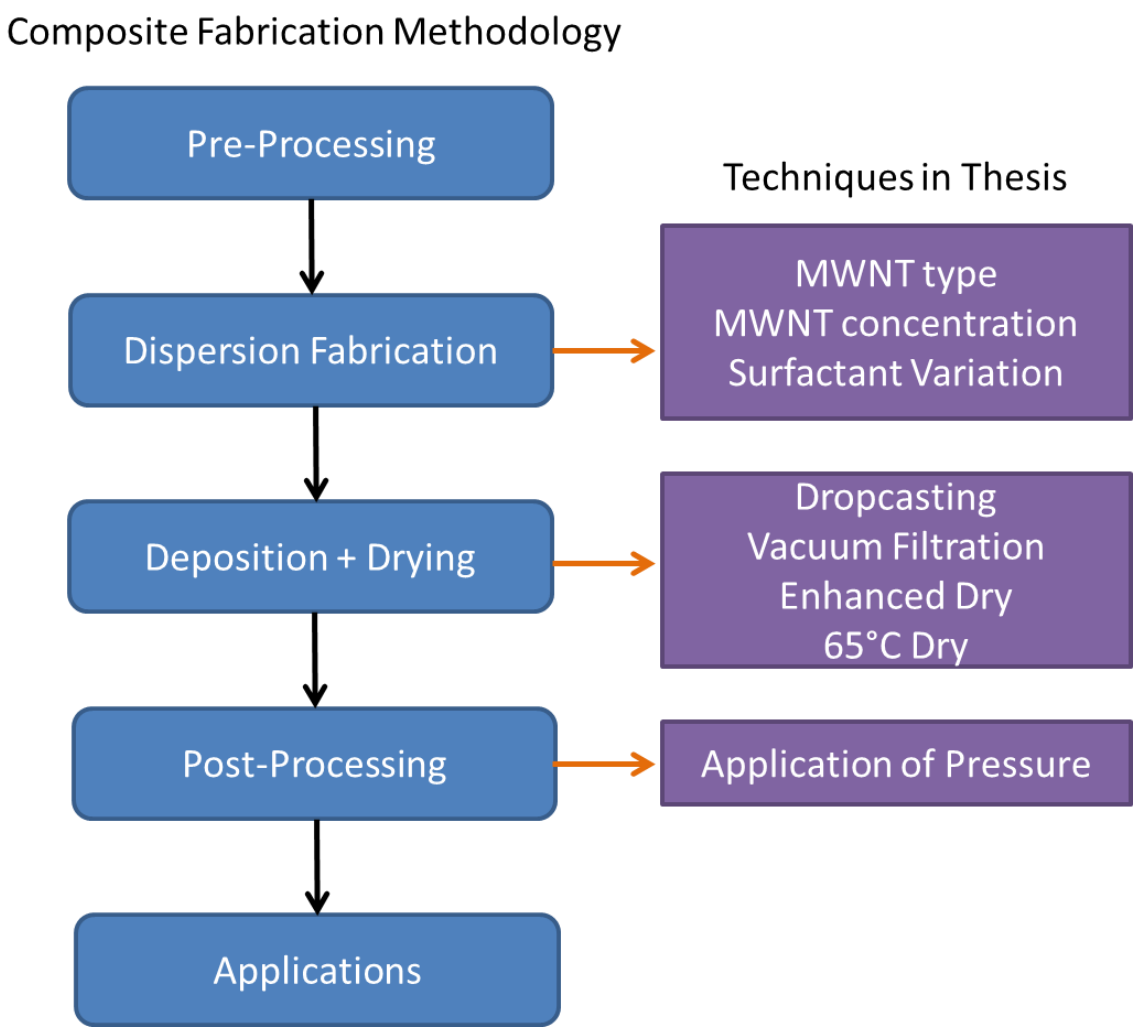

Figure 8.1: Established composite fabrication methodology and the experimental details employed in this thesis to determine the structure-property-processing relationships in the MWNT-paper materials.

APPENDIX A

POWER LAW MODELING TO PREDICT IN-PLANE AND THRU-PLANE RESISTANCE VALUES

Curve fitting of experimental percolation data allows for the determination of the critical threshold value along with some geometric information of the material. For fitting, it is very common to use a scaling law which, in this thesis, takes the form of Equation A.1, where c is a fitting constant, L is the number of deposited MWNT layers, L_c is the critical layer number threshold, and β is the critical exponent. The scaling law is a power law and can only be used to determine properties when $L > L_c$. For rod fillers, such as CNTs, β is a dimensionality constant that should take on a value between 1.3 and 2.0 for purely 2D and purely 3D networks, respectively [82].

$$R = c(L - L_c)^{-\beta} \quad \textbf{(A.1)}$$

A.1 In-Plane

In Chapter 3, Figure 3.12 presented the DC resistance vs. the number of deposited MWNT layers for both the in-plane (Figure 3.12a) and the thru-plane (Figure 3.12b) of the layered MWNT-paper composites. For the in-plane behavior shown in Figure 3.12a, the MWNT-410 composite materials are already percolated at 1 deposited layer and the resistance continues to drops with an increased number of deposited layers. An insulator-to-conductor transition is present during the layering process for the in-plane behavior of the MWNT-413 composite materials. Before 4 layers, the MWNT-413 composites have a similar resistance to that of pure paper, these composites percolate at 4 deposited layers,

and after 4 deposited layers, the in-plane resistance continued to drop. For the MWNT-415 composites, the resistance was high for all layer numbers and percolation never occurred. The onset of percolation occurs when the electrical behavior of the composite material switches from insulating matrix dominant to conducting filler dominant. Generally, this value, the percolation threshold, is determined by plotting the electrical property vs. some sort of quantified amount of filler and estimating the onset of percolation from that graph [65]. However, impedance spectroscopy of these materials systems provides that information without estimation.

As was discussed in Chapter 4, there is an impedance behavior and equivalent circuit that can be used to describe paper-dominated electrical transport, or the insulating matrix behavior. As more layers of MWNTs are added to the paper, the resistance measured for the paper surface drops until the MWNTs are able to form an interconnected network across the entire paper surface. At that discrete layer number (critical layer number or L_c), the impedance behavior and equivalent circuit used to describe the electrical behavior of the surface switches from paper-dominated to MWNT thin film dominated. The layer at which the first appearance of the thin film and the Nested-RL equivalent circuit used to fit its impedance data denotes the percolation threshold of these composites. For the MWNT-410 composites, L_c is 1. For the MWNT-413 composites L_c is 4. For the MWNT-415 paper composites, the electrical behavior of the surfaces is always paper-dominated ($L_c >> 20$). In addition to the critical layer number, impedance spectroscopy can also provide the DC resistance value for the materials as the DC resistance is equivalent to the low frequency x-intercept of the impedance graph [43].

Figure A.1 shows the impedance vs. (L-L_c) (where L_c = 1) for the in-plane of the 410-MWNT paper composites as well as the standard deviation for the impedance values. Also included in Figure A.1 is the power law fit for the data. As is shown in the inset of the chart, the power law fit has an R^2 value of 0.925. It is likely that this value would move closer to 1 if impedance values for the layer numbers between (L-L_c) = 3 to 7 had been obtained. However, this fit overlaps all of the data points. The power law equation fit to the MWNT-410 paper data is shown in Equation A.2.

$$R = (96200 \pm 27100)(L - L_c)^{-2.19 \pm 0.11} \quad \textbf{(A.2)}$$

The value of the power law constant is fit to be slightly above -2. As was discussed previously, -2 is the value of the exponent for 3D random networks of rods, such as CNTs [83]. 3D networks of CNTs are known as buckypaper, a mechanically strong and highly conducting freestanding sheet of CNTs [83, 84]. A value of $\beta = 2$ suggests that after percolation, the thick surface layer of CNTs, which exhibits bulk, metallic-like conducting behavior, is actually simulating buckypaper. Impedance scans done on commercial buckypaper found that across their surface, the behavior detected is that of a straight line in the fourth quadrant which is fit by the $(R\text{-}L)_s$ equivalent circuit, further confirming the model results. For the overall model, β is set equal to -2.08, the minimum value determined from the fitting.

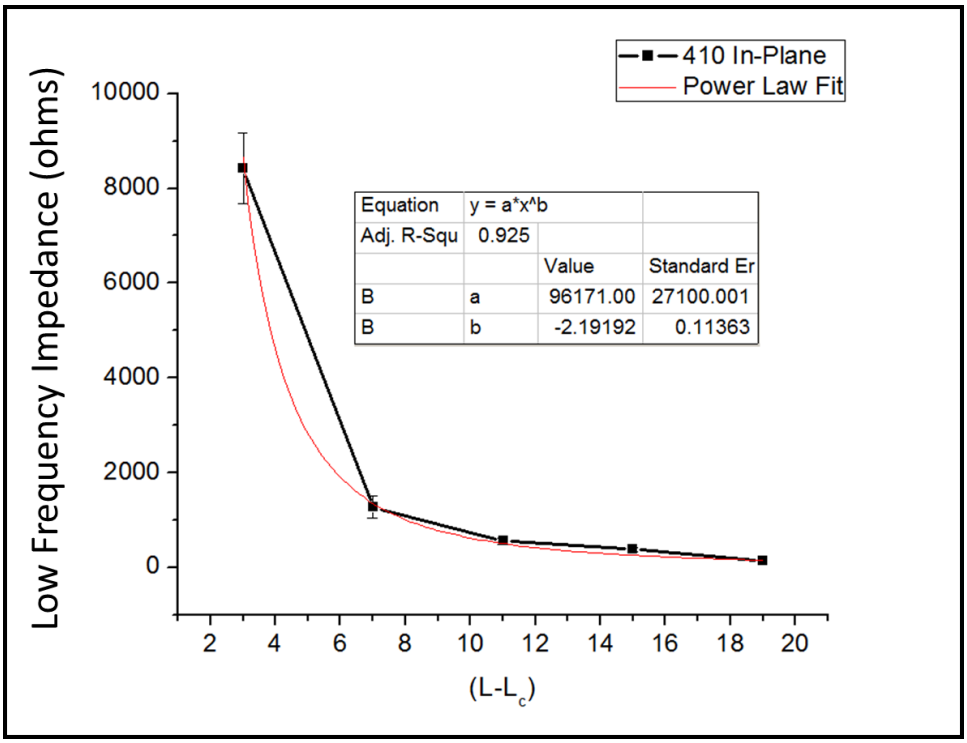

Figure A.1: Low frequency impedance vs. (L-L_c) for the in-plane of the MWNT-410 composites as well as the power law fit. The impedance value is the low frequency x-intercept value which is equivalent to the DC resistance of the material. The constants for the curve fit are available inside the chart.

For the constant, c, shown in Figure A1, the power law fit suggests a value of 96171 Ω ± 27100 Ω. The constant for fitting should take into account some resistance value as well as the paper and CNT properties. Using the data for the MWNT-410 composites as well as the MWNT 413 composites (shown in Figure 3.12a) along with addition composite materials including 1-20 layered L-MWNT-410 composites and 1-20 layered SWNT-410 composites [64], the relationships which formulate the constant could be elucidated. The constant can be calculated using Equation A.3,

$$c = \frac{R_{percolation}}{(L_b / d_p)} n\pi \qquad \textbf{(A.3)}$$

where $R_{percolation}$ is the resistance of the in-plane at the critical layer number, (L_b/d_p) the ratio of CNT bundle length to the diameter of the pore in the paper, and nπ where n has some relationship to the location of deposition. For the MWNT-410 composites, $R_{percolation}$ is $1.5x10^5$ Ω, L_b/d_p is 5, and n = 1. The value of c is 75400 Ω which falls within the range predicted by the power scaling law curve fit.

Therefore, the overall equation which can be used to predict the resistance of the MWNT-paper composites measured is given by Equation A.4 (also listed in Chapter 3 as Equation 3.1). The experimentally measured resistance values were plotted with the predicted values from Equation A.4 in Figures 3.13a and 3.13b for the MWNT-410 and MWNT-413 paper composites, respectively.

$$R_{in-plane} = \frac{R_{percolation}}{(L_b / d_p)} n\pi (L - L_c)^{-2.08} \quad \textbf{(A.4)}$$

Similarly, Equation A.4 could be used to predict the resistance values for two other CNT-based surface conducting composite systems (L-MWNT-410 and SWNT-410 [64]) and the results are plotted in Figure A.2. The values used to get the fitted data presented both in Figure A.2 and in Figure 3.13 are given in Table A.1. For all of the composites in which $L_b/d_p > 1$, n takes a value of 1. Conversely, when $L_b/d_p = 1$, n takes on a value of 2. It seems that for paper materials in which the MWNTs can only deposit on the surface, n = 1. When both surface and internal deposition occurs, n = 2. n can be used as a dimensionality constant.

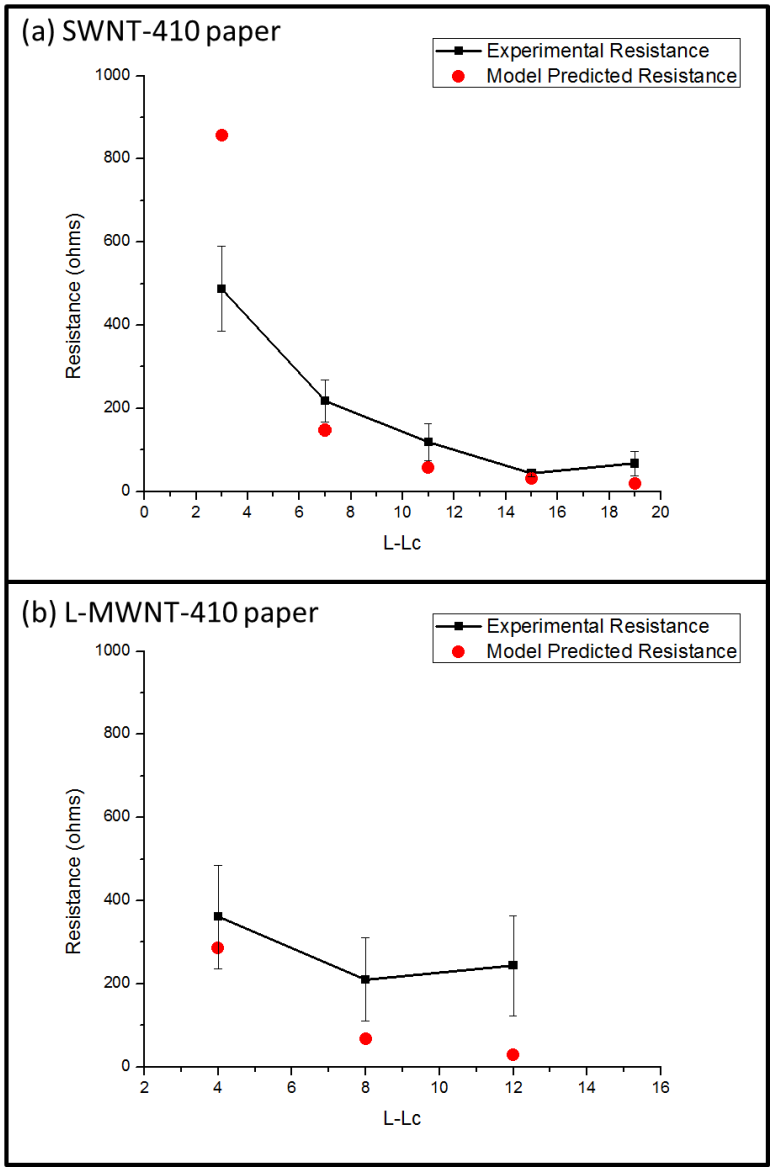

Figure A.2: The measured resistance values and the model predicted resistance values for the a) SWNT-410 composite system given the inputs of $R_{percolation}$ = 67000 Ω, L_b/d_p = 25, n = 1, and L_c = 1; and b) L-MWNT-410 composite system and the predicted values given the inputs of $R_{percolation}$ = 8150 Ω, L_b/d_p = 5, n = 1, and L_c = 8.

Table A.1: Parameters used to create the percolation curves in Figure 3.13 and Figure A.2.

	$R_{percolation}$ Ω	L_b/d_p	n	L_c
MWNT-410	$1.2x10^5$	5	1	1
MWNT-413	6400	1	2	4
L-MWNT-410	8150	5	1	8
SWNT-410	67000	25	1	1

The predictions for the SWNT-410 composites are within the experimental range, with the exception of the first data point after percolation for the SWNT-410 composites (Figure A.2a). At this data point, the model overestimated the experimental resistance by 2x; however, both the experimental and predicted value are still in the same order of magnitude. The SWNTs used in this study were fabricated using a laser growth method and purified at Oak Ridge National Lab (Knoxville, TN) and have an average diameter of 1.5 nm with a yield of 1/3 metallic and 2/3 semiconducting SWNTs. These SWNTs formed composites with highly conductive in-planes which decreased in resistance with increased loading. The SWNTs deposited as non-agglomerated bundles and formed dense, randomly oriented networks. They also exhibited no internal deposition on the 410 paper as the length of the SWNTs was much larger than the 1 μm pore size paper [64].

For the L-MWNT-410 composites (Figure A.2b), the model predicted values that were always less than the experimentally determined values. The L-MWNTs do not deposit on the paper surfaces as rods; instead, as was shown in Chapter 4, the rods agglomerate and form rounded clumps of L-MWNTs (with an average clump size of 5 μm). Since the L-MWNTs have a length of 10-30 μm, the tubes contained in these

clumps are highly folded and likely full of defects. While bulk behavior is still occurring, the pathway that current flows from clump to clump is much more tortuous than the pathway current would flow for rods of the same size or even for long tubes which lay flat. This deviation from rod behavior causes the model to underestimate the actual resistance values.

A.2 Thru-Plane

As was shown in Figure 3.12b, the DC resistance for the entire range of MWNT-410 composites as well as for the first percolation event in the MWNT-413 composites is a statistically constant resistance value. However, the resistance for the MWNT-415 composites thru-plane decreases with increasing layer number. Additionally, the resistance of the surface of the MWNT-415 paper composites is very large and close to that of the pure paper, and the pore size of the material is much larger than the bundle length of the MWNTs. It can be assumed that 100% of the material that is dropcasted and not pulled through the paper completely deposits within the thickness of the 415 paper. It will also be assumed that deposition occurs in a *continuous* manner: increased layer number leads to increased deposition within the pore and a decreased resistance within the pore.

Figure A.3 shows the impedance vs. $(L-L_c)$ (where $L_c = 1$) for the thru-plane of the 415-MWNT paper composites as well as the standard deviation for the impedance values. Also included within this Figure is the power law fit for the data with an R^2 value of 0.892. However, the curve does run through at least the standard deviation of all the

experimental points. The power law equation which fits the MWNT-415 paper data is shown in Equation A.5.

$$R = (396000 \pm 98100)(L - L_c)^{-0.79 \pm 0.12} \quad \textbf{(A.5)}$$

Unlike the in-plane fitting constant, β does not fall within the 2D or 3D rod network range of values (1.3-2.0) for the thru-plane. Rather, β = -0.79 ± 0.12. This type of response is not a geometric response, which suggests that even post-percolation in the thru-plane, the paper fibers play a huge role in the spatial arrangement of the CNTs. A value of β = 0.85 has been seen before for a polyvinylidene difluoride-MWNT composite material with an exceptionally low percolation threshold (0.016 vol%). In that material, clusters of MWNTs are embedded in an insulating matrix, and the primary mechanism for conduction was interfiller tunneling [85].

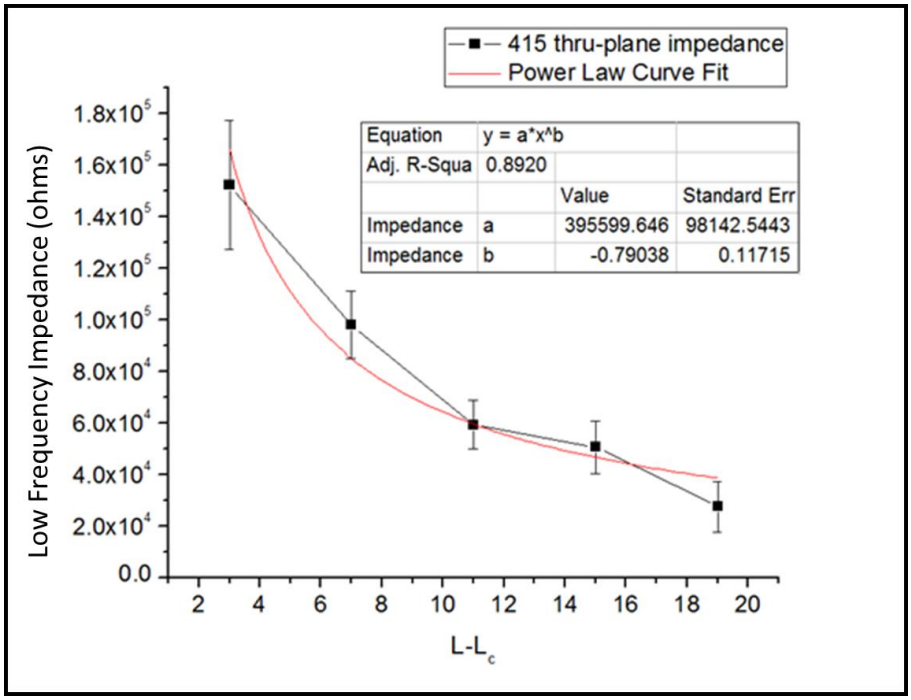

Figure A.3: Low frequency impedance vs. (L-L_c) for the thru-plane results for the MWNT-415 composites as well as the power law fit. The impedance value is the low frequency x-intercept value which is equivalent to the DC resistance of the material. The constants for the curve fit are available inside the chart.

Recalling Figure 3.3, the pore structure of the 20 layer MWNT-415 composite contained clusters of MWNTs along with some fiber coating. The fiber coating showed a density gradient from top to bottom: the fibers toward the bottom of the pore were coated fairly densely. However, as you move up from the bottom of the pore to the top, if MWNTs coated the fibers at all, it would be in small areas surrounded by void space. Clusters of MWNTs bridged the top and bottom of the pore as was shown in Figure 4.20, an SEM image of a pore in the 20 layered MWNT-415 composite. It is reasonable to assume that the coating at the lower layer numbers would be even less dense. The pore fibers and the MWNT clusters would work together for conduction to occur. In addition, as the circuit which describes the conduction through the MWNT-415 paper composite requires a CPE over a capacitor for fitting, inhomogeneity was already suspected within the pore. For the thru-plane model, β will be set to 0.85.

Using the same methodology as what was done to fit the in-plane results, the constant, c, was determined. For the thru-plane, c is described by Equation A.6. Interestingly, the bundle length to pore size ratio is not needed to describe the thru-plane behavior. As long as deposition is happening in a *continuous* manner, the ratio is unnecessary. The ratio only helps predict that the *continuous* deposition will occur. If L_b/d_p is much smaller than 1, *continuous deposition* always occurs. If $L_b/d_p = 1$, *continuous deposition* will occur in the composites but only after some number of layers (in this case, 10 layers). If $L_b/d_p > 1$, the assumption made is that only surface deposition is occurring (or surface deposition is by far the dominant location), and this equation does not apply.

$$c = R_{percolation} \frac{\pi}{2} \quad \textbf{(A.6)}$$

Therefore, the overall equation which can be used to predict the resistance of the MWNT-paper composites in the thru-plane direction is given by Equation A.7 (also presented as Equation 3.2 in Chapter 3). The experimentally measured resistance values were plotted with the predicted values in Figure 3.14a for the MWNT-415 paper composites and Figure 3.14b for the MWNT-413 paper composites (L_c = 10 and $R_{percolation}$ = 7.5x10^4 Ω). In both cases, the model predicted values that fall within the experimentally determined resistance, with the exception of one data point in each system.

$$R_{thru-plane} = R_{percolation} \frac{\pi}{2} (L - L_c)^{-0.85} \quad \textbf{(A.7)}$$

APPENDIX B

EQUIVALENT CIRCUIT FITTING OF NESTED-RL CIRCUIT:

DIFFERENT IMMITTANCE FUNCTIONS

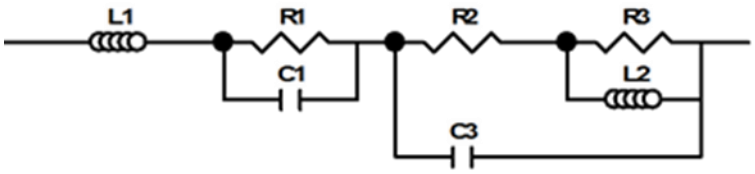

$L1 = 0.00057$

$R1 = 902$

$C1 = 1.4415 \times 10^{-11}$

$R2 = 5.3574 \times 10^{5}$

$C3 = 1.5763 \times 10^{-12}$

$R3 = 2.0858 \times 10$

$L2 = 0.0089302$

Figure B.1: Nested-RL Circuit and Fitting Values

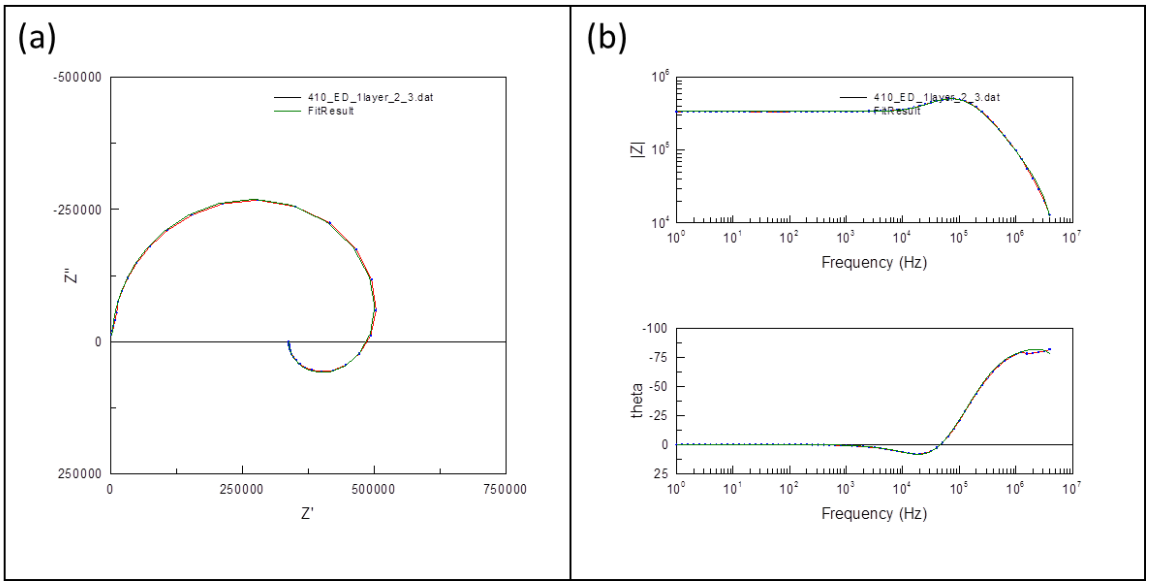

Figure B.2: Real data and curve fit result for impedance (Z*) results. a) Z" vs. Z'; b) log(|Z|) vs. log(f) (top) and θ vs. log(f) (bottom).

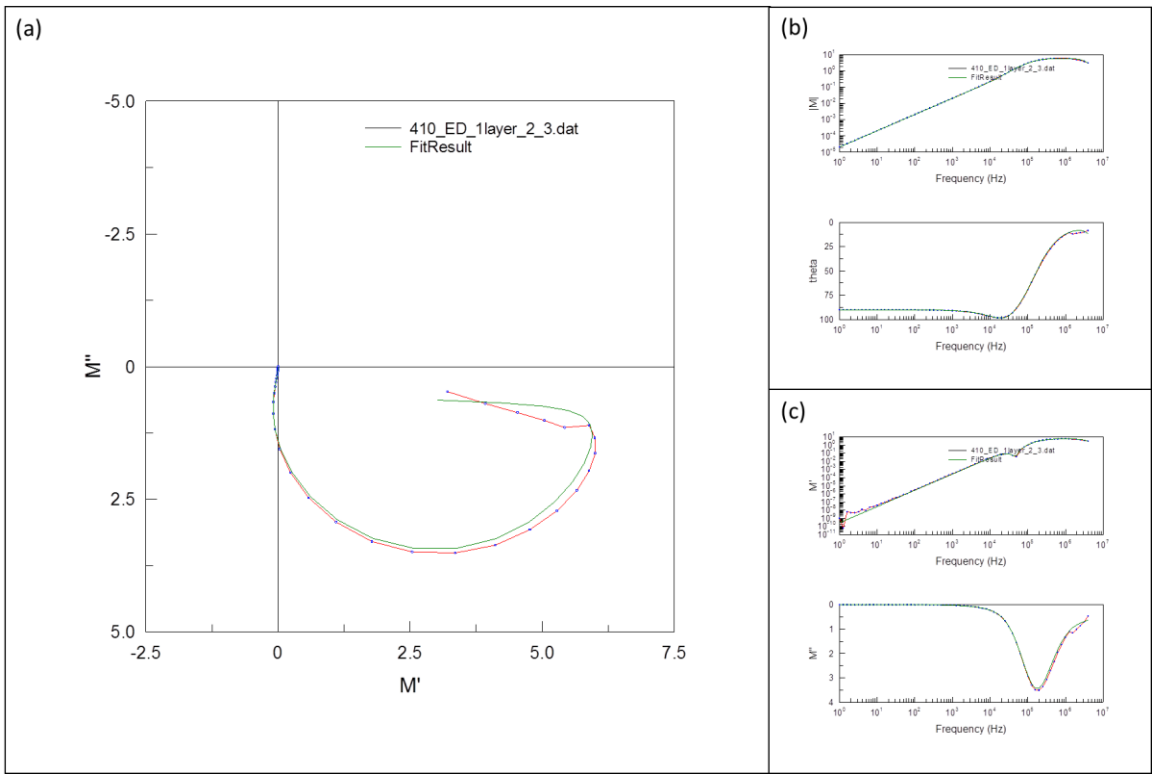

Figure B.3: Real data and curve fit result for electronic modulus (M*) results. a) M" vs. M'; b) log(|M|) vs. log(f) (top) and θ vs. log(f) (bottom); c) M' vs. log(f) (top) and M" vs. log(f) (bottom).

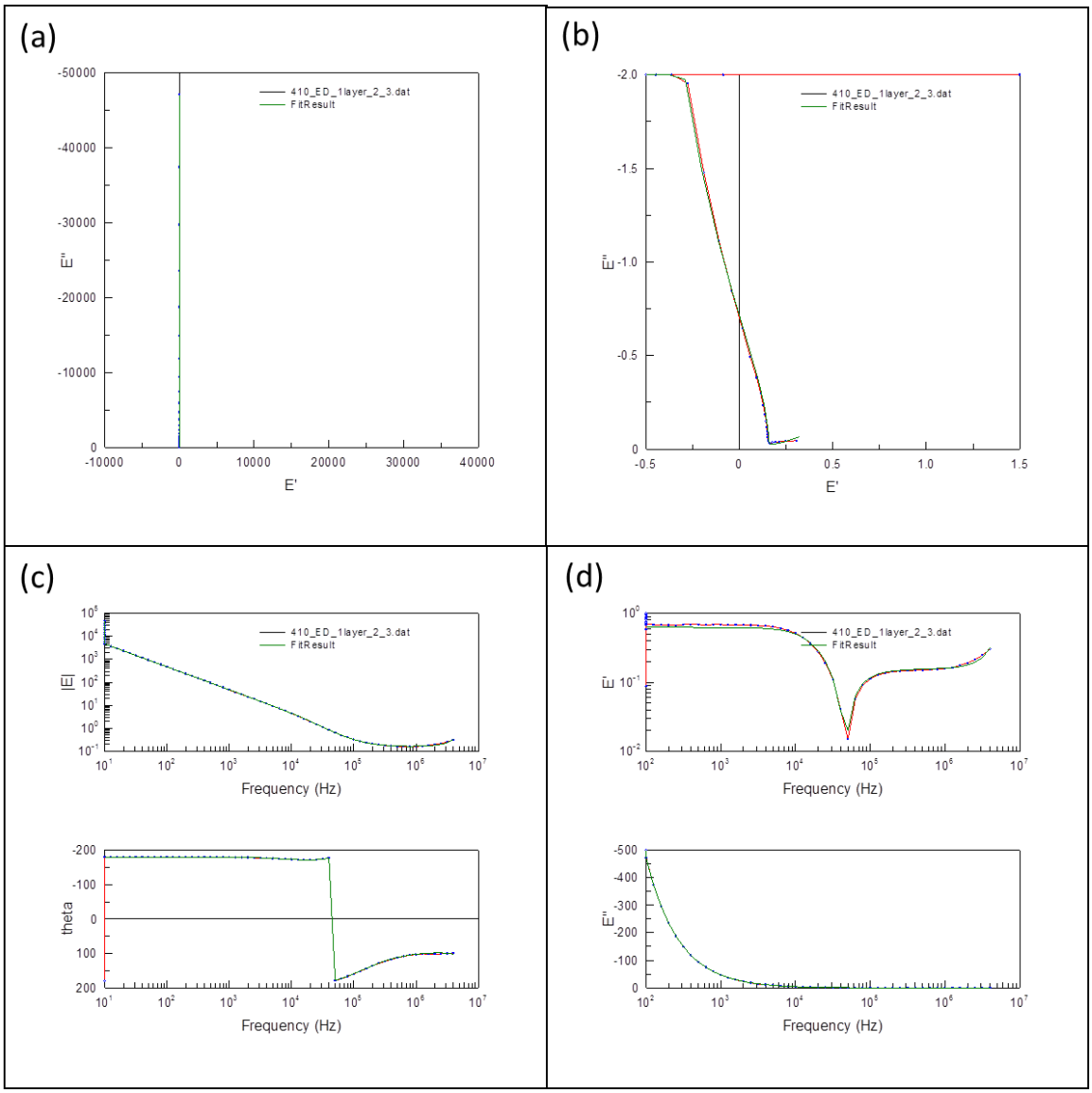

Figure B.4: Real data and curve fit result for permittivity (ε*) results. a) ε" vs. ε'; b) zoomed in ε" vs. ε'; c) log|(ε|) vs. log(f) (top) and θ vs. log(f) (bottom); d) ε' vs. log(f) (top) and ε" vs. log(f) (bottom).

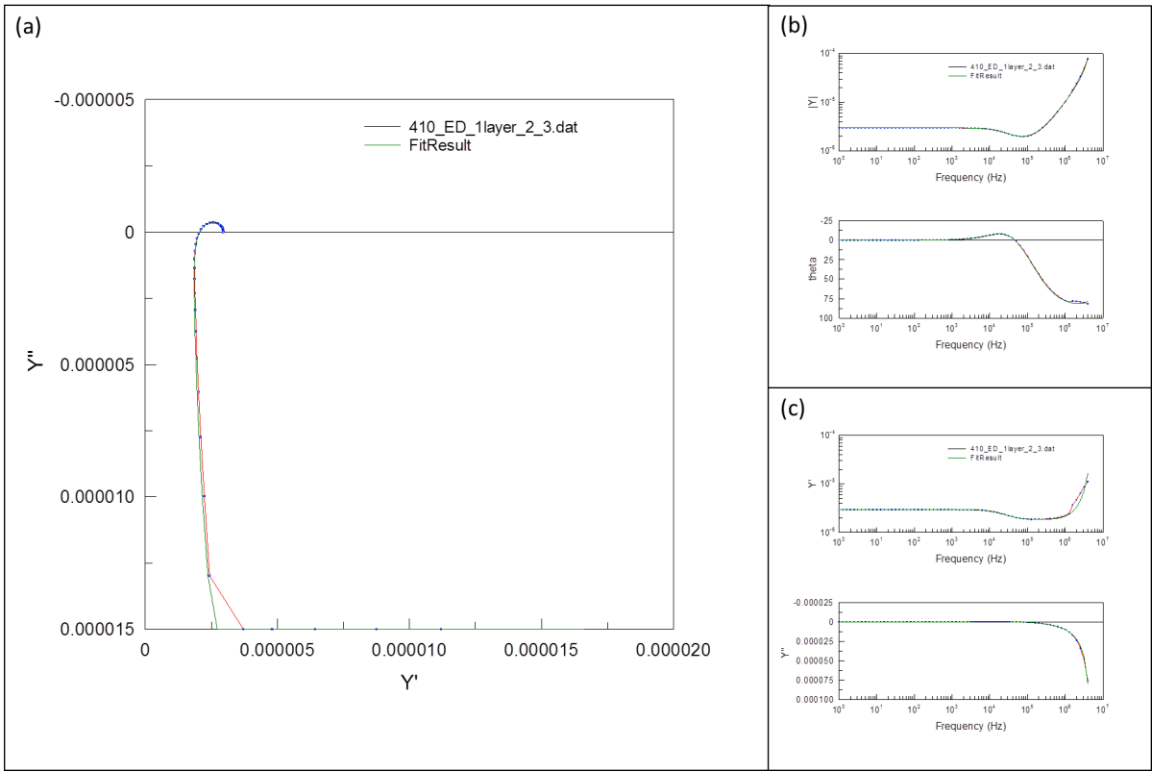

Figure B.5: Real data and curve fit result for admittance (Y*) results. a) Y" vs. Y'; b) log(|Y|) vs. log(f) (top) and θ vs. log(f) (bottom); c) Y' vs. log(f) (top) and Y" vs. log(f) (bottom).

REFERENCES

[1] M. C. Barr, J. A. Rowehl, R. R. Lunt, J. Xu, A. Wang, C. M. Boyce, S. G. Im, V. Bulovic, and K. K. Gleason, "Direct Monolithic Integration of Organic Photovoltaic Circuits on Unmodified Paper," *Adv. Mater.,* vol. 23, pp. 3500-3505, 2011.

[2] Z. Weng, Y. Su, D.-W. Wang, F. Li, J. Du, and H.-M. Cheng, "Graphene-Cellulose Paper Flexible Supercapacitors," *Advanced Energy Materials,* vol. 1, pp. 917-922, 2011.

[3] X. Li, W. Liu, M. Li, Y. Li, and M. Ge, "Characterization and Cr (VI) Adsorption Properties of Polyaniline/Filter-Paper Composite," *Polymer Composites,* 2013.

[4] Y. Meng, Y. Lai, X. Jiang, Q. Zhao, and J. Zhan, "Silver nanoparticles decorated filter paper via self-sacrificing reducation for membrane extraction surface-enhanced Raman spectroscopy detection," *Analyst,* vol. 138, pp. 2090-2095, 2013.

[5] R. L. Muhlbauer, S. M. Joshi, and R. A. Gerhardt, "The effect of substrate pore size on the network interconnectivity and electrical properties of dropcasted multiwalled carbon nanotube thin films," *Journal of Materials Research,* vol. 28, pp. 1617-1624, 2013.

[6] H. W. Haslach, "The Moisture and Rate-Dependent Mechanical Properties of Paper: A Review," *Mechanics of Time-Dependent Materials,* vol. 4, pp. 169-210, 2000.

[7] S. Borodulina, "Micromechanical Behavior of Fiber Networks," KTH School of Engineering Sciences, Department of Solid Mechanics, Royal Institute of Technology, Stockholm, Sweden, 2013.

[8] R. Martins, L. Pereira, and E. Fortunato, "Electrics With and On Paper," in *Transparent Oxide Electronics: From Materials to Devices*, P. Barquinha, Ed., ed Hoboken, NJ: John Wiley & Son, LTD, 2012, pp. 211-266.

[9] S. Simula, S. Ikalainen, K. Niskanen, T. Varpula, H. Seppa, and A. Paukku, "Measurement of the Dielectric Properties of Paper," *Journal of Imaging Science and Technology,* vol. 43, pp. 472-477, 1999.

[10] E. J. Murphy, "The dependence of the conductivity of cellulose, silk, and wool on their water content," *Journal of Physics and Chemistry of Solids,* vol. 16, pp. 115-122., 1960.

[11] D. Tobjörk and R. Österbacka, "Paper Electronics," *Advanced Materials,* vol. 23, pp. 1935-1961, 2011.

[12] C. Q. Peng, Y. S. Thio, and R. A. Gerhardt, "Conductive paper fabricated by layer-by-layer assembly of polyelectrolytes and ITO nanoparticles," *Nanotechnology,* vol. 19, p. 505603, 2008.

[13] K. Kordas, T. Mustonen, G. Toth, H. Jantunen, M. Lajunen, C. Soldano, S. Talapatra, S. Kar, R. Vajtai, and P. M. Ajayan, "Inkjet Printing of Electrically Conductive Patterns of Carbon Nanotubes," *Small,* vol. 2, pp. 1021-1025, 2006.

[14] S. M. Lyth and S. R. Silva, "Field emission from multiwall carbon nanotubes on paper substrates," *Appl. Phys. Lett.,* vol. 90, p. 173124, 2007.

[15] S. M. Lyth, S. J. Henley, and S. R. P. Silva, "Improved Field Emission via Laser Processing of Carbon Nanotubes on Paper Substrates, ," *J. Vac. Sci. Technol. B,* vol. 27, pp. 1068-1071, 2009.
[16] L. Hu, J. W. Choi, Y. Yang, S. Jeong, F. LaMantia, L.-F. Cui, and Y. Cui, "Highly Conductive Paper for Energy-Storage Devices," *PNAS,* vol. 106, pp. 21490-21494, 2009.
[17] L. Hu and Y. Cui, "Energy and environmental nanotechnology in conductive paper and textiles," *Energy Environ. Sci.,* vol. 5, pp. 6423-6435, 2012.
[18] S. Hu, R. Rajamani, and X. Yu, "Flexible solid-state paper based carbon nanotube supercapacitor," *Appl. Phys. Lett.,* vol. 100, p. 104103, 2012.
[19] S. Iijima, "Helical Microtubes of Graphitic Carbon," *Nature,* vol. 354, 1991.
[20] S. Iijima and T. Ichinashi, "Single-Shell Carbon Nanotubes of 1-nm Diameter," *Nature,* vol. 363, pp. 603-605, 1993.
[21] D. Hecht, L. Hu, and G. Irvin, "Emerging Transparent Electrodes Based on Thin Films of Carbon Nanotubes, Graphene, and Metallic Nanostructures, ," *Advanced Materials,* vol. 23, pp. 1482-1513, 2011.
[22] T. Durkop, S. A. Getty, E. Cobas, and M. S. Fuhrer, "Extraordinary Mobility in Semiconducting Carbon Nanotubes," *Nano Lett,* vol. 4, pp. 35-39, 2004.
[23] Z. Yao, C. L. Kane, and C. Dekker, "High-Field Electrical Transport in Single-Wall Carbon Nanotubes," *Phys. Rev. Lett.,* vol. 84, pp. 2941-2944, 2000.
[24] J. Hone, "Carbon Nanotubes: Thermal Properties," in *Dekker Encyclopedia of Nanoscience and Nanotechnology*, ed New York: Marcel Dekker Inc, 2004.
[25] A. Peigney, C. Laurent, E. Flahaut, R. R. Bacsa, and A. Rousset, "Specific surface area of carbon nanotubes and bundles of carbon nanotubes," *Carbon,* vol. 39, pp. 507-514, 2001.
[26] M. P. Anantram and F. Leonard, "Physics of carbon nanotube electronic devices," *Rep. Prog. Phys.,* vol. 69, pp. 507-561, 2006.
[27] R. Saito, M. Fujita, G. Dresselhaus, and M. S. Dresselhaus, "Electronic structure of chiral graphene tubules," *Appl. Phys. Lett.,* vol. 60, pp. 2204-2206, 1992.
[28] C. T. White and J. W. Mintmire, "Single-Walled Carbon Nanotubes: Structures and Symmetries," in *Dekker Encyclopedia of Nanoscience and Nanotechnology*. vol. 5, J. A. Schwarz, C. I. Contescu, and K. Putyera, Eds., ed New York: Marcel Dekker, Inc, 2004.
[29] M. Meyyanppan(ed), *Carbon Nanotubes: Science and Applications*. Boca Raton, Fl: CRC Press, 2005.
[30] R. Sharma, S.-W. Chee, A. Herzing, R. Miranda, and P. Rez, "Evaluation of the Role in Au in Improving Catalytic Activity of Ni Nanoparticles for the Formation of One-Dimensional Carbon Nanostructures," *Nano Lett,* vol. 11, pp. 2464-2471, 2011.
[31] X. Z. Liao, A. Serquis, Q. X. Jia, D. E. Peterson, Y. T. Zhu, and H. F. Xu, "Effect of catalyst composition on carbon nanotube growth," *Appl. Phys. Lett.,* vol. 82, pp. 2694-2696, 2003.
[32] W. S. Su, T. C. Leung, and C. T. Chan, "Work Function of Single-Walled and Multiwalled Carbon Nanotubes: First Principles Study," *Physical Review B,* vol. 76, p. 235413, 2007.

[33] O. Lee, J. Jung, S. Doo, S.-S. Kim, T.-H. Noh, K.-I. Kim, and Y.-S. Lim, "Effects of Temperature and Catalysts on the Synthesis of Carbon Nantotubes by Chemical Vapor Deposition," *Met. Mater. Int.*, vol. 16, pp. 663-667, 2010.
[34] R. L. Muhlbauer and R. A. Gerhardt, "A Review on the Synthesis of Carbon Nanotube Thin Films," in *Carbon Nanotubes: Synthesis and Properties*, A. Mishra, Ed., ed New York: Nova Science Publishers, Inc, 2012.
[35] S. G. Louie, "Electronic Properties, Junctions, and Defects of Carbon Nanotubes," in *Carbon Nanotubes, Topics in Applies Physics*, M. S. Dresselhaus, G. Dresselhaus, and P. Avouris, Eds., ed Heidelberg: Springer-Verlag, 2001.
[36] D. Hecht, L. Hu, and G. Gruner, "Conductivity scaling with bundle length and diameter in single walled carbon nanotube networks," *Appl. Phys. Lett.*, vol. 80, p. 133112, 2006.
[37] D. A. Jack, C.-S. Yeh, Z. Liang, S. Li, J. G. Park, and J. C. Fielding, "Electrical Conductivity Modeling and Experimental Study of Densely Packed SWCNT Networks," *Nanotechnology*, vol. 21, p. 195703, 2010.
[38] P. N. Nirmalraj, P. E. Lyons, S. De, J. N. Coleman, and J. J. Boland, "Electrical Connectivity in Single-Walled Carbon Nanotube Networks," *Nano Lett*, vol. 9, pp. 3890-3895, 2009.
[39] M. P. Garrett, I. N. Ivanov, R. A. Gerhardt, A. A. Puretzky, and D. B. Geohegan, "Separation of junction and bundle resistances in single wall carbon nanotube percolation networks by impedance spectroscopy," *Appl. Phys. Lett.*, vol. 97, p. 163105, 2010.
[40] P. Dharap, Z. Li, S. Nagarajaiah, and E. Barrera, "Nanotube film based on single-wall carbon nanotubes for strain sensing," *Nanotechnology*, vol. 15, pp. 379-382, 2004.
[41] J. Bahr, J. Yang, D. Kosynkin, M. Bronikowski, R. Smalley, and J. Tour, "Functionalization of Carbon Nanotubes by Electrochemical Reduction of Aryl Diazonium Salts: A Bucky Paper Electrode," *J. Am. Chem. Soc.*, vol. 123, pp. 6536-6542, 2001.
[42] E. Barsoukov and J. R. Macdonald, *Impedance Spectroscopy: Theory, Experiment, and Applications*, 2nd ed.: Wiley-Interscience, 2005.
[43] J. R. Macdonald, "Impedance Spectroscopy," *Ann. Biomed. Eng.*, vol. 20, pp. 289-305, 1992.
[44] R. A. Gerhardt, "Impedance and mobility spectra," in *Encyclopedia of Condensed Matter Physics*, ed New York: Elsevier, 2005.
[45] S. Joshi, "Effect of Heat and Plasma Treatments on the Electrical and Optical Properties of Colloidal Indium Tin Oxide Films," PhD, School of Materials Science and Engineering, Georgia Institute of Technology, Atlanta, GA, 2013.
[46] T. Pruyn, "Investigation of Percolation in Borosilicate Glass Matrix Composites Containing Conducting Segregated Networks," PhD, Materials Science and Engineering, Georgia Institute of Technology, Atlanta, GA, 2014.
[47] R. Gerhardt, ""MSE 7140: Impedance and Dielectric Spectroscopy"," ed. Georgia Institute of Technology, 2010.
[48] B. D. Bertram, "Effects of Interfaces and Preferred Orientation on the Electrical Response of Composites of Alumina and Silicon Carbide Whiskers," PhD,

Materials Science and Engineering, Georgia Institute of Technology, Atlanta, GA, 2011.
[49] R. Gerhardt and A. Nowick, "Grain-Boundary Effect in Ceria Dope with Trivalent Cations: I, Electrical Measurements," *J. Am. Ceram. Soc.*, vol. 69, pp. 641-646, 1986.
[50] W. Cao and R. Gerhardt, "Calculations of various relaxation times and conductivity for a single dielectric relaxation process," *Solid State Ionics,* vol. 42, pp. 213-221, 1990.
[51] R. Gerhardt, "Impedance and dielectric spectrocospy revisited: distinguishing localized relaxation from long-range conductivity," *Journal of Physics and Chemistry of Solids,* vol. 55, pp. 1491-1506, 1994.
[52] I. Hodge, M. Ingram, and A. West, "Impedance and modulus spectroscopy of polycrystalline solid electrolytes," *Journal of Electroanalytical Chemistry and Interfacial Electrochemistry,* vol. 74, pp. 125-143, 1976.
[53] L. Huang, K. Chen, C. Peng, and R. A. Gerhardt, "Highly conductive paper fabricated with multiwalled carbon nanotubes and poly(3,4-ethylenedioxythiophene)-poly(styrenesulfonate) by unidirectional drying," *J. Mater. Sci.*, vol. 46, pp. 6648-6655, 2011.
[54] A. Blanch, C. Lenehan, and J. Quinton, "Optimizing Surfactant Concentrations for Dispersion of Single-Walled Carbon Nanotubes in Aqueous Solution," *J. Phys. Chem. B,* vol. 114, pp. 9805-9811, 2010.
[55] M. Islam, E. Rojas, D. Bergey, A. Johnson, and A. Yodh, "High Weight Fraction Surfactant Solubilization of Single-Walle Carbon Nanotubes in Water," *Nano Letters,* vol. 3, pp. 269-273, 2003.
[56] R. Bandyopadhyaya, E. Nativ-Roth, O. Regev, and Y. Yerushalmi-Rozen, "Stabilization of Individual Carbon Nanotubes in Aqueous Solutions," *Nano Letters,* vol. 2, pp. 25-28, 2002.
[57] W. A. deHeer, W. S. Bacsa, A. Chatelain, T. Gerfin, R. Humphrey-Baker, L. Forro, and D. Ugarte, "Aligned carbon nanotube films: Production and optical and electronic properties," *Science,* vol. 268, p. 845, 1995.
[58] J. Waddell, R. Ou, C. Capozzi, S. Gupta, C. Parker, R. Gerhardt, K. Seal, S. Kalinin, and A. Baddorf, "Detection of Percolating Paths in Polyhedral Segregated Network Composites Using Electrostatic Force Microscopy and Conductive Atomic Force Microscopy," *Applied Physics Letters,* vol. 95, p. 233122, 2009.
[59] A. Rinzler, J. Liu, H. Dai, P. Nikolaev, C. Huffman, F. Rodriguez-Macias, P. Boul, A. Lu, D. Heymann, D. Colbert, R. Lee, J. Fischer, A. Rao, P. Eklund, and R. Smalley, "Large-scale purification of single-wall carbon nanotubes: process, product, and characterization," *Applied Physics A,* vol. 67, pp. 29-37, 1998.
[60] Z. Wu, Z. Chen, X. Du, J. Logan, J. Sippel, M. Nikolou, K. Kamaras, J. Reynolds, D. Tanner, A. Hebard, and A. Rinzler, "Transparent Conductive Carbon Nanotube Films," *Science,* vol. 305, pp. 1273-1276, 2004.
[61] J.-M. Bonard, J.-P. Salvetat, T. Stockli, W. deHeer, L. Forro, and A. Chatelain, "Field emission from single-wall carbon nanotube films," *Applied Physics Letters,* vol. 73, pp. 918-920, 1998.

[62] J. Lehman, M. Terrones, E. Mansfield, K. Hurst, and V. Meunier, "Evaluating the characteristics of multiwall carbon nanotubes," *Carbon,* vol. 49, pp. 2581-2602, 2011.
[63] (04-07-2014). Available: http://www.sigmaaldrich.com/spectra/ftir/FTIR004653.PDF
[64] R. Muhlbauer, T. Pruyn, W. Puckett, and R. Gerhardt, "Effect of graphitic filler size and shape on the microstructure, electrical percolation behavior and thermal properties of nanostructured multilayered carbon films deposited onto paper substrates," *J. Mater. Res.,* vol. 29, pp. 472-484, 2014.
[65] C.-W. Nan, Y. Shen, and J. Ma, "Physical Properties of Composites Near Percolation," *Annu. Rev. Mater. Res.,* vol. 40, pp. 131-151, 2010.
[66] R. Muhlbauer and R. Gerhardt, "Determining In-Plane and Thru-Plane Percolation Thresholds for Carbon Nanotube Thin Films Deposited on Paper Substrates Using Impedance Spectroscopy," *MRS Proc,* vol. 1549, pp. 117-122, 2013.
[67] G. J. Brug, A. L. G. vandenEeden, M. Sluyters-Rehbach, and J. H. Sluyters, "The analysis of electrode impedances complicated by the presence of a constant phase element," *Journal of Electroanalytical Chemistry and Interfacial Electrochemistry,* vol. 176, p. 275, 1984.
[68] P. Zoltowski, "On the electrical capacitance of interfaces exhibiting constant phase element behavior," *Journal of Electroanalytical Chemistry,* vol. 443, pp. 149-154, 1998.
[69] M. B. Nardelli, J.-L. Fattebert, D. Orlikowski, C. Roland, Q. Zhao, and J. Bernholc, "Mechanical properties, defects and electronic behavior of carbon nanotubes," *Carbon,* vol. 38, pp. 1703-1711, 2000.
[70] C. Berger, Y. Yi, Z. Wang, and W. deHeer, "Multiwalled carbon nanotubes are ballistic conductors at room temperature," *Applied Physics A,* vol. 74, pp. 363-365, 2002.
[71] J. Bai and A. Allaoui, "Effect of the length and the aggregate size of MWNTs on the improvement efficiency of the mechanical and electrical properties of nanocomposites- experimental investigation," *Composites: Part A,* vol. 34, pp. 689-694, 2003.
[72] M. Islam, E. Rojas, D. Bergey, A. Johnson, and A. Yodh, "High Weight Fraction Surfactant Solubilzation of Single-Wall Carbon Nanotubes in Water," *Nano Letters,* vol. 3, pp. 269-273, 2003.
[73] A. Ishaq, L. Yan, and D. Zhu, "The electrical conductivity of carbon nanotube sheets by ion beam irradiation," *Nuclear Instruments and Methods in Physics Research B,* vol. 267, pp. 1779-1782, 2009.
[74] S. Gupta, N. Smith, R. Patel, and R. Giedd, "Investigations of dc electrical properties in electron-beam modified carbon nanotube films: single- and multiwalled," *MRS Proc,* vol. 887, 2005.
[75] B. Dan, G. C. Irvin, and M. Pasqali, "Continuous and Scalable Fabrication of Transparent Conducting Carbon Nanotube Films," *ACS Nano,* vol. 3, pp. 835-843, 2009.

[76] A. Tewari and A. Gokhale, "Estimation of three-dimensional grain size distribution from microstructural serial sections," *Materials Characterization,* vol. 46, pp. 329-335, 2001.
[77] H. Agarwal, A. Gokhale, S. Graham, and M. Horstemeyer, "Void growth in 6061-aluminum alloy under triaxial stress state," *Materials Science and Engineering A,* vol. 341, pp. 35-42, 2003.
[78] M. Al-Khedler, C. Pezeshki, J. McHale, and F. Knorr, "Quality classification via Raman identification and SEM analysis of carbon nanotube bundles using artificial neural networks," *Nanotechnology,* vol. 18, p. 355703, 2007.
[79] J.-Y. Lee, S. Connor, Y. Cui, and P. Peumans, "Solution-Processed Metal Nanowire Mesh Transparent Electrodes," *Nano Letters,* vol. 8, pp. 689-692, 2008.
[80] J. Ryszkowska, "Quantitative image analysis of polyurethane/carbon nanotube composite microstructures," *Materials Characterization,* vol. 60, pp. 1127-1132, 2009.
[81] H. Okimoto, T. Takenobu, K. Yanagi, Y. Miyata, H. Shimotani, H. Kataura, and Y. Iwasa, "Tunable Carbon Nanotube Thin-Film Transistors Produced Exclusively via Inkjet Printing," *Adv. Mater.,* vol. 22, pp. 3981-3986, 2010.
[82] J. Runyan, R. Gerhardt, and R. Ruh, "Electrical Properties of Boron Nitride Matrix Composites: I, Analysis of McLachlan Equation and Modeling of the Conductivity of Boron Nitride–Boron Carbide and Boron Nitride–Silicon Carbide Composites," *J. Am. Ceram. Soc.,* vol. 84, pp. 1490-1496, 2001.
[83] L. Hu, D. S. Hecht, and G. Gruner, "Percolation in Transparent and Conducting Nanotube Networks," *Nano Lett,* vol. 4, pp. 2513-2517, 2004.
[84] S. Crawford and M. Buehler, "In silico assembly and nanomechanical characterization of carbon nanotube buckypaper," *Nanotechnology,* vol. 21, p. 265706, 2010.
[85] L. Wang and Z.-M. Dang, "Carbon nanotube composites with high dielectric constant at low percolation threshold," *Applied Physics Letters,* vol. 87, p. 042903, 2005.